

Microbial Surfaces

ACS SYMPOSIUM SERIES **984**

Microbial Surfaces

Structure, Interactions, and Reactivity

Terri A. Camesano, Editor
Worcester Polytechnic Institute

Charlene M. Mello, Editor
U.S. Natick Soldier Center

Sponsored by the
ACS Division of Colloid and Surface Chemistry



American Chemical Society, Washington, DC



Library of Congress Cataloging-in-Publication Data

Microbial surfaces : structure, interactions, and reactivity / [edited by] Terri A. Camesano, Charlene M. Mello.

p. cm.—(ACS symposium series ; 984)

“The symposium Structure, Interactions and Reactivity at Microbial Interfaces was held September 10–11, 2006 as part of the 232nd ACS National Meeting”—Preface

Includes bibliographical references and index.

ISBN 978-0-8412-7430-3 (alk. paper)

1. Bacterial cell surfaces—Congresses. 2. Microorganisms—Adhesion—Congresses. 3. Biofilms—Congresses.

I. Camesano, Terri A. II. Mello, Charlene M. III. American Chemical Society. Meeting (232nd : 2006 : San Francisco, Calif.)

QR77.35.M552 2007
579—dc22

2007060565

The paper used in this publication meets the minimum requirements of American National Standard for Information Sciences—Permanence of Paper for Printed Library Materials, ANSI Z39.48–1984.

Copyright © 2008 American Chemical Society

Distributed by Oxford University Press

All Rights Reserved. Reprographic copying beyond that permitted by Sections 107 or 108 of the U.S. Copyright Act is allowed for internal use only, provided that a per-chapter fee of \$36.50 plus \$0.75 per page is paid to the Copyright Clearance Center, Inc., 222 Rosewood Drive, Danvers, MA 01923, USA. Republication or reproduction for sale of pages in this book is permitted only under license from ACS. Direct these and other permission requests to ACS Copyright Office, Publications Division, 1155 16th Street, N.W., Washington, DC 20036.

The citation of trade names and/or names of manufacturers in this publication is not to be construed as an endorsement or as approval by ACS of the commercial products or services referenced herein; nor should the mere reference herein to any drawing, specification, chemical process, or other data be regarded as a license or as a conveyance of any right or permission to the holder, reader, or any other person or corporation, to manufacture, reproduce, use, or sell any patented invention or copyrighted work that may in any way be related thereto. Registered names, trademarks, etc., used in this publication, even without specific indication thereof, are not to be considered unprotected by law.

PRINTED IN THE UNITED STATES OF AMERICA

Foreword

The ACS Symposium Series was first published in 1974 to provide a mechanism for publishing symposia quickly in book form. The purpose of the series is to publish timely, comprehensive books developed from ACS sponsored symposia based on current scientific research. Occasionally, books are developed from symposia sponsored by other organizations when the topic is of keen interest to the chemistry audience.

Before agreeing to publish a book, the proposed table of contents is reviewed for appropriate and comprehensive coverage and for interest to the audience. Some papers may be excluded to better focus the book; others may be added to provide comprehensiveness. When appropriate, overview or introductory chapters are added. Drafts of chapters are peer-reviewed prior to final acceptance or rejection, and manuscripts are prepared in camera-ready format.

As a rule, only original research papers and original review papers are included in the volumes. Verbatim reproductions of previously published papers are not accepted.

ACS Books Department

Preface

The Symposium *Structure, Interactions, and Reactivity at Microbial Interfaces* was held September 10–11, 2006 as part of the 232nd American Chemical Society National Meeting. The chapters in this book describe research on several aspects of microbial interfaces, including bacterial detection, prevention of biofilm development, and prediction of bacterial transport in the environment. Experimental and modeling studies are represented as well as some reviews.

Acknowledgments

We greatly appreciate the efforts of the chapter reviewers, who helped strengthen and improve each contribution. In particular, we thank Paola Pinzon-Arango and Joshua Strauss for their additional rounds of editing and reviewing all of the chapters in this book.

We thank the Army Research Office and DARPA for providing financial support to the speakers to attend the Symposium in San Francisco, California.

Terri A. Camesano

Department of Chemical Engineering
Worcester Polytechnic Institute
100 Institute Road
Worcester, MA 01609

Charlene M. Mello

Macromolecular Science Team
Natick Soldier Research Development and Engineering Center
Kansas Street
Natick, MA 01760

Microbial Surfaces

Chapter 1

Introduction

Terri A. Camesano¹, Charlene M. Mello²

¹Department of Chemical Engineering, Worcester Polytechnic Institute,
Worcester, MA 01609²Natick Soldier Research Development and
Engineering Center, Natick, MA 01760

Overview

The Symposium *Structure, Interactions and Reactivity at Microbial Interfaces* was held September 10-11, 2006 as part of the 232nd ACS National Meeting. During the same week that we were gathered in San Francisco to learn about the latest research involving microbial systems and microbial interactions, the U.S. was facing an outbreak of *Escherichia coli* (*E. coli*) O157:H7 in spinach that affected persons in 26 states, leading ultimately to over 200 people becoming sick and several deaths. The need for research on microbial inactivation and microbial interactions with surfaces was made all the more obvious by this unfortunate situation.

This Symposium Series book features articles on a variety of topics related to microbial interfaces, with applications ranging from food safety, pathogen detection, bacterial inactivation strategies or novel therapies, to pathogen migration in porous media in natural and engineered biological processes. While most of the papers are geared towards a specific application, they all contain fundamental information regarding bacterial behavior at interfaces that allows their contents to translate to other problems, as well. For example, many parallels are noted between the way bacteria interact with protein-coated polymers on a catheter and bacterial-peptide interactions in a cellular detection assay. An overlying theme of all the manuscripts is that they represent studies of microbial interfaces using the most sophisticated experimental and modeling tools available, and many feature interdisciplinary approaches to tackling the given problems.

Signaling and Sensing

Microorganisms predominantly exist in communities rather than as free-living cells. These communities develop on a diverse array of surfaces generating biofilms. The behavior of individual organisms in the microbial community can be altered through chemical interactions. This mode of communication to ensure coordination, establish cues and chemical manipulations is often referred to as quorum sensing. In the first chapter, Kumari et al. provide an introduction to quorum chemical signaling and present an intriguing approach of utilizing signaling molecules as biomarkers of disease (1). The group has developed a whole cell sensing system for the detection of a common signaling molecule, N-acylated homoserine lactone (AHL), by regulating the expression of the luciferase reporter protein with an AHL inducible promoter system. Biological samples from healthy volunteers and a Crohn's patient were used to evaluate the sensing system.

More typically, microbial diagnostic tools are divided into two broad categories: cellular and acellular. Because of the potential to preserve cellular morphology as well as the structural and biochemical nature of the molecular targets within a cell; *in situ* or cellular microbial diagnostics are preferred. Two chapters in this section speak to this concept. Brehm-Stecher presents an excellent review of methods for *in situ*, culture-independent detection of microbial cells (2). Special emphasis is given to nucleic acid based methods, particularly fluorescence *in situ* hybridization (FISH). However, cell based sensors and the idea of utilizing antimicrobials as detection reagents are also discussed. The final chapter of this section expands upon the notion of employing antimicrobial peptides as detection reagents for selective microbial capture. Mello and Soares review published reports which reveal important peptide design features for selective antimicrobial activity (3). The focus of their chapter is on identification of peptide characteristics (i.e assembly state, hydrophobicity, charge and flexibility) which improve binding selectivity. The authors present results demonstrating selective peptide binding to pathogenic microorganisms, with an aim of unraveling the important peptide characteristics that control binding selectivity and antimicrobial activity.

Prevention of Biofilm Formation

Communities of microorganisms attached to a surface or interface are often referred to as biofilms. The formation of biofilms is a result of specific environmental cues, such as nutrient and oxygen availability (4). Microbially-induced corrosion of metallic materials and surface contamination by biofilms of foodborne pathogens lead to significant financial burdens for the average consumer. Biofilms are particularly important in the development of nosocomial infections on biomedical devices (5, 6). Implant surfaces, catheters, and

endotracheal tubes are among the most common substrates for biofilm formation. Growth of the infecting bacteria on a surface protects the organisms from the host immune system and antibiotic therapy. As a result, prevention of infection by hindering biofilm formation is an area of intense investigation. The contributions to this section all address this fundamental area of research.

First, Savage et al. describe a novel synthetic approach to creating antimicrobials that mimic the key aspects of naturally occurring peptide antibiotics: positive charge and facial amphiphilicity. They modify cholic acid by introducing amine functionality at three key hydroxyl groups and the inclusion of an alky chain (7). These new chemically altered molecules, identified as ceragenins, render the molecule cationic, amphiphilic, and protease resistant, while possessing broad spectrum antimicrobial activity. When attached covalently to polyurethane based polymers, the ceragenins retrain their activity. Furthermore, thin film coatings onto medical grade foams result in a slow release of polymer and retain their activity for at least three weeks, which will help to impede the formation of biofilms.

Self-assembled monolayers (SAMs) represent an excellent class of molecules to use for coating materials due to their versatility, uniformity, and ease of construction. Strauss et al. optimized the design of batch assays to evaluate the performance of SAMs in preventing retention and monitoring viability of *Staphylococcus epidermidis* (8). SAMs based on ten carbon alkyl chains with varying terminal functional groups were characterized by atomic force microscopy (AFM), ellipsometry and contact angle measurements. All SAMs investigated decreased bacterial retention compared to control surfaces. Furthermore, the performance of the SAMs was evaluated in the presence of fetal bovine serum, to ensure that the anti-adhesion and antibacterial effects were still operative when serum proteins were present. These fundamental investigations of adhesion and viability are relevant to a number of biomedical applications.

The final two chapters of this section probe the basis for cranberry juice as a preventive measure for urinary tract infections. B. Johnson and co-workers identify high molecular weight proanthocyanidins as the active component in the juice (9). Purification of proanthocyanidins from cranberry juice, grape juice, black tea, and whole cranberries revealed a concentration dependent binding of lipopolysaccharide. The authors suggest that this interaction may interfere with membrane binding of mammalian cells. In a more applied study, Camesano et al., in the final chapter of this section, coat silicone rubber (urinary catheter mimic) with cranberry juice extract to explore its affect on *E. coli* adhesion (10). To simulate a realistic environment, sterilized artificial urine carried the cells through a flow chamber designed to investigate colonization of model catheters. Cranberry extract dramatically reduced the attachment of *E. coli* to the polymer surfaces. In a separate experiment, the authors demonstrated that bacterial cells grown in the presence of cranberry juice had a significant propensity to

aggregate. Further work in these areas will lead to improved understanding of the role of cranberry compounds on inhibiting bacterial adhesion.

Surface Characterization and Microscopy Experiments

“New truths become evident when new tools become available.”

---Dr. Rosalyn Yalow, Nobel Prize Laureate in
Physiology or Medicine, 1977

Dr. Yalow's statement is extremely appropriate to the description of new tools that allow forces to be measured that characterize bacterial interactions at surfaces. The chapters in this section address techniques such as AFM as an imaging and force quantifying technique, the Surface Forces Apparatus (SFA) for measuring bacterial adhesion and elastic properties, and a newly extended micropipette method for measuring very strongly adhesive bacterial forces.

The section starts with an overview of the use of AFM to examine bacterial ultrastructure and surface physical properties and interactions, by Abu-Lail (11). Scanning probe microscopes, which for biological applications predominantly involve AFM, have become the instrument of choice for characterizing bacterial ultrastructure, physicochemical properties, and adhesion forces, having been used to study bacteria or microbes in >900 studies (12). Abu-Lail reports on recent fundamental advances in the use of AFM imaging techniques for bacterial characterization of structures including flagella and other proteins. From a more quantitative perspective, the AFM can be used to detect changes in the surface potential of the bacterial cell membrane, to quantify cell surface roughness and cellular elasticity, and to detect forces of adhesion between bacteria and surfaces, which can range from pico- to nano-Newtons in magnitude. A natural complement is the proceeding chapter by Liu and Camesano, where currently available techniques for immobilizing bacterial cells for AFM experiments in imaging or force characterization are discussed (13). Proper preparation of biological samples for the AFM has long been a problem and an important consideration for researchers in this field. This chapter presents new experimental evidence demonstrating a relationship between chemical and mechanical immobilization methods for Gram-negative and Gram-positive bacteria and the observed AFM images. The authors highlight important considerations for researchers wishing to obtain artifact-free AFM images and measurements on bacterial cells.

An AFM chapter by Yongsunthon et al. (14) uses the AFM to tackle a very difficult question for the medical microbiology community right now- how do healthy vs. infected bacterial cells differ in their molecular adhesion properties? This chapter demonstrates exciting evidence showing that strains of

Staphylococcus aureus isolated from infected patients display different binding profiles with a fibronectin-coated AFM tip than observed for non-infective strains of the same bacterium. This molecular-level information can help us to better understand the differences between pathogenic and non-pathogenic bacterial strains, which will ultimately lead to better therapies.

The chapter by Basel et al. (15) concerns the world's most grave pathogen, *Mycobacterium tuberculosis*, which is responsible for tuberculosis infections (TB). Tuberculosis is the leading cause of death from a single pathogenic agent in the world today (16). There is a deadly synergy between TB and HIV, with HIV causing latent TB to develop into the active form, and TB in turn accelerating HIV into progressive AIDS (17). Mycobacteria are impermeable to many antimicrobial agents because of the waxy barrier provided by their cell envelope. Basel et al. use AFM to characterize the outer leaflet of the cell membrane of this bacterium, and to measure how difficult it is to shear the bacteria from a mica surface. These results can lead to better developments of disinfection strategies.

In addition to AFM, two other techniques are discussed which can be very useful and complementary in helping to quantify bacterial adhesion and surface properties. Curry et al. use SFA to measure the elastic and adhesive properties of *Pseudomonas aeruginosa* PAO1 films under dried conditions (18). The genome of *P. aeruginosa* PAO1 contains over 6.3 million base pairs, making it the largest known bacterial genome (19). The genome's size and complexity are believed to be responsible for the bacterium's resistance to many antibacterial agents and adaptability to numerous environments. PAO1 often is present in biofilm communities, rather than as individual or planktonic cells. Curry et al. measure the adhesion and elastic properties of PAO1 dried films with SFA. The larger geometry of the SFA offers an advantage for probing bacterial clusters and films, compared to AFM, which is better for probing individual cells.

Micropipette aspiration is a classic force measurement technique that has been used widely to probe mammalian cells (20). A single cell is brought into contact with a planar substrate, such as a vesicle or membrane bilayer, and at a given time point, a pipette holding the cell (perpendicular to the bilayer) is retracted, and the aspiration pressure is used to calculate the adhesion force between the two. In a later advancement, (21), the biomembrane force probe (BFP) was developed. This probe was used as a way of carefully controlling the loading force applied between ligand-receptor pairs (22). Li and Tang report on a new technique by which two micropipettes are used to measure the adhesion forces between the aquatic and soil bacterium *Caulobacter crescentus* and a glass surface (23). It is striking that the magnitude of the forces measured by this technique were on order of μN , representing forces that are orders of magnitude larger than those typically detected with SFA and AFM.

Experiments and Modeling of Bacterial and Colloid Transport in the Environment

A subsection of our Symposium dealt with the important topic of predicting the transport and fate of bacteria in saturated porous media. Pathogenic bacteria, viruses, and protozoa can contaminate drinking water supplies through livestock waste or incompletely treated wastewater effluents (24, 25). Bacterial transport is also a key component in the success of bioremediation (26) and influences the fate of other molecules such as metals and organic macromolecules (27). One key challenge in this field of research is that researchers must consider the multiple scales of interactions, from nanometer-scale bacterial-pore interactions up to field scale predictions of transport (28).

Chen et al. describe how surface energy calculations are being used to improve predictions of bacterial transport from a thermodynamic perspective (29). By incorporating thermodynamic free energy calculations into DLVO interaction force profiles, better predictions can be made of bacterial transport in the subsurface, based on consideration of microbial physicochemical properties.

The most widely used method for describing bacterial deposition in porous media is colloid filtration theory (CFT) (30). CFT has been applied to describe the filtration of non-living colloids as well as biological colloids in numerous studies [see, for example ref. (31)]. One of the limitations in using the colloidal model for living bacteria is that it is difficult to gain detailed molecular-level information on bacteria to include in such models. In order to capture the "unique traits of bacteria" into CFT, Nelson describes how mechanistic modeling can be used to better predict certain parameters in CFT (32). Namely, he presents new methodology for modeling the collector efficiency term (the frequency at which colloids contact porous media surfaces or energy barriers) and applies the modified CFT to a bacterial system that accounts for surface biopolymers.

The last chapter, by W.P. Johnson, provides a detailed explanation of how biological and non-biological colloids can be better modeled in porous media by accounting for some important factors that were neglected in prior research, particularly in the dynamic nature of the colloid deposition process (33). Specifically, he shows how hydrodynamic drag forces cause a reduction in actual colloid deposition and cause re-entrainment of deposited colloids. Also, the pore geometry is mathematically altered to account for stagnant flow areas and grain-to-grain contacts.

Conclusions

In summary, the protection of human and animal health and the environment requires that we continue to seek answers to explain the fundamental behavior of

microbes at interfaces. This book can serve as a useful reference tool for those wishing an overview of the field, as well as a launching point for researchers to develop new experimental and modeling tools to investigate bacterial interfacial behavior.

References

1. Kumari, A.; P. P.; S.K. Deo; D. Fomenhoff; H. Shashidhar, and S. Daunert, *Biosensors for quorum chemical sensing molecules: implications of bacterial communication in gastrointestinal disorders*, in *Structure, Interactions and Reactivity at Microbial Interfaces*, ACS Symposium Series, T.A. Camesano and C.M. Mello, Editors. Oxford University Press: New York. In press.
2. Brehm-Stecher, B.F., *Methods for whole cell detection of microorganisms*, in *Structure, Interactions and Reactivity at Microbial Interfaces*, ACS Symposium Series, T.A. Camesano and C.M. Mello, Editors. Oxford University Press: New York. In press.
3. Mello, C.M. and J.W. Soares, *Membrane selectivity of antimicrobial peptides*, in *Structure, Interactions and Reactivity at Microbial Interfaces*, T.A. Camesano and C.M. Mello, Editors. Oxford University Press: New York. In press.
4. Furukawa, S.; S.L. Kuchma, and G.A. O'Toole. *J Bacteriol* **2006**, *188*, 1211.
5. Triandafillu, K.; D.J. Balazs; B.-O. Aronsson; P. Descouts; P. Tu Quoc; C. van Delden; H.J. Mathieu, and H. Harms. *Biomaterials* **2003**, *24*, 1507.
6. An, Y.H. and R.J. Friedman. *Journal of Biomedical Materials Research* **1998**, *43*, 338.
7. Savage, P.B.; J. Nielsen; X.-Z. Lai; Y. Feng; Y. Li; G. Nelson; M.R. Linford, and C. Genberg, *Antibacterial activities of thin films containing ceragenins*, in *Structure, Interactions and Reactivity at Microbial Interfaces*, ACS Symposium Series, T.A. Camesano and C.M. Mello, Editors. Oxford University Press: New York. In press.
8. Strauss, J.; Y. Liu; E. Milkani; W.G. McGimpsey, and T.A. Camesano, *Retention and viability of Staphylococcus epidermidis on protein-coated self-assembled monolayers*, in *Structure, Interactions and Reactivity at Microbial Interfaces*, ACS Symposium Series, T.A. Camesano and C.M. Mello, Editors. Oxford University Press: New York. In press.
9. Johnson, B.J.; J.B. Delehanty; B. Lin, and F.S. Ligler, *New biological activities of plant proanthocyanidins*, in *Structure, Interactions and Reactivity at Microbial Interfaces*, ACS Symposium Series, T.A. Camesano and C.M. Mello, Editors. Oxford University Press: New York. In press.
10. Camesano, T.A.; J.R. Pouliot; J.B. Lofgren, and P.A. Pinzon-Arango, *Cranberry extract as a bacterial anti-adhesive coating*, in *Structure*,

- Interactions and Reactivity at Microbial Interfaces, ACS Symposium Series*, T.A. Camesano and C.M. Mello, Editors. Oxford University Press: New York. In press.
11. Abu-Lail, N.I., *An atomic force microscopy look at the molecular world of living bacteria*, in *Structure, Interactions and Reactivity at Microbial Interfaces, ACS Symposium Series*, T.A. Camesano and C.M. Mello, Editors. Oxford University Press: New York. In press.
 12. *ISI Web of Knowledge, Web of Science*.
 13. Liu, Y. and T.A. Camesano, *Immobilizing Bacteria for Atomic Force Microscopy Imaging or Force Measurements in Liquids*, in *Structure, Interactions and Reactivity at Microbial Interfaces, ACS Symposium Series*, T.A. Camesano and C.M. Mello, Editors. Oxford University Press: New York. In press.
 14. Yongsunthon, R.; V.G.J. Fowler, and S.K. Lower, *Binding forces associated with Staphylococcus aureus biofilms on medical implants*, in *Structure, Interactions and Reactivity at Microbial Interfaces, ACS Symposium Series*, T.A. Camesano and C.M. Mello, Editors. Oxford University Press: New York. In press.
 15. Basel, M.T.; K. Janik; M. Niederweis, and S.H. Bossmann, *Characterization of the outer membrane of M. tuberculosis with atomic force microscopy methods*, in *Structure, Interactions and Reactivity at Microbial Interfaces, ACS Symposium Series*, T.A. Camesano and C.M. Mello, Editors. Oxford University Press: New York. In press.
 16. Zimmerman, B.E. and D.J. Zimmerman, *Killer Germs*. McGraw-Hill: Chicago, IL, 2003.
 17. El-Sadr, W. *The PRN Notebook* **2001**, 6, 4.
 18. Curry, J.E.; C.H. Heo, and R.M. Maier, *Directly measuring the adhesive and elastic properties of bacteria using a surface force apparatus*, in *Structure, Interactions and Reactivity at Microbial Interfaces, ACS Symposium Series*, T.A. Camesano and C.M. Mello, Editors. Oxford University Press: New York. In press.
 19. Stover, C.K.; X.Q. Pham; A.L. Erwin; S.D. Mizoguchi; P. Warrenner; M.J. Hickey; F.S.L. Brinkman; W.O. Hufnagle; D.J. Kowalik; M. Lagrou; R.L. Garber; L. Goltry; E. Tolentino; S. Westbrook-Wadman; Y. Yuan; L.L. Brody; S.N. Coulter; K.R. Folger; A. Kas; K. Larbig; R. Lim; K. Smith; D. Spencer; G.K.S. Wong; Z. Wu; I.T. Paulsen; J. Reizer; M.H. Saier; R.E.W. Hancock; S. Lory, and M.V. Olson. *Nature* **2000**, 406, 959.
 20. Tozeren, A.; K.-L.P. Sung; L.A. Sung; M.L. Dustin; P.-Y. Chan; T.A. Springer, and S. Chien. *J Cell Biol* **1992**, 116, 997.
 21. Evans, E.; K. Ritchie, and R. Merkel. *Biophys J* **1995**, 68, 2580.
 22. Merkel, R.; P. Nassoy; A. Leung; K. Ritchie, and E. Evans. *Nature* **1999**, 397, 50.
 23. Li, G. and J.X. Tang, *Measuring the strength of bacterial adhesion by micromanipulation*, in *Structure, Interactions and Reactivity at Microbial*

- Interfaces, ACS Symposium Series*, T.A. Camesano and C.M. Mello, Editors. Oxford University Press: New York. In press.
24. Mawdsley, J.L.; R.D. Bardgett; R.J. Merry; B.F. Pain, and M.K. Theodorou. *Appl. Soil Ecol.* **1995**, *2*, 1.
 25. Smith, J.E. and J.M. Perdek. *Crit. Rev. Environ. Sci. Technol.* **2004**, *34*, 109.
 26. Fontes, D.E., A.L. Mills, G.M. Hornberger, and J.S. Herman. *Appl. Environ. Microbiol.* **1991**, *57*, 2473.
 27. Fein, J.B. *Chem Geol* **2000**, *169*, 265.
 28. Wood, B.D. and R.M. Ford. *Advances in Water Resources* **2007**, *30*, 1387.
 29. Chen, G.; A.H. Hilton, and M. Williams, *Modeling bacterial adhesion and transport in the environment*, in *Structure, Interactions and Reactivity at Microbial Interfaces*, T.A. Camesano and C.M. Mello, Editors. Oxford University Press: New York. In press.
 30. Yao, K.-M.; M.T. Habibian, and C.R. O'Melia. *Environ. Sci. Technol.* **1971**, *5*, 1105.
 31. Tufenkji, N. *Advances in Water Resources* **2007**, *30*,
 32. Nelson, K.E., *Mechanistic modeling of bacterial transport in saturated porous media*, in *Structure, Interactions and Reactivity at Microbial Interfaces, ACS Symposium Series*, T.A. Camesano and C.M. Mello, Editors. Oxford University Press: New York. In press.
 33. Johnson, W.P., *Mechanisms of retention of biological and non-biological colloids in porous media: wedging and retention in flow stagnation zones in the presence of an energy barrier to deposition*, in *Structure, Interactions and Reactivity at Microbial Interfaces, ACS Symposium Series*, T.A. Camesano and C.M. Mello, Editors. Oxford University Press: New York. In press.

Chapter 2

Biosensors for Quorum Chemical Signaling Molecules: Implications of Bacterial Communication in Gastrointestinal Disorders

Anjali Kumari¹, Patrizia Pasini¹, Sapna K. Deo¹,
Deborah Flomenhoft², Harohalli Shashidhar², and Sylvia Daunert^{1*}

¹Department of Chemistry, University of Kentucky, Lexington, KY, USA.

²Division of Gastroenterology & Nutrition, Department of Pediatrics,
University of Kentucky, Lexington, KY, USA

The role of bacteria in causing biofouling and a wide variety of health imbalances has been long established. Moreover, bacterial load plays a fundamental role in these processes. Bacteria regulate expression of certain specialized genes, including certain behaviors/phenotypes, as a function of their population density. They employ chemical language, i.e., signaling molecules for their communication and group-based coordination. This phenomenon is known as quorum sensing (QS). The signaling molecules generally are *N*-acylated homoserine lactones (AHLs) in Gram-negative bacteria, small peptides in Gram-positive bacteria and a furanosyl borate diester, which is common to both types of bacteria. Thus, to better elucidate the mechanism of pathogenicity in bacteria, it is important to understand bacterial communication. The first step toward that end is to be able to detect the signaling molecules in a sensitive and selective manner. We hypothesize that the levels of these quorum sensing molecules (QSMs) in individuals may correlate with their health status, thus QSMs may be significant as biomarkers of diseases. These biomarkers may serve in the monitoring of disease activity and a patient's health. In that regard, we have developed whole-cell sensing systems for the detection of AHLs. Further,

we employed these sensing systems in the analysis of biological samples. Specifically, we detected AHLs in biological matrixes, such as saliva and stool, of healthy subjects as well as patients with gastrointestinal (GI) disorders. We envision that these whole-cell sensing systems will allow for the monitoring of bacterial activity in biological fluids, and, consequently, the management of a patient's health. In addition, the aforementioned QS biosensing systems could be employed in the screening of potential anti-microbial drugs that interfere with bacterial communications. Furthermore, the method is non-invasive, fast, and cost-effective and requires simple sample preparation, which makes it amenable for high throughput detection as well as for miniaturization.

Quorum Sensing

In 1965, Tomasz reported that *Streptococcus pneumoniae*, a Gram-positive bacterium, required a self-produced extracellular factor for attaining competent state (1). Later in 1970, Nealson and Hastings observed a similar behavior in the Gram-negative marine bacterium *Vibrio fischeri*, and were the first to propose the phenomenon of quorum sensing (QS) (2). They observed that a bacterium required a certain minimum concentration of a self-manufactured molecule to turn on bioluminescence, and that the concentration of this molecule was directly related to the population density. In 1994, almost twenty five years after the discovery of the phenomenon, Greenberg introduced the term "quorum sensing" (3). Currently, there are a plethora of reports in the literature that establish that the QS phenomenon is not just involved in few rare cases, but actually is a regular event in the microbial world (4).

Quorum sensing is a cell-to-cell communication phenomenon that allows bacteria to coordinate their behavior in a group-based manner (5). Bacteria sense their quorum density by detecting an increase in concentration of a signaling molecule in their environment, and respond by regulating gene expression. In essence, bacteria regulate expression of certain specialized genes, hence certain behaviors/phenotypes, in response to variations in their population density. The signaling molecules employed for such communications are mainly *N*-acyl homoserine lactones (AHLs) in Gram-negative bacteria, short peptides in Gram-positive bacteria and a furanosyl borate diester ((2S, 4S)-2-methyl-2,3,3,4-tetrahydroxytetrahydrofuran-borate, (S-THMF-borate)) named autoinducer-2 (AI-2) in both Gram-positive and Gram-negative types of bacteria (6, 7, 8).

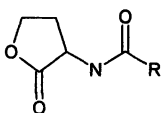
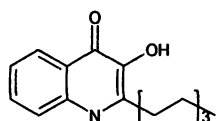
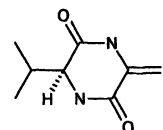
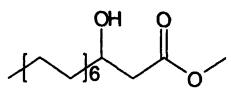
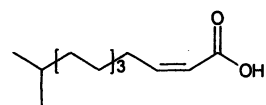
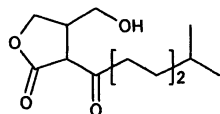
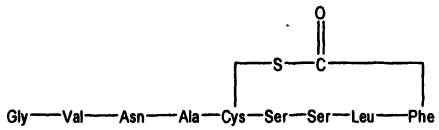
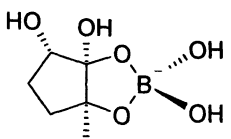
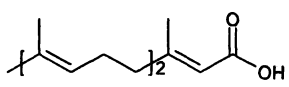
There are an increasing number of reports showing that individual species of bacteria commonly utilize more than one type of quorum sensing molecule (QSMs) (Table I). For instance, *Pseudomonas aeruginosa*, a plant and human pathogen, makes use of additional molecules, besides AHLs, as its chemical signaling language molecules. These include 2-heptyl-3-hydroxy-4-quinolone (also known as *Pseudomonas* Quinolone Signal) (9) and cyclic peptides such as diketopiperazines (10). Similarly, *V. harveyi*, a luminescent marine bacterium, utilizes *N*-(3-hydroxybutanoyl)-L-homoserine lactone (Autoinducer-1, AI-1) and the furanosyl borate diester AI-2 as chemical signaling language molecules for its intra- and inter-species communications, respectively (6, 11, 12). Gram-positive bacteria, such as the *Streptomyces* species, have been shown to exploit structural homologues of AHLs, specifically, γ -butyrolactones molecules, along with oligopeptides for their communication (13). Moreover, a few other signaling molecules produced by microbes for these cell-to-cell communications have been identified. These include cyclic thiolactones in *Staphylococcus aureus*, hydroxy-palmitic acid methyl ester in *Ralstonia solanacearum*, methyl dodecenoic acid (diffusible signal factor, DSF) in *Xanthomonas campestris*, and farnesoic acid in *Candida albicans* (14). In addition to the above mentioned signaling molecules, an autoinducer-3 (AI-3) has recently been described and thought to be involved in inter-kingdom chattering (15).

Quorum sensing regulates several bacterial activities/phenotypes that are not beneficial when manifested by a single bacterium, but become effective and useful when undertaken in a group-based manner (4, 16). In that regard, QS enables bacteria to harvest benefits that are not common in a single bacterium, rather they are more in tune with the behavior of a higher organism. Few examples of bacterial processes that are regulated by QS are: bioluminescence in *V. harveyi* and *V. fischeri* (2), competence in *S. pneumoniae* (1), *Bacillus subtilis* (13) and *V. cholerae* (4), antibiotic production in *Erwinia carotovora*, *Chromobacterium violaceum* and *P. aureofaciens* (17), sporulation in *B. subtilis* (13), nodulation in *Rhizobium leguminosarum* (3), clumping in *Yersinia pseudotuberculosis* (18), motility in *Serratia liquefaciens* (5, 19) and *Y. pseudotuberculosis* (18), conjugation in *Agrobacterium tumefaciens* (3) and *Enterococcus faecalis* (20), virulence in *P. aeruginosa*, *Staphylococcus aureus*, *A. tumefaciens* (5), *V. cholerae*, and *Escherichia coli* (4), development of fruiting body in *Myxococcus xanthus* (21), and proper formation of biofilms in *P. aeruginosa* (22) and *V. cholerae* (23).

Role of QS in Pathogenesis

Expression of virulence factors responsible for causing infections and inflammations in a host is often regulated by QS. Cell-to-cell communication

Table I. QS signaling molecules utilized by various organisms.

I. Gram-negative bacteria		
		
A. <i>N</i> -acyl-homoserine lactone (AHL), R = 3-17	B. <i>Pseudomonas</i> quinolone signal (PQS), 2-heptyl-3-hydroxy-4-quinolone	C. Cyclic peptides, e.g., diketopiperazines
		Structure unknown
D. Hydroxy-palmitic acid methyl ester (PAME)	E. Methyl dodecenoic acid (DSF)	F. Autoinducer-3
II. Gram-positive bacteria		
		
A. γ -butyrolactones ERGMT	B. Cyclic thiolactones	
C. Oligopeptides		
III. Both Gram-pos and Gram-neg bacteria		IV. Fungi
		
A. Autoinducer-2 (AI-2)	A. Farnesoic acid	

allows pathogenic bacteria to delay the expression of virulence factors until there is a sufficient number of bacteria capable of overwhelming the host defenses (24). It is well established that QS is involved in pathogenesis, and has been unequivocally demonstrated through *in vitro* as well as *in vivo* experiments, both in plant and animal models. For instance, the type III secretion system responsible for the expression of virulence determinants in enteropathogenic *E. coli* (EPEC) (23, 25, 26, 27) and enterohemorrhagic *E. coli* (EHEC) (23, 26) was proven to be regulated by cell-to-cell banter. The role of cell-to-cell communication in the regulation of other virulence-related processes, such as motility in enteric pathogens, has also been proven (23, 28). The involvement of QS in *P. aeruginosa* pathogenicity has been confirmed via animal models such as the neonatal mouse model of pneumonia (29), the burned mouse (30) and the nematode *Caenorhabditis elegans* (31). *P. aeruginosa* also form biofilms, using cell-to-cell communications, in the lungs of infected mice (32) as well as patients with cystic fibrosis (33). *In vivo* studies showed that a thermally injured mouse model, which was infected with a *P. aeruginosa* QS-defective mutant, had lowered levels of pro-inflammatory cytokines when compared to those observed in the same model infected with wild-type *P. aeruginosa*, thus resulting in attenuated pathogenesis and mortality (34). Both *in vitro* (35, 36) and *in vivo* (37, 38, 39) studies have established that an AHL molecule produced by this bacterium, specifically *N*-(3-oxododecanoyl)-L-homoserine lactone (3-oxo-C12-HSL), has immunomodulatory effects. For instance, 3-oxo-C12-HSL activated interleukin-8 (IL-8) production in human lung fibroblasts and epithelial cells (36). Smith *et al* also demonstrated through *in vivo* studies that *P. aeruginosa* contributed to its pathogenicity by both forming virulence factors and inducing inflammation (39). In a recently published study, immunization of mice with a 3-oxo-C12-HSL-carrier protein conjugate elicited lower levels of pulmonary tumor necrosis factor alpha (TNF- α), thus reducing on-site inflammation (40). It was observed that the numbers of bacteria were similar in the control and immunized mice infected with *P. aeruginosa*, despite the observed differences in local inflammation. The antibodies produced against 3-oxo-C12-HSL resulted in reduced levels of the active AHL, and consequently, reduced 3-oxo-C12-HSL-mediated inflammations as well, thus confirming 3-oxo-C12-HSL immunomodulatory activity. In addition, there are several plant models that have been used to demonstrate the QS regulation of expression of pathogenic factors in bacteria. For instance, the regulation of virulence by cell-to-cell signaling in *P. aeruginosa* has been established in plants such as *Arabidopsis thaliana* (31). The production of plant tissue destructive proteins by *E. carotovora* (31, 41, 42) and the transfer of tumor inducing plasmid in plants by *A. tumefaciens* are also the outcome of QS regulation (31, 42, 43), as well as induction of Stewart's wilt and leaf affliction of sweet corn and maize by *Pantoea stewartii* (42).

The contribution of bacterial quorum sensing in the formation of complex surface-attached biofilms is also supported by numerous reports in the literature (22, 23, 44, 45, 46, 47). According to a recent survey by the National Institutes of Health (NIH), about eighty percent of infections caused by microbes involve biofilm formation (48). The greatest clinical challenge in developing an effective therapy for infections caused by bacteria in biofilms is their resistance towards antibiotics, chemical disinfectants and host defenses. The involvement of QS in the resistance of bacteria in biofilms towards antibiotics may be significant, but is still unclear (49).

The proven role of QS in bacterial virulence, as well as in biofilm formation, suggests that detection of QS signaling molecules could be a useful tool for the early diagnosis and monitoring of bacteria-related diseases. Although there are a few available physical/chemical methods for the detection of AHLs, such as HPLC-UV (50), GC-MS (51) and LC-MS-MS (52), they are neither quantitative nor sufficiently sensitive for the detection of very low amounts of signaling molecules produced by bacteria, especially *in vivo*, in real time and in biological matrices. In addition, these techniques are expensive, cumbersome and time-consuming. Hence, there is a need for methods adept not only at detecting and quantifying AHLs in biological and environmental samples, but also at screening for compounds that interfere with and disrupt bacterial quorum sensing. In that regard, whole-cell sensing systems have successfully been employed for the detection of AHLs in various types of samples, the evaluation of AHL analogs capable of interfering with QS, and for the design and selection of potential QS blockers, as summarized in the following section.

Whole-cell Sensing Systems for Quorum Sensing

Biosensors integrate a biological component, capable of selectively and reversibly bind an analyte, with a transducer that produces a measurable signal in a dose-dependant manner. The biological biospecific component of biosensors may either be molecular in nature, for instance, enzymes, antibodies, nucleic acids, ion channels, lipid bilayer, or intact cells or tissues. The mode of transducing the signal, which determines the biosensor's sensitivity, can be based either on electrochemical, calorimetric, mass or optical principles. There are several advantages in using whole-cell-based biosensors, for instance, their ability to provide information on the bioavailability of the analyte and their innate stability at a wide range of temperatures, pH and other environmental fluctuations (53, 54). These sensing systems are relatively inexpensive to prepare and easy to handle, when compared to conventional analytical systems. Whole-cell sensing systems usually contain a plasmid engineered by coupling a sensing element with a reporter gene, which is placed under the transcriptional

control of a specific promoter. The sensing element is comprised of a regulatory gene sequence encoding a regulatory protein and an operon promoter region. The regulatory protein recognizes and forms a complex with the analyte and, upon binding the specific promoter, allows the transcription of the operon genes along with the reporter gene. The expressed reporter protein produces a measurable signal as a function of the concentration of analyte present. Hence, the amount of analyte present can be correlated with the intensity of the signal produced by the reporter protein. Whole-cell sensing systems allow easy, rapid, sensitive, selective and cost-effective analysis of several samples at once, which makes them amenable to high-throughput screening, miniaturization and automation (53, 54). Thus, applications of whole-cell sensing systems range from molecular biology to biotechnology, pharmacy, biochemistry, and environmental, clinical and medicinal chemistry.

Few whole-cell sensing systems have been engineered for the detection of quorum sensing molecules, utilizing different QS regulatory systems and reporter genes such as *lacZ*, *gfp* or *lux*, which code for β -galactosidase, green fluorescent protein and bacterial luciferase, respectively. For instance, *lacZ* gene constructs have been employed to understand the mechanism of QS operating in the Gram-negative plant pathogen *A. tumefaciens* (55, 56). A whole-cell sensing system employing a *gfp*-based gene construct has been used to study AHL-mediated interspecies cell-to-cell communications, in situ and at a single-cell level (57). Whole-cell sensing systems based on *gfp* reporter gene have also been used to study biofilm formation in *P. aeruginosa* (45) and detect AHLs in bulk soil (58).

Pigment production/inhibition in *Chromobacterium violaceum* has also been employed for sensing purposes (58, 59, 60). The wild-type of *C. violaceum*, a Gram-negative bacterium, produces a distinctive purple pigment, violaceum (59, 60). A violaceum-negative mutant (CV026) has been exploited for the detection of short chain AHLs and QS interferants. There are reports that cyclic dipeptides can also activate this sensing system (10).

Rasmussen and colleagues have recently designed a quorum sensing inhibitor selector (QSI) (61), which screens for compounds that are QS inhibitors/antagonists. In the whole-cell QSI system, the genetic construct consists of a *luxR* homologue gene and a killing gene, as a reporter gene. In the presence of stimulatory signaling molecules, the transcription of the killing gene is induced, which consequently results in cell death. When sensing inhibitors (QSI) are added to the system, transcription of the reporter killing gene is prohibited. Therefore, the presence of QSI in pure form or in a sample is detected by measuring the bacterial growth.

Many researchers have also utilized *luxAB* (62) and *luxCDABE* reporter gene constructs (63, 64, 65) for engineering whole-cell sensing systems for the detection of QSMs. The *luxA* and *luxB* genes code for bacterial luciferase, which is responsible for producing bioluminescence. The *luxC*, *luxD* and *luxE*

genes in the *luxCDABE* cassette encode for the enzymes essential for the synthesis and recycling of the substrate for luciferase, tetradecanoyl aldehyde, thus enabling the system to function without the external addition of substrate. It has been reported that bacterial luciferase offers one of the lowest limits of detection when used as a reporter (66).

Detection of AHLs in Biological Samples Using Whole-Cell Sensing Systems

Rather recently, our laboratory developed a biosensor for quorum signaling molecules by employing two whole-cell sensing systems based on *E. coli* JM109 bacterial cells harboring either plasmid pSB406 or pSB1075 (67). Each of these plasmids contained the *luxCDABE* gene cassette under control of the AHL-inducible promoter system. AHLs, which are commonly produced by Gram-negative bacteria, are characterized by different lengths of the acyl side chains (4-18 carbon atoms) and different substitutions at the C-3 of the acyl side chain, including hydroxyl or keto groups and unsaturation in the side chain. The plasmids pSB406 and pSB1075 were constructed based on well-described quorum sensing systems of *P. aeruginosa*, i.e., the RhlI/RhlR and LasI/LasR regulatory systems, respectively (65). As mentioned above, LasI and RhlI are AHL synthases, while LasR and RhlR are regulatory proteins that bind to AHLs. The resulting complexes induce the expression of genes that are under the transcriptional control of specific promoters, including the promoters of the *lasI* and *rhlI* genes, P_{lasI} and P_{rhlI} , respectively. The plasmids pSB406 and pSB1075 are genetic constructs bearing the *rhlR* and *lasR* genes, respectively, and the *luxCDABE* reporter under control of the corresponding promoters, P_{rhlI} and P_{lasI} . The whole *rhlI* and *lasI* genes were not cloned in the sensing plasmids because they encode AHL synthases. Thus, the whole-cell sensing systems containing these plasmids express the regulatory proteins RhlR and LasR, respectively. In the presence of activating AHLs, these proteins form complexes with them that bind to their respective promoters and enable transcription of the *luxCDABE* genes in a dose-dependent fashion. Hence, using appropriate calibration curves the concentration of AHL in samples can be determined from the intensity of the bioluminescence signal produced by the luciferase reporter protein.

Dose-Response Curves for Standard AHLs

For the purpose of calibration of both sensing systems we made use of commercially available AHL standard compounds. The response of both sensing systems differed depending on the length of the acyl chain of the AHL

analyzed. The sensing system harboring the plasmid pSB406 showed higher signal response to short acyl chain AHLs than long acyl chain ones. For instance, the response to *N*-butyryl-DL-homoserine lactone (C4-HSL) and *N*-hexanoyl-DL-homoserine lactone (C6-HSL) was higher than to *N*-octanoyl-DL-homoserine lactone (C8-HSL), *N*-dodecanoyl-DL-homoserine lactone (C12-HSL) and *N*-tetradecanoyl-DL-homoserine lactone (C14-HSL). A representative dose-response curve for C6-HSL is reported in Figure 1, left panel. On the contrary, the sensing system harboring the plasmid pSB1075 was more responsive towards the long acyl chain AHLs, namely, C8-HSL, C12-HSL and C14-HSL than the short acyl chain AHLs. The ability of these sensing systems to respond to different AHLs with variable length of the acyl side chain allows us to detect the whole range of AHLs produced by various bacteria present in nature. This method of detection of AHLs proved to be precise and reproducible, with relative standard deviations less than 7%. The detection limits for both whole-cell sensing systems were 1×10^{-9} M, which is appropriate to detect AHLs produced by bacteria. For example, concentrations of 1-10 μ M are within the physiological range of AHLs produced by laboratory cultures of *P. aeruginosa*, while about nanomolar concentrations are necessary for cell-to-cell communication to begin (68).

Analysis of Biological Samples

The detection of AHLs in biological samples such as saliva and stool may be affected by components of the sample matrix. In order to evaluate whether such an effect occurred with our whole-cell sensing systems, we generated dose-response curves in pooled saliva and stool samples, respectively. The most active AHL compounds were used, i.e., C6-HSL and C14-HSL for the sensors harboring plasmids pSB406 and pSB1075, respectively. Saliva samples were centrifuged to remove viscous components and debris, while stool samples were suspended and diluted in distilled deionized water. Calibration curves were also obtained in the absence of the biological matrix as a reference within the same analytical run. Spiked pooled saliva samples were analyzed with both whole-cell sensing systems. It was observed that the slopes of the dose-response curves generated either in saliva or stool were similar to those of the dose-response curves prepared in the absence of matrix, thus demonstrating that in the chosen experimental conditions, the biological sample matrix components did not affect the sensor response. As mentioned above, this was achieved by means of simple sample preparation, i.e., centrifugation of the saliva samples and dilution of the stool samples. Higher signal intensities were observed in the presence of the biological matrices, which was possibly due to the fact that a certain amount of AHLs was present in the pooled samples.

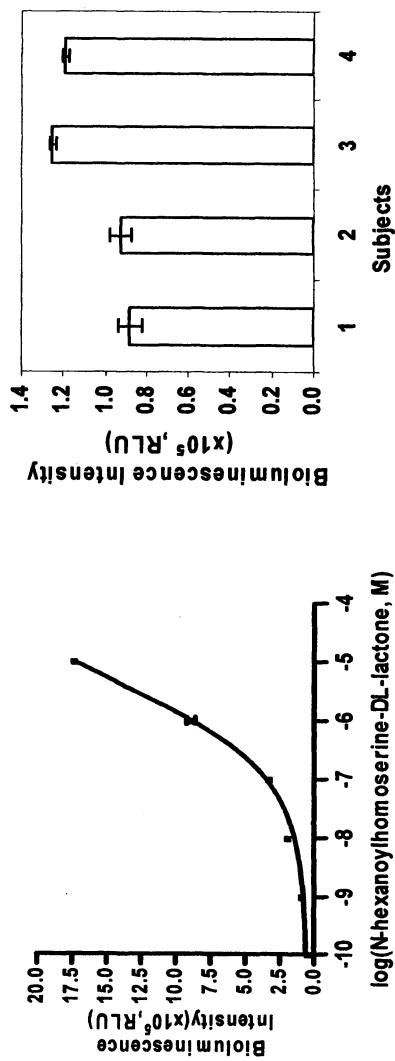


Figure 1. Dose-response curve for the pSB406 whole-cell sensing system (left).
Detection of AHLs in stool samples (right).

Subsequently, the whole-cell sensing systems were employed to detect the presence of AHLs in biological samples such as saliva and stool. Saliva specimens were collected from healthy volunteers and a Crohn's patient, whereas stool specimens were obtained from infants in the Newborn Intensive Care Unit (NICU) of the University of Kentucky Children's Hospital. A reference calibration curve was generated using commercially available AHLs in each analytical run. We have demonstrated that AHLs could be detected in biological matrixes such as saliva and stool samples (Figure 1, right panel). Replicate analysis of the same samples produced consistent results, thus showing the reproducibility of the sensing systems when applied to real samples. The levels of these molecules varied among different subjects, while no significant variations were observed for a single normal subject over time.

In summary, we have developed a whole-cell biosensing system that can be employed as an effective simple tool for detection of quorum sensing molecules in biological matrices such as saliva and stool of healthy individuals as well as patients with GI disorders such as Crohn's disease. The levels of these QSMs in such non-invasively collected samples may correlate with the health status of the subjects, thus allowing for QSMs to be employed as biomarkers of disease. These biomarkers may not only serve in the monitoring of disease activity, but also help in the management of patient's health. In addition, the developed biosensing system could be employed in the screening of potential anti-microbial drugs that target bacterial communication. Furthermore, the method is sensitive, fast, and cost-effective, which renders it amenable for high throughput detection and miniaturization.

Acknowledgements

This work was partly supported by the National Science Foundation (Grant CHE-0416553) and the Children's Miracle Network. We thank the Office of the Vice President of Research of the University of Kentucky for a University Research Professorship to SD. AK and SD acknowledge support from a Gill Fellowship and a Gill Eminent Professorship, respectively. We also thank Dr. Paul Williams (University of Nottingham, Nottingham, UK) for providing the plasmids pSB406 and pSB1075.

References

1. Tomasz, A., *Nature* **1965**, *208*, 155-159.
2. Nealson, K. H.; Platt, T.; Hastings, J. W., *J. Bacteriol.* **1970**, *104*, 313-322.
3. Fuqua, W. C.; Winans, S. C.; Greenberg, E. P., *Journal of Bacteriology* **1994**, *176*, (2), 269-275.

4. Bassler, B. L.; Losick, R., *Cell* **2006**, *125*, (2), 237-246.
5. Miller, M. B.; Bassler, B. L., *Annual Review of Microbiology* **2001**, *55*, (1), 165-199.
6. Bassler, B. L.; Greenberg, E. P.; Stevens, A. M., *J. Bacteriol.* **1997**, *179*, (12), 4043-4045.
7. Surette, M. G.; Miller, M. B.; Bassler, B. L., *PNAS* **1999**, *96*, (4), 1639-1644.
8. Federle, M. J.; Bassler, B. L., *J. Clin. Invest.* **2003**, *112*, (9), 1291-1299.
9. Pesci, E. C.; Milbank, J. B. J.; Pearson, J. P.; McKnight, S.; Kende, A. S.; Greenberg, E. P.; Iglewski, B. H., *PNAS* **1999**, *96*, (20), 11229-11234.
10. Holden, M. T. G.; Ram Chhabra, S.; de Nys, R.; Stead, P.; Bainton, N. J.; Hill, P. J.; Manefield, M.; Kumar, N.; Labatte, M.; England, D.; Rice, S.; Givskov, M.; Salmond, G. P. C.; Stewart, G. S. A. B.; Bycroft, B. W.; Kjelleberg, S.; Williams, P., *Molecular Microbiology* **1999**, *33*, (6), 1254-1266.
11. Surette, M. G.; Bassler, B. L., *PNAS* **1998**, *95*, (12), 7046-7050.
12. Chen, X.; Schauder, S.; Potier, N.; Van Dorsselaer, A.; Pelczar, I.; Bassler, B. L.; Hughson, F. M., *Nature* **2002**, *415*, (6871), 545-549.
13. Kleerebezem, M.; Quadri, L. E. N.; Kuipers, O. P.; De Vos, W. M., *Molecular Microbiology* **1997**, *24*, (5), 895-904.
14. Zhang, L.-H.; Dong, Y.-H., *Molecular Microbiology* **2004**, *53*, (6), 1563-1571.
15. Sperandio, V.; Torres, A. G.; Jarvis, B.; Nataro, J. P.; Kaper, J. B., *PNAS* **2003**, *100*, (15), 8951-8956.
16. Schauder, S.; Bassler, B. L., *Genes Dev.* **2001**, *15*, (12), 1468-1480.
17. Swift, S.; Throup, J. P.; Williams, P.; Salmond, G. P. C.; Stewart, G. S. A. B., *Trends in Biochemical Sciences* **1996**, *21*, (6), 214-219.
18. Atkinson, S.; Throup, J. P.; Stewart, G. S. A. B.; Williams, P., *Molecular Microbiology* **1999**, *33*, (6), 1267-1277.
19. Eberl, L.; Winson, M. K.; Sternberg, C.; Stewart, G. S. A. B.; Christiansen, G.; Chhabra, S. R.; Bycroft, B.; Williams, P.; Molin, S.; Givskov, M., *Molecular Microbiology* **1996**, *20*, (1), 127-136.
20. Lyon, G. J.; Novick, R. P., *Peptides* **2004**, *25*, (9), 1389-1403.
21. Kim, S. K.; Kaiser, D., *Cell* **1990**, *61*, (1), 19-26.
22. Davies, D. G.; Parsek, M. R.; Pearson, J. P.; Iglewski, B. H.; Costerton, J. W.; Greenberg, E. P., *Science* **1998**, *280*, (5361), 295-298.
23. Kaper, J. B.; Sperandio, V., *Infect. Immun.* **2005**, *73*, (6), 3197-3209.
24. Hentzer, M.; Givskov, M., *J. Clin. Invest.* **2003**, *112*, (9), 1300-1307.
25. Jarvis, K. G.; Giron, J. A.; Jerse, A. E.; McDaniel, T. K.; Donnenberg, M. S.; Kaper, J. B., *PNAS* **1995**, *92*, (17), 7996-8000.
26. Sperandio, V.; Mellies, J. L.; Nguyen, W.; Shin, S.; Kaper, J. B., *PNAS* **1999**, *96*, (26), 15196-15201.

27. Sircili, M. P.; Walters, M.; Trabulsi, L. R.; Sperandio, V., *Infect. Immun.* **2004**, *72*, (4), 2329-2337.
28. Falcao, J. P.; Sharp, F.; Sperandio, V., *Current Issues in Intestinal Microbiology* **2004**, *5*, (1), 9-18.
29. Tang, H. B.; DiMango, E.; Bryan, R.; Gambello, M.; Iglewski, B. H.; Goldberg, J. B.; Prince, A., *Infect. Immun.* **1996**, *64*, (1), 37-43.
30. Rumbaugh, K. P.; Griswold, J. A.; Iglewski, B. H.; Hamood, A. N., *Infect. Immun.* **1999**, *67*, (11), 5854-5862.
31. de Kievit, T. R.; Iglewski, B. H., *Infect. Immun.* **2000**, *68*, (9), 4839-4849.
32. Wu, H.; Song, Z.; Hentzer, M.; Andersen, J. B.; Heydorn, A.; Mathee, K.; Moser, C.; Eberl, L.; Molin, S.; Hoiby, N.; Givskov, M., *Microbiology* **2000**, *146*, (10), 2481-2493.
33. Middleton, B.; Rodgers, H. C.; Camara, M.; Knox, A. J.; Williams, P.; Hardman, A., *FEMS Microbiology Letters* **2002**, *207*, (1), 1-7.
34. Rumbaugh, K. P.; Hamood, A. N.; Griswold, J. A., *Journal of Surgical Research* **2004**, *116*, (1), 137-144.
35. Telford, G.; Wheeler, D.; Williams, P.; Tomkins, P. T.; Appleby, P.; Sewell, H.; Stewart, G. S. A. B.; Bycroft, B. W.; Pritchard, D. I., *Infect. Immun.* **1998**, *66* (1), 36-42.
36. Smith, R. S.; Fedyk, E. R.; Springer, T. A.; Mukaida, N.; Iglewski, B. H.; Phipps, R. P., *J Immunol* **2001**, *167*, (1), 366-374.
37. DiMango, E.; Zar, H. J.; Bryan, R.; Prince, A., *Journal of Clinical Investigation* **1995**, *96*, (5), 2204-10.
38. Wu, H.; Song, Z.; Givskov, M.; Doring, G.; Worlitzsch, D.; Mathee, K.; Rygaard, J.; Hoiby, N., *Microbiology* **2001**, *147*, (5), 1105-1113.
39. Smith, R. S.; Harris, S. G.; Phipps, R.; Iglewski, B., *J. Bacteriol.* **2002**, *184*, (4), 1132-1139.
40. Miyairi, S.; Tateda, K.; Fuse, E. T.; Ueda, C.; Saito, H.; Takabatake, T.; Ishii, Y.; Horikawa, M.; Ishiguro, M.; Standiford, T. J.; Yamaguchi, K., *J Med Microbiol* **2006**, *55*, (10), 1381-1387.
41. Jones, S.; Yu, B.; Bainton, N. J.; Birdsall, M.; Bycroft, B. W.; Chhabra, S. R.; Cox, A. J.; Golby, P.; Reeves, P. J.; Stephens, S., *The Embo Journal* **1993**, *12*, (6), 2477-82.
42. von Bodman, S. B.; Bauer, W. D.; Coplin, D. L., *Annual Review of Phytopathology* **2003**, *41*, (1), 455-482.
43. Zhang, L.; Murphy, P. J.; Kerr, A.; Tate, M. E., *Nature* **1993**, *362*, (6419), 446-448.
44. Singh, P. K.; Schaefer, A. L.; Parsek, M. R.; Moninger, T. O.; Welsh, M. J.; Greenberg, E. P., *Nature* **2000**, *407*, (6805), 762-764.
45. De Kievit, T. R.; Gillis, R.; Marx, S.; Brown, C.; Iglewski, B. H., *Appl. Environ. Microbiol.* **2001**, *67*, (4), 1865-1873.
46. Zhu, J.; Mekalanos, J. J., *Developmental Cell* **2003**, *5*, (4), 647-656.

47. Hammer, B. K.; Bassler, B. L., *Molecular Microbiology* **2003**, *50*, (1), 101.
48. Davies, D., *Nature Reviews Drug Discovery* **2003**, *2*, (2), 114.
49. Mah, T.-F. C.; O'Toole, G. A., *Trends in Microbiology* **2001**, *9*, (1), 34-39.
50. Reimmann, C.; Beyeler, M.; Latifi, A.; Winteler, H.; Foglino, M.; Lazdunski, A.; Haas, D., *Molecular Microbiology* **1997**, *24*, (2), 309-319.
51. Charlton, T. S.; de Nys, R.; Netting, A.; Kumar, N.; Hentzer, M.; Givskov, M.; Kjelleberg, S., *Environmental Microbiology* **2000**, *2*, (5), 530-541.
52. Morin, D.; Grasland, B.; Vallee-Rehel, K.; Dufau, C.; Haras, D., *Journal of Chromatography A* **2003**, *1002*, (1-2), 79-92.
53. Daunert, S.; Barrett, G.; Feliciano, J. S.; Shetty, R. S.; Shrestha, S.; Smith-Spencer, W., *Chem. Rev.* **2000**, *100*, (7), 2705-2738.
54. Feliciano, J.; Pasini, P.; Deo, S. K.; Daunert, S., Wiley-VCH Verlag GmbH & Co. KGaA: Weinheim, Germany, 2006 p131-154.
55. Fuqua, C.; Winans, S. C., *J. Bacteriol.* **1996**, *178*, (2), 435-440.
56. Shaw, P. D.; Ping, G.; Daly, S. L.; Cha, C.; Cronan, J. E., Jr.; Rinehart, K. L.; Farrand, S. K., *PNAS* **1997**, *94*, (12), 6036-6041.
57. Andersen, J. B.; Heydorn, A.; Hentzer, M.; Eberl, L.; Geisenberger, O.; Christensen, B. B.; Molin, S.; Givskov, M., *Appl. Environ. Microbiol.* **2001**, *67*, (2), 575-585.
58. Burmolle, M.; Hansen, L. H.; Oregaard, G.; Sorensen, S. J., *Microbial ecology* **2003**, *45*, (3), 226-36.
59. McClean, K. H.; Winson, M. K.; Fish, L.; Taylor, A.; Chhabra, S. R.; Camara, M.; Daykin, M.; Lamb, J. H.; Swift, S.; Bycroft, B. W.; Stewart, G. S.; Williams, P., *Microbiology* **1997**, *143*, (12), 3703-3711.
60. McLean, R. J. C.; Pierson, I. I. L. S.; Fuqua, C., *Journal of Microbiological Methods* **2004**, *58*, (3), 351-360.
61. Rasmussen, T. B.; Bjarnsholt, T.; Skindersoe, M. E.; Hentzer, M.; Kristoffersen, P.; Kote, M.; Nielsen, J.; Eberl, L.; Givskov, M., *J. Bacteriol.* **2005**, *187*, (5), 1799-1814.
62. Swift, S.; Winson, M. K.; Chan, P. F.; Bainton, N. J.; Birdsall, M.; Reeves, P. J.; Rees, C. E. D.; Chhabra, S. R.; Hill, P. J.; Throup, J. P.; Bycroft, B. W.; Salmond, G. P. C.; Williams, P.; Stewart, G. S. A. B., *Molecular Microbiology* **1993**, *10*, (3), 511-520.
63. Swift, S.; Karlyshev, A. V.; Fish, L.; Durant, E. L.; Winson, M. K.; Chhabra, S. R.; Williams, P.; Macintyre, S.; Stewart, G. S., *J. Bacteriol.* **1997**, *179*, (17), 5271-5281.
64. Winson, M. K.; Camara, M.; Latifi, A.; Foglino, M.; Chhabra, S. R.; Daykin, M.; Bally, M.; Chapon, V.; Salmond, G. P. C.; *et al.*, *Proceedings of the National Academy of Sciences of the United States of America* **1995**, *92*, (20), 9427-31.
65. Winson, M. K.; Swift, S.; Fish, L.; Throup, J. P.; Jorgensen, F.; Chhabra, S. R.; Bycroft, B. W.; Williams, P.; Stewart, G. S. A. B., *FEMS Microbiology Letters* **1998**, *163*, (2), 185-192.

66. Van Dyk, T. K.; Rosson, R., *Methods Mol. Biol.* **1998**, *102*, 931-938 or 85-96.
67. Kumari, A.; Pasini, P.; Deo, S. K.; Flomenhoft, D.; Shashidhar, H.; Daunert, S., *Anal. Chem.* **2006**, *78*, (22), 7603-7609.
68. Pearson, J. P.; Passador, L.; Iglewski, B. H.; Greenberg, E. P., *PNAS* **1995**, *92*, (5), 1490-1494.

Chapter 3

Methods for Whole Cell Detection of Microorganisms

Byron F. Brehm-Stecher

Department of Food Science & Human Nutrition, Iowa State University

Microbes are ubiquitous, and can be found occupying nearly every imaginable niche on Earth. These include organic and inorganic surfaces, interfacial boundaries and within macroscopically solid matrices, such as the pore space of rocks. Because phylogenetically divergent microbes may be visually indistinguishable, understanding the species distribution and ecological significance of environmental microbes requires diagnostic tools that extend beyond simple phenotypic description. Methods for microbial diagnostics can be divided into two broad categories: cellular and acellular. Acellular techniques, such as the polymerase chain reaction or certain immunoassay formats may be effective at detecting molecular, structural or biochemical targets associated with specific cell types, but this information is provided out of its “natural”, and arguably most meaningful context – that of the individual microbial cell. In contrast, cellular methods have the potential to preserve an abundance of valuable information. Apart from molecular identity, this includes information regarding cell morphology and other physiological characteristics, cell number and distribution within a sample, and physical or spatial associations with other cell types. The aim of this chapter is to provide an overview of whole cell methods for microbial detection, including both existing approaches and those still in development. The tools described here are expected to find wide application for the detection of microbes on surfaces or within complex matrices across a number of parallel or allied fields, including environmental, food and clinical microbiologies.

Introduction

Whether our interests lie in preventing or diagnosing disease, ensuring the productivity of biotransformative processes such as industrial and food fermentations or monitoring the quality of basic natural resources such as surface waters or soil, detection of microorganisms is an essential process. Microbes inhabit almost every surface niche imaginable, including soil particles, mineral veneers on desert rock surfaces, the worn stone surfaces of Roman catacombs and other monuments, the pore space *within* rocks, liquid inclusions within Arctic sea ice, plant surfaces or structures such as stems, leaves and roots, animal surfaces such as skin and teeth, food surfaces or digesta particulates within the gut, or manmade structures such as indwelling medical devices (1-8).

Although it has been over a century since Robert Koch first described the use of solid media for isolating microorganisms in pure culture (9), it has really only been within the last 20 years that microbiologists have been able to begin stepping outside the primarily phenotypic, “plate and see” framework developed by Koch and his contemporaries (10, 11). In this time, the rapid growth of the field of molecular microbiology has fueled an explosion of new methods and capabilities for detection of microbes (10, 12). These include methods for *in situ*, culture-independent detection of specific microbial cells and the tools of microbial forensics, which enable epidemiological tracking of pathogens from foodborne disease outbreaks and identification of natural (or deliberate) sources of environmental contamination (13-15). Such molecular techniques typically test for nucleic acids (rDNA, other genomic DNA sequences, mRNA, etc.) extracted in bulk from a sample, obviating the need for first isolating the target organism. Although the capacity to detect cell-specific nucleic acids without the need for culture may be considered an advantage of such acellular techniques, it is not without cost. The individual cell is the “...fundamental unit of biological organization...” (16, 17). Additional layers of information are therefore intrinsically linked to the “granular” or corpuscular nature of microbes. These include cell number, position or distribution within a sample, co-localization with other cell types, attachment to or interaction with specific substrates, as well as more ephemeral data such as biochemical activities or behavioral properties of individual cells (12, 17). This chapter seeks to provide a basic overview of the methods available for whole cell microbial detection and their use in the allied fields of environmental, food and clinical analysis. Special emphasis will be given to fluorescence *in situ* hybridization (FISH), but additional whole cell approaches and their merits or limitations will also be discussed. Apart from providing convenience, rapidity is not necessarily an essential feature of methods focused on environmental microbiology. However, in clinical and food applications, timely results are paramount, as the health of a patient or the safety of the food supply are at stake. Because of its importance to these disciplines, rapidity will be a recurrent subtext in this chapter.

Microbial Habitats – The “Environment”

Microorganisms are indispensable coinhabitants of our ecosphere, responsible for driving the basic global geochemical cycles upon which all life depends (18). The field of environmental microbiology is tasked with investigating and describing the interactions between microbes and the physical spaces they inhabit. Typically, the word “environment” evokes familiar images from the natural world – surface waters, soils or sediments, the phyllosphere, hot springs and deep sea thermal vents, for example. Given microbial proclivities for filling and thriving in just about any exploitable space available, the word “environment” can also be extended to include such man-made environments as municipal wastewater treatment facilities (activated sludge), metalworking fluids, tannery effluents and acid mine drainages. As hosts to naturally-occurring assemblages of microbiota, our bodies may also be considered from an environmental perspective, with infectious disease representing an example of an ecosystem out of balance. Ecological concepts have also been applied to food systems (19, 20). As with our bodies, the foods we eat may be populated with a “natural flora” – the expected successions and end compositions of microbial populations in fermented foods, for example. These foods may also contain unwanted, or “invasive” species such as pathogens or spoilage flora.

These conceptual parallels between the fields of environmental, food and clinical microbiologies are mirrored in the practical features of these disciplines, with many similarities in the goals, tools and protocols existing between them (19). Of course, there are differences – environmental microbiology is typically more basic in nature, approaching the “big problems” of what large assemblages of microorganisms (potentially *thousands* of different species) are doing *in situ*, and how these activities impact on basic global processes such as geochemical cycling (12, 18). Thus, environmental microbiology incorporates methods for both microbial detection and ecophysiological characterization (12). Food and clinical microbiologies usually deal with more applied problems, such as detection of a relatively few cell types within foods or clinical specimens. Still, certain themes or phenomena cut across the boundaries of these disciplines. Biofilms, for example, are the most prevalent mode of microbial growth in nature (21). As such, they are a recurrent theme not only in the natural world, but also impact the food processing and health fields. Biofilms present challenges to effective cleaning of food processing environments and equipment, contribute to the establishment and persistence of oral infections or cystic fibrosis and may be important reservoirs of infectious disease through colonization and growth on indwelling medical devices (22, 23). Recognition of the overlaps between these three branches of microbiology can allow the advantageous adaptation of techniques for detection or characterization developed for one field for use in another. Examples include the adaptation of culture-independent approaches for

studying the *in situ* population composition and diversity originally developed for environmental microbiology for use in studying microbial populations in foods (19, 24).

Nucleic Acid-Based Methods: Generating Sequence-Specific Fluorescence Signals Within Whole Microbial Cells

The attraction of whole cell diagnostic methods is that they link detection of pathogen-specific markers to their cellular context, providing additional layers of information beyond simple “presence/absence” determinations. Over the past decade, several distinct methods for generating sequence-specific fluorescence signals within intact bacterial cells have been developed, primarily for environmental microbiology applications. These include *in situ* PCR (25-29), *in situ* reverse transcription-PCR (30-32), *in situ* reverse transcription (33), chromosomal painting (34, 35), *in situ* rolling circle amplification (36, 37), *in situ* loop-mediated signal amplification (38) and fluorescence *in situ* hybridization (FISH) (39-43). Descriptions of each method are given below, followed by a discussion of their potential benefits and drawbacks for use in routine diagnostics in environmental, food and clinical microbiology applications. Although presented together, these methods differ widely in assay complexity, sensitivity of detection and other factors, such as their abilities to localize signals within microbial cells. Additionally, many of these approaches are “homebrew” assays, rather than being commercially available in kit form, and are therefore realistically accessible only to specialist laboratories. However, some technologies such as DNA or PNA-FISH and rolling circle amplification (RCA) are now available commercially. The assay validation, reagent quality control and technical support that are available with these commercial kits will make these technologies more accessible to a wider user base.

At its simplest, FISH is likely the best candidate for robust, routine application in simple molecular diagnostics for environmental, food and clinical applications. This is because it does not require complex, multi-step, multi-component protocols involving potentially capricious reagents such as enzymes. Given the intrinsic physical restrictions of microscopic examination, only a relatively few cells can be examined on the surface of a microscope slide (36, 44). Therefore, any method that is restricted to a slide-based format may face substantial limitations in detection sensitivity. In-solution methods, such as FISH, can be combined with higher-throughput methods for liquid-phase analysis such as flow cytometry. This enables a larger portion of the sample to be screened, allowing increased detection sensitivities, even in the presence of high backgrounds of non-target cells or debris. However, as with any approach, FISH does have its limitations. Typically, FISH is used to target relatively high copy-

number targets within the cell. For cells containing limited copies of the target molecule, such as starved or dormant cells, standard FISH protocols may not be sensitive enough to ensure detection of all cells. However, it has been nearly 20 years since its first description for use in detecting bacteria (39), and in recent years, several variant FISH techniques have been developed to target lower copy-number targets, thereby pushing the resolution of this approach toward low-copy and single copy (e.g. genomic) sensitivities (43). These adaptations and improvements of the FISH approach will be described briefly in a later section. Other key technologies for generating sequence-specific fluorescence signals within whole microbial cells are discussed below. Typically, these have been developed for detection of bacteria, but in principle may also be used for detection of other microorganisms, with few, if any modifications.

***In Situ* PCR and *In Situ* Reverse Transcription-PCR**

For *in situ* PCR (ISPCR) or *in situ* reverse transcription-PCR (ISRT-PCR), amplification of a target sequence using appropriate primers and fluorescently-labeled dNTP's results in the production of a labeled PCR product within the cell (25). Alternatively, digoxigenin-labeled dNTP's or biotinylated primers may be used and the amplicon detected with fluorescently-labeled or enzyme-labeled antibodies specific for digoxigenin or biotin (29, 30, 32). Although these methods can be used for the detection of specific microorganisms at the genus, species or subspecies level (25, 27), their true strength lies in their abilities to detect low-abundance targets, such as single-copy genes or mRNA, which are below the sensitivities of methods such as (conventional) FISH (29, 32). From a standpoint of practicality, these analyses are complex and time-consuming, and involve multiple steps in addition to cell fixation, including cell immobilization on glass slides, permeabilization with lysozyme, protease and/or RNase digestions, the PCR reaction itself, and post-PCR detection of labeled amplicons with fluorescently-labeled antibodies or enzyme-based fluorescent signal amplification steps (29, 30, 32). In light of this, ISPCR and ISRT-PCR are much better suited to fine-structure analyses such as examining the distribution of a gene in representative samples of a population or following the expression of specific mRNA's than for routine identification of bacterial species (29, 30, 32).

***In Situ* Reverse Transcription**

In situ reverse transcription (ISRT) (25) is an isothermal method for amplification of rRNA or mRNA targets within target cells for fluorescence detection. In this method, cells are fixed, spotted onto microscope slides, permeabilized and hybridized with unlabeled DNA primers specific for the

desired target within the cell. After hybridization, reverse transcriptase, RNase inhibitors, and a mixture of unlabeled and fluorescently-labeled dNTP's are added. Reverse transcriptase activity results in primer extension and the incorporation of fluorescently-labeled dNTP's into the resulting extension products. Cells in which successful extension has taken place are fluorescent and can be detected by fluorescence microscopy or other suitable methods.

Although ISRT does not result in the exponential amplification of target RNA, this method can still yield bright fluorescence without thermal cycling because multiple fluorophores are incorporated into the extension product (25). ISRT may be especially useful for the detection of multi-copy targets such as rRNA where target levels are below the detection limits of methods such as FISH, as may be the case with dormant cells. However, under conditions where rRNA levels were high enough to yield adequate FISH signals, Hodson et al. (25) reported that cells labeled through ISRT were not substantially brighter than those labeled using FISH. Although ISRT is considerably less complex than ISPCR or ISRT-PCR, the relatively modest gains in signal strength vis-à-vis FISH argue against its routine use for detection of target cells under conditions where they are expected to be actively-growing (and therefore detectable via FISH) (25).

Bacterial Chromosome Painting

Another method for generating a sequence-specific fluorescence response within whole cells is bacterial chromosome painting (BCP) (34, 35, 43). In this method, chromosomal DNA from the organism to be targeted is randomly digested with restriction enzymes, yielding an undefined mixture of fragments ranging from 50 to 200 bp. This complex pool of DNA fragments is then enzymatically labeled with fluorescent reporter molecules and the resulting fluorescent probes are hybridized against formalin-fixed, RNase-treated cells spotted onto microscope slides. Because the target, chromosomal DNA, is present in all living cells, BCP should be applicable to fast-growing, as well as dormant cells (34). BCP is able to differentiate closely-related bacteria, but prehybridization with unlabeled chromosome digests of non-target *Salmonella* (chromosome *in situ* suppression) is required to differentiate between *Salmonella* species (34). A major drawback of BCP is the time required to achieve a sufficient signal. Reassociation rates for long nucleic acid probes are inversely proportional to the sequence complexity of the probes being hybridized (45). Because BCP relies on a large set of probes generated from random genomic digestion, the sequence complexity is high and the reassociation rate is very low, requiring 2 days to yield adequate signals from target cells (34, 43).

***In Situ* Rolling Circle Amplification**

Rolling Circle Amplification (RCA) is an isothermal method for nucleic acid amplification that targets short sequences (~ 40 or fewer bases) and generates long, single-stranded amplicons comprised of tandemly repeated sequences that can subsequently be detected via hybridization (36, 37, 46). In standard RCA techniques, amplicon production proceeds in a linear fashion; however, modifications of this technique variously termed “ramification”, “cascade” or “hyperbranched” RCA have been developed to yield geometric amplicon production (46). In the RCA reaction, a circularizable probe is hybridized to its target on a plasmid or on the chromosome, then the circle is closed via ligation. A primer then directs DNA polymerase to extend the circular sequence progressively around the circle, leading to the formation of the long linear product of tandem repeats (36, 37, 46). The population of products formed is generally distributed over a wide range of lengths, typically appearing as a continuous smear of high molecular weight DNA when viewed on an electrophoretic gel (46). Detection of the tandemly repeated sequences in the amplicon is then facilitated using fluorescently-labeled detector or “decorator” probes (36, 37, 47). For *in situ* RCA, this entire process is carried out within the context of whole bacterial cells. As with the other *in situ* amplification processes mentioned above, this entails using a complicated protocol involving multiple steps (washes, enzyme digestions, hybridization, ligation, etc.). Therefore, to avoid cell loss, cells are first attached to a membrane filter, then embedded in agarose (36). Next, cells are permeabilized with lysozyme and proteinase K and RNA is removed via digestion with DNase-free RNase (36). Ligation reagents are added, the sample is incubated on ice and given time (15 min) to diffuse into the cells, followed by the ligation reaction (90 min) to form circularized probes within the cells (36). After buffer and distilled water rinses, the cell-containing membranes are then dehydrated in an ethanol series and dried. Next, RCA reagents are added and again incubated on ice (15 min) to allow perfusion into the cells, followed by the isothermal RCA reaction at temperatures appropriate to the amplicon (55°C - 63°C in the example provided by Maruyama et al., 2005, reference 36) for 90 min, followed again by rinsing and final detection of the amplicon via a FISH reaction utilizing a 16 h incubation at 46°C (36). Because the RCA conditions are relatively mild (compared to those of *in situ* PCR, for example), additional whole cell analyses, such as antibody-based staining may also be performed on cells after RCA, enabling correlation of immunophenotypic and genomic data (36). Although complicated, *in situ* RCA provides a method for detection of low-copy gene sequences within whole bacterial cells. The ability to detect single-copy genes carried on plasmids or on the chromosome provides additional discriminatory power, allowing target cells to be distinguished from closely-related, non-target cells. For example, Maruyama et al. (36) were able to detect the single-copy Shiga-like toxin (*stx*₁)

gene on the chromosomes of enterohemorrhagic *E. coli*. Techniques such as this, which are able to detect pathogen-specific virulence factors, will enable detection of pathogenic variants of these bacteria, distinguishing them from “garden variety” strains of little or no public health impact.

***In Situ* Loop-Mediated Isothermal Amplification**

Maruyama and colleagues have also adapted another isothermal sequence amplification method for the *in situ* detection of low-copy sequences within whole, permeabilized bacterial cells. As originally described, loop-mediated isothermal amplification of DNA (LAMP) is a method capable of quickly amplifying select DNA sequences, enabling production of up to 10^9 copies within one hour (48). The LAMP procedure relies on a self-sustaining strand displacement reaction carried out by a DNA polymerase having high strand displacement activity, in this case the *Bst* large fragment from *Bacillus stearothermophilus* (38, 48). The technique uses up to six distinct primers that hybridize with the target sequence to create the topologically unique nucleic acid structures used for amplification (38, 48). As adapted for *in situ* detection of target genes within bacterial cells, only four LAMP primers were required and specific amplification products could be detected either via FISH with amplicon-specific probes, or via incorporation of fluorescently-labeled dCTP during amplicon formation (38). As with *in situ* RCA, *in situ* LAMP has no requirement for complicated, expensive cycling equipment and the relatively low temperature used (63°C) is potentially less destructive to delicate cell structures, preserving cell morphology and diagnostic epitopes (38).

Fluorescence *In Situ* Hybridization

The last method considered here is fluorescence *in situ* hybridization (FISH), first described for bacteria in 1989 (39). The FISH technique (also aptly termed “phylogenetic staining”) uses fluorescently-labeled nucleic acid probes targeted to complementary rRNA targets located on ribosomes within intact cells. An advantage of targeting rRNA is that it is a multi-copy target - several thousand copies are typically present within active microbial cells (44). The cumulative signal from multiple probe-target binding events after hybridization provides the basis for sequence-specific fluorescence of target cells. Of all the techniques discussed here, FISH is by far the most straightforward and least complex. As described above, unlike ISPCR, ISRT-PCR, ISRT, *in situ* RCA or *in situ* LAMP, FISH does not depend on enzymatic activity (e.g. DNA polymerase or reverse transcriptase) to generate a detectable product. Unlike BCP, FISH uses well-defined probes or probe sets and hybridizations can be

carried out in a fraction of the time needed for BCP. Additionally, FISH can be performed in solution, allowing the subsequent analysis of a large number of cells, especially if hybridization results are analyzed by flow cytometry (49, 50). A typical FISH protocol involves the following steps: harvesting of cells (via centrifugation or filtration), fixation (this step has multiple purposes, including permeabilization of cells to probes, preservation of cell morphology, inactivation of endogenous enzymes, prevention of target molecule leakage from cells), hybridization (heating of cells in the presence of probe(s) in a simple buffer system containing salt and detergent), washing (used to remove excess, non-specifically bound probe – not always required, depending on the properties of the probe used and the sample being tested), harvesting cells again via centrifugation, and detection of hybridized cells via microscopy or another appropriate method. Because of its simple and streamlined nature, FISH can be used to achieve rapid molecular detection of target cells in complex matrices such as natural waters, food or bodily fluids (51-54).

Although most DNA-based FISH reactions are typically carried out for several hours at relatively low temperatures (e.g. 3 h at 46°C) (42, 44, 51), these parameters can be adjusted to enable more rapid detection of bacteria, particularly with Gram-negative bacteria, which are relatively easy to permeabilize (53, 54; Brehm-Stecher and Johnson, unpublished data, **Figure 1**), although this approach has also been used successfully for rapid on-slide hybridizations of certain Gram-positive bacteria, such as the 5 min hybridization of *Streptococcus pneumoniae* reported by Jansen et al. (55).

FISH has been shown to be remarkably robust in its ability to detect bacterial cells exposed to stressors typical of food processing environments, including high salt, low pH and low or freezing temperatures (51). In some circumstances, however (e.g. environmental applications), FISH-based detection of target cells may be complicated by poor signal quality. This can occur with poorly-permeabilized cells, with cells having an intrinsically low rRNA content, with starved or stressed cells containing fewer or degraded ribosomes (42, 44, 56) or in cells displaying low signal-to-noise ratios due to sample autofluorescence (57). In these situations, a more efficient means of permeabilization, an enrichment or repair step, or some means of signal amplification may be needed in order to detect FISH signals from target cells. Alternatively, probes having improved properties of penetration or binding, such as peptide nucleic acid probes (PNAs) may be used to enhance the sensitivity of the FISH approach.

Specialized Applications of FISH

A key drawback to FISH, as it is typically used, is its inability to detect low-copy or single-copy targets. As discussed above, this does not pose a problem

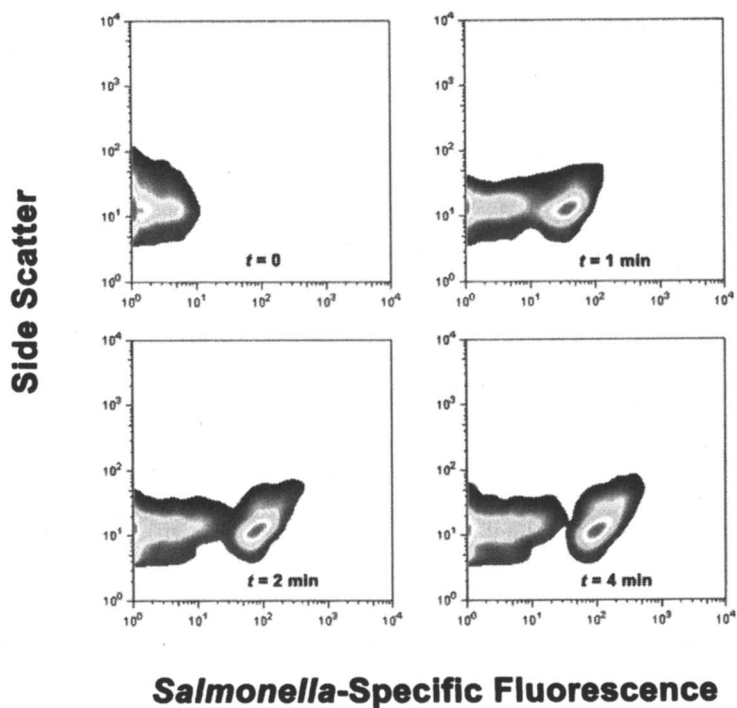


Figure 1. Detection of Target Cells From Within a Complex Mixture Via Rapid DNA-FISH and Flow Cytometry. A complex mixture containing *Salmonella typhimurium* and several strains of closely-related non-target bacteria (*Escherichia coli*, *Citrobacter freundii*, *Proteus vulgaris* and *Shigella dysenteriae*) was fixed with 10% buffered formalin and hybridized at 55 °C for up to 4 min with an rRNA-targeted DNA probe (*Sal3-Cy5*, 5ng μl^{-1}). The progress of the hybridization reaction was examined via flow cytometry (FACSCalibur, BD Biosystems) at the following intervals: prior to hybridization [$t = 0$ min] and after 1, 2 or 4 min hybridization. After only one minute, the subpopulation of *Salmonella* was easily resolved from the background flora (geometric mean fluorescence of *Salmonella* population = 46.3). At two minutes, the probe-conferred fluorescence of the *Salmonella* population increased further (geometric mean fluorescence of *Salmonella* population = 85.6); *Salmonella*-specific staining with this probe reached near-maximal value after four minutes (geometric mean fluorescence of *Salmonella* population = 111). These data highlight the rapidity of DNA-FISH as a means for genotypic detection of specific microbial cells within complex mixtures.

for use of this technique to detect rRNA-encoded targets, as the ribosome is a naturally-amplified target molecule. However, not all microorganisms can be identified successfully on the basis of “signature” 16S or 23S rRNA sequences. For example, typical FISH formats cannot be used to discriminate toxigenic *E. coli* from non-pathogenic *E. coli*, as the virulence determinants carried by this pathogen are chromosomally encoded. Apart from rRNA, additional targets for FISH analyses have been explored, including other forms of RNA (e.g. tmRNA, mRNA) and plasmid DNA (43). Although these are multicopy targets, the low abundance of these species requires the concurrent use of some method for signal amplification, such as catalyzed reporter deposition (CARD) (58, 59). Recent breakthroughs in FISH technology using polynucleotide probes now allow the detection of low copy (< 10 copies per cell) targets within individual cells (43). These probes not only hybridize to their targets within the cells, but also apparently interact with each other to form networks outside of the cell. With such networks “anchored” to the cell via specific hybridization with internal targets, excess, non-specifically bound probe can be removed via washing. With each probe containing multiple fluorophores, this external “mesh” of probes serves as a means for signal amplification, allowing detection of targets present at very low copy number (43, 56).

Additional modifications and variations that have expanded the capabilities of the FISH technique for environmental and clinical applications include combined microautoradiography and FISH (MAR-FISH) (12), which enables correlation of substrate uptake with cell type, and FISH-based detection of antibiotic susceptibility (60). This latter approach takes advantage of the fact that in certain pathogen-antibiotic pairs (*Helicobacter pylori* and clarithromycin, for example), antimicrobial resistance can be traced to point mutations on the 23S ribosomal subunit, which can be detected via FISH using mismatch-sensitive probe sets (60). Similar possibilities may also exist for other pathogen-antibiotic pairs, and a searchable database (the Ribosomal RNA Mutation Database) has been described, which could facilitate development of similar tests (61).

These innovations have pushed the envelope of what is possible using the FISH technique. Outside of environmental applications, though, most microbial testing requirements do not extend beyond presence/absence testing or detection and enumeration of a single target cell type. Although “classic” or traditional FISH is not as exquisitely sensitive as some of the other available methods for generating sequence-specific fluorescence signals within whole microbial cells, it is arguably the simplest and most robust method for doing so. As such, it can be readily used for routine detection of target cells within environmental samples, foods or clinical specimens, providing a rapid and sensitive means for molecular detection of pathogens in these samples. For more detailed background on the FISH technique, readers are referred to several excellent reviews, which cover everything from the basics of the process, to food, clinical and environmental and other specialized applications of the method (40-44).

Combining FISH & Flow Cytometry

A problem central to environmental, food and clinical microbiologies is the detection of specific microorganisms within physically and microbiologically complex sample matrices. Environmental samples, contaminated foods, infected tissues or bodily fluids or liquid dilutions made from such samples may contain high loads of particulate matter or non-target microflora, both of which present challenges to the direct detection of target cells. Flow cytometry is a general detection platform that enables the rapid, multiparametric analysis of complex microbial populations. In flow cytometric analysis, liquid samples are taken up and hydrodynamically focused to form a laminar flow within a surrounding sheath fluid (usually phosphate buffered saline). Within this stable stream, the cells (ideally) form a single file line and tumbling or other potentially interfering movements are minimized. The cells are then passed through the “heart” of the flow cytometer - the flow cell – where they are illuminated with a high-intensity light source, typically a laser or laser diode. Detectors and appropriate filter sets are then used to collect data on cellular responses, including forward angle light scatter (providing information on cell number and some size information), side angle scatter (providing information on the internal content, or opacity of the cells) and probe or dye-conferred fluorescence characteristics. As a multiparameter technique, flow cytometry can be used to distinguish between cellular and acellular particles, and when combined with an appropriate molecular probe, to detect specific microbial cells.

The combination of FISH and flow cytometry (FISH-FC) has found wide use for the analysis of complex samples in environmental, food and clinical applications. An example of this for environmental analysis is combined FISH and Fluorescence Activated Sorting (FISH-FACS) for the detection and sorting-based enrichment of specific cell types from natural samples. Kalyuzhnaya *et al.* (62) used this approach to examine methanotrophic bacteria from lake sediments and Sekar *et al.* (63) used similar methods to investigate the composition of marine bacterioplankton communities. Post-sorting genomic techniques were used in both cases for additional sample characterization (62, 63). Food applications of FISH-FC include the use of a *Pseudomonas*-specific DNA probe to detect this spoilage organism in milk (64) and detection of *Salmonella* spp. in raw, cubed pork using DNA probes specific for this genus (Bisha and Brehm-Stecher, unpublished data, **Figure 2**). Perhaps the ultimate test of this technique’s performance in a “noisy” environment (and linking both food and clinical analyses) is the use of FISH-FC to quantify specific cell types in feces (65, 66). As FISH is a culture-independent technique, this approach may be used to study the ecology of unculturable gut microflora (66). In the clinical realm, FISH-FC using both DNA and PNA probes has been explored for rapid detection of pathogens in blood cultures, including Gram-negative rods, *Staphylococcus aureus* and *Candida* spp. (52, 67). Access to rapid, robust and

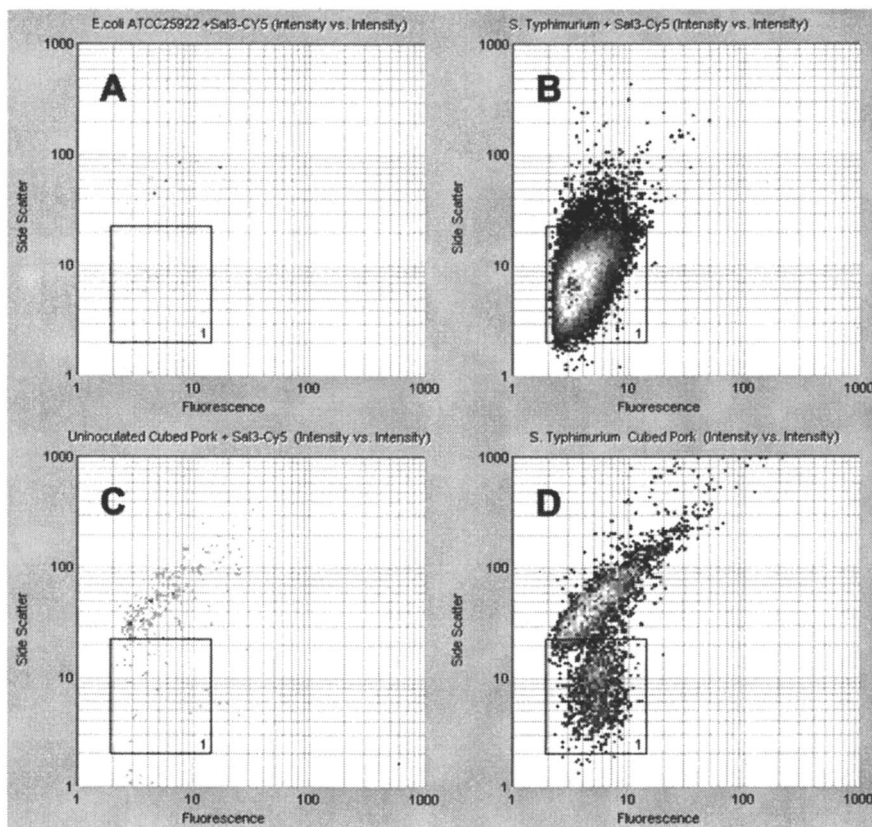


Figure 2. Direct Cytometric Detection of Salmonella spp. in Raw, Cubed Pork Meat Using Combined FISH and Flow Cytometry. This series demonstrates the specificity of fluorescence in situ hybridization (FISH) combined with flow cytometry for the rapid detection of Salmonella spp. in raw meat. Hybridization conditions were similar to those used in Figure 1. Panel A shows a high load of Escherichia coli hybridized with a Salmonella-specific DNA probe (control for non-specific staining of non-target cells). Panel B shows a pure culture of *S. typhimurium* hybridized with the probe (positive control for target cells). Panel C shows uninoculated cubed pork hybridized with the probe (control for non-specific staining of food particles). Panel D is a sample of cubed pork containing 10^5 CFU/ml *S. typhimurium* hybridized with the probe. These data demonstrate that although there is some interference from non-specific binding of the probe to food particles, target cells can still be easily discriminated from such background on the combined basis of scatter and fluorescence signals. An RBD-3000 cytometer (Advanced Analytical, Ames, IA) was used for these analyses.

culture-independent methods for pathogen detection or surveillance is expected to be important to this sector, as the benefits of rapid clinical diagnostics have been clearly identified in terms of both cost savings and improved patient outcome (reduced mortality) (68, 69).

With applications in environmental, food and clinical microbiologies, FISH-FC is a powerful combination, allowing the study of complex natural populations in the environment, as well as rapid detection of pathogens in both foods and clinical samples. Harmonization of FISH-FC protocols between the latter two areas should enable the detection of foodborne pathogens throughout the consumption-to-disease continuum, potentially improving food safety through disease intervention and patient outcomes through more timely diagnoses of disease. The availability of a new generation of smaller, task-dedicated cytometers designed specifically for microbial detection may also help speed the adoption of FISH-FC for more routine use by food and clinical microbiologists (52).

Biomimetics

Literally defined, “biomimetics” implies the direct copying of biology. More precisely defined, the term refers to nature-inspired design of molecules, materials or devices (70). Biomimetic approaches have been successfully applied for the development of antifouling “superglues” based on mussel adhesion strategies (71), artificial antibodies and enzymes (“plastibodies” and “plastizymes”) based on molecular imprinting techniques (72) and synthetic antimicrobial polymers that mimic the structure and function of host defense peptides (73). Using examples from nature as templates, new and advantageous synthetic analogs can be made, ranging in scale from molecules to materials. In molecular biology, biomimetic bioaffinity reagents are synthetic molecules that interact with natural ligands, including cell surface structures, proteins and nucleic acids. Because they may incorporate “unnatural” or artificial elements of design, such as use of a synthetic polymer backbone or scaffold, rather than naturally-occurring biopolymeric scaffolds, these reagents may be engineered to have very different and advantageous properties. Examples may include chemical or physical robustness vis-à-vis their biopolymeric counterparts, different charge densities or chiralities and the ability to modulate and “fine tune” biological activity using combinatorial approaches, ultimately yielding novel synthetic biorecognition reagents having distinct advantages over their natural counterparts.

Peptide nucleic acids (PNAs) have emerged as key biomimetic reagents for use in nucleic acid-based diagnostics. PNAs are synthetic DNA mimics made by grafting either natural or non-natural nucleobases onto a repeating backbone of

amide-linked *N*-(2-aminoethyl) glycine (AEG) units (74). Like DNA probes, PNAs hybridize to complementary DNA or RNA sequences via Watson-Crick base pairing, but their uncharged, hydrophobic backbones confer several advantageous properties over DNA-based probes. These include intrinsic resistance to enzymatic degradation (they are not natural substrates for either nucleases or proteases), faster hybridization kinetics, higher binding affinities for their targets, and the ability to penetrate “difficult” biological structures such as the exosporium of freshly-germinated bacterial endospores, the cysts of parasites such as *Cryptosporidium* and *Giardia* (Jens Hyldig-Nielsen, personal communication) and the thick cell walls of bacteria such as *Mycobacterium* and *Listeria* spp. (49, 75, 76). An additional advantage of PNA probes is their capacity for binding to portions of the ribosome that are physically inaccessible to traditional DNA probes, enabling detection of organism-specific diagnostic sequences that are otherwise “buried” in the higher-order structure of the ribosome (49, 50, 74, 77). This latter property stems largely from the fact that PNA probes are typically hybridized under low salt (0 – 100 mM NaCl), high temperature (55°C or higher), high pH (pH 9.0) conditions that destabilize the higher order structures of target nucleic acids. Together, these properties give PNA probes unique advantages as FISH probes over conventional DNA-based probes for whole cell detection of several important classes of microorganisms. As an interesting aside, Nelson et al., (78) have demonstrated the formation of AEG from methane, nitrogen, ammonia and water in electric discharge reactions designed to simulate conditions present in Earth’s primordial atmosphere. From these data, PNA has been suggested as being the first molecule of heredity, serving as a potential bridge from the pre-RNA world to the RNA world (78)

Additional nucleic acid mimics having applications in whole cell diagnostics include locked nucleic acids (LNAs). LNAs are conformationally-restricted (“locked” via 2'-*O*,4'-*C*-methylene linkages) ribonucleotide derivatives that have been developed in recent years (79, 80). Advantages of LNAs include rapid hybridization, very high thermostabilities for LNA-DNA or LNA-RNA hybrids (~ 8 - 10°C increase in melting temperature per LNA residue), high water solubility (often problematic with PNAs) and the ability to combine DNA and LNA monomers to form chimeric “mixmer” molecules (80). This latter capability enables greater control of probe melting temperature and allows placement of LNA moieties within a probe where they can potentially be used to confer position-specific effects (80, 81). Like PNAs, LNAs have been used advantageously in acellular diagnostics as capture probes and reporter probes in real-time PCR, but recent reports have also focused on their use in whole cell detection as FISH probes (81, 82). In this regard, they have been reported for use to detect sequences on lymphocyte metaphase chromosomes and interphase nuclei (82) and for increasing the hybridization brightness of probes directed against Gram-negative bacteria such as *Escherichia*, *Anaerolinea* and *Comamonas* spp. (81). As charged molecules, however, it will be interesting to

see if LNAs can be used to target “difficult” microbes with the same facility as is currently done using PNAs.

Several approaches to the development of antibody-like (and therefore biomimetic) binders have also been described in recent years. These include bioimprinted sol-gel polymers for binding whole yeast cells (83), peptide-based binders (84, 85, 86) and “affibodies” – non-antibody binders derived from randomizable small protein scaffolds (e.g. staphylococcal protein A) (87, 88).

Biomimetic affinity reagents such as these are expected to play an important role in future molecular detection strategies, as they have the capacity to mimic or improve upon “natural” ligand-receptor interactions, can be engineered for unique physicochemical properties or target specificities and may be combinatorial in nature, enabling “biopanning” or other similar discovery strategies, leading to rapid generation of new pathogen-specific binders or disease diagnosis without the need for prior knowledge of target sequence, or for emerging diseases, of the pathogen responsible for symptoms (89).

High-Throughput Methods for Reagent Discovery

Combinatorial or library-based methods for discovery of binding partners have several advantages over manual, “hunt and peck” approaches. First, a comparatively large dataspace can be searched for bioaffinity reagents that bind specifically to the target cell or desired cell surface feature. Second, libraries containing combinatorially synthesized variants of a parent compound can be screened to identify those variations that contribute to a desired property (binding specificity or avidity, for example) and these features can be incorporated into subsequent molecular design in order to refine or focus the activity of the compound. Bioinformatics tools can also be used to mine large virtual dataspace (e.g. the continually growing rRNA sequence dataspace) to assist in or automatically identify group- or species-specific oligonucleotide probes or primers, speeding what once was a fully manual or database-assisted process (90-93). Multiple layers of *in silico* mining and *in vitro* selection processes can be combined using high throughput wet chemistry evaluation to create a discovery pipeline for microbial signature sequences. In this way, many of the same informational tools developed for use in the Human Genome Project can also be marshaled to feed a discovery pipeline leading to new molecular diagnostics for bacteria and viruses (94).

Antimicrobials as Detection Reagents; Advantages of External Binders

In order for antimicrobial peptides (AMPs) to exert their actions on microbial cells, they must first bind to structures on the surfaces of target cells

(85). With this in mind, several researchers have exploited the selective binding properties of naturally-occurring AMPs for use in bacterial capture or immobilization (84, 85, 95). For example, Kulagina et al. (85) used magainin I as a capture reagent for a proof-of-concept silanized glass array detector targeting *Salmonella* and *E. coli* O157:H7. Blais et al. (95) used the AMP polymyxin B, which has been well-characterized for its interactions with lipopolysaccharide (LPS) of the Gram-negative outer membrane, to selectively bind Gram-negative bacteria in a microtiter-based assay. A subsequent immunochemical reaction with serotype-specific antibodies enabled detection of *E. coli* O111 and O26 serotypes in foods. Benefits of using polymyxin as an adsorbant in this type of application include its high-binding capacity for the LPS of Gram-negative bacteria, its chemical stability, low cost and ready availability (95). The availability of combinatorially synthesized biomimetic antimicrobial polymers (73) opens the exciting possibility for their development as next-generation binders. If this approach proves feasible, the potential plasticity in chemical, physical and binding properties offered by such reagents could be substantial. As fully synthetic compounds, such reagents may also have the added advantages of relatively simple and scalable production and the ability to incorporate surface-binding chemistries, facilitating their attachment to sensor surfaces. Apart from detection, the use of AMPs to selectively bind bacteria and even discriminate pathogenic and non-pathogenic cell types may also be very useful in such wide-ranging applications as cell-based immobilized bed reactors for industrial fermentations, water purification and bioremediation of contaminated materials (84).

Bioaffinity reagents that bind to cell surfaces, such as recombinant and natural antibodies, peptide binders, or the AMPs discussed above, have advantages in live cell applications over binders that interact with intracellular targets. Cell-surface binders do not require cell permeabilization to access their targets and can be reacted with target cells under physiological conditions, enabling the detection of living cells. The ability to detect living cells adds another dimension to the detection process, as it may facilitate more rapid and streamlined detection assays and target cells may be subsequently grown for additional characterization.

Cell-Based Sensors

Thus far, this chapter has primarily focused on the use of exogenous molecular reagents (probes, primers, enzymes, AMPs, etc.) to detect whole microbial cells. In other work, intact microbial cells have themselves been used as detection reagents in chemical or environmental sensing applications. These applications involve whole cell biosensors consisting of engineered microbial

strains containing stress-regulated promoters (*recA*, *uvrA*, etc.) upstream of suitable reporter genes (e.g. *gfp* or *lux*). In the presence of genotoxic agents such as formaldehyde, these “cellular canaries” produce a detectable product (e.g. green fluorescent protein or luciferase), effectively reporting the presence of environmental toxins (96). Whole (non-microbial) cells can also be made to serve as pathogen-specific detectors. For example, Rider et al., (97) engineered a line of murine B cells expressing both cytosolic aequorin and pathogen-specific, membrane-bound immunoglobulin M (IgM). Contact with the target pathogen causes cross-linking of surface-displayed IgM’s, which triggers an intracellular biochemical cascade (release of calcium). In the presence of calcium, the aequorin emits light, providing a detectable output (97). To perform the assay, the live-cell sensor is mixed with the test sample, allowed to interact briefly, the mixture centrifuged, and the tube placed in a luminometer for reading. The system has been examined with foot-and-mouth disease virus and several bacterial pathogens including *Yersinia pestis*, *Bacillus anthracis* spores and *E. coli* O157:H7, and is claimed to be capable of detecting as few as 50 colony-forming units within minutes (97).

Conclusions

Microbes are ubiquitous on Earth and occupy surfaces and microniches in a variety of complex environments, both organic and inorganic. Sophisticated diagnostic tools are needed in order to characterize the species distribution and ecological significance of the organisms present in and on these matrices. Methods for microbial diagnostics can be divided into two basic categories: cellular and acellular. Although acellular techniques can provide rapid and actionable information on the presence of specific microorganisms in various samples, including foods and clinical specimens, microbes are fundamentally cellular in nature, and additional layers of information are available within the context of the whole cell. This has spawned the development of a number of methods for detection and characterization of microbes at the level of the individual cell. Although such methods are sensitive, most are presently still too complex for use in routine analysis. At its simplest (basically a “shake and bake” approach), FISH provides a straightforward, robust and sensitive (enough) method for the molecular detection of individual microbial cells. It can be combined, to great effect, with single cell detection platforms such as flow cytometry to facilitate the sensitive detection of specific cells within microbially and physically complex matrices such as environmental samples, foods and clinical specimens.

Although they are often considered separately, many parallels exist between the disciplines of environmental, food and clinical microbiologies. These include

commonalities in goals, reagents, detection hardware and target organisms. Protocols developed for the detection of organisms in one area may often be adapted for use in another area, sometimes with minimal need for adjustment. Further harmonization and cross-pollination across the somewhat artificial boundaries between these disciplines will advance the state of the art for practical single cell detection in general.

This review has been focused primarily on the reagent side of the detection equation. This is an exciting time - new advances in biomimetic reagents, methods for combinatorial and bioinformatics-based reagent discovery are converging to push the envelope of whole cell diagnostics development. Synergies between next-generation reagents and newer, faster (and smarter?) detection platforms will continue to explore the limits of what is possible for whole cell detection of individual microorganisms.

References

1. Caracciolo, A. B.; Grenni, P.; Cupo, C.; Rossetti, S. *FEMS Microbiol. Lett.* **2005**, *253*, 55.
2. Kuhlman, K.R.; Fusco, W. G.; La Duc, M. T.; Allenbach, L. B.; Ball, C. L.; Kuhlman, G. M.; Anderson, R. C.; Erickson, I. K.; Stuecker, T.; Benardini, J.; Strap, J. L.; Crawford, R. L. *Appl. Environ. Microbiol.* **2006**, *72*, 1708.
3. La Cono, V.; Urzi, C. *J. Microbiol. Methods* **2003**, *55*, 71.
4. Walker, J. J.; Spear, J. R.; Pace, N. R. *Nature* **2005**, *434*, 1011.
5. Junge, K.; Eicken, H.; Deming, J. W. *Appl. Environ. Microbiol.* **2004**, *70*, 550.
6. Shinkai, T.; Kobayashi, Y. *Appl. Environ. Microbiol.* **2007**, *73*, 1646.
7. Diaz, P. I.; Chalmers, N. I.; Rickard, A. H.; Kong, C.; Milburn, C. I.; Palmer R. J. Jr.; Kolenbrander, P. E. *Appl. Environ. Microbiol.* **2006**, *72*, 2837.
8. Macfarlane, S.; Macfarlane, G. T. *Appl. Environ. Microbiol.* **2006**, *72*, 6204.
9. Koch, R. In *Milestones in Microbiology*; Brock T. D., Ed.; ASM Press: Madison, WI, **1999**; p. 101.
10. Cebula, T. A.; Jackson, S. A.; Brown, E. W.; Goswami G., LeClerc, J. E. *J. Food Prot.* **2005**, *68*, 1271.
11. Woese, C. R.; Kandler, O.; Wheelis, M. L. *Proc. Natl. Acad. Sci. USA* **1990**, *87*, 4567.
12. Wagner, M.; Nielsen P. H., Loy, A.; Nielsen J. L.; Daims, H. *Curr. Opin. Biotechnol.* **2006**, *17*, 83.
13. Fletcher J.; Bender, C.; Budowle, B.; Cobb, W. T.; Gold, S. E.; Ishimaru, C. A.; Luster, D.; Melcher, U.; Murch, R.; Scherm, H.; Seem, R. C.; Sherwood, J. L.; Sobral, B. W.; Tolin, S. A. *Microbiol. Mol. Biol. Rev.* **2006**, *70*, 450.

14. Gerner-Smidt, P.; Hise, K.; Kincaid, J.; Hunter, S.; Rolando, S.; Hyytia-Trees, E.; Ribot, E. M.; Swaminathan, B.; Pulsenet Taskforce *Foodborne Pathog. Dis.* **2006**, *3*, 9.
15. Simpson, J. M.; Santo Domingo, J. W.; Reasoner, D. J.; *Environ. Sci. Technol.* **2002**, *36*, 5279.
16. Harold, F. M. *Microbiol. Mol. Biol. Rev.* **2005**, *69*, 544.
17. Brehm-Stecher, B. F.; Johnson, E. A. *Microbiol. Mol. Biol. Rev.* **2004**, *68*, 538.
18. Schmidt, T. M. *Int. Microbiol.* **2006**, *9*, 217.
19. Giraffa, G.; Neviani, E. *Int. J. Food Microbiol.* **2001**, *67*, 19.
20. Gould, G.W. *Soc. Appl. Bacteriol. Symp. Ser.* **1992**, *21*, 59S.
21. Shapiro, J. A. *Annu. Rev. Microbiol.* **1998**, *52*, 81.
22. Costerton, J. W.; Stewart, P. S.; Greenberg, E. P. *Science* **1999**, *284*, 1318.
23. Donlan, R. M. *Emerg. Infect. Dis.* **2002**, *8*, 881.
24. Ercolini, D.; Hill, P. J.; Dodd, C. E. R. *J. Microbiol. Methods* **2003**, *52*, 267.
25. Hodson, R. E.; Dustman, W. A.; Garg, R. P.; Moran, M. A. *Appl. Environ. Microbiol.* **1995**, *61*, 4074.
26. Porter, J.; Pickup, R.; Edwards, C. *FEMS Microbiol. Lett.* **1995**, *134*, 51.
27. Tani, K.; Kurokawa, K.; Nasu, M. *Appl. Environ. Microbiol.* **1998**, *64*, 1536.
28. Tolker-Nielsen, T.; Holmstrøm, K.; Boe, L.; Molin, S. *Mol. Microbiol.* **1998**, *27*, 1099.
29. Hoshino, T.; Noda, N.; Tsuneda, S.; Hirata, A.; Inamori, Y. *Appl. Environ. Microbiol.* **2001**, *67*, 5261.
30. Holmstrøm, K.; Tolker-Nielsen, T.; Mølin, S. *J. Bacteriol.* **1999**, *181*, 1733.
31. Chen, F.; Binder, B.; Hodson, R. E. *FEMS Microbiol. Lett.* **2000**, *184*, 291.
32. Lange, M.; Tolker-Nielsen, T.; Molin, S.; Ahring, B. K. *Appl. Environ. Microbiol.* **2000**, *66*, 1796.
33. Chen, F.; González, J. M.; Dustman, W. A.; Moran, M. A.; Hodson, R. E. *Appl. Environ. Microbiol.* **1997**, *63*, 4907.
34. Lanoil, B. D.; Giovannoni, S. J. *Appl. Environ. Microbiol.* **1997**, *63*, 1118.
35. Lanoil, B. D.; Carlson, C. A.; Giovannoni, S. J. *Environ. Microbiol.* **2000**, *2*, 654.
36. Maruyama, F.; Kenzaka, T.; Yamaguchi, N.; Tani, K.; Nasu, M. *Appl. Environ. Microbiol.* **2005**, *71*, 7933.
37. Maruyama, F.; Tani, K.; Kenzaka, T.; Yamaguchi, N.; Nasu, M. *Appl. Environ. Microbiol.* **2006**, *72*, 6248.
38. Maruyama, F.; Kenzaka, T.; Yamaguchi, N.; Tani, K.; Nasu, M. *Appl. Environ. Microbiol.* **2003**, *69*, 5023.
39. DeLong, E. F.; Wickham, G. S.; Pace, N. R. *Science* **1989**, *243*, 1360.
40. Amann, R.; Ludwig, W. *FEMS Microbiol. Rev.* **2000**, *24*, 555.

41. Amann, R.; Fuchs, B. M.; Behrens, S. *Curr. Opin. Biotechnol.* **2001**, *12*, 231.
42. Moter, A.; Göbel, U. B. *J. Microbiol. Methods* **2000**, *41*, 85.
43. Zwirgmaier, K. *FEMS Microbiol. Lett.* **2005**, *246*, 151.
44. Amann, R. I.; Ludwig, W.; Schleifer, K. –H.; *Microbiol. Rev.* **1995**, *59*, 143.
45. Anderson, M.L.M. *Nucleic Acid Hybridization*; BIOS Scientific Publishers: Oxford, UK, 1999; pp. 23-25.
46. Demidov, V. V. In *Encyclopedia of Diagnostic Genomics and Proteomics*, Fuchs, J., Podda, M., Eds. Marcel Dekker, Inc., New York, **2005**; pp. 1175-1179.
47. Zhong, X.; Lizardi, P. M.; Huang, X.; Bray-Ward, P. L.; Ward, D. C. *Proc. Natl. Acad. Sci. USA* **2001**, *98*, 3940.
48. Notomi, T.; Okayama, H.; Masubuchi, H.; Yonekawa, T.; Watanabe, K.; Amino, N.; Hase, T. *Nucleic Acids Res.* **2000**, *28*, E63.
49. Brehm-Stecher, B. F.; Hyldig-Nielsen, J. J.; Johnson, E. A. *Appl. Environ. Microbiol.* **2005**, *71*, 5451.
50. Fuchs, B. M.; Wallner, G.; Beisker, W.; Schwippl, I.; Ludwig, W.; Amann, R. *Appl. Environ. Microbiol.* **1998**, *64*, 4973.
51. Fang, Q.; Brockman, S.; Botzenhart, K.; Wiedenmann, A. *J. Food Prot.* **2003**, *66*, 723.
52. Hartmann, H.; Stender, H.; Schäfer, A.; Autenrieth, I. B.; Kempf, V. A. J. *J. Clin. Microbiol.* **2005**, *43*, 4855.
53. Ootsubo, M.; Shimizu, T.; Tanaka, R.; Sawabe, T.; Tajima, K.; Ezura, Y. *J. Appl. Microbiol.* **2003**, *95*, 112.
54. Tang, Y. Z.; Hoong Gin, K. Y.; Lim, T. H. *Appl. Environ. Microbiol.* **2005**, *71*, 8157.
55. Jansen, G. J.; Mooibroek, M.; Idema, J.; Harmsen, H. J. M.; Welling, G. W.; Degener, J. E. *J. Clin. Microbiol.* **2000**, *38*, 814.
56. Zwirgmaier, K.; Ludwig, W.; Schleifer, K. –H. *Mol. Microbiol.* **2004**, *51*, 89.
57. Hammer, B.; Moter, A.; Kahl, O.; Alberti, G.; Göbel, U. B. *Microbiology* **2001**, *147*, 1425.
58. Pernthaler, A.; Amann, R. *Appl. Environ. Microbiol.* **2004**, *70*, 5426.
59. Schönhuber, W.; Guenhael, L. B.; Tremblay, J.; Amann, R.; Kulakauskas, S. *BMC Microbiol.* **2001**, *1*, 20.
60. Rüssmann, H.; Adler, K.; Haas, R.; Gebert, B.; Koletzko, S., Heesemann, J. *J. Clin. Microbiol.* **2001**, *39*, 4142.
61. Triman, K. L.; Peister, A.; Goel, R. A. *Nucleic Acids Res.* **1998**, *26*, 280.
62. Kalyuzhnaya, M. G.; Zabinsky, R.; Bowerman, S.; Baker, D. R.; Lidstrom, M. E.; Chistoserdova, L. *Appl. Environ. Microbiol.* **2006**, *72*, 4293.
63. Sekar, R.; Fuchs, B. M.; Amann, R.; Pernthaler, J. *Appl. Environ. Microbiol.* **2004**, *70*, 6210.

64. Gunasekera, T. S.; Dorsch, M. R.; Slade, M. B.; Veal, D. A. *J. Appl. Microbiol.* **2003**, *94*, 936.
65. Vaahtovuori, J.; Korkeamäki, M.; Munukka, E.; Viljanen, M.K.; Toivanen, P. *J. Microbiol. Methods* **2005**, *63*, 276.
66. Zoetendal, E. G.; Ben-Amor, K.; Harmsen, H. J. M.; Schut, F.; Akkermans, A. D. L.; de Vos, W. M. *Appl. Environ. Microbiol.* **2002**, *68*, 4225.
67. Kempf, V. A. J.; Mändle, T.; Schumacher, U.; Schäfer, A.; Autenrieth, I. B. *Int. J. Med. Microbiol.* **2005**, *295*, 47.
68. Alexander, B. D.; Ashley, E. D.; Reller, L. B.; Reed, S. D. *Diagn. Microbiol. Infect. Dis.* **2006**, *54*, 277.
69. Barenfanger, J.; Drake, C.; Kachich, G. *J. Clin. Microbiol.* **1999**, *37*, 1415.
70. Bar-Cohen, Y. *Bioinsp. Biomim.* **2006**, *1*, P1.
71. Fan, X.; Lin, L.; Dalsin, J. L.; Messersmith, P. B. *J. Am. Chem. Soc.* **2005**, *127*, 15843.
72. Bruggeman, O. *Adv. Biochem. Eng. Biotechnol.* **2002**, *76*, 127.
73. Tew, G. N.; Liu, D.; Chen, B.; Doerksen, R. J.; Kaplan, J.; Carroll, P. J.; Klein, M. L.; DeGrado, W. F. *Proc. Natl. Acad. Sci. USA* **2002**, *99*, 5110.
74. Stender, H.; Fiandaca, M.; Hyldig-Nielsen, J. J.; Coull, J. *J. Microbiol. Methods* **2002**, *48*, 1.
75. Ferrari, B. C.; Veal, D. *Cytometry A* **2003**, *51*, 79.
76. Lefmann, M.; Schweickert, B.; Buchholz, P.; Göbel, U.B.; Seiler, P.; Theegarten, D.; Moter, A. *J. Clin. Microbiol.* **2006**, *44*, 3760.
77. Lehtola, M. J.; Loades, C. J.; Keevil, C. W. *J. Microbiol. Methods* **2005**, *62*, 211.
78. Nelson, K.E.; Levy, M.; Miller, S. L. *Proc. Natl. Acad. Sci. USA* **2000**, *97*, 3868.
79. Koshkin, A. A.; Nielsen, P.; Meldgaard, M.; Rajwanshi, V. K.; Singh, S. K.; Wengel, J. *J. Am. Chem. Soc.* **1998**, *120*, 13252.
80. Petersen, M.; Wengel, J. *Trends Biotechnol.* **2003**, *21*, 74.
81. Kubota, K.; Ohashi, A.; Imachi, H.; Harada, H. *Appl. Environ. Microbiol.* **2006**, *72*, 5311.
82. Silahtaroglu, A. N.; Tommerup, N.; Vissing, H. *Mol. Cell Probes* **2003**, *17*, 165.
83. Dickert, F. L.; Hayden, O. *Anal. Chem.* **2002**, *74*, 1302.
84. Gregory, K.; Mello, C. M. *Appl. Environ. Microbiol.* **2005**, *71*, 1130.
85. Kulagina, N. V.; Lassman, M. E.; Ligler, F. S.; Taitt, C. R. *Anal. Chem.* **2005**, *77*, 6504.
86. Petrenko, V. A.; Sorokulova, I. B. *J. Microbiol. Methods* **2004**, *58*, 147.
87. Fernández, L. A. *Curr. Opin. Biotechnol.* **2004**, *15*, 364.
88. Renberg, B.; Shiroyama, I.; Engfeldt, T.; Nygren, P. -Å.; Karlström, A. E. *Anal. Biochem.* **2005**, *341*, 334.
89. Kouzmitcheva, G. A.; Petrenko, V. A.; Smith, G. P. *Clin. Diagn. Lab Immunol.* **2001**, *8*, 150.

90. Ashelford, K. E.; Weightman, A. J.; Fry, J. C. *Nucleic Acids Res.* **2002**, *15*, 3481.
91. Emrich, S. J.; Lowe, M.; Delcher, A. L. *Nucleic Acids Res.* **2003**, *31*, 3746.
92. Xing, E. P.; Wolf, D. M.; Dubchack, I.; Spengler, S.; Zorn, M.; Muchnik, I.; Kulikowski, C. *J. Theor. Biol.* **2001**, *212*, 129.
93. Zhang, Z.; Willson, R. C.; Fox, G. E. *Bioinformatics* **2002**, *18*, 244.
94. Fitch, J. P.; Gardner S. N.; Kuczmarksi, T. A.; Kurtz, S.; Myers, R.; Ott, L. L.; Slezak, T. R.; Vitalis, E. A.; Zemla, A. T.; McCready, P.M., *Proc. IEEE* **2002**, *90*, 1708.
95. Blais, B. W.; Bosley J.; Martinez-Perez, A.; Popela, M. *J. Microbiol. Methods* **2006**, *65*, 468.
96. Sørensen, S. J.; Burmølle, M.; Hansen, L. *Curr. Opin. Biotechnol.* **2006**, *17*, 11.
97. Rider, T. H.; Petrovick, M. S.; Nargi, F. E.; Harper J. D.; Schwoebel, E. D.; Mathews, R. H.; Blanchard, D. J.; Bortolin L. T.; Young, A. M.; Chen, J.; Hollis, M. A. *Science* **2003**, *301*, 213.

Chapter 4

Membrane Selectivity of Antimicrobial Peptides

Charlene M. Mello and Jason W. Soares

**Macromolecular Science Team, Natick Soldier Research Development and
Engineering Center, Natick Massachusetts**

Antimicrobial peptides are ubiquitous, classified primarily based upon secondary structure, and often possess broad spectrum activity. Our laboratory investigates the class of amphipathic α -helical peptides with an aim to elucidate the principles that determine peptide selectivity for bacterial membranes. Here we will review the current state of knowledge surrounding peptide characteristics that influence selective bacterial activity and present new data demonstrating Gram selective binding. Furthermore, we suggest that tailoring the binding affinity and selectivity of native peptides to capture and detect pathogenic cells will be realized in the near future.

Background

Antimicrobial peptides are part of an innate immune defense system in all organisms, fighting against microbial infection and ensuring survival in an ever-changing environment (1). Hundreds of antimicrobial peptides have been identified which are generally classified based upon their secondary structure (2). β -sheet peptides with one or more disulfide bonds (3), and α -helical peptides (4) comprise the majority of the peptides investigated in the current literature. Despite their differing conformations, most form an amphipathic structure with a distinct hydrophobic and cationic face in membrane environments. In general, they exhibit broad spectrum activity against Gram-positive and Gram-negative bacteria, fungi, and viruses. However, peptides with similar structures can possess rather different activity profiles.

Initial binding to target cells does not involve specific receptors on the cell membrane, but non-specific electrostatic interactions between the positively charged residues of the peptide and the anionic membrane (5). Due to the non-specific nature of the interaction, many antimicrobial peptides also lyse red blood cells and are cytotoxic to mammalian cells. Model phospholipid membranes have been studied to understand the mechanism of cytotoxicity. Peptides that bind preferentially to bacterial membranes efficiently disrupt the packing of anionic phospholipids while zwitterionic phospholipids are only permeated by peptides active upon mammalian cells (6). Lipid chemistry and peptide properties are collectively responsible for preferential bacterial activity. This chapter will summarize investigations focused upon peptide characteristics that may define bacterial selectivity.

Principles for Bacterial Membrane Specificity

An area of intense investigation has been focused on structure/function relationships of native, truncated, and rationally designed peptides to enhance antimicrobial activity while reducing hemolysis. Based upon these numerous reports, a few overarching principles are emerging. A well controlled balance of peptide structure, charge, hydrophobicity, flexibility, and assembly state appear to be important for selective binding and activity towards bacterial cell membranes relative to eukaryotic membranes.

Peptide Length and Assembly State

To explore the impact of self-assembly on bacterial selectivity, Glukhov *et al.* studied a family of cationic antimicrobial peptides in SDS micelles and

phospholipid vesicles capable of inserting into anionic lipid membranes but not zwitterionic membranes. The observed binding to model membranes, high antimicrobial activity and low hemolytic activity were attributed to peptide dimerization. SDS resistant dimers were confirmed by gel electrophoresis and the presence of such peptide dimers in anionic membranes revealed by fluorescence resonance energy transfer. The authors suggest that the sequence motif, AXXXA where X is any amino acid, is responsible for promoting dimerization, and possibly higher oligomerization states (7). It is not clear from this study, however, whether dimer formation occurs in aqueous conditions or following membrane binding

Peptide length and preassembly state of cationic antimicrobial peptides were investigated by Sal-Man and co-workers to determine if these are important discriminating factors for bacteria and erythrocytes. Lysine/Leucine rich peptides with variable lengths (13, 16, and 19 amino acids long) and covalently linked pentameric peptide bundles were evaluated for their activity and binding affinity to model membranes. The antibacterial activity of the monomeric peptides increased as a function of peptide length while activity towards erythrocytes remained constant. However, the activity of all bundles was not dependent upon peptide length. Preassembly increased activity towards erythrocytes which is supported by an observed 300-fold increase in peptide-membrane binding affinity toward zwitterionic vesicles compared with negatively charged vesicles. Therefore, preassembly of pentameric structures results in a loss of bacterial selectivity (8). Similarly, a single amino acid substitution in the leucine zipper motif of melittin, which has a propensity for oligomerization, results in a dramatic reduction of hemolytic activity but not antimicrobial activity. Disruption of oligomerization in high ionic strength conditions as well as membrane environments was demonstrated (9). Cooperatively, these results suggest that bacterial selectivity may require peptides to be monomeric and linear prior to membrane binding, but have the propensity to self-assemble in bacterial membrane environments. Furthermore, the composition of bacterial membranes may be more favorable to oligomerization of selective peptides than the zwitterionic lipids.

Hydrophobicity and Charge

Sequence analogs of pseudin-2, a naturally occurring 24 amino-acid amphipathic α -helical antimicrobial peptide, were utilized to explore the role of cationicity and hydrophobicity in bacterial selectivity. Neutral and acidic amino acid residues were increasingly substituted on the hydrophilic face of the α -helix with the cationic amino acid, L-lysine. An increase in activity towards a number of Gram-negative and Gram-positive bacteria while retaining low hemolytic activity was observed. Increasing the number of lysine residues in the

hydrophilic face to 4 and 5; however, did not further enhance antimicrobial potency but did increase hemolytic activity (10). Alternatively, modifying the hydrophobic face of antimicrobial leucine zippers by substituting leucine residues with alanine lowered the hemolytic activity while maintaining similar secondary structure; suggesting that minimizing hydrophobicity while maintaining amphiphilicity may preserve bacterial selectivity (9,11). Finally, molecular dynamic simulations were used to explore the effect of charge at the C-terminus of protegrin-like peptides on activity and toxicity (12). Removing a positively charged residue at the C-terminus does not significantly alter the peptide's toxicity, but replacing the positive charge with a negative charge reduces mammalian toxicity. These results hold great promise to rapidly advance the field by coupling simulations with model membrane experimental studies predicting both activity and selectivity.

Central Hinge or Helix Flexibility

IsCT is a natural amphipathic α -helical peptide with high activity against both mammalian and bacterial cells. Lee *et al.* designed several novel peptide analogs with bacterial cell selectivity based on the IsCT peptide sequence. Solution structures were determined by 2D-NMR spectroscopy and revealed that three peptides exhibiting the greatest selectivity also had a central hinge structure (13). A similar conclusion by this group was obtained by investigating a lysine/leucine peptide possessing limited selectivity (14). Sequence variants of these peptides were designed with proline substitutions to evaluate the impact of proline-induced bends on activity. Substitution of a central leucine residue yielded strong antibacterial activity but had no detectable hemolytic activity. Furthermore, proline substitutions in the hydrophobic face resulted in a much greater reduction of hemolytic activity than substitution in the hydrophilic face and D-proline substitutions improve bacterial selectivity more than L-proline (15). It is unlikely, however, that these substitutions have generated a bend in the structure; circular dichroism revealed a dramatic reduction in helix content (50% to 10%) suggesting a significant disruption of the helix. Nonetheless these results suggested that a central proline and α -helical content contribute to bacterial cell selectivity.

Shin *et al.* explored the role of two central glycine residues in pleurocidin. The tertiary structure determined by NMR spectroscopy revealed that pleurocidin has a flexible structure between the long helix from Gly3 to Gly17 and the short helix from Gly17 to Leu25 (16). Alanine substitutions at these central glycine residues (pleurocidin-AA) yielded antibacterial activities similar to pleurocidin but had dramatically increased hemolytic activity (17). The non-cell-selective antimicrobial peptide, pleurocidin-AA, interacted strongly with both negatively charged and zwitterionic phospholipid membranes.

Furthermore, the α -helical content of the peptide variant when bound to SDS micelles increased dramatically and is consistent with the removal of a hinge region. Shin *et al.* also demonstrated that an insertion of a Gly-Pro sequence into dermaseptin S3 resulted in a drastic reduction in hemolytic activity, with retention of the antibacterial activity (18); presumably due to a proline induced bend. Bend or hinge regions of peptides have also been resolved with molecular dynamics simulations. An 8-residue helical antimicrobial peptide ovispirin-1 and its analogs novispirin-G10 and novispirin-T7 in SDS micelles were predicted to contain bend or hinge regions and are in good agreement with membrane-bound peptide structures predicted by solid state NMR (19). Collectively, the studies presented here suggest that structural flexibility between two helices may play a key role in bacterial cell selectivity of antimicrobial peptides.

Methodology

Elucidation of Binding Selectivity

Contrary to the literature summary presented here, which focuses upon activity based selectivity, our research centers around the determination of native binding affinity and varied binding selectivity for Gram-negative and Gram-positive bacteria to improve our understanding of the mechanisms of peptide discriminatory behavior. To probe peptide binding behavior, a whole cell binding assay (Figure 1) was developed utilizing antimicrobial peptides synthesized via Fmoc solid-phase peptide synthesis with the addition of a c-terminal cysteine for site-directed immobilization onto a maleimide reactive microplate. Whole bacterial cells (e.g. *Escherichia coli* O157:H7, *S. aureus*) grown to mid-log phase ($OD_{600}=1$) were harvested, washed and resuspended in phosphate buffered saline, pH 7.2 (10^8 cfu/ml). The cell suspension is added to the wells (10^7 cfu/well) containing immobilized peptide. Peptide binding for the respective cells is evaluated by adding a horseradish peroxidase (HRP)-conjugated polyclonal antibody for the target cell. A 2-component TMB peroxidase substrate system is then added and absorbance at 650nm after 30-minute incubation is recorded.

Antibody Normalization

To accurately depict peptide binding for the whole cells, the binding data must be normalized; compensating for antibody affinity differences for their

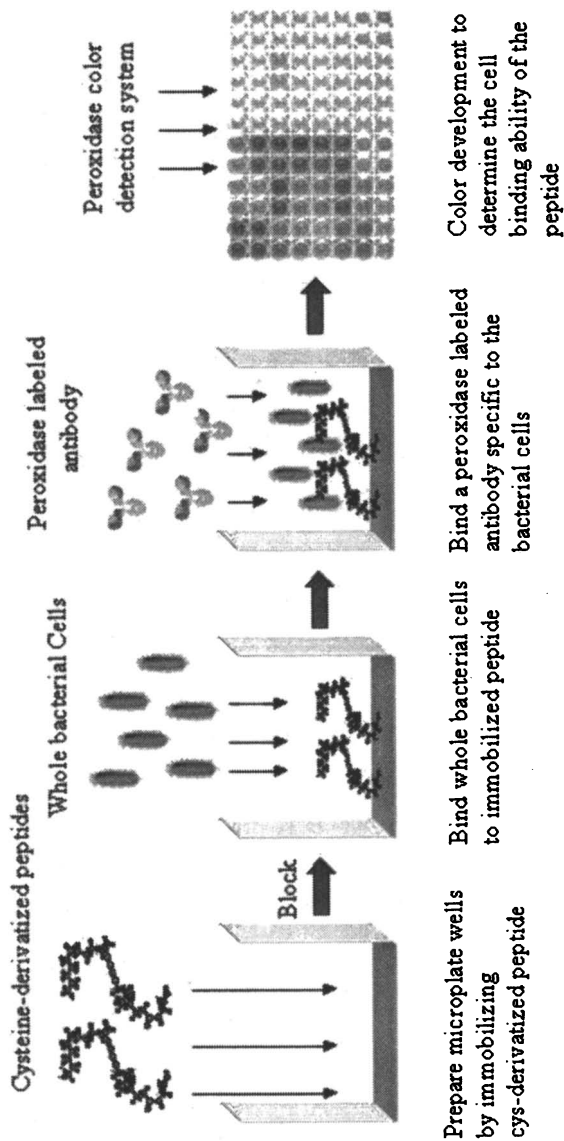


Figure 1. Schematic of whole cell binding assay. Whole cells are grown to mid-log and bound to the immobilized peptides. Peptide binding for the whole cells is evaluated with horseradish peroxidase (HRP)-conjugated polyclonal antibodies. Color development was measured at absorbance of 650nm after 30 minutes incubation.

respective target cells. At an identical number of cells, each antibody (Horseradish-peroxidase conjugated anti-*E. coli* O157:H7, anti-*S. aureus* (general species), and anti-*E. coli* (general species)) produced significantly different responses for their respective cells (Figure 2). It is not currently possible to quantitate the number of cells bound per peptide; therefore, correction formulas were determined to correlate initial peptide binding affinity for *E. coli* ML35 and *S. aureus* to a corrected value. The corrected value is relative to an effective normalization of *E. coli* ML35 (ATCC 43827) and *S. aureus* 27217 (ATCC 27217) antibody affinity to that of *E. coli* O157:H7 (ATCC 43888).

The antibody affinity curves were fit exponentially and linearized. Curves were fit with linear equations and analyzed at $X_{O157} = X_{ML35} = X_{S. aureus}$ where $X = \log$ (cells bound). Subsequent linearization results in the following linear equations:

$$\ln y_{O157} = 1.057X_{O157} - 7.326 \quad (1)$$

$$\ln y_{ML35} = 1.742X_{ML35} - 14.670 \quad (2)$$

Solving for number of cells (X),

$$X_{O157} = (\ln y_{O157} + 7.326) / 1.057 \quad (3)$$

$$X_{ML35} = (\ln y_{ML35} + 14.67) / 1.742 \quad (4)$$

Evaluate at equal X,

$$(\ln y_{O157} + 7.326) / 1.057 = (\ln y_{ML35} + 14.670) / 1.742 \quad (5)$$

$$\ln y_{O157} = 0.607 \ln y_{ML35}(\text{org}) + 1.579 \quad (6)$$

Translation of the corrected antibody curves enables the direct correlation of the *E. coli* ML35 (y_{ML35}) and *S. aureus* ($y_{S. aureus}$) with *E. coli* O157:H7 absorbance (y_{O157}) and thus the development of *E. coli* ML35 and *S. aureus* 27217 peptide binding affinity correction formulas (Table I). These correction formulas allow for accurate depiction of a peptide's relative binding affinity for *S. aureus* and *E. coli* ML35. This antibody normalization method can be implemented for any combination of bacterial cells and relevant antibodies.

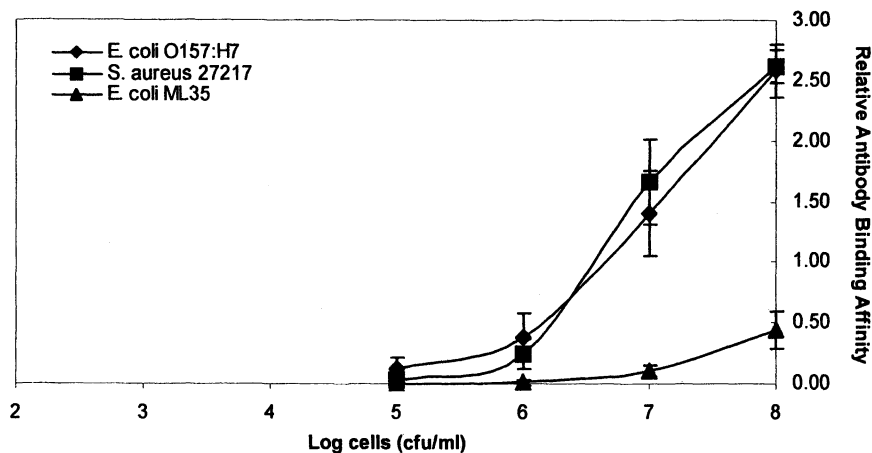


Figure 2. Antibody affinity curves of Anti-E. coli O157:H7, Anti-S. aureus (*gen spec*), and Anti-E. coli (*gen spec*) for E. coli O157:H7, S. aureus 27217, and E. coli ML35 whole cells respectively.

Table I. Antibody Correction Formulas

Bacteria	Correction formula
<i>E. coli</i> ML35	$\ln y_{\text{ML35}(\text{corr})} = 0.607 \ln y_{\text{ML35}(\text{org})} + 1.579$
<i>S. aureus</i> 27217	$\ln y_{\text{S.aureus}(\text{corr})} = 0.657 \ln y_{\text{S.aureus}(\text{org})} + 0.156$

y_{org} = initial peptide binding affinity for the respective cell. y_{corr} = corrected peptide binding to compensate for relative differences in respective antibody affinities. Both are in measures of absorbance (Abs 650nm)

Antimicrobial Peptide Binding

To select peptide candidates for investigation, an antimicrobial peptide database was developed classifying peptides based on structural characteristics, antimicrobial activity, and amino acid sequence. Downselection was based on a lack of post-translational modifications, absence of cysteine residues, and activity for Gram-negative *E. coli*. The selection criteria were motivated by the need for rapid chemical synthesis and the desire to control peptide orientation during immobilization for subsequent whole cell binding assays. Cecropin P1 isolated from a pig intestinal parasitic nematode (*Ascaris suum*) (21), vector mosquito cecropin A (*Aedes albopictus*) (23), winter flounder pleurocidin (*Pleuromectes americanus*) (20), African clawed frog PGQ (*Xenopus laevis*) (22), medfly ceratotoxin A (*Ceratitits capitata*) (24), and sheep SMAP-29 (*Ovis aries*) (25) were all chosen for this study. The full-length peptides were evaluated for binding of *E. coli* O157:H7 relative to non-pathogenic *E. coli* ML35 and Gram-positive *S. aureus* (Table II). All six of the peptides exhibited preferential binding for the Gram-negative *E. coli* O157:H7 relative to the Gram-positive *S. aureus*. Cecropin P1 and PGQ also exhibited preferential binding for the pathogenic *E. coli* O157:H7 relative to non-pathogenic *E. coli*.

Conclusions

Despite a significant amount of experimental data centered around molecular mechanisms and characteristics of peptide-mediated cell lysis, degree of peptide insertion into the membranes, the extent and significance of pore formation, membrane destabilization process and other studies; few reports have focused on the the selectivity of these peptides. The limited studies in current literature suggest that bacterial selective antimicrobial activity may be driven by several factors including assembly state, hydrophobicity, charge, and flexibility. Peptides which favor anionic model membranes may require a monomeric state prior to membrane binding. Increasing charge in the hydrophilic face can improve selectivity as well as minimizing hydrophobicity while maintaining the amphipathic structure. In addition, structural flexibility particularly in the center of the molecule appears to play a role in minimizing mammalian toxicity while maintaining antimicrobial activity. Finally, we have demonstrated that antimicrobial selectivity can be extended beyond the eukaryotic/prokaryotic discrimination to Gram specific binding of selected peptides. These results suggest that tailoring peptide sequence may yield improved selectivity for pathogen specific capture and destruction.

Table II. Antimicrobial peptide discriminatory capability

<i>Antimicrobial peptide</i>	<i>E. coli</i> O157:H7 <i>binding</i> ^a	<i>E. coli</i> ML35 <i>binding</i> ^b	<i>D</i> _{Gram neg.} ^c	<i>S. aureus</i> 27217 <i>binding</i> ^b	<i>D</i> _{Gram pos.} ^d
pleurocidin	1.256	0.984	1.276	0.076	16.526
cecropin p1	2.026	1.205	1.681	0.217	9.336
PGQ	1.934	1.055	1.833	0.216	8.954
ceratotoxin A	1.252	0.925	1.354	0.247	5.069
cecropin A	1.069	0.822	1.300	0.140	7.636
SMAP-29	1.334	1.087	1.227	0.179	7.453

^aAbsorbance values at 650nm

^bcorrected absorbance values at 650nm for *E. coli* ML35 ($\ln y_{\text{ML35corr}} = 0.607 \ln y_{\text{ML35}} + 1.579$) and for *S. aureus* 27217 ($\ln y_{\text{S.aureus(corr)}} = 0.657 \ln y_{\text{S.aureus(org)}} + 0.156$)

^c*D*_{Gram neg.} = antimicrobial peptide discriminatory binding capability for *E. coli* O157:H7 relative to a non-pathogenic Gram negative *E. coli* ML35

^d*D*_{Gram-pos.} = antimicrobial peptide discriminatory binding capability for *E. coli* O157:H7 relative to Gram-positive *S. aureus*

References

1. Boman, H. G. *Annu. Rev. Immunol.* **1995**, *13*, 61-92.
2. Nicolas, P.; Mor, A. *Annu. Rev. Microbiol.* **1995**, *49*, 277-304.
3. Lehrer, R. I.; Lichtensien, A.; Ganz, T. *Annu. Rev. Immunol.* **1993**, *11*, 105-128.
4. Tossi, A.; Sandri, L.; Giangaspero, A. *Biopolymers* **2000**, *55*, 4-30.
5. Shai, Y. *Biochim. Biophys. Acta* **1999**, *1462*, 55-70.
6. Papo, N.; Shai, Y. *Peptides* **2003**, *24*, 1693-703.
7. Glukhov, E.; Stark, M.; Burrows, L. L.; Deber, C. M. *J. Biol. Chem.* **2005**, *280*, 33960-7.
8. Sal-Man, N.; Oren, Z.; Shai, Y. *Biochemistry* **2002**, *41*, 11921-30.
9. Asthana, N.; Yadav, S. P.; Ghosh, J. K. *J. Biol. Chem.* **2004**, *279*, 55042-50.
10. Pal, T.; Sonnevend, A.; Galadari, S.; Conlon, J. M. *Regul. Pept.* **2005**, *129*, 85-91.
11. Ahmad, A.; Yadav, S. P.; Asthana, N.; Mitra, K.; Srivastava, S. P.; Ghosh, J. K. *J. Biol. Chem.* **2006**, *281*, 22029-38.
12. Langham, A. A.; Kaznessis, Y. N. *Molecular Simulation* **2006**, *32*, 193-201.
13. Lee, K.; Shin, S. Y.; Kim, K.; Lim, S. S.; Hahm, K. S.; Kim, Y. *Biochem. Biophys. Res. Commun.* **2004**, *323*, 712-9.
14. Shin, S. Y.; Hahm, K. S. *Biotechnol. Lett.* **2004**, *26*, 735-9.
15. Song, Y. M.; Yang, S. T.; Lim, S. S.; Kim, Y.; Hahm, K. S.; Kim, J. I.; Shin, S. Y. *Biochem. Biophys. Res. Commun.* **2004**, *314*, 615-21.

16. Yang, J. Y.; Shin, S. Y.; Lim, S. S.; Hahm, K.-S.; Kim, Y. *Journal of Microbiology and Biotechnology* **2006**, *16*, 880-888.
17. Lim, S. S.; Song, Y. M.; Jang, M. H.; Kim, Y.; Hahm, K. S.; Shin, S. Y. *Protein and Peptide Letters* **2004**, *11*, 35-40.
18. Shin, S. Y.; Yang, S.-T.; Eom, S. H.; Song, W. K.; Kim, Y.; Hahm, K.-S.; Kim, J. I. *Protein and Peptide Letters* **2001**, *8*, 281-288.
19. Khandelia, H.; Kaznessis, Y. N. *Peptides* **2005**, *26*, 2037-49.
20. Cole, A. M.; Weis, P.; Diamond, G. *J. Biol. Chem.* **1997**, *272*, 12008-12013.
21. Andersson, M.; Boman, A.; Boman, H. G. *Cell. Mol. Life Sci.* **2003**, *60*, 599-606.
22. Moore, K. S.; Bevins, C. L.; Brasseur, M. M.; Tomassini, N.; Turner, K.; Eck, H.; Zasloff, M. *J. Biol. Chem.* **1991**, *266*, 19851-19857.
23. Sun, D.; Eccleston, E. D.; Fallon, A. M. *Biochem. Biophys. Res. Commun.* **1998**, *249*, 410-415.
24. Marchini, D.; Giordano, P. C.; Amons, R.; Bernini, L. F.; Dallai, R. *Insect Biochem.* **1993**, *23*, 591-598.
25. Bagella, L.; Scocchi, M.; Zanetti, M. *FEBS Lett.* **1995**, *376*, 225-228.

Chapter 5

Antibacterial Activities of Thin Films Containing Ceragenins

Paul B. Savage,^{1*} Jason Nielsen,¹ Xin-Zhong Lai,¹ Yanshu Feng,¹
Yang Li,¹ Gard Nelson,¹ Matthew R. Linford,¹ Carl Genberg²

¹Department of Chemistry and Biochemistry, Brigham Young University,
Provo, UT 84602

²Ceragenix Pharmaceuticals, Denver, CO 80202

Ceragenins are small molecule mimics of naturally occurring antimicrobial peptides and display potent antimicrobial activities against a range of Gram-negative and positive organisms. When covalently attached to polymers, ceragenins retain antimicrobial activity. Materials, such as medical grade foams, coated with thin films of polymeric ceragenins release the polymers slowly into aqueous solution providing sustained antimicrobial activity in the surrounding solution over periods greater than three weeks.

Antimicrobial peptides have been isolated in organisms ranging from humans to insects, and over 1,000 examples have been characterized (1). Their study has attracted great interest due to the prevalence of these peptides and the central role they play in innate immunity of higher organisms. Particularly noteworthy is the fact that bacteria have been exposed to these antimicrobial agents for eons and generally remain susceptible to their bactericidal action. Faced with ever growing numbers of drug-resistant organisms, there is a need for new approaches to control bacterial growth, especially those that do not readily engender bacterial resistance. Consequently, there is considerable interest in clinical use of antimicrobial peptides (1, 2). However, costs of preparing and purifying peptides is much higher than those associated with more traditional antimicrobial agents. In addition, antimicrobial peptides are typically susceptible to proteases, and bacteria have evolved means of producing and releasing proteases as a means of avoiding the bactericidal actions of antimicrobial peptides (3, 4). These problems have hampered, to some extent, the development of antimicrobial peptides for clinical use.

Considering the large number of antimicrobial peptides that have been developed, it is possible to determine common features of these compounds that are likely to be responsible for their bactericidal activity. Many antimicrobial peptides form cationic, facially amphiphilic alpha-helices in the presence of bacterial membranes (1, 5). For example, the amphiphilic structures of cathelicidin LL-37, found in humans, and magainin I, found in amphibians, are shown in Figure 1. On one face of the helix cationic groups are clustered, while on the other, hydrophobic groups are presented. Other antimicrobial peptides form beta-sheets with similar facially amphiphilic morphologies. Facial amphiphiles differ from typical amphiphiles in that rather than contain a polar head group and a hydrophobic tail, they present a hydrophobic face juxtaposed with a polar or ionic face.

Development of Ceragenins

We (5, 6), along with other groups (7, 8), reasoned that the cationic, facially amphiphilic morphologies of antimicrobial peptides could be mimicked using scaffolding other than that found in peptides. Cholic acid (Figure 2) is a common bile acid, and is itself a facial amphiphile with three hydroxyl groups oriented on one face of the steroid. To convert cholic acid into a mimic of antimicrobial peptides, we attached amines, through hydrocarbon tethers, to the hydroxyl groups on cholic acid. Examples of ceragenins are given in Figure 2. Due to the simplicity of ceragenins, they can readily be prepared on a large scale, and they are not substrates for proteases.

Through structure activity studies (5, 6), we determined that a three carbon tether between the amines and the steroid provided the most potent antibacterial activity. We also found that the group appended at C24 (see Figure 2 for steroid numbering) greatly influenced antibacterial activity. A hydrophobic chain at C24, as in CSA-13, yields a compound that effectively kills both Gram-negative and positive bacteria. Ceragenins lacking this hydrophobic chain, such as CSA-8, retain the ability to kill Gram-positive organisms, but are only weakly active against Gram-negative bacteria (9). Nevertheless, CSA-8 has high affinity for Gram-negative bacterial membranes (10), and concomitant with association CSA-8 permeabilizes the outer membranes and sensitizes these organisms to hydrophobic antibiotics (e.g., erythromycin, rifampin), that ineffectively traverse the outer membranes of Gram-negative bacteria (11).

Comparisons of the antimicrobial activities of ceragenins and alpha helix-forming antimicrobial peptides indicate that their mechanisms of action are very similar if not identical (12). Ceragenins rapidly depolarize bacterial membranes, demonstrate high affinity for bacterial membrane components, and cause blebbing in bacterial membranes. Furthermore, bacteria respond to ceragenins by turning on the same genes that they do in the presence of sublethal concentrations of antimicrobial peptides. Consequently, it is anticipated that ceragenins, like antimicrobial peptides, will not readily engender resistance in bacteria. In testing the antimicrobial activities of ceragenins against drug-resistant bacteria, these compounds have demonstrated very high activities without any cross resistance with clinically used antibiotics.

Preparation of Polymeric Forms of Ceragenins and Coating on Foam Disks

The rationale for attaching ceragenins to polymers is to be able to prevent biofilm formation on medical devices. Bacterial infections associated with medical devices are a leading cause of illness among hospitalized patients (13). Two general methods for preventing biofilm formation on medical devices have been investigated: (1) covalent attachment of an antimicrobial agent to a surface, and (2) elution of an antimicrobial agent from a surface. We reasoned that a thin film made up of a bactericidal, ceragenin-based polymer would prevent biofilm formation by killing bacteria that came in contact with the film. In addition, if the solubility properties of the polymer were adjusted appropriately, the film would slowly dissolve and generate a new surface, thus preventing fouling of the antimicrobial surface.

Ceragenins are bactericidal due to their interactions with bacterial membranes. Consequently, it was expected that covalent attachment of ceragenins to a polymer backbone would not abrogate their activity. This may

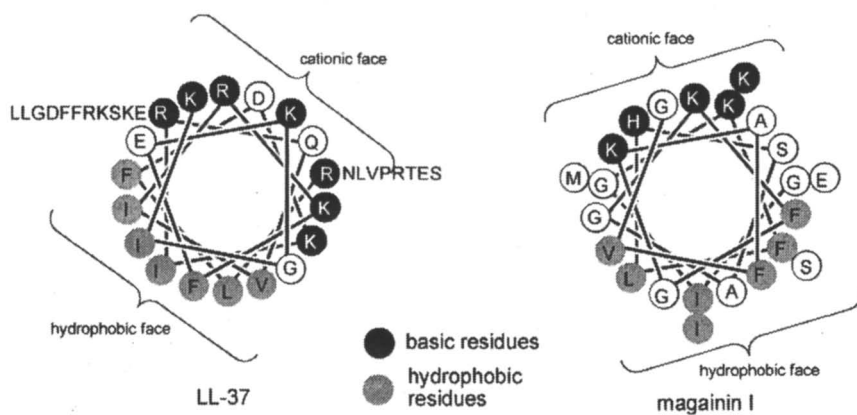


Figure 1. Helix wheel representations of antimicrobial peptides LL-37 and magainin I showing the facial amphiphilic character of the compounds.

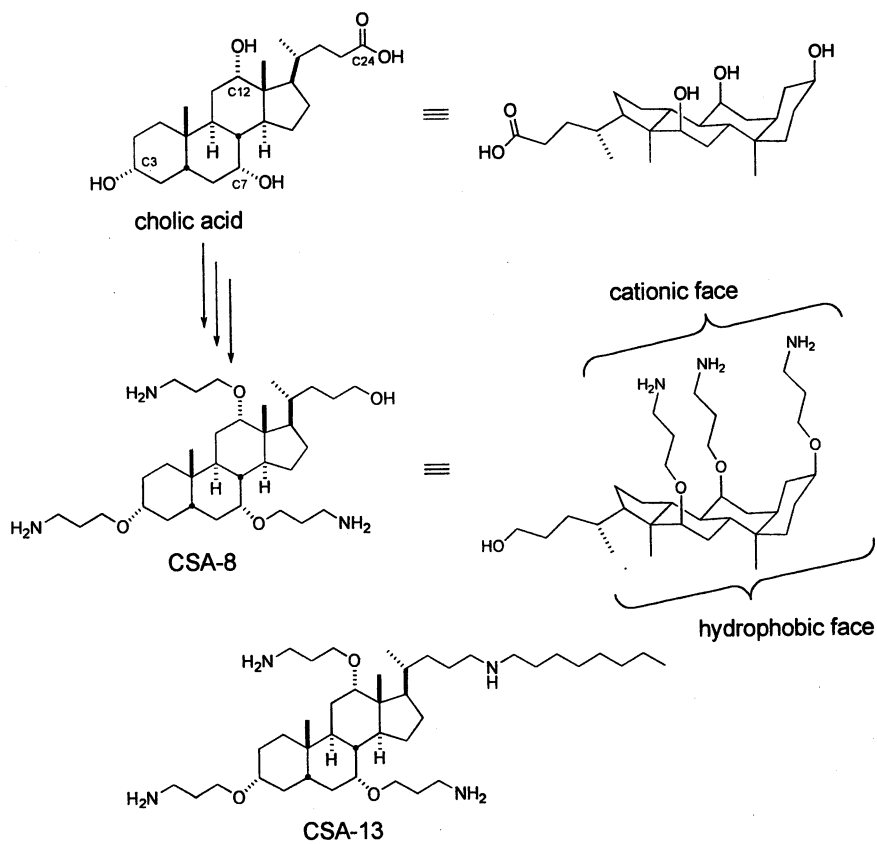


Figure 2. Structures of cholic acid, CSA-8, and CSA-13 showing the facial amphiphilic character of the compounds.

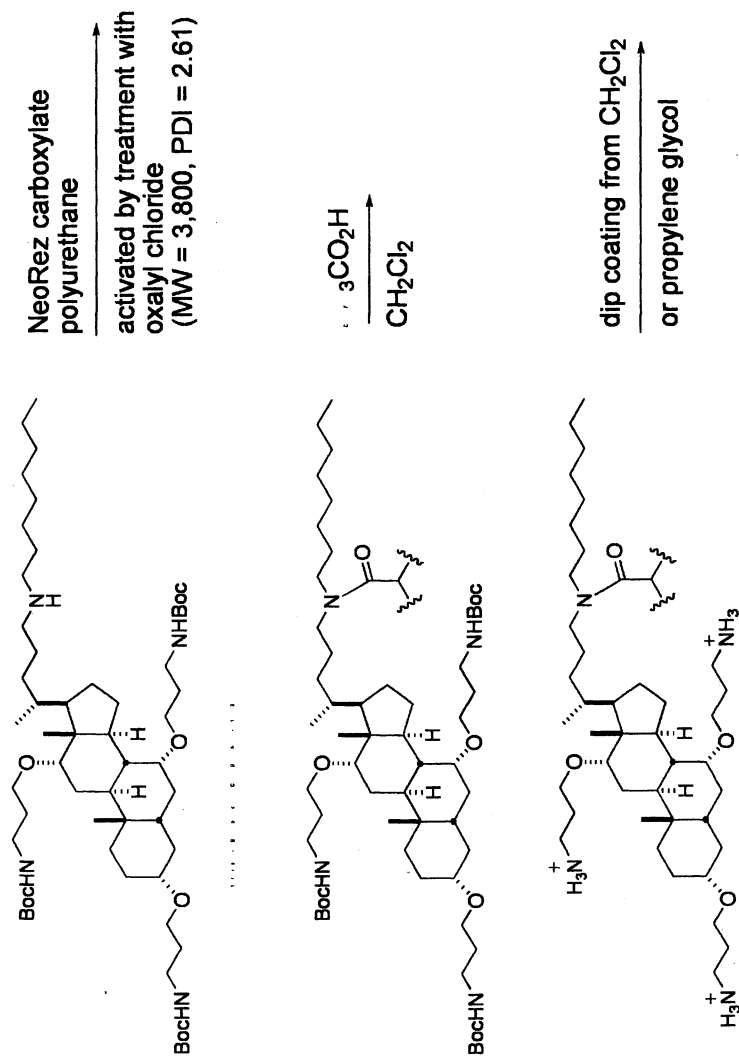
not be true for antibiotics that exhibit their antibacterial activities on protein or nucleic acid targets within bacteria. But because ceragenins act on the outside of the cell, a multivalent form of a ceragenin was expected to retain bactericidal activity.

We elected to use a proprietary polyurethane with a high acid number (19) from AST Products, Inc (Billerica, MA) for generating the ceragenin polymer. This type of polymer is routinely used as a medical device coating, and the carboxylic acid groups provide a site at which a ceragenin can be covalently attached. The acid number is the number of milligrams of KOH neutralized by one gram of the polymer (an acid number of 19 equates to 0.34 mmol of acid groups per gram of polymer).

The acid groups in the polymer were activated using oxalyl chloride to generate the polyacid chloride. This material was dissolved in dichloromethane and treated with an excess of tris-Boc CSA-13 (Scheme 1). Unreacted acid chlorides were capped with butyl amine. Tris-Boc CSA-13 is readily available in the course of synthesis of CSA-13, and the compound provides one reactive secondary amine group for amide formation. We have established that the amine groups on CSA-13 at C3, C7, and C12 are required for antibacterial activity; consequently, it was necessary to protect them to avoid amide formation with these primary amines. Use of tris-Boc CSA-13 ensures that only the dispensable amine at C24 is used for immobilization. Formation of the amide gave a link to the polymer that is not cleaved under testing or physiological conditions (*vide infra*). After tris-Boc CSA-13 was attached to the polymer, it was deprotected using trifluoroacetic acid in dichloromethane. The resulting polymer had a molecular weight of ca. 3,800 with a polydispersity of 2.61 as determined using gel permeation chromatography with polystyrene standards.

Mass differences indicated that the ceragenin, after deprotection, comprised ca. 15% of the material. With an acid number of 19, the theoretical maximum amount of ceragenin that could be attached would comprise 18% of the mass. Consequently, the ceragenin occupies over 80% of the available sites in the polymer conjugate. Two experiments were performed to ensure that the ceragenin was covalently attached to the polymer. First, no free ceragenin was observed on TLC. The second experiment took advantage of the solubility difference between CSA-13 and the ceragenin-polymer conjugate. CSA-13 is highly soluble in water (solutions of > 5% are possible), whereas the polymer conjugate is sparingly soluble in water. The resulting ceragenin-polymer conjugate was dispersed in water, and the resulting solution/suspension was filtered through a 0.2 micron filter. The filtrate exhibited no measurable antibacterial activity. Apparently, the limited solubility of the polymer conjugate prevented it from passing through the filter, while we have routinely used filtration to sterilize solutions of CSA-13.

The material on which a coating was generated was a medical grade foam in the shape of a disk (with a hole in the center; see Scheme 1). This material was selected because it allowed direct comparison to a similar foam product that is



Scheme 1. Generation of the polymer-ceragenin conjugate and dip coating on a foam disk.

impregnated with chlorhexidine and is used to inhibit infections of indwelling catheters and pins (14, 15). Foam disks (~250 mg) were coated by dipping into solutions of the polymer conjugate in either dichloromethane or propylene glycol. The residual solvent was removed under vacuum to yield the coated foam (~450 mg).

Antibacterial Testing of Foam Coated with the Ceragenin-Polymer Conjugate

We used a rigorous means of testing the antimicrobial impregnated materials by exposure to large volumes of solution and high inocula of bacteria. Because the foam disks were not expected to be exposed to flowing solutions, we used relatively large volumes of solution in a static environment.

Testing was performed by immersing a foam disk in 45 mL of phosphate buffered saline for 24 h. The disk was removed, and the resulting solution was inoculated with either methicillin-resistant *Staphylococcus aureus* (clinical isolate from Dr. Henry F. Chambers) or tobramycin-resistant *Pseudomonas aeruginosa* (clinical isolate from Dr. Jane L. Burns) to give ca. 10^6 CFU/mL. The kinetics of bactericidal activity were determined at 2, 4, and 6 h by removing samples of the solutions at the indicated time periods, serially diluting the samples, plating the diluted sample on Mueller-Hinton agar, incubating for 24 h, and counting colonies. The same procedure was repeated, with fresh solutions every 24 h. Experiments were performed in triplicate and representative data are shown. Variations in results at the 4 and 6 h time points were less than 20% and in all trials the ceragenin-polymer releasing foam eradicated the inocula by 6 h after more than 18 repeated soaks.

The chlorhexidine-releasing foam (Johnson & Johnson) rapidly eradicated the inocula of *P. aeruginosa* for the first 7 to 8 days (Figure 3, top), but began to lose activity after day 9, and even after 6 h only a three log reduction in CFU/mL was measured. This result was not unexpected; instructions for use of chlorhexidine-releasing foam call for replacement after 7 days. The ceragenin-polymer conjugate releasing foam demonstrated a 6 log reduction in CFU/mL in 4 h for nearly 21 days and still gave a 3 log reduction after 27 days (Figure 3, bottom).

Surprisingly, the chlorhexidine-releasing foam was only weakly active against MRSA (Figure 4, top). After 15 days, the experiment was terminated because little activity was observed. In contrast, the ceragenin-polymer conjugate releasing foam was very active against MRSA; after soaking the foam in 24 separate aliquots of 45 mL over the course of 24 days, the inoculum was completely eradicated within 6 h by the solution from day 24 (Figure 4, bottom).

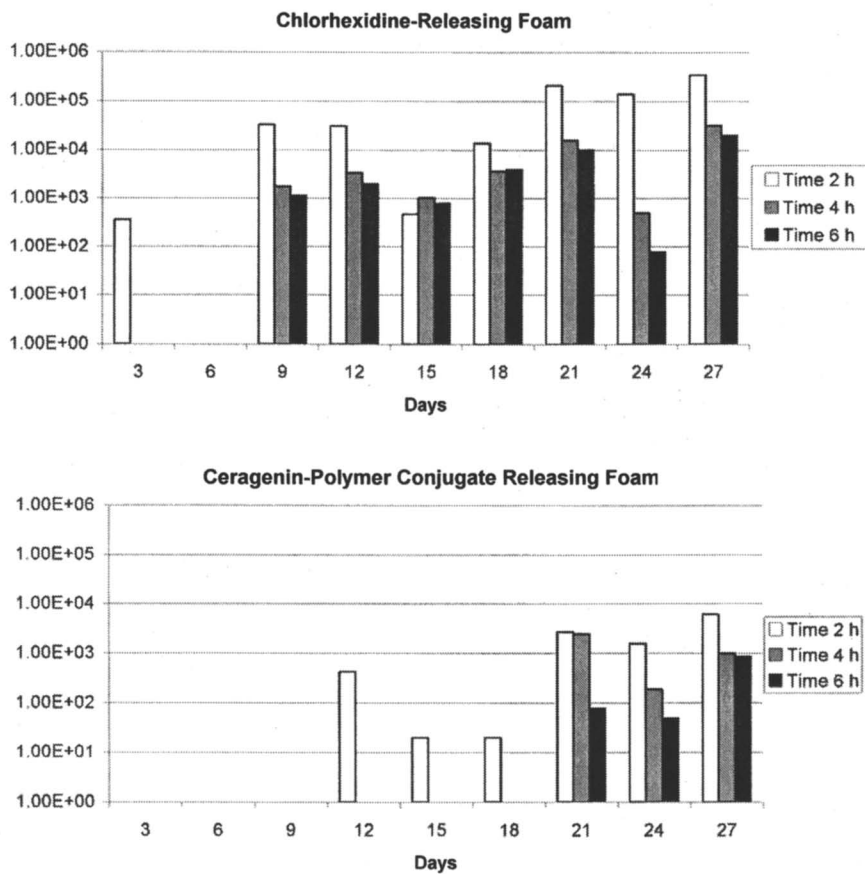


*Figure 3. Reduction in initial inocula (ca. 10^6 CFU/mL) of *P. aeruginosa* in separate 45 mL samples prepared by soaking the foam disks for 24 h, then removing the disks and inoculating. This procedure was repeated daily for 27 days. Top: log reduction in inoculation by chlorhexidine-releasing foam. Bottom: log reduction in inoculation by ceragenin-polymer conjugate releasing foam.*

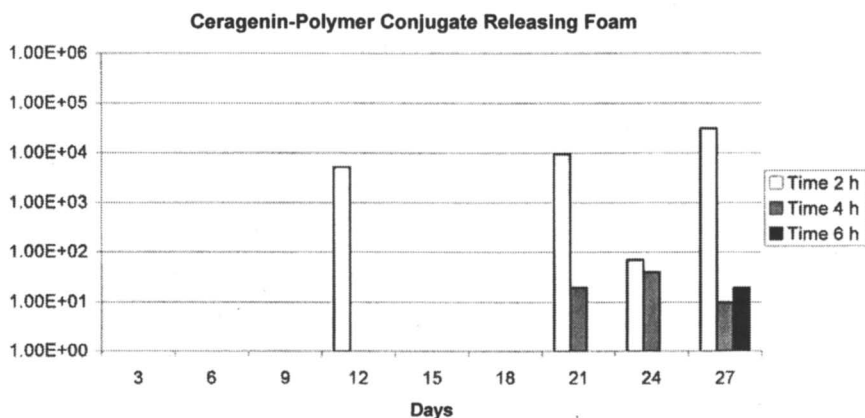
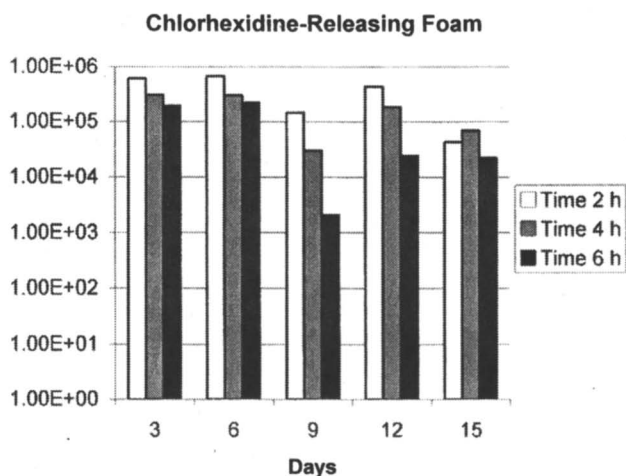


Figure 4. Reduction in initial inocula (ca. 10^6 CFU/mL) of *S. aureus* in separate 45 mL samples prepared by soaking the foam disks for 24 h, then removing the disks and inoculating. This procedure was repeating daily for 27 days. Top: log reduction in inoculation by chlorhexidine-releasing foam. Bottom: log reduction in inoculation by ceragenin-polymer conjugate releasing foam

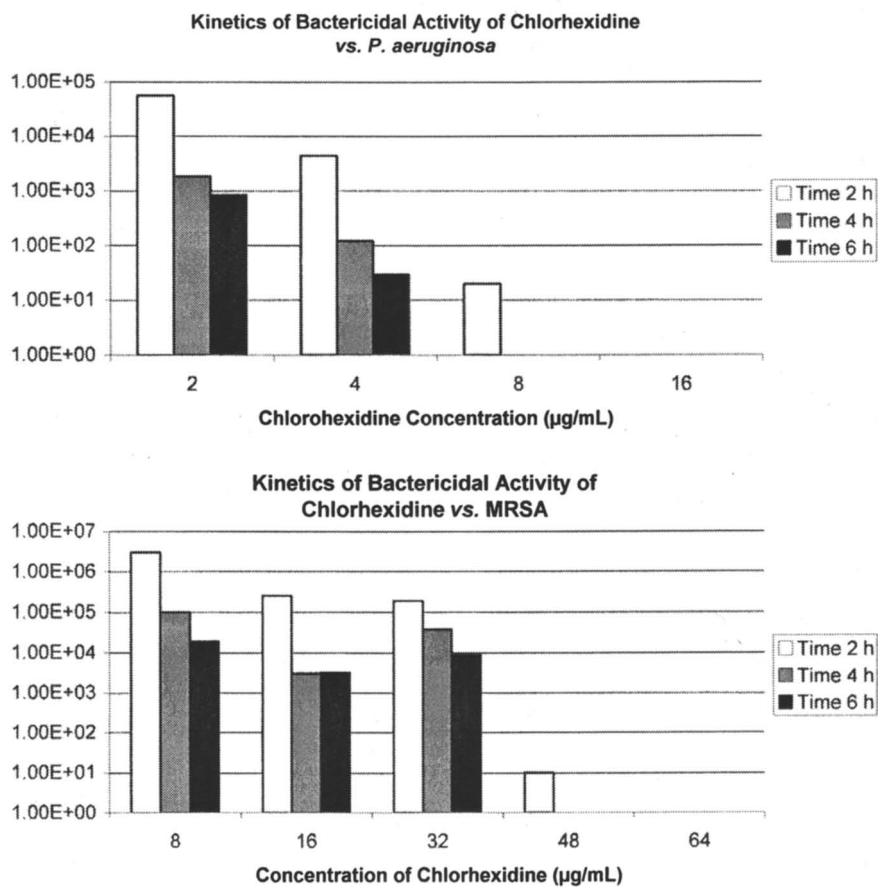


Figure 5. Kinetics of bactericidal activities of chlorhexidine against tobramycin-resistant *P. aeruginosa* and MRSA. Assays were performed in phosphate buffered saline. Top: remaining inoculum of *P. aeruginosa* after exposure to chlorhexidine for the indicated time periods. Bottom: remaining inoculum of MRSA after exposure to chlorhexidine for the indicated time periods.

To better understand the activities of the chlorhexidine foam and the ceragenin-polymer releasing foam, the kinetics of bactericidal activities of chlorhexidine and ceragenin CSA-13 were compared. Due to the limited solubility of the ceragenin-polymer conjugate, it was not possible to accurately measure the kinetics of the bactericidal activity of the conjugate. As an approximation, CSA-13 was used as a comparator for chlorhexidine.

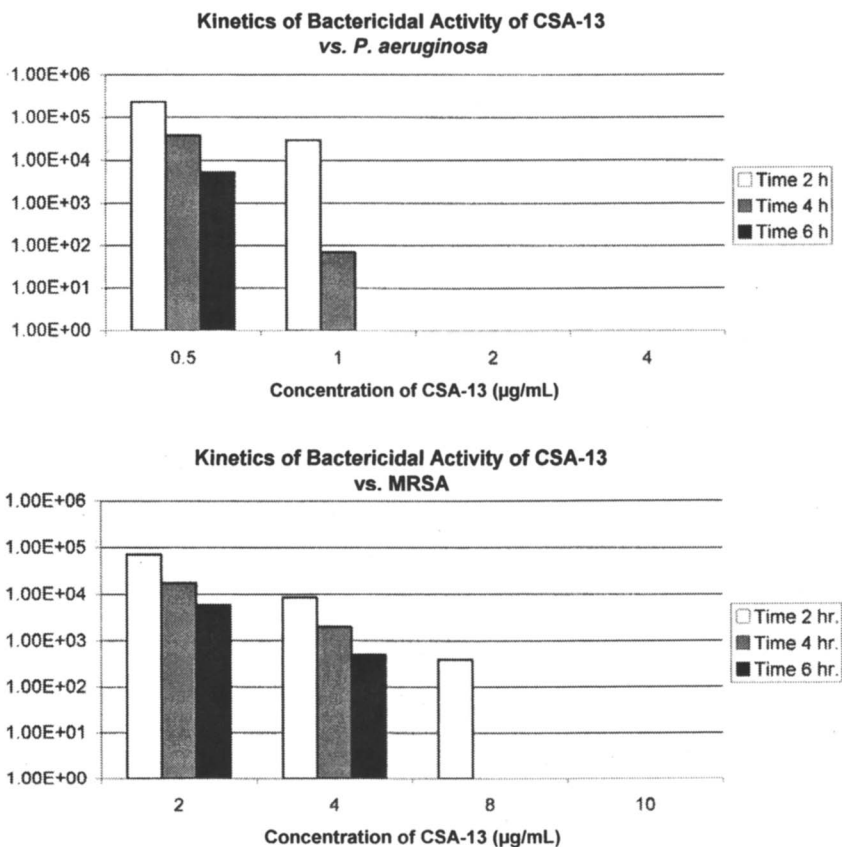


Figure 6. Kinetics of bactericidal activities of the ceragenin-polymer conjugate against tobramycin-resistant *P. aeruginosa* and MRSA. Assays were performed in phosphate buffered saline. Top: remaining inoculum of *P. aeruginosa* after exposure to CSA-13 for the indicated time periods. Bottom: remaining inoculum of MRSA after exposure to CSA-13 for the indicated time periods.

Chlorhexidine rapidly eradicated the inoculum of tobramycin-resistant *P. aeruginosa*, but was much less active against the MRSA strain used (Figure 5). Only at concentrations above 32 $\mu\text{g}/\text{mL}$ was chlorhexidine active against this strain.

Ceragenin CSA-13 proved to be very active against the *P. aeruginosa* strain used; at 2 $\mu\text{g}/\text{mL}$ the inoculum was completely eradicated by 2 h (Figure 6). This concentration is comparable to the minimum inhibition concentration measured for CSA-13 with a standard strain of *P. aeruginosa*. With the strain of MRSA used, CSA-13 eradicated the inoculum at a relatively low concentration, and this difference, as compared to chlorhexidine, may explain in part the differences in activities of the foams against MRSA. The differences may also depend upon the relative elution rates of chlorhexidine and the ceragenin-polymer conjugate.

As mimics of antimicrobial peptides, ceragenins apparently share a mechanism of action with many alpha-helix forming peptides. Most of these antimicrobial agents function via the "carpet" mechanism (16). According to this model, the antimicrobial agent accumulates on the bacterial surface, and when a threshold concentration is reached, the membrane is compromised. Attachment of the ceragenin to a polymer may facilitate aggregation on the bacterial surface and improve the kinetics of bactericidal activity of the ceragenin.

Conclusions

Use of foams impregnated with antimicrobial agents provides a means of inhibiting infections associated with indwelling catheters and pins, and sustained release of the antimicrobial agent allows extended use of the foams. The chlorhexidine-releasing foam has proven useful in a clinical setting; however, this material was only weakly active against the MRSA strain used in this study. In contrast, the ceragenin-polymer conjugate releasing foam was active against both *P. aeruginosa* and the MRSA strain used. In addition, this foam eradicates relatively high inocula of bacteria for a longer duration than the chlorhexidine releasing foam. Consequently, the ceragenin-polymer conjugate releasing foam may offer advantages over the chlorhexidine releasing foam.

Acknowledgements

Funding for this research provided by Ceragenix Pharmaceuticals Incorporation is gratefully acknowledged.

References

1. Jenssen, H.; Hamill, P.; Hancock, R. E. W. *Clin. Microbiol. Rev.* **2006**, *19*, 491.
2. Andrés, E.; Dimarcq, J. L. *J. Internal Med.* **2004**, *255*, 519.
3. Rooijackers, S. H. M.; van Kessel, K. P. M.; van Strijp, J. A. G. *Trends Microbiol.* **2005**, *13*, 596.
4. Peschel, A.; Sahl H.-G. *Nature Rev. Microbiol.* **2006**, *4*, 529.
5. Savage, P. B. *European J. Org. Chem.* **2002**, 759.
6. Savage, P. B.; Li, C.; Taotafa, U.; Ding, B.; Guan, Q. *FEMS Lett.* **2002**, *217*, 1.
7. Hamuro, Y.; Schneider, J. P.; DeGrado, W. F. *J. Am. Chem. Soc.* **1999**, *121*, 12200.
8. Porter, E. A.; Wang, X. Lee, H.-S.; Weisblum, B.; Gellman, S. H. *Nature* **2000**, *404*, 565.
9. Li, C.; Budge, L. P.; Driscoll, C. D.; Willardson, B. M.; Allman, G. W.; Savage, P. B. *J. Am. Chem. Soc.* **1999**, *121*, 931.
10. Ding, B.; Yin, N.; Liu, Y.; Cardenas-Garcia, J.; Evanson, R.; Orsak, R.; Fan, M.; Turin, G.; Savage, P. B. *J. Am. Chem. Soc.* **2004**, *126*, 13642.
11. Schmidt, E. J.; Boswell, S. R.; Walsh, J. P.; Schellenberg, M. M.; Winter, T. W.; Li, C.; Allman, G. W.; Savage, P. B. *J. Antimicrob. Chemother.* **2001**, *47*, 671.
12. Ding, B.; Guan, Q.; Walsh, J. P.; Boswell, J. S.; Winter, T. W.; Winter, E. S.; Boyd, S. S.; Li, C.; Savage, P. B. *J. Med. Chem.* **2002**, *45*, 663.
13. Ma, Z.; Morris, T. W.; Combrink, K. D. *Ann. Rep. Med. Chem.* **2004**, *39*, 197.
14. Levy, I.; Katz, J.; Solter, E.; Samra, Z.; Vidne, B.; Birk, E.; Askenazi, S.; Dagan, O. *Pediatric Infect. Disease J.* **2005**, *24*, 676.
15. Egol, K. A.; Paksima, N.; Puopolo, S.; Klugman, J.; Heibert, R.; Koval, K. *J. J. Bone Joint Surg.* **2006**, *88A*, 349.
16. Shai, Y. *Biopolymers* **2004**, *66*, 236.

Chapter 6

Retention and Viability of *Staphylococcus epidermidis* on Protein-Coated Self-Assembled Monolayers

Joshua Strauss^a, Yatao Liu^a, Eftim Milkani^b,
W. Grant McGimpsey^{b,c}, and Terri A. Camesano^{a,*}

^aDepartment of Chemical Engineering

^bDepartment of Chemistry and Biochemistry

^cBioengineering Institute, Worcester Polytechnic Institute,
100 Institute Rd, Worcester, MA, USA 01609

Coatings for biomaterials, such as self-assembled monolayers (SAMs), are being developed to resist biofilm formation on catheters and other devices. Researchers need to have fast and simple laboratory assays for assessing the properties of the SAMs, and many use batch or dip tests, although a variety of experimental procedures can be found in the literature. We optimized the design of simple batch assays to test the performance of a variety of SAMs in preventing retention of or in deactivating a clinically isolated strain of *Staphylococcus epidermidis*, with the goal of rapid screening to allow for the development of new implant coatings to prevent implant-associated infections. Ten carbon chain SAMs terminating in 4-(16-bromo hexadecyloxy)pyridine (PDT), 5-(10-mercaptodecyloxy)isophthalic acid (IPA), and isophthalic acid complexed with silver (IAG) were constructed on gold-coated glass slides. The retention and viability of *S. epidermidis* to the varying substrates was quantified via fluorescence microscopy. Parallel experiments were designed in order to help mimic *in vivo* conditions, in which a model protein, fetal bovine serum (FBS), was deposited onto the SAMs to determine how protein presence affected bacterial retention

and viability. The deposited protein layers were examined by atomic force microscopy (AFM) and quantified in terms of height and roughness. Optimal batch test conditions were 30 min incubation of substrates in bacterial solutions with concentrations of 2×10^7 cells/mL. All of the SAMs promoted decreased bacterial retention compared to the control surface, bare gold. For the protein deposition phase, incubating the slide in 10% FBS solution for 80 min yielded uniform and reproducible protein structures. Bacteria were less prone to retention on an FBS deposited substrate, with reductions of 79.3% on FBS + gold, 92.4% on FBS + IAG, and 95.5% on FBS + IPA, compared to the substrates without proteins.

Introduction

Hospital patients with a catheter-related bloodstream infection (CRBSI) bear both physical and financial burdens. Costs incurred by these nosocomial infections are commonly over \$25,000 per patient (1), with hospital stays prolonged by 12 days (2). Annually, there are over 250,000 CRBSIs (3) in U.S. hospitals, and it has been estimated that nearly every person in an industrialized nation will serve as host to a catheter at least once (4). The biofilm is responsible for the pathogenic nature of bacteria such as *Staphylococcus epidermidis*, which provides protection against environmental stresses (5). *S. epidermidis* and other coagulase-negative *Staphylococci* are implicated in ~50% of CRBSIs (2). Treatments against biofilms associated with *S. epidermidis* involve the use of powerful antibiotics such as vancomycin that do not always eradicate the infection (6, 7), and often removal of the infected catheter is the only option (8).

Due to the limited options for treating CRBSIs, prevention represents a more practical approach. Hospitals often lead educational campaigns to stress the importance of hand washing and the practice of sterile techniques by health-care workers. In addition, researchers are working to design better catheters that resist biofilm formation. Self-assembled monolayers (SAMs) have received much attention in this area due to their versatility, uniformity, and facile construction. SAMs such as poly(ethylene oxide) can prevent the retention of *S. epidermidis* to gold substrates by altering the surface characteristics such as wettability, roughness, and surface free energy (9).

The methods by which researchers study bacterial retention *in vitro* must account for key variables *in vivo*. Although important to study direct retention between bacteria and SAMs, this direct interaction may not occur *in vivo* since

catheters are rapidly coated with plasma proteins such as fibronectin (10), fibrinogen (11), and laminin (12) following implantation of a medical device. Researchers postulate that bacterial retention to a catheter is promoted by and occurs after proteins such as fibronectin are adsorbed to the surface (13).

Although bacterial retention has been investigated with a variety of substrates, most studies have not considered the effects of plasma proteins coating the substrates (9, 14-16). We studied the retention and viability of a clinically isolated strain of *S. epidermidis* under two sets of conditions: 1) bacteria interacting directly with substrates coated with SAMs; and 2) bacteria interacting with SAMs coated with deposited model proteins, fetal bovine serum (FBS). The SAMs in this study were all based on ten-carbon alkyl chains, but the terminal functional group was varied to include 4-(16-bromo hexadecyloxy)pyridine (PDT), 5-(10-mercaptodecyloxy)-isophthalic acid (IPA), and isophthalic acid complexed with silver (IAG). This group of SAMs was selected so that the effects of certain key functional groups could be isolated.

A dual staining (live/dead) kit consisting of propidium iodide (PI) and Syto 9™ was used to detect the number and condition of bacteria retained to the varying substrates. Atomic Force Microscopy (AFM), ellipsometry, and contact angle measurements were used to characterize the SAMs. The optimization of protein deposition and the washing processes of the substrates were also found to significantly affect the measured bacterial retention and viability. Therefore, we also discuss experimental details that need to be considered for further studies of bacterial-biomaterial interactions.

Materials and Methods

Preparation of Self-Assembled Monolayers (SAMs) on Gold-Coated Surfaces

Glass slides with a 5 nm chromium sublayer, followed by 100 nm of gold were purchased (Evaporated Metal Films; Ithaca, NY). Before use, gold slides were cleaned in piranha solution (30:70, 30% aqueous H₂O₂, concentrated H₂SO₄) for 10-20 min at 90°C. Slides were thoroughly rinsed with ultrapure water (Milli-Q water, Millipore Corp., Billerica, MA), followed by rinsing with ethanol, and dried in a nitrogen stream.

To construct the SAMs (Figure 1), clean gold slides were rinsed with anhydrous ethanol, dried with nitrogen gas, and used immediately. Monolayers were prepared by immersing the clean slides in a 1 mM ethanol solution of the desired compound overnight, or up to 24 h. SAMs terminating in isophthalic acid (IPA), isophthalic acid with silver (IAG), and pyridine decanethiol (PDT)

were prepared following published procedures [IPA (17), IAG(18), and PDT (19)]. Immediately prior to use, the slides were rinsed with ultrapure water and ethanol, and dried under nitrogen.

Characterization of SAMs

Ellipsometry

Ellipsometric measurements were obtained in air with a Manual Photoelectric Rudolf 439L633P ellipsometer (Rudolph Instruments, Fairfield NJ). The measurements were taken at a 70° angle of incidence using a HeNe laser light (principal wavelength = 632.8 nm). The reported thickness values for each film are the average of values obtained from three different freshly prepared samples. The thickness calculations were obtained with the software package that accompanies Rudolph ellipsometers. Values for the extinction coefficient and refractive index of the samples were assumed to be 0 and 1.457, respectively.

Contact Angle Measurements

Contact angle measurements were obtained with a goniometer (Ramé-Hart Model 100-00) at room temperature using the sessile drop technique (20). The gold slides were dried under a stream of nitrogen gas. Using an automatic pipettor, 2 μ L droplets of ultrapure water were gently placed on the surface of the slide. The contact angle was measured as quickly as possible (approximately 30 to 60 s after placing the droplet on the surface), because evaporation of a portion of the liquid can cause the contact angle to change. At least three values were recorded per slide.

Protein Deposition on SAMs

Fetal bovine serum (FBS) (Atlanta Biologicals, Atlanta, GA) was diluted in 0.1 M MES buffer solution (0.1 M 2-(N-morpholino)ethanesulfonic acid at pH=7.1) to yield a 10% volume concentration. The SAM slide of interest was placed in a Petri dish, to which four mL FBS solution was added, enough to completely immerse the SAM-coated slide. The Petri dish was placed in the incubator at 37°C for 80 min and removed. The SAM-coated slides were left to

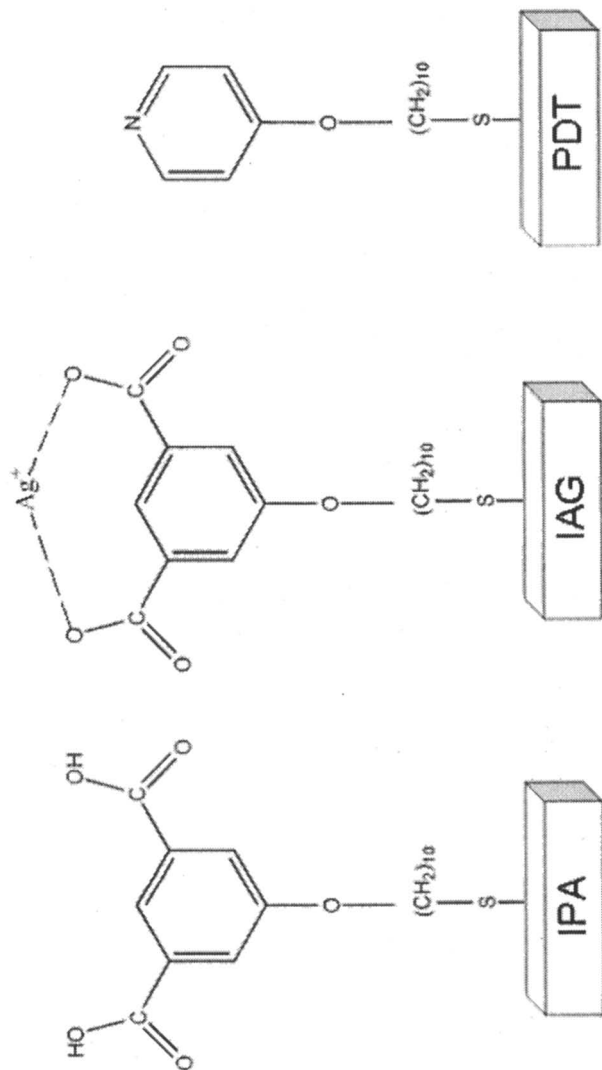


Figure 1. Schematic of the SAMs on gold slides. The SAMs are ten carbon chains with unique functional groups. IPA terminates with 5-(10-mercaptodecyloxy)isophthalic acid, IAG is IPA complexed with silver, and PDT terminates with 4-(16-bromo hexadecyloxy)pyridine. The location of the silver cation for IAG has not been confirmed, since either one or both of the single-bonded oxygens may be complexed with the silver cation.

air dry in the incubator, which is a common protocol for studying the topography of adsorbed proteins with AFM (21-23).

Contact angle experiments were conducted on protein-deposited slides, in the same manner as described above.

The topography of the substrates was characterized with AFM (Digital Instruments Dimension 3100 with Nanoscope IIIa controller; Veeco Metrology Corp., Valencia, CA) in air at room temperature and ambient humidity. Prior to tip engagement, an optical microscope (resolution ~1800x) mounted with the AFM and connected to the computer monitor was used to locate the region of interest and adjust the distance between the AFM tip and the protein-coated SAMs. The images were acquired using triangular cantilevers (DNPS, Digital Instruments, Valencia, CA, USA) with conical silicon nitride tips, having a nominal spring constant of 0.06 N m^{-1} and a typical probe radius of curvature of $40 \pm 20 \text{ nm}$, according to the manufacturer's specifications. With this type of tip, preliminary images appeared very similar, regardless of whether contact or tapping mode AFM was employed. Contact mode was then chosen for further experiments due to its high resolution and ease of operation, with deflection and height images collected for each sample. The scan rate was 1.0 Hz and the images were recorded at 512×512 pixel resolution. The only processing performed on the images was application of a second order filter to flatten height images, such that background slope and non-linear scanner effects were removed before performing section and roughness analyses of each measured region.

The "section analysis" operation within the AFM software (Nanoscope version 5.12r5) was used to acquire vertical height information for each image. The root-mean-square roughness (R_{rms}) was obtained with the same software, from measured areas of sizes ranging from $(50 \times 50) \text{ nm}^2$ to $(200 \times 200) \text{ nm}^2$, taking into account the features of interest of the samples. Although the surface roughness values obtained are highly dependent on the type of measurement technique that is used (24), relative comparisons can be made for measurements using the same technique at the same scale.

Bacterial Culture and Retention Experiments (Batch Assays)

Culture Preparation

Staphylococcus epidermidis, a clinical isolate, was kindly provided by Dr. Stephen Heard (Department of Anesthesiology, University of Massachusetts Medical School, Worcester, MA, USA). Bacteria were long-term stored at -80°C in glycerol solution (65% glycerol, 0.1 M MgSO_4 , and 0.025 M Tris-Cl, pH=8). From the frozen stock, a sample was inoculated on Tryptic Soy Agar (30 g/L; Sigma, St. Louis, MO; TSA) plates for short-term storage in the refrigerator

at 2-8°C. Single bacteria colonies were precultured in 20 mL of Tryptic Soy Broth (30 g/L, Sigma, St. Louis, MO; TSB) in the incubator at 37°C overnight. One mL of the precultured bacteria solution was added to 30-50 mL of TSB at 37°C in a water shaker bath. After 2-3 h, mid-exponential growth phase bacteria were harvested, corresponding to an absorbance of ~0.5 at 600 nm (ThermoSpectronic Spectrophotometer, Waltham, MA). Cells were harvested by centrifuging at 1400 g for 15 min (Fisher Scientific, Model 225, Pittsburgh, PA). The supernatant was removed and replaced with MES buffer solution. Cells were resuspended by manually vortexing the centrifuge tube for 1 min.

The concentration of bacteria in solution was determined by counting cells under a light microscope, using phase contrast. A counting chamber was employed to facilitate this calculation (Spermometer Sperm Counting Chamber Zander Medical Supplies, INC., Vero Beach, FL; Nikon 400 E microscope; Nikon, Tokyo, Japan), at a magnification of 600X.

Bacterial Retention Experiments

We evaluated the deposition of bacteria to bare gold, SAM-coated slides, and SAM-coated slides with deposited FBS. Using gold as the control substrate, we optimized the conditions of the batch assays by testing the time of incubation of the substrate with the bacterial solution (0.5, 1, and 24 h), and the bacterial solution concentration (2×10^7 cells/mL and 2×10^9 cells/mL). Each SAM-slide or SAM+FBS-slide was placed in a Petri dish, to which 4 mL of bacterial solution was added (bacterial concentration = 2×10^7 cells/mL). Following the incubation period (30 min at 37°C), the liquid was removed and 4 mL 0.1 M MES buffer solution was pipetted onto the slide to remove loosely attached bacteria and prevent cells from dehydrating.

Quantifying Bacterial Retention and Viability.

A BacLight™ live/dead kit (Molecular Probes, Faraday, CA) was employed to determine whether exposure to the SAMs affected bacterial viability. The kit contains 2 nucleic acid staining chemicals: 20 mM propidium iodide (PI) (Excitation/Emission: 490/635 nm) and 3.34 mM Syto 9 (Ex/Em: 480/500 nm). Syto 9 is a small molecule that can be taken up by all bacteria. These cells appear green under a FITC filter (Ex/Em: 465-495/515-555 nm). Cells with compromised membranes are stained by PI and appear red under the Texas red filter (Ex/Em: 540-580/600-660 nm). The manufacturer suggests 3 μ L of each dye per mL of bacterial suspension yielding a solution of 0.01 mM Syto 9 and 0.06 mM PI. However, these concentrations were found to be too high for our

Gram-positive bacteria. Through experimentation, we determined that a further 10 and 100 fold dilution, respectively, were sufficient to accurately represent cell viability.

Syto 9 and PI, diluted in dimethyl sulfoxide (DMSO) (Sigma, St. Louis, MO, USA), were added to the 4 mL bacterial solution to yield a final concentration of 0.835 μM and 0.5 μM , respectively. After 5 min, the cells were examined with fluorescence microscopy (Nikon Eclipse 400 fluorescence microscope, Tokyo, Japan with a mounted 18.2 Color Mosaic Camera; Diagnostic Instruments, Inc., Sterling Heights, MI), using a 100X oil immersion lens. Fifteen locations were randomly captured per slide and the Spot Advanced software (Diagnostic Instruments, Inc., Sterling Heights, MI) was used to facilitate the analysis of the live/dead cells. At least 4 slides were analyzed for each substrate.

Verification of Cell Viability through Plate Counting

Since the live/dead kit was initially designed to test viability of bacteria in a solution, we needed to validate that the technique could produce accurate results for bacteria retained on a surface. This was done through verification with a more traditional method of testing bacterial viability, namely that of counting colonies on agar plates.

Bacteria on the glass slides were removed from the top of the slides by sonication of the slide with 0.1 M MES buffer for 10 min (40 KHz, 130 W; Branson, Model 2510, Danbury, CT). Preliminary experiments determined that this sonication time and strength did not affect bacterial viability. A 10 μL solution from the flask was inoculated onto a TSA plate and cultured in an incubator at 37°C overnight, after which colonies were counted. Prior to this step, we eliminated bacteria adhered on the bottom and four lateral sides of the slide by scraping those surfaces with a sterile cotton swab. Control experiments verified that the bottom of the slide treated in this way produced no colonies when incubated on an agar plate.

Results

Ellipsometry

We measured the thickness of the IPA and IAG films, which helped to confirm that silver was complexed with the isophthalic acid for the IAG case.

The thicknesses were 1.1 ± 0.2 nm and 1.4 ± 0.1 nm thick for IPA and IAG, respectively. The thickness of PDT was not measured.

Hydrophobicity of the Substrates

When the contact angle of water on gold was measured immediately after cleaning (within 1 min), a water contact angle of $36 \pm 0^\circ$ was obtained. In practice, it is very difficult to maintain this level of hydrophilicity for the gold since small organic and inorganic particles suspended in the air almost immediately adsorb to the surface (25). For experimental gold surfaces in which the contact angle was measured after exposure to air for a few min, the contact angles were consistently much higher ($89 \pm 2^\circ$). After the SAMs were uniformly immobilized on the gold slide, the surfaces became more hydrophilic with contact angles of 72° and 75° , for IPA and IAG, respectively.

Optimal Conditions of Protein Deposition on SAMs Slides

To develop an optimal protein coating, different immersion times for the substrates were evaluated, from 80 min to 12 h, with 10% FBS. After performing the roughness analysis and section analysis with the AFM software, no significant differences among the roughness and heights were found ($P > 0.10$). An 80 min immersion was then chosen for the following experiments.

The morphology of the proteins adsorbed on gold was characterized as a function of concentration (Figure 2A-2D). Gold slides immersed for 80 min in concentrations of 10%, 50%, and 100% FBS were dried and imaged by AFM in air. Only 10% FBS yielded a uniformly ordered structure, while the other structures were irregular. This concentration has also been commonly used in other experiments with cells (26-30) and therefore, 10% FBS was chosen for all protein deposition experiments.

Hydrophobicity on Protein Deposited Substrates

After the deposition of FBS, the surface became more hydrophilic. Gold incubated in 10% FBS/90% MES solution yielded a water contact angle of 75° , while 50% FBS/50% MES solution yielded a water contact angle of 51° . Unexpectedly, when the proteins were deposited on the hydrophobic SAMs slides, the water contact angle decreased from 51° on the gold substrate to 23° and 29° on IPA and IAG substrates, respectively. This could be due to the arrangement of the proteins on the surfaces, since proteins may have both hydrophobic and hydrophilic domains.

Optimal Conditions of Bacterial Contact with SAMs Slides

Gold slides were exposed to MES + bacteria solutions at varying contact times and cell concentrations to determine optimal conditions for bacteria coating and counting. Contact times included 0.5 h, 1 h, and 24 h. For each contact time, cell concentrations of 2×10^7 cells/mL and 2×10^9 cells/mL were investigated. Using the undiluted cell concentration of 2×10^9 cells/mL, no significant difference in the number of retained cells was observed among the times tested using an ANOVA test ($P > 0.1$). The retained cells on the gold slides were consistently >300 cells/image, or $30,000$ cells/mm², which could not be accurately counted. For the diluted initial cell concentration of 2×10^7 cells/mL, there were ~ 30 cells/image or 3000 cells/mm² for the gold slides.

For the diluted initial cell concentration of 2×10^7 cells/mL, there were ~ 30 cells/image or 3000 cells/mm² for the gold slides incubated for 0.5, 1, or 24 h. Direct cell counts on acid cleaned glass slides indicated that incubating for the longer time period produced considerable losses in bacterial viability, with approximately 80% of bacteria being non-viable after 24 hr, compared to 10% non-viable after 0.5 hr. The optimization experiments showed that 0.5 h of incubation with bacterial solutions containing 2×10^7 cells/mL would be used for all other experiments, since these conditions allowed for best reproduction of experiments with minimal artifacts.

Optimizing Use of Live/Dead Staining Kit

The manufacturer suggests 3 μ L of each dye from the live/dead kit per mL of bacterial suspension to stain for 15 min. Experiments conducted at the original manufacturer's concentrations resulted in all of the *S. epidermidis* cells fluorescing red under the Texas Red filter. The manufacturer recommended a 100-fold dilution for Gram-positive bacteria (31). Modifications to the dye concentrations were made such that the final concentrations in bacteria solution were 0.835 μ M Syto 9 and 0.5 μ M PI. Cells no longer emitted the faint red glow that could have caused false-positives when summing dead cells. The staining time was varied for 5, 15, and 60 min, to further optimize the protocol and minimize stresses on the cells. There were no observed differences between these staining durations. The minimum duration of 5 min was sufficient for the experiments and hence was chosen. Also, 5 min helped the bacteria retain viability for the following plate counting experiments.

Verification of Live/Dead Viability Counting

When using a bacterial cell concentration below $\sim 1 \times 10^7$ cells/mL, there were significant deviations between the number of cells calculated based on the

live/dead counting and the plate counting. The cells on the SAMs slides were not evenly distributed. Usually 15 random locations for each slide were counted, corresponding to a total area of $0.0105 \times 15 = 0.158 \text{ mm}^2 = 0.00158 \text{ cm}^2$. Compared to the total surface area, approximately 2 cm^2 , only 0.079% of the slide's area was counted. The total numbers of bacteria on the slides were counted for 15 randomly chosen locations by the live/dead method by assuming a uniform attachment of bacteria.

When using a higher cell concentration ($>1 \times 10^7$ cells/mL), the slides were much more evenly covered by bacteria. The enumerations of bacteria given by the two methods were similar (Figure 3). The plate counting method always yielded a smaller number of cells than the live/dead staining assay, around $91.5 \pm 4.3 \%$. The percentage of apparently living cells that could not be detected by the plate counting method (8.5%) is close to the percentage of viable but non-culturable cells obtained by other experiments done in our lab (data not shown).

Comparison of Bacterial Retention on Varying SAMs Slides

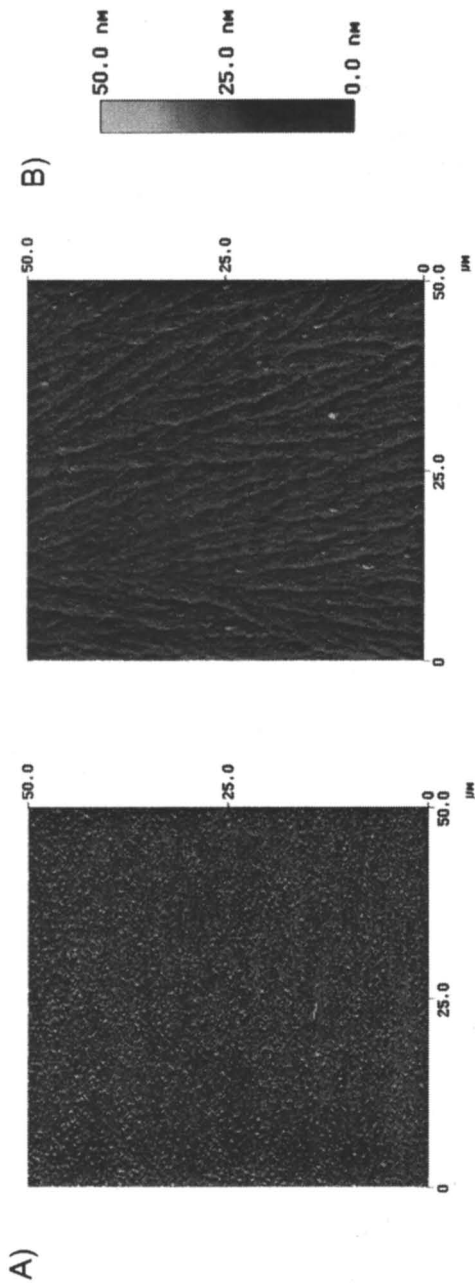
All the SAMs resulted in decreased bacterial retention compared to bare gold. IPA and IAG were most effective at reducing retention, with values decreased by 54-69% compared to gold. Based on an ANOVA test, there was a statistically significant difference between cellular retention on the gold and IPA, IAG ($P < 0.05$). Gold had a standard deviation of 6 cells, while PDT had a standard deviation of 4 cells. IPA and IAG had very high deviations, with 8 cells each, relative to the average number of cells retained (Figure 4A).

Viability of Retained Bacteria to SAMs

Most of the substrates caused a loss of bacterial viability (Figure 4B). The percentage of dead cells for gold and PDT were statistically similar ($P > 0.10$). For these two substrates, on average 83-93% of the cells were non-viable, based on the staining protocol. For IPA and IAG, fewer were dead, with 36% and 64%, respectively. Standard deviations of the percent of cells dead were large, especially for IPA ($\pm 16\%$) and IAG ($\pm 28\%$). There was no significant correlation between the total cell count and the viability of the cells.

Optimizing Bacterial Retention Assays with Proteins

For bacterial retention assays, the AFM revealed that the rinsing procedure removed many of the bacteria by sweeping away the underlying protein on gold (Figure 5A), but had minimal impact on the viability (Figure 5B). The substrate



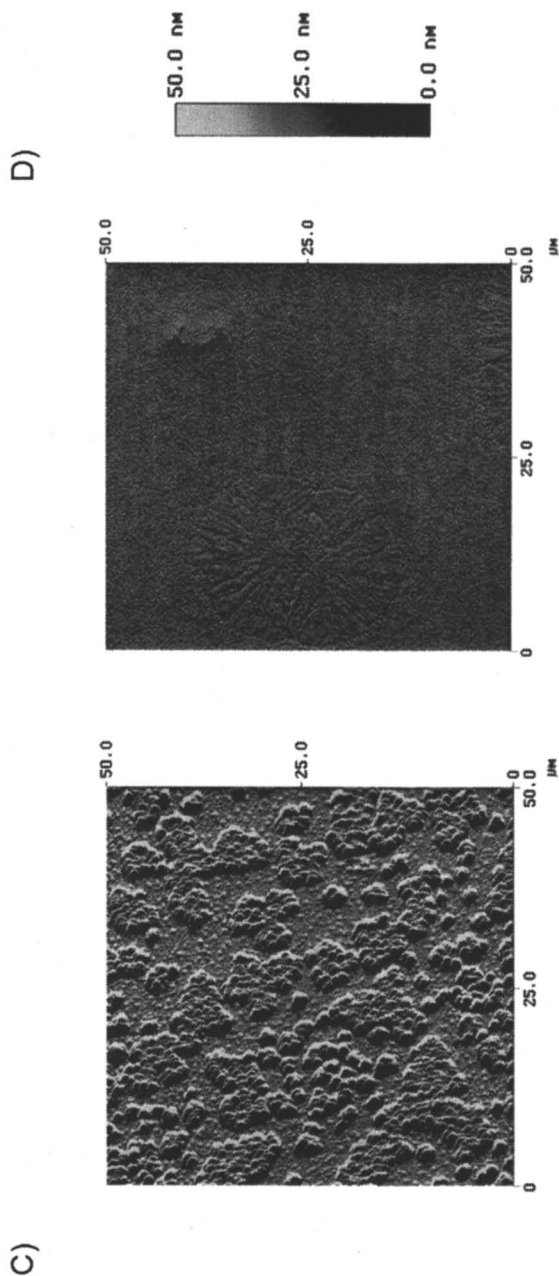


Figure 2. AFM images demonstrating the topography of structures formed when protein was deposited on the gold slides. Images captured in air using intermittent contact mode at a scan rate of 1.0 Hz. A) Bare gold substrate. B) Gold substrate incubated in 10% FBS solution for 80 min. C) Gold substrate incubated in 50% FBS solution for 80 min. D) Gold substrate incubated in 100% FBS solution for 80 min (Bar shows Z scale)

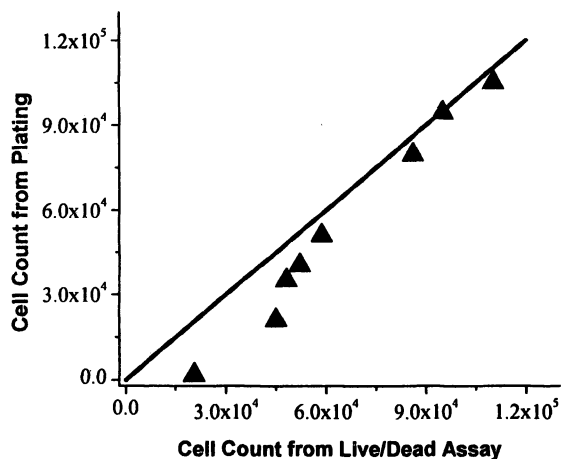
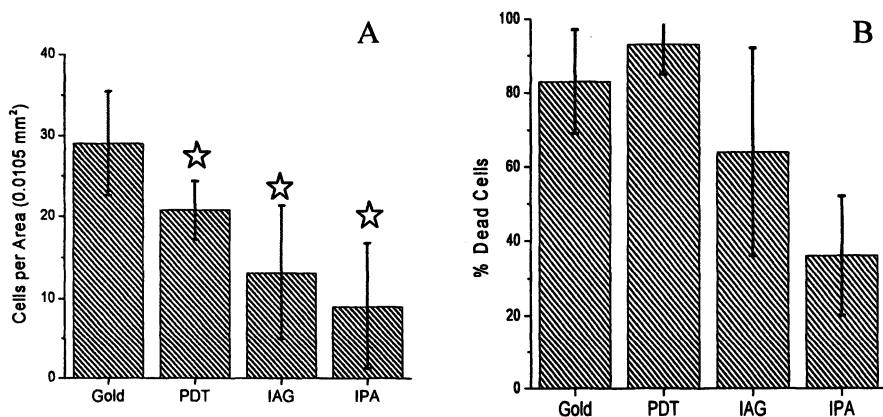


Figure 3. Comparison of cell counts obtained from live/dead staining with numbers obtained from plate counting. The solid line represents $y=x$. The plate counting method under-predicted the cell count from the live/dead assay at lower cell counts, but accurately fit the expected trend for higher cell counts.



*Figure 4. Bacterial retention and viability experiments on SAMs without FBS following 30 min incubation period. Stars represent statistically different results compared to that of bare gold. A) Cells per area on slides without deposited proteins. B) Cellular viability based on dual stain technique. Gold and PDT were equally effective against cellular viability ($P>0.10$). IAG was more effective in decreasing the viability of *S. epidermidis* than for the analogous molecule without silver (IPA) ($P<0.05$).*

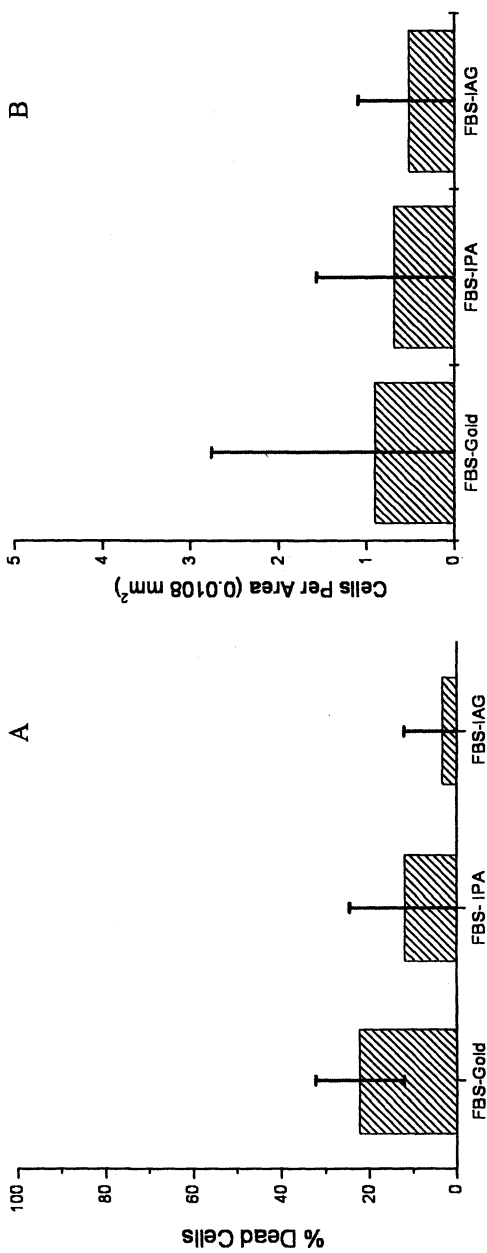


Figure 5. A) Bacterial viability and B) bacterial retention on SAMs with deposited proteins. The substrates gold, IPA, and IAG with deposited FBS and incubated in bacterial solution.

height was reduced from 386.65 ± 111.5 to 113.95 ± 43.48 nm following rinsing. In addition, the surface roughness was reduced by rinsing, from 11.15 ± 3.40 to 2.19 ± 0.63 nm. When the protein coated slide was immersed in bacterial solution, the *S. epidermidis* attached to the loose protein. Rinsing removed both the protein and bacteria that were not firmly attached to the gold substrate.

Discussion

Bacterial Viability and Retention in Batch Assays

Batch experiments have been used in a variety of settings to test both viability and retention of bacteria on protein-coated glass (32), sterile steel (33), and SAMs such as silver-coated (polyethylene terephthalate) (34). There have been concerns regarding the reproducibility of conducting batch assays and avoiding influencing viability of the bacteria via experimental procedures. Cellular physicochemical and morphological changes have been observed for *E. coli* and *S. epidermidis* depending on the preparation procedure such as type of buffer, centrifugation speed, and washing protocol (35). In addition, maintaining the cells at the optimal temperature through the duration of the experiment is important to avoid shocking the cells (36). Cell viability is also governed by the state at which cells are harvested and accessibility of critical nutrients (35).

Gómez-Suárez *et al.* (37) reported that irregular retention results can occur depending on the passage of bacteria (*Streptococcus sobrinus* HG1025, *Streptococcus oralis* J22, *Actinomyces naeslundii* T14V-J1, *Bacteroides fragilis* 793E, and *Pseudomonas aeruginosa* 974K) through an air-liquid interface. In addition, the shear force applied by the rinsing method should also be quantified for consistency (37). The reported deviations were not attributed to “errors”, but caused by the spread in data due to natural heterogeneity and the complexity of the bacterial retention process.

In our study, varying the washing process did not change the retention of the bacteria, probably because of the highly “sticky” exopolysaccharide of *S. epidermidis* (38). Bacteria that had attached to the substrates remained even after rinsing. There was, however, a significant effect of washing protocol on cellular retention when the substrate was coated with FBS. These results suggest that the interaction of FBS with the substrates is weaker than the interaction between *S. epidermidis* and the substrates.

Influence of SAMs on Bacterial Retention and Viability

The SAMs inhibited bacterial retention compared to bare gold. A prior investigation measured adhesion forces between *S. epidermidis* bacteria immobilized to an AFM tip, and the same SAMs. The adhesion forces between the bacteria and IPA and IAG were extremely low, suggesting very little interaction between these coatings and the bacterium (18).

When cellular viability was considered, bare gold and PDT were most effective at deactivating the bacteria. The results between the two were statistically similar ($P < 0.05$). For IPA and IAG, a lower percentage of retained cells were dead. The silver ions likely had some negative effect against the bacteria, although it did not completely kill all cells, similar to results that others have reported (5).

Effect of Proteins on SAM-Bacterial Interaction

There was a significant reduction of cellular retention once FBS was introduced on the substrates. In all cases investigated, cellular retention was reduced by at least 75% below levels found with the bare substrates. Kristinsson (39) found that whole human serum reduced the retention of *S. epidermidis* on polyurethane and silicone catheters, consistent with our results. Furthermore, Curtin *et al.* (40) reported that *S. epidermidis* viability was enhanced on catheter surfaces coated with 3% human serum. For our study, when gold was coated with FBS, bacterial retention was reduced by ~95% over bare gold. For IAG and IPA with deposited FBS, the numbers of adhering bacteria on the slides were reduced to nearly zero. Although the chemical effects of the underlying substrates were masked by the deposited FBS, the washing procedure became critical to interpreting the results of the protein-SAMs experiments. Viability tests on FBS-covered IPA and IAG showed that the SAMs were inactive against the bacteria due to proteins blocking the functional groups of the SAMs.

Staining techniques

The BacLight Live/Dead staining kit includes two components having different penetration ability to stain either the nucleic acid in all cells (Syto 9) or only the nucleic acid inside damaged cell membranes. It has been widely used for enumeration of bacteria and for differentiation between live and dead cells (41, 42). Cells with a damaged membrane are considered “dead” since they cannot sustain proper electrochemical gradients with the environment. With traditional plate counting (CFU), cells that are not culturable are considered dead. However, viable but non-culturable (VBNC or VNC) cells cannot

reproduce, possibly due to some transitional stages during the process of constantly adapting themselves to their environment (43). Deviations of the cell counts for different locations on the same plate may be caused by the conjugation of bacteria both in the inoculation solution and in colonies on the TSA plate. In addition, the overlapping of colonies and the existence of viable but nonculturable bacteria also can yield significant counting errors (44).

Although these artifacts can be moderated to some extent by using higher concentrations of cells to balance the relative difference or by applying sonication to get better mixing, the standard plate counting assay always underestimates the number of living cells. By calculating the real doubling time from the absorbance measurements and comparing to the projected value from the theoretical exponential growth formula, the monitored bacterial growth rate in the mid-exponential phase is $88.7\% \pm 6.7\%$ of the theoretical projection (unpublished data from our lab). The ratio of the plate counting number over the live/dead counting was very close at 91.5 %, which indicates ~9% of the cells were alive but non-culturable in the total population.

The dual stain kit segregates between live/dead cells by taking advantage of cellular membrane status. Syto 9 combines with the nucleic acid of all the cells, but for the dead cells, PI must replace the Syto 9 to be able to fluoresce red. Cells stained by both dyes appear a lighter green under the FITC filter, as reported in prior studies (41). PI has a stronger affinity for nucleic acid, but the ratio of the two stains is also important to facilitate the replacement of Syto 9 by PI since the concentration should vary according to whether Gram-negative or Gram-positive bacteria are being studied (31). An overdose of PI can induce a faint red signal, which occurred when using the manufacture's recommended concentration. A possible discrepancy between the dye concentration we required and the amount recommended was that our experiments evaluated cells on a surface, whereas the manufacturer made the recommendations for evaluating cells in solution. In addition, Gram-positive bacteria require less dye. A further consideration if this work is to be extended to characterization of cellular viability on biomaterials is that polymer surfaces as substrates may require the further optimization of the dye concentrations and ratios since many polymers may exhibit background fluorescence that can interfere with the assay. For the current system, careful validation experiments showed that the dual stain technique is efficient and accurate for quantifying the number of live bacterial cells retained on a substrate.

Summary

Fundamental studies of the initial adhesion of bacteria to a substrate are important for numerous biomedical applications. *In vitro* experiments help

isolate and focus on key parameters, hence they are widely used. Nevertheless, these experiments must be carefully controlled and optimized in order to produce meaningful results.

SAMs have unique molecular structures that provide potential scaffolds for implanted medical devices. A fairly homogeneous substrate can be created for testing bacterial retention, and the effects of different chemistries can be studied by simply modifying the terminal functional group.

We successfully optimized and verified the experimental conditions needed to achieve uniform serum protein coating, and to evaluate bacterial retention and viability. To form well coated surfaces, 10% serum protein is required to contact the substrata for 80 min. The time threshold for *S. epidermidis* to firmly grasp to the substrate was found to be approximately 30 min. The optimized staining concentrations were found to be 0.835 μM for Syto 9 and 0.5 μM for PI. The dual staining technique was verified through traditional plate counting.

Using these methods, IPA and IAG each could prevent *S. epidermidis* retention and instigate losses in bacterial viability. However, when serum proteins covered the material surface, the underlying chemistry of the substrate could not exert an influence on bacterial retention and viability. Follow-up experiments are being conducted with another model protein, fibronectin, which researchers think acts as a binding receptor for *S. epidermidis* (45). Fibronectin also has been identified as a vital component for cellular adhesion (46) and wound healing (47), which would be important to study in conjunction with SAM functionality. In addition, we are collecting AFM force data that will be related to the retention experiments in our future work. We will then be able to evaluate the potential longevity of the SAMs *in vivo* and further evaluate the effectiveness of IPA and IAG against *S. epidermidis*.

Acknowledgements

We would like to thank Dr. Stephen Heard, Dr. Cuong Vuong, Dr. Ray Emerson, and Ms. Xiaoshu Dai for helpful discussions and assistance with this work. This work was supported in part by a grant from the National Science Foundation (BES 0238627).

References

1. Higuera, F.; V.D. Rosenthal; P. Duarte; J. Ruiz; G. Franco, and N. Safdar. *Crit. Care Med.* **2005**, *33*, 2022.
2. Blot, S.I.; P. Depuydt; L. Annemans; D. Benoit; E. Hoste; J.J. de Waele; J. Decruyenaere; D. Vogelaers; F. Colardyn, and K.H. Vandewoude. *Clin. Infect. Dis.* **2005**, *41*, 1591.

3. Raad, I. *Lancet* **1998**, *351*, 893.
4. Gristina, A. and H.H. Sherk. *Clin. Orthop. Rel. Res.* **2004**, *4*.
5. Chaw, K.C.; M. Manimaran, and F.E.H. Tay. *Antimicrob. Agents Chemother.* **2005**, *49*, 4853.
6. Garrett, D.O.; E. Jochimsen; K. Murfitt; B. Hill; S. McAllister; P. Nelson; R.V. Spera; R.K. Sall; F.C. Tenover; J. Johnston; B. Zimmer, and W.R. Jarvis. *Infect. Cont. Hosp. Ep.* **1999**, *20*, 167.
7. Evans, C.R. and C.J. Holmes. *Antimicrob. Agents Ch.* **1987**, *31*, 889.
8. Moller, T.; N. Borregaard; M. Tvede, and L. Adamsen. *J. Hosp. Infect.* **2005**, *61*, 330.
9. Ista, L.K.; H.Y. Fan; O. Baca, and G.P. Lopez. *FEMS Microbiol. Lett.* **1996**, *142*, 59.
10. Francois, P.; J. Schrenzel; C. Stoerman-Chopard; H. Favre; M. Herrmann; T.J. Foster; D.P. Lew, and P. Vaudaux. *J. Lab. Clin. Med.* **2000**, *135*, 32.
11. Que, Y.A.; J.A. Haefliger; L. Piroth; P. Francois; E. Widmer; J.M. Entenza; B. Sinha; M. Herrmann; P. Francioli; P. Vaudaux, and P. Moreillon. *J. Exp. Med.* **2005**, *201*, 1627.
12. Herrmann, M.; P.E. Vaudaux; D. Pittet; A. R.; P.D. Lew; F. Schumacher-Perdreau; G. Peters, and F.A. Waldvogel. *J. Infect. Dis.* **1988**, *158*, 693.
13. Delmi, M.; P. Vaudaux; D.P. Lew, and H. Vasey. *J. Orthop. Res.* **1994**, *12*, 432.
14. Qian, X.P.; S.J. Metallo; I.S. Choi; H.K. Wu; M.N. Liang, and G.M. Whitesides. *Anal. Chem.* **2002**, *74*, 1805.
15. Reid, G.; S. Sharma; K. Advikolanu; C. Tieszer; R.A. Martin, and A.W. Bruce. *Antimicrob. Agents Chemother.* **1994**, *38*, 1490.
16. Polonio, R.E.; L.A. Mermel; G.E. Paquette, and J.F. Sperry. *Antimicrob. Agents Chemother.* **2001**, *45*, 3262.
17. Soto, E.; J.C. MacDonald; C.G.F. Cooper, and W.G. McGimpsey. *J. Am. Chem. Soc.* **2003**, *125*, 2838.
18. Emerson, R.J.; T.S. Bergstrom; Y. Liu; E.R. Soto; C.A. Brown; W.G. McGimpsey, and T.A. Camesano. *Langmuir* **2006**, *22*, 11311.
19. Hu, J. and M.A. Fox. *J. Org. Chem.* **1999**, *64*, 4959.
20. Busscher, H.J.; A.H. Weerkamp; H.C. Van der Mei; A.W.J. Van Pelt; H.P. De Jong, and J. Arends. *Appl. Environ. Microbiol.* **1984**, *45*, 980.
21. Grunwald, C.; W. Eck; N. Opitz; J. Kuhlmann, and C. Wolf. *PCCP* **2004**, *6*, 4358.
22. Ohta, R.; N. Saito; T. Ishizaki, and O. Takai. *Surf. Sci.* **2006**, *600*, 1674.
23. Thomson, N.H. *Ultramicroscopy* **2005**, *105*, 103.
24. Henke, L.N., N. and U.J. Krull. *Biosens. Bioelectron.* **2002**, *17*, 547.
25. Wanner, M. and D. Gerthsen. *Colloid. Polym. Sci.* **2004**, *282*, 1126.
26. Li, Y.; R.H. Lu; G.F. Luo; W.J. Pang, and G.S. Yang. *Cryobiology* **2006**, *53*, 240.

27. Lee, H.S.; X.J. Yin, and I.K. Kong. *Theriogenology* **2006**, *66*, 1468.
28. Kawarai, S.; K. Hashizaki; S. Kitao; S. Nagano; H. Madarame; S. Neo; T. Ishikawa; M. Furuichi; M. Hisasue; R. Tsuchiya; H. Tsujimoto, and T. Yamada. *Vet. Immun. Immunopath.* **2006**, *113*, 30.
29. Okano, S.; D.J. Hurley; M.S. Bergh; M.L. Vandenplas; S.C. Budsberg, and J.N. Moore. *Vet. Immun. Immunopath.* **2006**, *112*, 234.
30. Campoccia, D.; L. Montanaro; H. Agheli; D.S. Sutherland; V. Pirini; M.E. Donati, and C.R. Arciola. *Int. J. Artif. Organs* **2006**, *29*, 622.
31. *Personal Communication, ASM 106th General Meeting.* May 22, 2006: Invitrogen, Inc.
32. Jarvis, R.A. and J.D. Bryers. *J. Biomed. Mater. Res. Part A* **2005**, *75A*, 41.
33. Bagge, D.; M. Hjelm; C. Johansen; I. Huber, and L. Grami. *Appl. Microbiol. Biotechnol.* **2001**, *67*, 2319.
34. Klueh, U.; V. Wagner; S. Kelly; A. Johnson, and J.D. Bryers. *J. Biomed. Mater. Res.* **2000**, *53*, 621.
35. Pembrey, R.S.; K.C. Marshall, and R.P. Schneider. *Appl. Environ. Microbiol.* **1999**, *65*, 2877.
36. Wright, S.D. and R.P. Levine. *J. Immun.* **1981**, *3*, 1146.
37. Gomez-Suarez, C.; H.J. Busscher, and H.C. Van der Mei. *Appl. Environ. Microbiol.* **2001**, *67*, 2531.
38. Tojo, M.; N. Yamashita; D.A. Goldman, and G.B. Pier. *J. Infect. Dis.* **1988**, *157*, 713.
39. Kristinsson, K.G. *J. Med. Microbiol.* **1989**, *28*, 249.
40. Curtin, J.J. and R.M. Donlan. *Antimicrob. Agents Chemother.* **2006**, *50*, 1268.
41. Boulou, L.; M. Prevost; B. Barbeau; J. Coallier, and R. Desjardins. *J. Microbiol. Meth.* **1999**, *37*, 77.
42. Keer, J.T. and L. Birch. *J. Microbiol. Meth.* **2003**, *53*, 175.
43. Baena-Ruano, S.; C. Jimenez-Ot; I.M. Santos-Duenas; D. Cantero-Moreno; F. Barja, and I. Garcia-Garcia. *Process Biochem.* **2006**, *41*, 1160.
44. Pitt, W.G.; M.O. McBride; A.J. Barton, and R.D. Sagers. *Biomaterials* **1993**, *14*, 605.
45. Bustanji, Y.; C.R. Arciola; M. Conti; E. Mandello; L. Montanaro, and B. Samori. *P. Natl. Acad. Sci. USA* **2003**, *100*, 13292.
46. Mercurius, K. and A. Morla. *BMC Cell Biol.* **2001**, *2*, 18.
47. Grinnell, F.; R.E. Billingham, and L. Burgess. *J. Investig. Dermatol.* **1981**, *76*, 181.

Chapter 7

New Biological Activities of Plant Proanthocyanidins

**Brandy J. Johnson, James B. Delehanty, Baochuan Lin, and
Frances S. Ligler***

**Center for Bio/Molecular Science and Engineering, Naval Research
Laboratory, Washington, DC 20375**

Proanthocyanidins (PACs) from cranberries, tea, and grapes interact with bacterial cell surface components. The interaction of cranberry PACs with p-fimbriae proteins of *Escherichia coli* has been shown to interfere with bacterial cell adhesion to mammalian cells. Here we present data on the inhibition of bacterial cell adhesion to glass surfaces mediated by cranberry PACs. The reported anti-adhesive activity is unique to PACs obtained from *Vaccinium* species. We further demonstrate that PACs from various sources interact with bacterial lipopolysaccharides (LPS) and abrogate endocytosis of LPS. This LPS-PAC interaction can be used to remove LPS from solution providing a potential method for filtration or concentration.

Proanthocyanidins obtained notoriety due to research demonstrating the health promoting antioxidant activity of red wines (1-4). More recently, these compounds have been shown to provide protection against heart disease and atherosclerosis in addition to mediating nitric oxide release (5-9). PACs have been shown to inhibit the growth of certain types of cancerous cells while enhancing normal cell growth (10). The antioxidant activity of PACs has been shown to extend the life span of some vitamins while enhancing the activity of others (11-13). PACs from cranberries (*Vaccinium macrocarpon*) have been shown to inhibit the adhesion of bacterial cells responsible for urinary tract infection (14-16), ulcers in the stomach lining (17,18), and oral caries (19,20). The mechanisms of these biological activities are only beginning to be understood, but the health value of proanthocyanidins has been well established.

Grape seeds (*Vitis vinifera*) and white pine (*Pinus maritima*) are excellent sources of proanthocyanidins, but the compounds are also found in food items such as teas, coffees, chocolate, apples, berries, and barley, to name a few. PACs are found in heterogeneous mixtures consisting of various numbers of monomer subunits. Catechin and epicatechin are the most common of the subunits. Intersubunit linkages are usually via single intermolecular bonds between carbon atoms, but in some species subunits are linked by two intermolecular bonds: one carbon-carbon and one carbon-oxygen (Figure 1) (21,22). These are referred to as B-type and A-type proanthocyanidins, respectively. Differing biological activities have been shown for A-type and B-type proanthocyanidins as well as for proanthocyanidins of differing subunit composition and differing degrees of polymerization (10,15).

Non-specific Adhesion of *E. coli*

The Naval Research Laboratory Array Biosensor employs a protein-coated glass waveguide for the detection of analytes of interest (23-25). The surface of the waveguide has a patterned array of capture molecules with non-specific passivating molecules used to coat other regions of the surface (26-28). Fluorescence-based detection of targets is dependent on discrimination of capture molecule areas from other areas of the waveguide. Non-specific adhesion of targets to unexpected areas of the surface negatively impacts limits of detection as well as false positive/negative rates for the Array Biosensor.

The combination of a nonpathogenic *E. coli* strain (ATCC 35218) and a low affinity antibody (rabbit polyclonal antibody to *E. coli*; Abcam, Inc; Cambridge, MA) was found to produce a degree of nonspecific binding which made discrimination of signal from background intensities difficult (29). Bacterial cells adhere through interactions involving surface proteins and/or lipopolysaccharide (LPS). Traditional approaches to reduction of nonspecific binding (for example blocking waveguide surfaces or spiking samples with

proteins or sugars) were unsuccessful. Based on the impact of cranberry juice on bacterial cell adhesion in the urinary tract, the juice was investigated as a potential mediator of adhesion in the Array Biosensor. Figure 2 presents data on the ratio of background intensity to signal intensity for samples assayed with

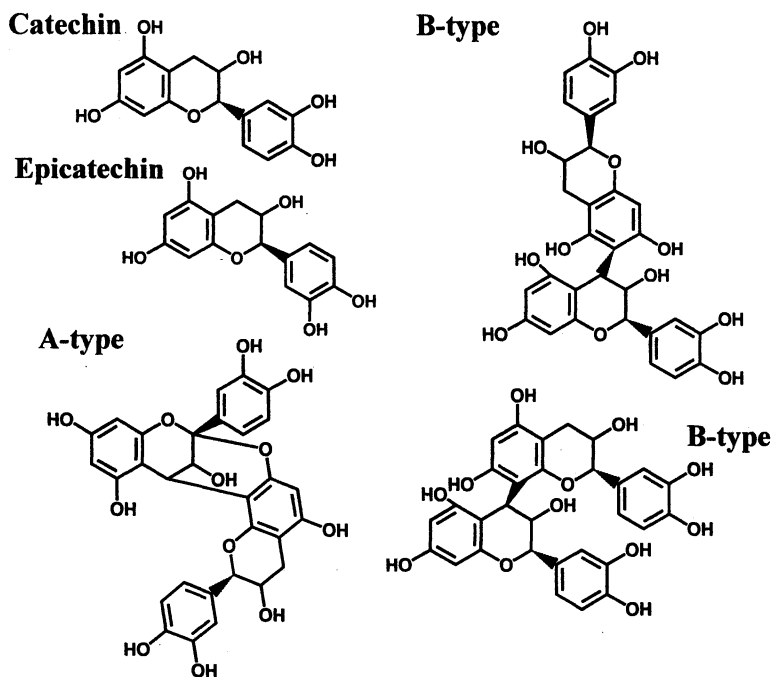


Figure 1. Proanthocyanidin structure. PACs are composed of subunits such as catechin and epicatechin. B-Type PACs contain a single intermolecular bond either between carbons 4 and 8 or between carbons 4 and 6 while A-type PACs contain two intermolecular bonds between carbons 4 and 8 and carbon 2 and the oxygen of carbon 7 (14).

varying concentrations of cranberry juice. Ocean Spray 100% Cranberry and Concord Grape juice blend containing 27% cranberry juice was used. In the absence of juice, background intensity was 67% of the total signal. Addition of 50% juice blend (equivalent to 13.5% cranberry juice) reduced the background intensity to less than 1% of the total signal (29). Spiking samples with grape juice was not found to produce this effect on the background signal (Welch's Purple 100% Grape Juice). Spiking of samples with apple juice, orange juice, and even white cranberry juice (Ocean Spray 100% Juice Blend) also did not

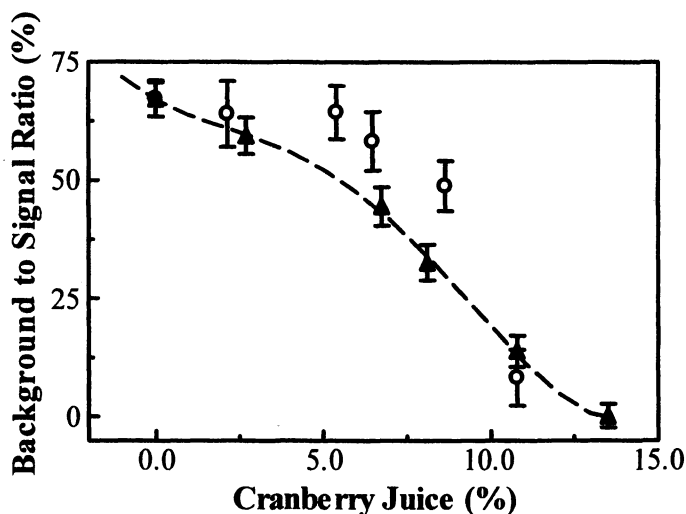


Figure 2. The impact of cranberry juice on non-specific adhesion. The background intensity is expressed as the ratio of the mean background intensity to the mean fluorescence signal intensity. Spiking of bacterial samples with cranberry juice (▲) and dialyzed filtered cranberry juice (○) produces similar improvement in background signals.

result in reduction of background signals. White cranberry juice is produced from cranberries harvested early before the red color and tart flavor are developed. The white cranberry juice blend used contains 13.5% cranberry juice. This difference in concentration was accounted for when samples were spiked so that concentrations similar to those used with the red cranberry juice were investigated.

Several mechanisms have been described for the inhibition of bacterial cell adhesion by cranberry juice (30-32). The acidity of the juice, the sugar content including the rare D-mannose component, and the presence of a rare polyphenolic component have been proposed as contributing factors. Controlling the pH of the juice spiked samples eliminated acidity as a causative factor. The sugar content of the juice was eliminated as a factor through spiking of *E. coli* samples with similar concentrations of fructose, glucose, and mannose. Waveguide surface passivation was also eliminated as a potential mechanism through studies of the impact of sample spiking on advancing contact angle. Though the contact angle was strongly impacted on clean glass slides when standard bacterial cell preparations were spiked, there was no noticeable impact on the protein coated slides used in the Array Biosensor.

The interaction of *E. coli* with human epithelial cells in the urinary tract is inhibited by A-type proanthocyanidins from cranberry juice through interference with the p-fimbriae proteins on the bacterial cell surface (16,33). In order to

investigate the potential impact of PACs on adhesion to the glass waveguides, sugars and other small molecules were eliminated from cranberry juice (Langer's Cranberry Concentrate) through dialysis against water (Spectra/Por Membrane MWCO 6-8000) (30). Colloidal particles were removed through filtration of the dialyzed material using a 0.2 μm filter (Acrodisc PF; Gelman Sciences, Ann Arbor, MI). The dialyzed material was reconcentrated under nitrogen to a 27% cranberry juice equivalent and used to spike samples for Array Biosensor assays. This dialyzed filtered cranberry juice produced results similar to those observed when samples were spiked with the cranberry juice blend.

Purification of Proanthocyanidins

The high molecular weight non-dialyzable component of cranberry juice contains proanthocyanidins. In order to study the interaction of this component of the juice with bacterial cells, proanthocyanidins were purified from Welch's purple 100% grape juice, Lipton black tea, Mountain Sun pure unsweetened cranberry juice, and from whole cranberries via hydrophobic adsorption chromatography using LH20 Sephadex (34,35). Extraction of tea was accomplished by sonication for 20 mins of one family sized tea bag in 200 mL 70% acetone for three cycles. The solutions were combined, vacuum filtered using Whatman #3 filter paper, reduced by turbo evaporation (40°C), and resuspended in 300 mL 75% ethanol. Extraction of whole cranberries was accomplished by blending followed by sonication for 1 hour in 200 mL 70% acetone. The solution was then filtered using Whatman #3 filter paper. The sonication and filtering steps were repeated on the solids for three additional cycles. All solutions were combined, reduced by turbo evaporation (40°C), and resuspended to 300 mL in 75% ethanol. Extraction of juices was accomplished by concentrating via turbo evaporation at 60° C followed by sonication in the starting volume of 70% acetone for 30 mins (36). The resulting solution was filtered using Whatman #3 filter paper and the remaining solids were resuspended and sonicated for two further cycles. All solutions were combined, reduced by turbo evaporation (40°C), and resuspended in twice the starting volume of 75% ethanol.

Extracts in 75% ethanol were applied to Sephadex LH20 (Amersham Biosciences, Piscataway, NJ) columns in batches equal to the bed volume. Elution by ethanol was used to remove small phenolics and other material (total volume used equivalent to five times the bed volume). PACs were eluted from the column using three bed volumes of 70% acetone. Acetone solutions were reduced to a minimum by turbo evaporation (40°C) followed by drying under nitrogen stream to powder. Purified proanthocyanidins from cranberries were separated into four fractions by dialysis against water containing 25% ethanol: those which pass through 2,000 MWCO tubing (Spectra/Por) (Fraction 4); those which pass through 3,500 MWCO tubing (Spectra/Por CE) but are retained by

the 2,000 MWCO (Fraction 3); those that pass through 6,000 MWCO tubing (Spectra/Por Membrane MWCO 6-8000) but are retained by the 3,500 MWCO tubing (Fraction 2); and those which are retained by the 6,000 MWCO tubing (Fraction 1). Radial diffusion assays were used to determine tannic acid equivalents (TAE) for the materials (35,37). The modified vanillin assay was used in conjunction with the acid butanol assay to determine average degrees of polymerization (Table I) (35,38). Catechin was employed as a standard for these assays.

Table I. Proanthocyanidin Specifications

<i>PAC Source</i>	<i>Tannic Acid Equiv. (μM) (1 mg/mL)</i>	<i>Average Degree of Polymerization</i>
Cranberries	63.4	12.6
Black Tea	49.8	4.1
Grape Juice	29.9	7.2
Cranberry Juice	39.0	8.9
Cranberries, Fraction 1	38.3	21.7

Lipopolysaccharide and Polymyxin B

Lipopolysaccharide (LPS) is a major component of the outer membrane of Gram-negative bacteria. LPS enhances structural integrity and protects the cell from certain types of chemical attack (39). LPS, also referred to as bacterial endotoxin, is responsible for the body's inflammatory response to infection. LPS hyper stimulation can result in over stimulation of the inflammatory cascade, a condition referred to as systemic inflammatory response syndrome or sepsis (40). Polymyxin B (PMB) is a cationic cyclic polypeptide used to treat Gram-negative bacterial infections. PMB binds to the lipid A portion of LPS in Gram-negative cell membranes. This interaction results in disruption of the cytoplasmic membrane and pore formation in the cell wall allowing leakage of nucleotides and inhibiting cellular respiration (41). The interaction also inactivates lipopolysaccharide (42).

Polymyxin B was used to investigate the impact of PAC presence on the PMB-LPS interaction. Polymyxin B immobilized onto agarose beads (Sigma-Aldrich, St. Louis, MO) can be used to capture LPS from solution with quantification accomplished through the use of a fluorescent antibody (43). Alternatively, interference with the capture of LPS by immobilized polymyxin B can be quantified through the use of a fluorescently labeled LPS analog. Polymyxin B beads (10 μM PMB) were mixed with FITC-labeled LPS (100 nM;

E. coli 055:B5; Sigma-Aldrich) in the absence or presence of purified PACs (total volume 250 μL in 50 mM TRIS pH 8.5). Samples were stirred for 1 hour at room temperature. Excess FITC-LPS was removed by three cycles of washing (250 μL 50 mM TRIS) and centrifugation (5 min at 9,000 rpm in bench top micro centrifuge). Following the final wash, samples were resuspended in 200 μL nuclease-free water. Serial dilutions were prepared in a 96-well plate and fluorescence of the bound LPS was determined using excitation at 495 nm and emission at 535 nm on a Safire™ fluorescence plate reader (Tecan, Durham, NC).

Addition of increasing concentrations of PACs from cranberry juice, tea, and grape juice to the LPS assay resulted in a corresponding decrease in bound fluorophore. Figure 3 presents this impact as percent inhibition versus PAC concentration. PACs from all three sources were found to have 50% inhibition constants (IC_{50}) of approximately 2.8 μM . Addition of the catechin monomer to LPS assays did not reproduce this effect. Quenching of FITC-LPS fluorescence by PACs occurred only at high PAC concentrations and did not contribute to the inhibition reported in Figure 3. The inhibition of the LPS assay by each of the PAC fractions produced using dialysis was investigated using the PMB pull-down assay described above. The larger PAC components (retained by 6,000 MWCO) were found to have the highest inhibitory activity on the assay as shown in Figure 4.

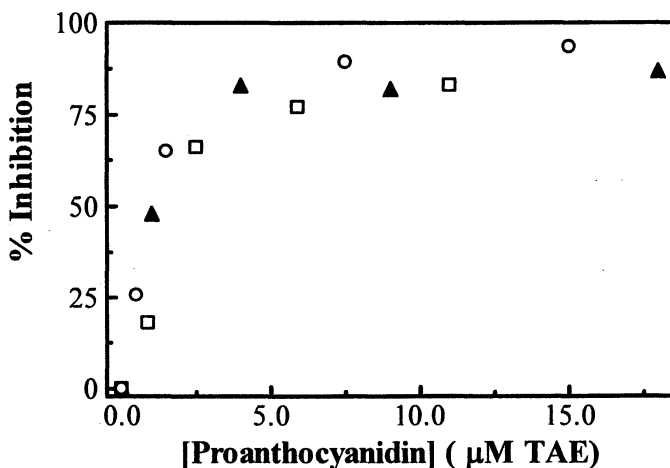


Figure 3. The polymyxin B pull-down assay. Binding of LPS by polymyxin B is inhibited by PACs from cranberry juice (○), grape juice (□), and black tea (▲).

Lipopolysaccharide and Mammalian Cells

Mammalian cells recognize LPS via the interplay of soluble and membrane-bound receptor proteins. The generally accepted scenario of LPS recognition is as follows: LPS released from Gram-negative bacterial cells is captured by soluble LPS-binding protein (LBP), a specific lipid transfer protein present in serum, which then delivers LPS to the membrane-bound receptor, CD14. CD14, in turn, presents the LPS to Toll-like receptor-4 (TLR4) (44,45). Functional recognition of LPS by TLR4 also requires the accessory protein, MD-2 (46). Binding of LPS to TLR4 activates inflammatory gene expression through NF- κ B-mediated intracellular signaling, resulting in a concerted immune response to neutralize the invading bacterial pathogen. Based on the ability of PACs to bind LPS, we investigated the potential for PAC-mediated inhibition of LPS interaction with the LPS receptor complex on mammalian cells.

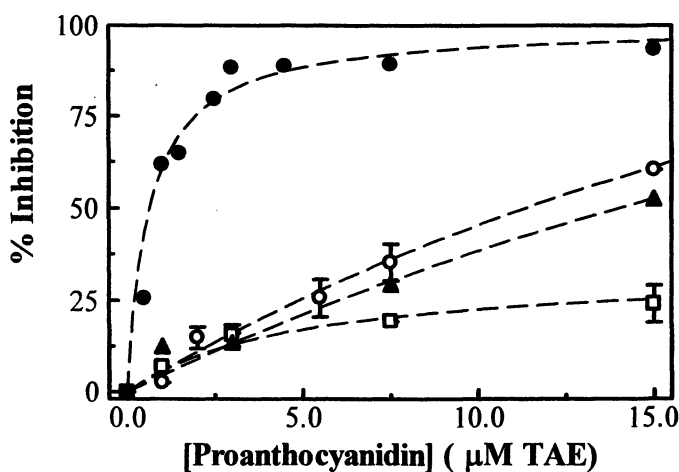


Figure 4. Comparison of PAC fractions. The LPS binding activity of the PACs from cranberry varies for differing degrees of polymerization. Fraction 1 (●) shows the highest activity, while other fractions containing lower molecular weight components show significantly less activity: fraction 4 (□), fraction 3 (○), and fraction 2 (▲).

Human embryonic kidney cells (HEK 293) stably expressing the LPS receptor complex comprised of TLR4, CD14, and MD-2 (Invivogen, Inc.) were exposed to LPS (25 nM) or to LPS plus various potential inhibitors for 1.5 hours. After the incubation period, the cells were washed and fixed (for

detection of membrane-bound LPS) or fixed and permeabilized (for detection of internalized LPS). Bound LPS was detected using a goat anti-*E. coli* LPS-FITC conjugate (Abcam, Inc., O and K serotype-specific, 30 $\mu\text{g}/\text{mL}$). Figure 5 (Panel A) shows the resulting fluorescence signals obtained for the detection of membrane-bound LPS (fixed cells) collected using an Olympus IX-71 microscope at 60x magnification. In the absence of any inhibitor, a distinct membranous staining pattern corresponding to LPS was observed (frame labeled "LPS") while the negative control displayed negligible nonspecific signal (frame labeled "No LPS"). The co-incubation of LPS with an anti-CD14 function-perturbing antibody (Abcam, Inc., 500 nM in binding sites, frame labeled "LPS+ α -CD14") completely inhibited LPS binding to the cell surface. However, when LPS was co-incubated with 5 μM (TAE) PAC from cranberry (fraction 1), an anti-TLR4 function-perturbing antibody, or a combination of the two, LPS binding was only partially blocked. Co-incubation of LPS with 1 μM lipid A appeared to have no significant impact on LPS binding. These results, therefore, suggest that PAC plays a role in abrogating the interaction of LPS with TLR4 but not with CD14. Examination of internalized LPS demonstrated that cranberry PAC also inhibits the endocytosis of LPS. In the absence of any inhibitor, a distinct vesicular staining pattern corresponding to endocytosed LPS was observed. This staining pattern was completely inhibited when LPS was co-incubated with either PAC, lipid A, the CD14 function-perturbing antibody or the combination of PAC with either of the two function-perturbing antibodies. Abrogation of TLR4 with the function-perturbing antibody did not completely inhibit endocytosis as some intracellular vesicular staining was apparent. Thus, these data suggest that while cranberry PAC partially inhibits binding of LPS to its cognate receptor complex, it nearly completely inhibits the endocytosis of LPS. Studies are currently ongoing in our laboratory to elucidate the exact nature of the molecular interaction of cranberry PAC with the LPS receptor complex.

Proanthocyanidins as Capture Molecules

The use of PACs as capture molecules was investigated in order to determine their potential for application in detection, purification, and concentration schemes. PACs were immobilized onto Sepharose beads (activated thiol-Sepharose 4B, Sigma-Aldrich) via a PMPI crosslinker (*N*-[*p*-Maleimido-phenyl]isocyanate; Pierce Biotech, Inc; Rockford, IL). The maleimide group of the PMPI reacts with the thiol group on the Sepharose while the isocyanate group reacts with the hydroxyl groups of the PACs. In order to accomplish PAC immobilization, Sepharose was swelled in deionized water for 1 hour (1 g dry material in 15 mL H_2O). The material was then washed using

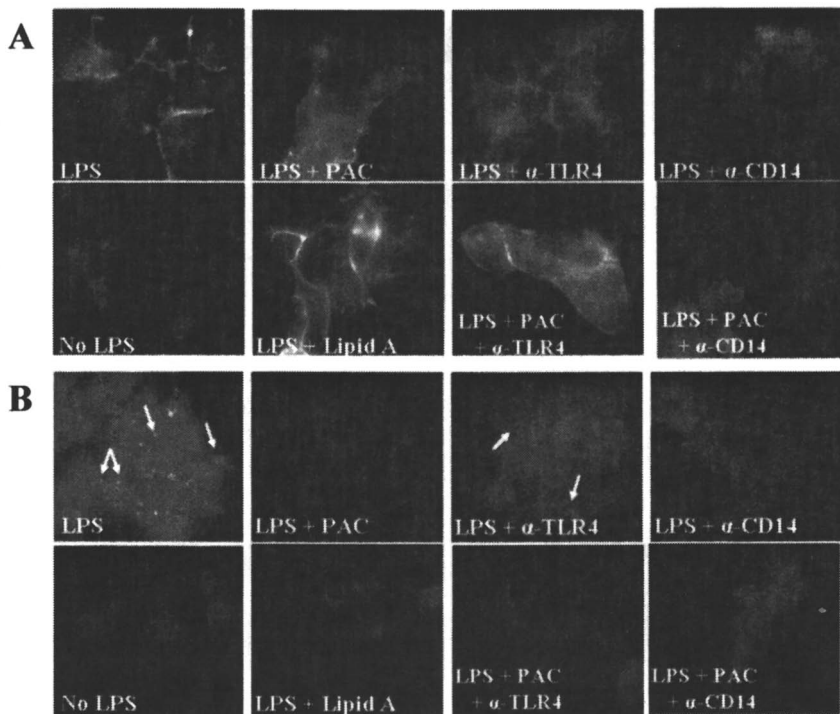


Figure 5. Interaction of cranberry PAC with the Toll-like receptor complex. Membrane association (Panel A) and endocytosis (Panel B) of *E. coli* O55:B5 LPS was examined in HEK 293 cells stably expressing the LPS receptor complex (TRL4, CD14, and MD-2). While PAC appears to only slightly inhibit membrane binding of LPS, it completely inhibits endocytosis of LPS.

fresh dI-H₂O over five suspend/centrifuge/decant cycles (total 50 mL per gram dry starting material). Suspension was accomplished using a vortex and centrifuge steps were conducted at 3,000 g for five minutes (Eppendorf 5415C). The Sepharose material (total volume 5 mL per gram starting material) was then rinsed three times with ethanol (total volume 30 mL per gram starting material). Sepharose was mixed with a 10-fold molar excess of PMPI over the thiol-group concentration with 3% dimethylsulfoxide in ethanol (total 10 mL per gram starting material with 8 mg PMPI). After incubation for 1 hour at room temperature under constant agitation, the Sepharose was centrifuged, decanted, and rinsed in 50% ethanol for three cycles. The Sepharose was then incubated overnight at 4°C in ethanol with purified PAC or catechin using a 10-fold molar excess of analyte in 50% ethanol (total 10 mL per gram starting material, PAC

concentrations based on tannic acid equivalents). As a final step, the Sepharose was rinsed over four cycles using 50% ethanol (40 mL total per gram starting material) and resuspended in 0.02% sodium azide in H₂O (16 mL final volume per gram starting material). The materials were stored in the dark at 4°C until use. PAC concentrations for bead sets were determined using the Prussian blue assay (35,47) as compared to solutions of the same PAC materials: PAC-tea concentration 40 μM (TAE), PAC-berry concentration 49 μM (TAE), PAC-grape concentration 35 μM (TAE).

PAC capture of LPS was quantified by pull-down assay. PAC-beads were incubated with FITC-LPS in 50 mM TRIS pH 8.0 at room temperature with constant agitation. Figure 6 presents the dependence of fluorescence intensity on the concentration of FITC-LPS in solution. Catechin-coated beads were used as controls. Addition of soluble PACs to assays inhibited the binding of FITC-LPS by immobilized PACs. IC₅₀ values of 6.5 and 9.7 μM (TAE) were obtained for PACs from tea and cranberries, respectively, when beads coated in the same material were challenged. Side-by-side comparison of polymyxin B beads to proanthocyanidin beads indicated that the capture efficiency of beads coated with PACs from cranberries and PMB beads was competitive based on molar concentrations of capture molecules. PAC beads coated with PACs from tea performed slightly better than PMB and PAC-berry coated beads.

Summary and Conclusions

An interaction between bacterial lipopolysaccharide and naturally occurring proanthocyanidins has been described which directly competes with polymyxin B binding of LPS. The interaction of proanthocyanidins with LPS has been demonstrated to interfere with membrane binding and endocytosis of LPS by mammalian cells. The binding of LPS by immobilized proanthocyanidins has been applied for the removal of LPS from solution providing a potential method for filtration or concentration of the compound or of bacterial cells.

References

1. E. Middleton, *Int J Pharm.* **1996**, *34*, 344.
2. E.B. Rimm; M.B. Katan; A. Ascherio; M.J. Stampfer; W.C. Willett, *Ann Intern Med.* **1996**, *125*, 384.
3. P. Knekt; R. Jarvinen; A. Reunanen; J. Maatela, *Brit Med J.* **1996**, *312*, 478.
4. J. Dumas; Masqueli.J, *Ann I Pasteur.* **1971**, *121*, 69.
5. L. Fremont; L. Belguendouz; S. Delpal, *Life Sci.* **1999**, *64*, 2511.
6. J. Yamakoshi; S. Kataoka; T. Koga; T. Ariga, *Atherosclerosis.* **1999**, *142*, 139.

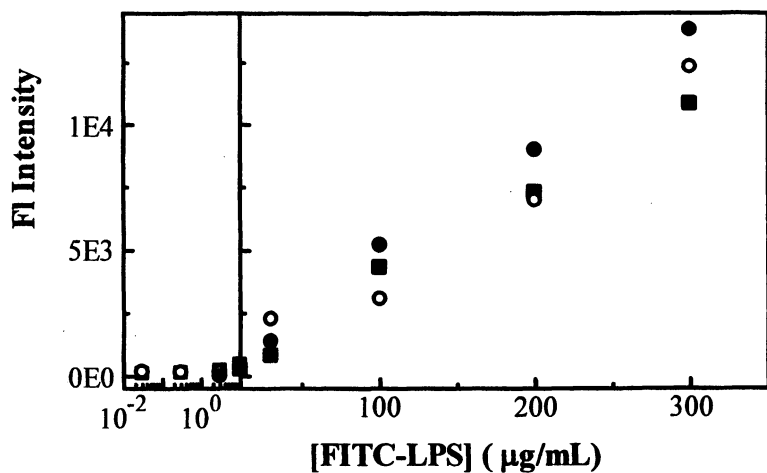


Figure 6. PACs as capture molecules. PACs from tea ($5.5 \mu\text{M}$, ●), grape juice ($6.1 \mu\text{M}$, ○), and cranberries ($6 \mu\text{M}$, ■) bind LPS from solution as indicated by the increase in fluorescence intensity for increasing FITC-LPS concentration.

7. F. Ursini; A. Zamburlini; G. Cazzolato; M. Maiorino; G.B. Bon; A. Sevanian, *Free Radical Bio Med.***1998**, *25*, 250.
8. F. Virgili; H. Kobuchi; L. Packer, *Free Radical Bio Med.***1998**, *24*, 1120.
9. D.F. Fitzpatrick; S.L. Hirschfield; R.G. Coffey, *Am J Physiol.***1993**, *265*, H774.
10. H. Kolodziej; C. Haberland; H.J. Woerdenbag; A.W.T. Konings, *Phytother Res.***1995**, *9*, 410.
11. F. Virgili; D. Kim; L. Packer, *FEBS Lett.***1998**, *431*, 315.
12. E. Cossins; R. Lee; L. Packer, *Biochemistry and Molecular Biology International.***1998**, *45*, 583.
13. R.M. Facino; M. Carini; G. Aldini; M.T. Calloni; E. Bombardelli; P. Morazzoni, *Planta Med.***1998**, *64*, 343.
14. L.Y. Foo; Y.R. Lu; A.B. Howell; N. Vorsa, *J Nat Prod.***2000**, *63*, 1225.
15. A.B. Howell; J.D. Reed; C.G. Krueger; R. Winterbottom; D.G. Cunningham; M. Leahy, *Phytochemistry.***2005**, *66*, 2281.
16. Y. Liu; M.A. Black; L. Caron; T.A. Camesano, *Biotechnol Bioeng.* **2006**, *93*, 297.
17. L. Zhang; J.L. Ma; K.F. Pan; V.L.W. Go; J.S. Chen; W.C. You, *Helicobacter.***2005**, *10*, 139.
18. O. Burger; E. Weiss; N. Sharon; M. Tabak; I. Neeman; I. Ofek, *Crit Rev Food Sci.***2002**, *42*, 279.
19. H. Koo; P.N. de Guzman; B.D. Schobel; A.V.V. Smith; W.H. Bowen, *Caries Res.***2006**, *40*, 20.
20. E.I. Weiss; R. Lev-Dor; Y. Kashamn; J. Goldhar; N. Sharon; I. Ofek, *J Am Dent Assoc.***1998**, *129*, 1719.
21. T. Yoshida; T. Hatano; H. Ito, *J Syn Org Chem Jpn.***2004**, *62*, 500.
22. L.Y. Foo; Y.R. Lu; A.B. Howell; N. Vorsa, *Phytochemistry.***2000**, *54*, 173.
23. C.A. Rowe; S.B. Scruggs; M.J. Feldstein; J.P. Golden; F.S. Ligler, *Anal Chem.***1999**, *71*, 433.
24. C.R. Taitt; J.P. Golden; Y.S. Shubin; L.C. Shriver-Lake; K.E. Sapsford; A. Rasooly; F.S. Ligler, *Microbial Ecol.***2004**, *47*, 175.
25. J.P. Golden; C.R. Taitt; L.C. Shriver-Lake; Y.S. Shubin; F.S. Ligler, *Talanta.***2005**, *65*, 1078.
26. K.E. Sapsford; P.T. Charles; C.H. Patterson; F.S. Ligler, *Anal Chem.***2002**, *74*, 1061.
27. M.M. Ngundi; L.C. Shriver-Lake; M.H. Moore; M.E. Lassman; F.S. Ligler; C.R. Taitt, *Anal Chem.***2005**, *77*, 148.
28. L.C. Shriver-Lake; K.A. Breslin; P.T. Charles; D.W. Conrad; J.P. Golden; F.S. Ligler, *Anal Chem.***1995**, *67*, 2431.
29. B. Johnson-White; L. Buquo; M. Zeinali; F.S. Ligler, *Anal Chem.***2006**, *78*, 853.

30. D. Steinberg; M. Feldman; I. Ofek; E.I. Weiss, *J Antimicrob Chemoth.* **2004**, *54*, 86.
31. W. Brumfelt; A. Percival, *Lancet.* **1962**, *1*, 186.
32. T.B. Klepser; B. Berryhill; K. Dixon; M. McGinnis; S. Mullholland; S. Pomeroy, *J Infect Dis Pharmaco.* **2003**, *6*, 1.
33. A.B. Howell; M. Leahy; E. Kurowska; N. Guthrie, *Faseb J.* **2001**, *15*, A284.
34. D.H. Strumeyer; M.J. Malin, *J Agr Food Chem.* **1975**, *23*, 909.
35. A.E. Hagerman. 2002. *Tannin Handbook*.
<http://www.users.muohio.edu/hagermae/>
36. R.L. Prior; S.A. Lazarus; G.H. Cao; H. Muccitelli; J.F. Hammerstone, *J Agr Food Chem.* **2001**, *49*, 1270.
37. A.E. Hagerman, *J Chem Ecol.* **1987**, *13*, 437.
38. L.G. Butler; M.L. Price; J.E. Brotherton, *J Agr Food Chem.* **1982**, *30*, 1087.
39. M. Vaara, *Microbiol Rev.* **1992**, *56*, 395.
40. R.C. Bone, *Ann Intern Med.* **1991**, *115*, 457.
41. R.L. Danner; K.A. Joiner; M. Rubin; W.H. Patterson; N. Johnson; K.M. Ayers; J.E. Parrillo, *Antimicrob Agents Ch.* **1989**, *33*, 1428.
42. R.A. Moore; N.C. Bates; R.E.W. Hancock, *Antimicrob Agents Ch.* **1986**, *29*, 496.
43. A.C. Issekutz, *J Immunol Methods.* **1983**, *61*, 275.
44. R. Medzithov, *Nat Rev Immunol.* **2001**, *1*, 135.
45. A. Adrem, and Ulevitch, R.J. , *Nature.* **2000**, *406*, 782.
46. R. Shimazu; S. Akashi; H. Ogata; Y. Nagai; K. Fukudome; K. Miyake; M. Kimoto, *J Exp Med.* **1999**, *189*, 1777.
47. M.L. Price; L.G. Butler, *J Agr Food Chem.* **1977**, *25*, 1268.

Chapter 8

Cranberry Extract as a Bacterial Anti-adhesive Coating

Terri A. Camesano¹, Jeffrey R. Pouliot^{1,3}, Joel B. Lofgren^{1,4}, and Paola A. Pinzon-Arango²

¹Department of Chemical Engineering, Worcester Polytechnic Institute, Worcester, MA ²Department of Biomedical Engineering, Worcester Polytechnic Institute, Worcester, MA

³Current Address: Amgen, Inc., West Greenwich, RI

⁴Current Address: Boston University School of Law, Boston, MA

Cranberry extract in solutions of 0, 20, 60, and 100% was applied as a coating to silicone rubber, which simulated the material of a urinary catheter. The attachment of *Escherichia coli* JR1 to the treated polymers was quantified under flow conditions, using artificial urine as the suspending phase. Increasing the concentration of cranberry extract that was applied to the polymer decreased the attachment of *E. coli*. The polymer was sampled in 15 or 30 minute intervals from 0 to 180 minutes. No trend with time could be seen in the number of bacteria attaching for any of the cranberry extract concentrations, over the range of 15 to 180 min, since it appeared that the number of attached bacteria reached a steady-state within the first 15 min. The coatings with varying cranberry extract concentrations produced statistically different numbers of bacteria attaching, according to the Kruskal-Wallis one-way analysis of variance on the ranks ($P < 0.001$). However, a more detailed test revealed that all pairwise comparisons were significantly different from one another ($P < 0.05$) except for the 20% and 60% treatment groups (Dunn's method). These results suggest that a coating of cranberry extract is an effective barrier to bacterial adhesion for short-term use (tested up to 3 hrs).

Introduction

Accounting for nearly 900,000 infections annually, urinary tract infections (UTIs) are among the most common, yet also among the most costly and time consuming hospital-induced infections in the U.S. Nosocomial-acquired UTIs increase the average cost of a hospital stay by \$675 per patient, and by \$2800 if bacteremia develops (1), as well as increasing the time of hospitalization.

UTIs are the result of an accumulation of bacteria in the urinary tract. Ordinarily, this bacterial level in the urine is controlled by regular urination. However, for bed-ridden hospital or nursing home patients, the bacterial level can rise quickly. This finding is especially true for catheterized patients, since insertion of the catheter disrupts the sterile environment, and the biomaterial itself can provide an excellent colonization ground for bacteria. Some sources estimate that more than 60% of all UTIs are catheter-related (2), and 13% of these catheter-related infections are attributed solely to *Escherichia coli* (3).

For hundreds of years, cranberry juice has been used as a folk remedy for UTI prevention and treatment. Some clinical evidence has demonstrated that consumption of cranberry reduces the presence of bacteria in the urine and/or the prevalence of UTIs, with the first placebo-controlled, randomized trial having been conducted on elderly women over a 6-month period (4). Two recent randomized clinical trials showed benefits of cranberry consumption towards urinary health (5, 6). A recent review of the clinical literature suggested that cranberry juice consumption would be most beneficial as a prophylactic treatment for patients with recurrent UTIs who are willing to drink cranberry juice (7).

Scientifically, more work is needed to understand the mechanisms by which cranberry consumption benefits the urinary tract. Initially, it was hypothesized that the ingestion of cranberry juice caused acidification of human urine, and therefore created an unfavorable environment for bacteria in the urinary tract (8). More recently, researchers have come to accept the theory that certain constituents of cranberry juice inhibit bacterial adhesion to mucosal surfaces, such as the urinary tract. An *in vitro* study demonstrated that cranberry juice inhibited the adhesion of *E. coli* to uroepithelial cells suspended in mouse urine, demonstrating the link between cranberry juice and inhibition of bacterial adhesion (9).

Subsequently, researchers attempted to isolate and identify the specific compounds in cranberry juice which exhibit anti-adhesive activity against a specific type of adhesion in *E. coli* (10, 11). *E. coli* express a variety of surface factors, and the proteins P-fimbriae and type 1 fimbriae are particularly important in the development of UTIs. P-fimbriae-bearing *E. coli* are implicated with the more serious form of UTI, acute pyelonephritis, while type 1 fimbriae-bearing *E. coli* are commonly associated with cystitis and lower UTIs (12). When cranberry juice was dialyzed against phosphate buffered saline in

order to separate high and low molecular weight compounds, researchers learned that the compound affecting type 1 fimbriae was dialyzable, identified to be fructose, which is present in many fruit juices. However, the compound which inhibited type P adhesion appeared to be non-dialyzable and specific to cranberry juice, since it could not be found in orange or pineapple juices, and these latter juices did not inhibit P-fimbrial adhesion (13, 14). Later work showed that a family of proanthocyanidin compounds is responsible for activity against P-fimbrial adhesins in *E. coli* (11).

Limited *in vitro* studies have investigated the adhesion of *E. coli* in the presence of cranberry product or juice. One such study probed the adhesion of *E. coli* to borosilicate glass cover slips in the presence of cranberry extract (15). Cleaned borosilicate glass coverslips were inoculated with small aliquots of bacterial suspension. They were then placed face down on a series of plates. The strength of attachment of the cells to the surface was then correlated to the number of bacteria removed per blot. Cranberry was introduced by either incorporation into the inoculum or by pre-treatment of the slide surface with cranberry extract. No significant effect was seen from the introduction of a 1:100 cranberry concentrate:water dilution. However, with either treatment method, the application of a 1:10 dilution caused a significant decrease in bacterial attachment (15).

More recently, the molecular basis for the role of cranberry on *E. coli* was investigated using atomic force microscopy (AFM) (16). *E. coli* in ultrapure water or various solutions of cranberry juice cocktail (CJC) were probed with a silicon nitride tip. The forces of adhesion between the bacteria and the silicon nitride surface decreased as the concentration of CJC increased. This AFM study demonstrated that, at the molecular level, CJC could alter the adhesion properties and the confirmation of surface fimbriae for P-fimbriated *E. coli*. Future work is needed to further elaborate this molecular mechanism.

The primary goal of this research was to test the viability of a cranberry coated urinary catheter in preventing the adhesion of *E. coli*. We evaluated the anti-adhesive potential of a cranberry extract coating on a silicone rubber surface, using *E. coli* JR1 as a model microorganism.

Materials and Methods

Bacterial Cultivation

The strain that was chosen for this study was *Escherichia coli* JR1 serotype 04, kindly provided by Dr. Bernice Kaack from the Tulane University Primate Center (New Orleans, LA). This strain was originally isolated from a patient

with acute pyelonephritis, and potentially can produce both type 1 and P-fimbriae. However, when grown in liquid cultures under similar temperature and conditions, it has been shown to express only type 1 fimbriae (17). JR1 from a frozen stock (1 mL in a microcentrifuge tube) was grown in 10 mL of Tryptic Soy Broth (TSB; Sigma; 30.0 g/L) at 37°C, under agitation (using a test-tube rotator), overnight. This preculture was then transferred to 90 mL of fresh TSB in a 250 mL Erlenmeyer flask, and cultured at 37°C on a shaker table for approximately 18 hours to allow for bacterial growth. Bacteria were harvested at an OD₆₀₀ of 1.5, corresponding to the middle-late stage of exponential growth.

Bacterial Adhesion in a Flow Chamber

Bacterial adhesion was tested in a flow chamber that was designed to probe the effects of the coatings on intraluminal colonization of model catheters. Extraluminal colonization was not studied. The flow chamber was based on a model Robbins device (18, 19), and was similar to that described in ref. (20). Silicon rubber tubing served as the model catheter material. Laminar flow was used to prevent excessive shear forces from damaging bacterial cells and changing attachment behavior. All materials were sterilized before use by autoclaving for 15 minutes at 121 °C.

In order to test the effect of cranberry extract on bacterial adhesion to silicone rubber, sections of rubber tubing had to be treated with different concentrations of cranberry juice extract in deionized water. To create these solutions, cranberry extract (obtained from Ocean Spray Cranberries, Inc.; Middleboro, MA) was titrated to a pH of 7.0 using NaOH. Next, ultrapure water (Milli-Q, Millipore Corp., Bedford, MA) was added to create 150 mL each of 20% and 60% cranberry extract by volume. For 0% extract, deionized water was used (pH adjusted to 7.0), and pure titrated extract (pH 7.0) was used for the 100% solution. All solutions were neutralized so that any effects attributed to cranberry would not rely on acidification as the mechanism of action. Autoclaved silicon tubing was placed in these solutions and completely submerged to ensure that each tube was filled with fluid. Samples were stored in a refrigerator for 24 hours to allow for adsorption of cranberry constituents. After this period, excess fluid was gently removed. All control tubes were soaked in ultrapure water for an identical time period.

The fluid used in the flow experiments was artificial urine, prepared using (per L of ultrapure water): 3.694 g Na₂NO₃, 0.511 g MgNO₃, 4.64 g NH₄Cl, 12.13 g KCl, 0.452 g CaCl, 18.05 g NaCl, and 1.0 g Na₃C₆H₅O₇. After mixing, the artificial urine was autoclaved at 121°C for 60 min.

Samples were taken at predetermined time intervals in order to quantify bacterial attachment to the silicone rubber tubing. From times 15 min to 90 min, samples were collected in 15 min intervals. After 90 min, sampling continued in

30 min intervals until 180 minutes. Each test case (i.e. each cranberry extract concentration used as a coating) was repeated twice. Controls were also run with no bacterial solution in the feed.

At the pre-determined time interval, the tubing was removed from the system and gently rinsed with ultrapure water to remove loosely adhered bacteria. A one-inch sample was cut laterally from the middle of the tubing, anchored to a glass slide, and stained with 75 μL of acridine orange solution (1 g/L solution with 2% formaldehyde) for one min, followed by a rinse with ultrapure water. Samples were examined using a Nikon Eclipse E400 epifluorescent microscope with 20x and 40x objectives.

Complementary Bacterial Growth Studies

Complementary studies were conducted to determine how growth in the presence of cranberry juice affected bacterial cell morphology. Although the experimental conditions were slightly modified compared to those of the flow chamber/adhesion studies, some collaborating information is provided on how *E. coli* behave when grown in cranberry juice. Light cranberry juice cocktail (referred to hereafter as "CJC") was purchased (Ocean Spray Cranberries, Inc., Middleboro, MA). The pH was adjusted to 7.0 using 1M NaOH solution and the solution was passed through a 0.1 μm syringe filter (Acrodisc) for further purification.

Escherichia coli JR1 was grown in 30.0 g/L Tryptic Soy Broth (TSB; Sigma) supplemented with 10 wt.% CJC, in an overnight culture at 37°C, and harvested in the early stage of exponential growth ($\text{OD}_{600} \sim 0.9\text{-}1.0$). Bacterial cells were centrifuged for 15 minutes at $\sim 3500xg$ and resuspended in ultrapure water (Milli-Q water, Millipore Corp.; Bedford, MA). For control experiments *E. coli* JR1 was cultured in pure TSB without CJC, but treated for the same amount of time and by following the same washing protocols.

Bacteria cultured in the cranberry juice cocktail or appropriate control bacteria were stained with acridine orange, captured onto 0.2- μm polycarbonate membranes (Nuclepore[®], Whatman International Ltd.) and viewed using fluorescence microscopy. Some samples were also examined using phase contrast microscopy (unstained cells).

Results

Effect of cranberry extract concentration on bacterial attachment

The attachment of *E. coli* JR1 decreased as the cranberry extract concentration used to treat the silicone rubber increased (Figure 1). Two types

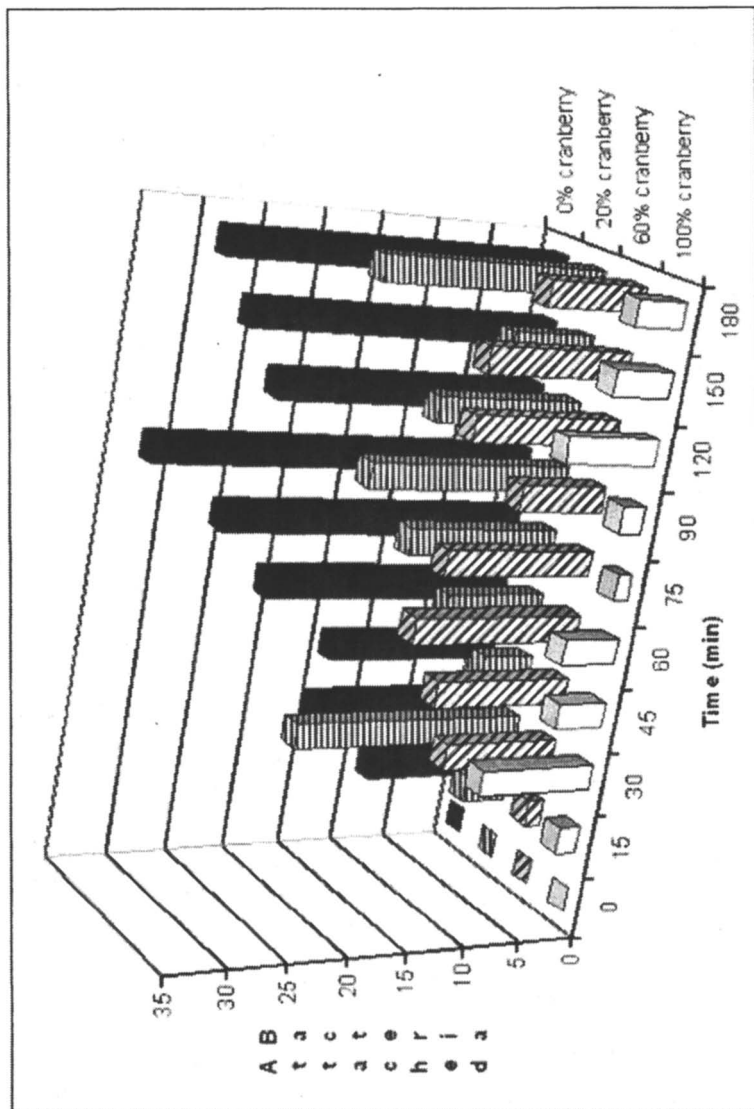


Figure 1. Effect of cranberry extract concentration and time on the number of *E. coli* bacteria that attached to the polymer.

of statistical tests were used to determine whether these treatments resulted in significant differences in the number of attached bacteria. The Kruskal-Wallis one way analysis of variance on ranks is a statistical testing method which compares the medians of multiple data sets to determine statistical significance. This test is useful for comparing 3 or more sets of experimental data, and for data that do not possess a normal or an equal variance. This test was applied using SigmaStat 2.03 software and with setting $P < 0.001$. The analysis showed that the difference in the median values of the treatment groups was greater than would be expected by chance.

A second comparison was performed that could give a more detailed picture of the differences between the individual treatment groups. Dunn's method allows for pairwise comparisons of all individual treatment groups. These results showed that all treatment conditions were statistically different from one another except for the silicone treated with 20% and 60%. These groups behaved too similarly to rule out the possibility that their variation was due to chance.

When the time variable was eliminated, it was easy to see the trend in bacterial attachment as a function of cranberry extract concentration (Figure 2).

None of the control experiments (i.e. in which no bacteria were used in the influent stream) showed any bacterial attachment to the biomaterials.

Time Dependence of Bacterial Attachment Effect

Bacterial attachment increased rapidly between 0 and 15-30 min, but there was no obvious trend in attachment as a function of time after that point (Figure 3). The error bars demonstrate the reproducibility of the three replicate assays per treatment condition, which was generally good. If bacterial attachment was dominated by diffusion, then attachment should have increased linearly as the square root of time increased (21). We attempted to apply this type of model to the data but it was clearly not valid (data not shown). We were unable to quantify the initial bacterial attachment rate (22, 23), because this calculation would have required more data points in the 0 to 30 min range in order to yield accurate results. These results suggested that a steady attachment profile was developed within the first 30 min of flow chamber operation, and that the coatings were stable over the 180 min of the experimental investigation.

Qualitative Observations

Images of the silicone rubber for the uncoated polymer and the polymer coated with 20% cranberry extract were qualitatively similar (Figures 4A and 4B). Each showed a fairly homogeneous coverage of bacteria. Bacterial cells

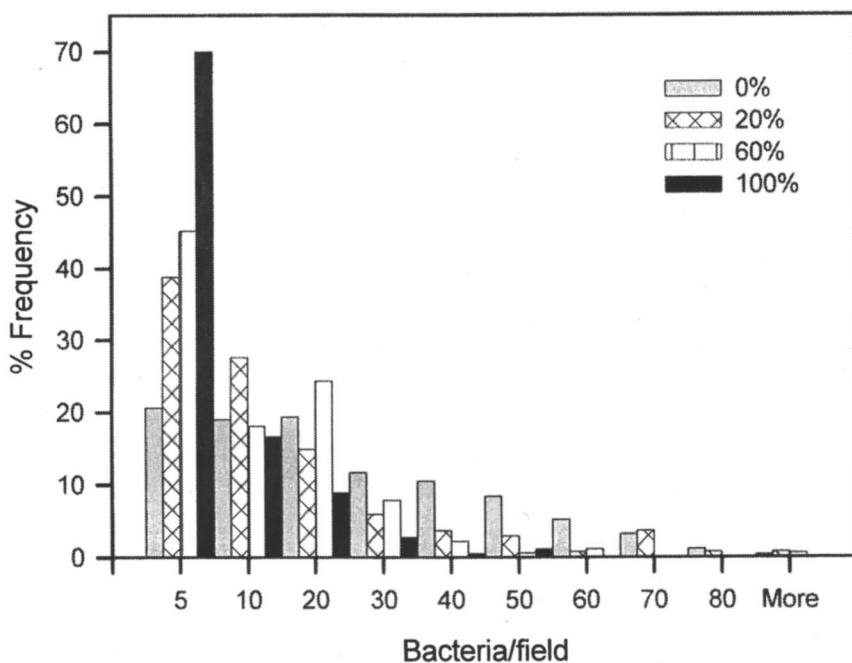


Figure 2. Effect of cranberry extract concentration on the number of E. coli bacteria that attached to the polymer. All of the time points for a given cranberry extract concentration were grouped together. This figure clearly demonstrates that cranberry extract concentration affected the number of attached bacteria.

were not aggregated with one another, and no areas were observed to lack bacteria. Some changes could be noted when higher cranberry concentrations were applied, beginning with the 60%-extract coated polymer. Although the total number of bacteria attaching to the 60% or 100%-extract polymer was substantially less, the bacteria that did attach tended to be in clumps or aggregates, as shown in a representative image of the 60%-extract coated polymer (Figure 4C). An increase in aggregation as a function of time, however, could not be noted, since even at the earliest time points sampled, aggregation was present. In some cases for the 100%-extract coated polymers, areas were observed that contained no bacteria (Figure 4D).

Qualitatively, the cranberry-free and 20% solution produces similar results, in terms of bacterial attachment, in that the bacteria attached individually and fairly evenly. While the total number of cells attaching to the polymer treated with 60% extract was less, those bacteria that did attach tended to be found

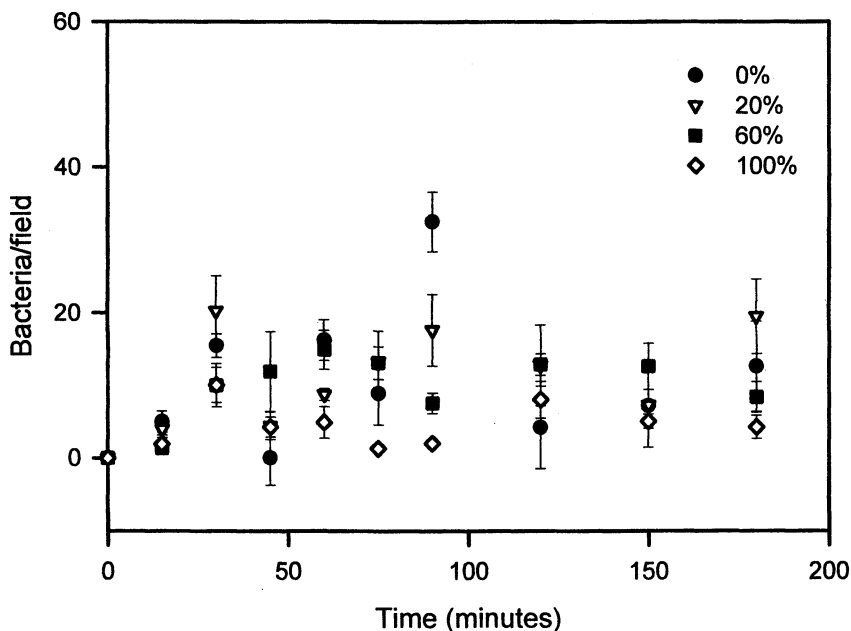
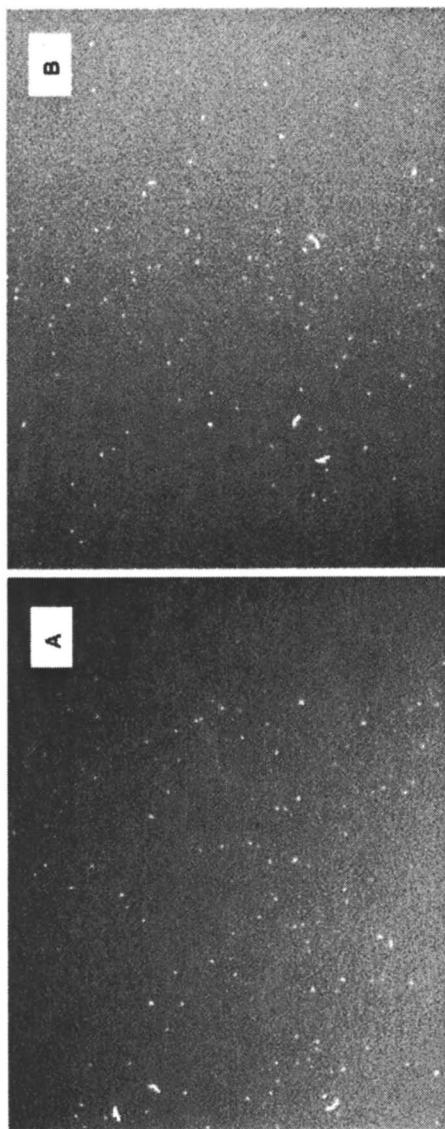


Figure 3. Isolation of the effect of time of exposure between the *E. coli* bacteria and the polymer, on the overall number of bacteria that attached. This figure shows that time was not an important variable in these experiments. Error bars represent the standard error of the mean for three replicate experiments.

more often in aggregates, as shown in panel C). The polymer that had been treated with 100% cranberry extract contained very few bacteria, and defects in the polymer itself were often seen in the images, as shown in panel D). All images were taken at a representative time point of 120 minutes. Since it appears that the activity at around 20-60% is most affected, future studies should focus on concentrations in this region. A concentration of 27% is particularly interesting since that corresponds to the concentration of cranberry juice usually used in commercially available cranberry juice cocktail.

Bacterial Cultured with Cranberry Juice Cocktail

Complementary growth studies suggested that *E. coli* surface properties change when bacteria are cultured in cranberry. When *E. coli* JR1 was grown in the presence of 10% (light) cranberry juice cocktail, individual bacterial cells became aggregated compared to cells from the control case, grown in cranberry juice-free TSB (Figure 5).



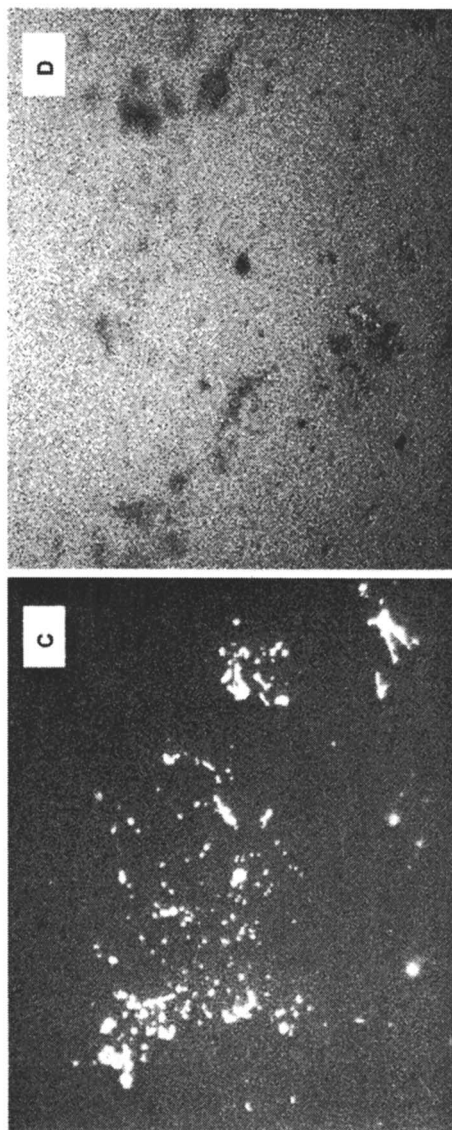


Figure 4. Representative images of polymer with attached bacteria, for A) polymer coated with no cranberry extract, B) 20% soln. of cranberry extract, C) 60% soln. of cranberry extract, and D) pure cranberry extract.

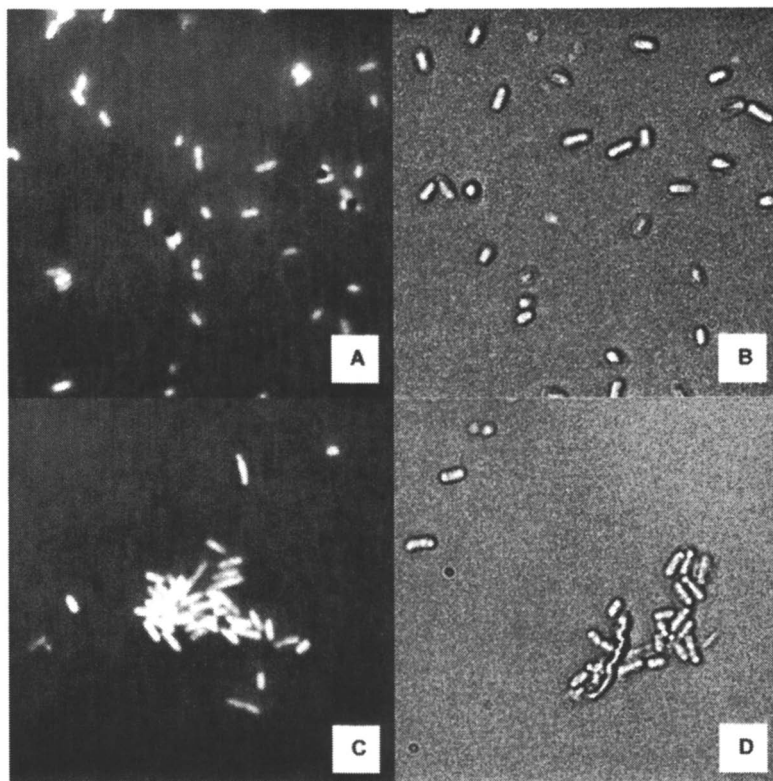


Figure 5. *E. coli JR1* cultured in A) and B) typical growth media or C) and D) in the presence of 10 wt. % light cranberry juice cocktail. Panels A) and C) show fluorescence microscopy images, B) and D) are phase contrast images.

Discussion

Prevention and treatment of catheter-associated UTIs remain major challenges in critical care settings throughout the world. The materials used commonly in catheters have limited abilities to resist microbial colonization. Much research is focused on studying the material properties of catheters and in developing catheter coatings that will resist microbial colonization. Some broad categories of coating materials include silver coated or silver-impregnated catheters (20), antibiotic-based coatings (24), and the use of block copolymer blends to create novel catheter materials (25).

In one study that utilized a qualitative grading scheme to assess microbial colonization of commonly-used catheters in ten patients, silicone and hydrogel materials had slightly better microbial resistance than rubber and latex catheters, after a one-week incubation period (20). Silver-impregnated urinary catheters have shown some promise, in that significantly lower rates of bacterial colonization have been observed in more than one clinical trial that used silver alloy or silver oxide catheters (26, 27). In a laboratory study using the Robbins device, a lecithin/silver coated catheter showed promising results in reducing the colonization of the catheter by *E. coli* over a 7 day period, when compared to silver, hydrogel/silver, and silicone catheters (20). Despite the benefits compared to uncoated catheters, patients still developed UTIs when silver-coated catheters were used for longer time periods (10 days or more), with 62.3% of patients developing a UTI by day 21 (28). In other cases, contradictory results have been shown. For example, Johnson et al. determined that a silver hydrogel urinary catheter was rather ineffective in preventing the migration of Gram-negative bacilli, including *E. coli* and *K. pneumoniae* isolates (29).

In the present study, coating of catheter material with cranberry extract significantly reduced the attachment of *E. coli*. This work demonstrated that treatment of a polymer with cranberry extract was feasible for short-term use (up to 3 hours), and that the anti-adhesive coating was not degraded by the urine environment in that time period. Further, we demonstrated that treatments with $\geq 20\%$ solution of cranberry extract could reduce the attachment of *E. coli* JR1, and that increasing concentrations of the coating had further benefits in terms of reduced bacterial adhesion.

The mechanism for the reduction in adhesion could be due to a combination of surface modification of the *E. coli*, and of changing the overall interaction forces between the catheter and the bacteria. The bacteria grown in cranberry juice cocktail changed their behavior by becoming aggregated and clumped together, compared to cells from the control case. The short residence times used in the adhesion studies makes it unlikely that the bacteria could have grown in the cranberry extract, but these complementary results provide further

evidence that cranberry compounds can change the way bacterial cells interact with one another.

In another study from our laboratory, exposure to cranberry juice cocktail solutions of 5 to 20% altered the conformation of the P fimbriae on *E. coli* HB101pDC1. This change in fimbrial properties caused a modification in the adhesion force of the bacteria with a model probe surface (silicon nitride), in an atomic force microscopy study (16). Therefore, we find that at the molecular scale and at the level of individual cells, cranberry can cause changes in *E. coli* which affect the bacterium's ability to adhere.

The efficacy of cranberry consumption in preventing UTIs is still being actively investigated through clinical studies. Additional *in vitro* studies, such as the present one, can help provide further scientific validation for the effects of cranberry components on *E. coli* uropathogens.

Acknowledgements

We thank Ocean Spray Cranberries, Inc. for providing the cranberry extract used in this work.

This publication was made possible in part by grant number BES-0238627 from the National Science Foundation. We also acknowledge the donors of the Petroleum Research Fund of the American Chemical Society, for partial support of this work (grant PRF 38988-G2).

References

1. Saint, S. *Am. J. Infect. Control* **2000**, *28*, 68.
2. Vincent, J.L.; D.J. Bihari, and P.M. Suter. *J. American Med. Assoc.* **1995**, *274*, 639.
3. Tambyah, P.A.; K.T. Halvorson, and D.G. Marki. *Mayo Clin. Proc.* **1999**, *74*, 131.
4. Avorn, J.; M. Monane; J.H. Gurwitz; R.J. Glynn; I. Choodnovskiy, and L.A. Lipsitz. *J. American Med. Assoc.* **1994**, *271*, 751.
5. Kontiokari, T.; K. Sundqvist; M. Nuutinen; T. Pokka; M. Koskela, and M. Uhari. *BMJ* **2001**, *322*,
6. Stothers, L.A. *Can. J. Urology* **2002**, *9*, 1558.
7. Kiel, R.J. and J. Nashelsky. *J. Family Practice* **2003**, *52*, 154.
8. Blatherwick, N.R. *Arch. Intern. Med.* **1914**, *14*, 409.
9. Sobota, A.E. *J. Urology* **1984**, *131*, 1013.
10. Foo, L.Y.; Y.R. Lu; A.B. Howell, and N. Vorsa. *Phytochemistry* **2000**, *54*, 173.

11. Foo, L.Y.; Y.R. Lu; A.B. Howell, and N. Vorsa. *J. Nat. Prod.* **2000**, *63*, 1225.
12. Svanborg, C. and G. Godaly. *Infectious Disease Clin. N. America* **1997**, *11*, 513.
13. Zafriri, D.; I. Ofek; R. Adar; M. Pocino, and N. Sharon. *Antimicrob. Agents Chemother.* **1989**, *33*, 92.
14. Ofek, I.; J. Goldhar; D. Zafriri; H. Lis; R. Adar, and N. Sharon. *N. Engl. J. Med.* **1991**, *324*, 1599.
15. Allison, D.G.; M.A. Cronin; J. Hawker, and S. Freeman. *J. Basic Microbiol.* **2000**, *40*, 3.
16. Liu, Y.; M.A. Black; L. Caron, and T.A. Camesano. *Biotechnol. Bioeng.* **2006**, *93*, 297.
17. Ahuja, S.; M.B. Kaack, and J.A. Roberts. *J. Urology* **1998**, *159*, 559.
18. Nickel, J.C.; I.W. Ruseska, J.B., and J.W. Costerton. *Antimicrob. Agents Chemother.* **1985**, *27*, 619.
19. Kumon, H. *J. Infection Chemother.* **1996**, *2*, 18.
20. Kumon, H.; H. Hashimoto; M. Nishimura; K. Monden, and N. Ono. *Int. J. Antimicrob. Agents* **2001**, *17*, 311.
21. Welty, J.; C.E. Wicks; R.E. Wilson, and G.L. Rorrer, *Fundamentals of momentum, heat, and mass transfer*. 4th ed. John Wiley & Sons: New York, 2001.
22. Rijnaarts, H.H.M.; W. Norde; E.J. Bouwer; J. Lyklema, and A.J.B. Zehnder. *Appl. Environ. Microbiol.* **1993**, *59*, 3255.
23. Smets, B.F.; D. Grasso; M.A. Engwall, and B.J. Machinist. *Colloids Surf., B* **1999**, *14*, 121.
24. Simhi, E.; H.C. van der Mei; E.Z. Ron; E. Rosenberg, and H.J. Busscher. *FEMS Microbiol. Lett.* **2000**, *192*, 97.
25. Reid, G.; C. Tieszer; A. Hesse; H.J. Busscher, and T.A. Fassel. *Cells And Materials* **1993**, *3*, 171.
26. Saint, S.; J.G. Elmore; S.D. Sullivan; S.S. Emerson, and T.D. Koepsell. *American J. Med.* **1998**, *105*, 236.
27. Liedberg, H. and T. Lundenberg. *Urology Res.* **1989**, 17.
28. Liedberg, H. and T. Lundenberg. *J. Urology* **1993**, *149*, 405A.
29. Johnson, J.R.; P. Delavari, and M. Azar. *Appl. Environ. Microbiol.* **1999**, *43*, 2990.

Chapter 9

An Atomic Force Microscopy Look at the Molecular World of Living Bacteria

Nehal I. Abu-Lail

School of Chemical Engineering and Bioengineering
Washington State University, Pullman, WA 99164

In recent years, atomic force microscopy (AFM) has been extensively used in studying bacteria. Owing to its high lateral and vertical resolutions and its dual ability for imaging and measuring interaction forces between bacteria and surfaces in liquid media, AFM offers a unique tool to characterize bacteria. Researchers worldwide realized the importance and the usefulness of AFM and employed it in many bacterial investigations. Over the years, AFM was successfully used to image bacteria and their ultrastructure, to measure specific and nonspecific interactions between bacteria and surfaces, and to estimate bacterial surface properties such as elasticity and charge distribution. This review highlights the rapid acceleration of the use of AFM as a tool for investigating live bacteria. The review is divided into two parts; an imaging part and a force measurements part.

Bacteria, members of the Monera kingdom, live unseen nearly everywhere, including in or on other organisms. Bacteria residing in the human gut and on human skin outnumber the cells making up the human body (1). Bacteria are characterized by a high population and huge diversity. Though considered to be the simplest form of life, bacteria are complex enough to vary in their structural organization, reproductive capacity, metabolic activity, and evolving ability (2), and proven to have tremendous impacts on earth and all its inhabitants. Harmful variants, known as pathogens, are the cause of many types of diseases including cancer (3) and middle ear infections (4). Many bacteria, however, are useful for applications such as chemical recycling (5), and bioremediation (6). Therefore, understanding and controlling the way bacteria interact with other surfaces is of extreme importance.

Examining bacterial communities, properties, and functions have been the focus of many research efforts that date back to the 17th century; when Robert Hooke with his simple light microscope observed a single bacterium (1). Research tools including those for imaging and surface characterization have significantly evolved since then. Transmission electron microscopy (TEM) (7) and scanning electron microscopy (SEM) (8) were for decades the primary techniques used for imaging the size, shape, and structure of bacterial cells, in vacuum. Although high resolution images of bacteria were obtainable via TEM and SEM, both techniques lacked the ability to image live cells and suffered from the requirements of cellular fixation and metal coating (9). In addition to imaging techniques, many other experimental tools were used to investigate properties of bacteria or interactions between bacteria and other surfaces. Electrophoresis measurements (10), contact angle measurements (11), and column transport experiments (12) are examples. However, and despite the importance of all these measurements, they all share being limited in their abilities to perform dual characteristic measurements of bacteria with high resolution (13).

In 1986, atomic force microscopy (AFM) was invented to mainly serve research in surface science (14). However, shortly afterwards, it was realized that AFM can be employed for biological research (15). AFM functions by measuring probes deflecting by means of laser detection upon surface scanning. Deflection values can then be translated into images or force values (16). AFM use in biological research has been continuously increasing mainly due to the capability of AFM to operate in liquid media (17). In addition, AFM is characterized by high lateral and vertical resolutions, and by its ability to measure very small forces (pN range) (18). Finally, the capability of AFM to multifunction on the same surface is extremely important for many applications including microbial experimentation. For example, AFM can be used to locate a bacterium via imaging, measure interaction forces between the bacterium and a surface modeled by probe functionality, and characterize bacterial cell properties such as elasticity and charge in a single experiment.

The aim of this review is to highlight the use of AFM for investigating bacterial properties and bacterial interactions with surfaces. The review is

partitioned into two main sections: an imaging part and a force measurements part. The use of AFM imaging in characterizing bacterial morphology, ultrastructure, and different surface properties such as colonization, and roughness will be addressed in the first part. A large portion of the second part will be devoted to the use of AFM force measurements to quantify bacterial adhesion to surfaces and to investigate the role of individual factors on the bacterial adhesion phenomenon. Additionally, modeling efforts of AFM force-indentation data to estimate elasticity of bacterial surface walls will be discussed. Finally, this review covers only a portion of the literature of AFM investigations of bacteria and is not intended as an exhaustive review of all the literature on this subject.

AFM Imaging of Bacteria

Since its invention, AFM was regarded as a very sensitive high resolution imaging tool (19). AFM has been employed successfully to image biological molecules and very fine details of biological surface ultrastructure in their native media. The AFM imaging capability in liquid media with such a high resolution was revolutionary since characterization of molecules and cells in their functional forms was possible (20). Examples of the molecules that were imaged adequately with AFM are DNA (21), RNA (22), ribozymes (23), proteins (24), and polysaccharides such as dextran (25). Imaging live cells with AFM was no exception. Examples of cells imaged with AFM are yeast (26), plant cells (27), epithelial cells (28), viruses (29), and bacteria (30). This section of the review will focus mainly on the AFM imaging power in characterizing bacteria with very little attention to sample preparation techniques, imaging modes, or imaging other types of cells. For details on these topics, the reader is referred to other excellent extensive reviews (13, 16, 17, 31-38).

AFM allows for imaging bacteria with minimal disruption of their membranes. Unlike other imaging tools, AFM does not require metal deposition, freeze etching, slicing, staining, or drying, but requires bacterial cell fixation. The requirement of cell fixation is mainly to prevent bacterial migration in the liquid media or their displacement due to vertical and shear forces exerted on the cell via the AFM probe. Although attaching bacteria to surfaces is required, most of the methods used to fix bacteria to surfaces for AFM measurements are minimally disruptive. Examples of the different approaches for fixing bacteria that have been proven successful in the literature are the covalent bonding via chemical treatment, entrapment in membrane pores, and physical attachment to a gelatin layer adsorbed on mica. With each of these methods, bacteria remained viable and functional (39-42).

Imaging bacteria with AFM can be performed in different modes, most commonly with tapping mode. In tapping mode, the bacterial surface is scanned by an oscillating probe that lightly taps on the surface. The cantilever's

oscillation amplitude changes with the bacterial surface topography. These changes are monitored using a closed z loop and reflected in a topography image (43). AFM tapping mode operates in fluid with a very minimal shear force; reducing the possibilities for bacterial membrane damage or rupture (44).

Tapping mode is also characterized by a secondary derived mode of imaging called phase imaging. Phase imaging goes beyond topographical data to detect variations such as those in composition and adhesion. Phase imaging is the mapping of the phase lag between the periodic signal that drives the cantilever and the oscillations of the cantilever. Changes in the phase lag often indicate changes in the properties of the sample surface (40).

Irrespective of the mode of operation, the fluid media in use, the imaging parameters, or the cellular fixation method; imaging bacteria with AFM offers exciting ways for characterizing bacterial morphology, ultrastructure, and surface properties. Detailed discussions of the use of AFM imaging of bacteria in these applications are given below.

Imaging Parameters

AFM offers a great tool for imaging bacterial morphology and ultrastructure under physiological conditions. Imaging bacteria using AFM is an art and requires the imaging parameters to be optimized in order to get a high quality image of the bacterium. Examples of the important imaging parameters that need to be optimized are the scan size, scan rate, scan angle, imaging force, and the type of liquid media in which imaging takes place. In a study to illustrate the importance of imaging parameters, contact mode was used to image *Lactococcus lactis* under water using varying imaging parameters (45). The study revealed that repeated imaging even with a low force (1nN) resulted in grooves on the bacterial surface. The grooves' depth increased as the imaging force increased. Changing the solution chemistry in which bacteria are imaged can sometimes result in higher quality images. For example, some researchers believe that imaging bacteria in alcoholic solutions leads to higher resolution images due to the minimization of the capillary forces between the probe and the bacterial surface molecules during imaging (46). However, in another study performed in our lab, we observed no advantage for imaging *Escherichia coli* JM109 in methanol over that for imaging the bacterium in water (47). Therefore, and if images of bacteria in water were as clear as those in alcoholic solutions, researchers are advised to image bacteria in water since alcoholic treatments kill the bacterial cells.

Bacterial Cell Morphology and Ultrastructure

AFM imaging can provide detailed description of bacteria such as their morphology, dimensions, ultrastructure, integrity, and homogeneity of the

population under certain experimental conditions. General morphology of bacterial cells can be easily determined from tapping mode imaging in solution. Most AFM studies performed on bacteria require imaging the bacterium as a part of the measurement. In some experiments, images are used to locate the cells, measure their dimensions, and confirm their correct morphology prior to measurements (48-51). For example, morphological differences between Gram-positive *Staphylococcus aureus* bacteria and Gram-negative *E. coli* bacteria were apparent via tapping mode images in liquid (39). In other experiments, imaging is used as a quantifying measurement of the effect of certain parameters on bacterial morphology. For example, morphological and height changes in confined cells of *Burkholderia cepacia* G4 and *Pseudomonas stutzeri* KC due to treatment with different binding chemicals were easily quantified from tapping mode images (40).

The ultrastructure of bacterial cells is arduous to obtain via AFM tapping mode imaging in solution. Bacteria usually appear to be well hydrated with a smooth surface when imaged in tapping mode under liquid. To reveal structural details, bacteria are usually imaged in contact mode at higher forces mostly in air (39, 52). Although imaging of bacteria in air will result in their collapsing, images often show very interesting structural details of the cells. AFM imaging of bacteria in air offers an alternative to imaging bacteria via other imaging techniques such as SEM, with the advantage of fewer sample preparation requirements. AFM imaging in air was used frequently to visualize the ultrastructure of bacteria. For example, imaging *E. coli* ZK1056 bacteria using contact mode in air showed the long flagella and the short pili surrounding the cell membrane (Figure 1) (17). Another example is the use of contact mode to reveal with unpredicted precision the details of the extracellular ultrastructure of *Myxococcus xanthus* in air (53). Interestingly, the AFM images showed the ability of *M. xanthus* cells to twist their cell bodies as a result of their flexibilities (Figure 2) (53).

Bacterial Properties via Imaging

Imaging bacteria with AFM is considered to be much more than a morphological technique. AFM imaging can be effectively used to probe bacterial surface properties such as the ability to colonize surfaces, surface potential charge, extracellular roughness, bio-sensing, and adhesion to surfaces. The use of AFM imaging to characterize these properties is discussed.

Colonization

Bacterial colonies on surfaces are usually referred to as biofilms (54-55). Matured biofilms can be easily imaged via AFM under different conditions. For

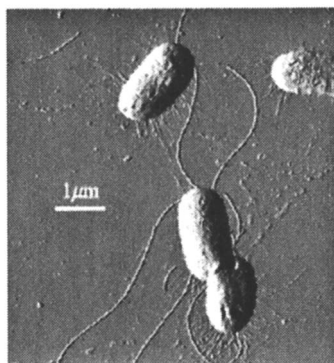


Figure 1. *AFM contact mode image of E. coli ZK1056 on a glass surface in air. [Reprinted from Núñez, M. E.; Martin, M. O.; Chan, P. H.; Duong, L. K.; Sindhurakar, A. R.; Spain, E. M., Atomic force microscopy of bacterial communities. Methods in Enzymology, 2005, 397, 256. (17) Copyright (2006) with permission from Elsevier.]*

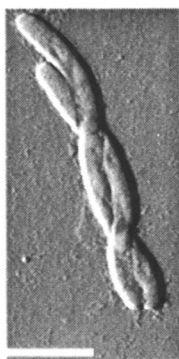


Figure 2. *Two cells of M. xanthus cells twisted against each other. [Reprinted from Pelling, A. E.; Li, Y.; Shi, W.; Gimzewski, J. K., Nanoscale visualization and characterization of Myxococcus xanthus cells with atomic force microscopy. Proceedings of the National Academy of Sciences of the United States of America 2005, 102, (18), 6489. (53) Copyright (2006) with permission from National Academy of Sciences, USA.]*

example, the influence of physiochemical parameters on the formation of biofilms was compared between wild type and mutants of *Pseudomonas chlororaphis* O6, a root colonizing bacterium. Images revealed that wild type strains were able to generate multilayer biofilms while mutant strains were mature only to generate a monolayer biofilm under the same conditions (55).

Surface Potential of Bacterial Cell Membrane

Direct measurements of the surface potential charge of bacterial membranes are possible using scanning surface potential microscopy (SSPM), an extended version of regular AFM. SSPM imaging was successfully used to study the differences in the photo-induced surface potentials of wild types and mutants of *D96N Bacteriorhodopsin* membranes. The results of the study indicated that surface potentials were generated by photo-formation of charges on the extracellular side of the membrane (56). In another study, the importance of charge distribution on the bacterial surface on the attachment of *Moraxella catarrhalis* to Pharyngeal epithelial cells was investigated via an AFM equipped with surface potential spectroscopy (57). The results of the study demonstrated that although both bacteria and epithelial cells have a net negative charge, bacteria attach to the positive domains of the microplicae of the epithelial cells (57).

Extracellular Roughness

Variations in the composition of the extracellular structure of a bacterium can be reflected as differences in the roughness. A nanoscale analysis of the roughness of different bacterial strains can be direct evidence of the differences in their composition. When the roughnesses of five strains of *Streptococcus mutans* were analyzed from AFM images; the differences were noticeable (58). The great variability in the roughness values between the different mutants were correlated directly with the differences in the structure as revealed by AFM deflection images obtained in air (58). Roughness analysis can be also used to indicate the effect of different chemical treatments on varying the cellular compositions (40).

Bio-Sensing

The use of stimulus responsive polymer brushes for selective adsorption of bacteria for sensing purposes can be demonstrated using AFM imaging. Stimulus responsive polymer brushes such as poly(*N*-isopropylacryl-

amide)(pNIPAAM) are sets of polymer brushes that change their conformation upon changing environmental stimuli such as temperature or solvent chemistry. For example, when the surrounding temperature increases above 32°C, pNIPAAM brush adopts a hydrophobically collapsed conformation (59). When pNIPAAM was hydrophobically collapsed (37°C), fewer *S. mutans* were attached to pNIPAAM polymer brushes as compared to the number attached when the polymer brush was in a hydrophilic conformation (4 °C) (60, 61). Figure 3 shows the attachment of *S. mutans* on the patterned lines of pNIPAAM at 4°C.

Bacterial Adhesion to Surfaces

Adhesion of bacteria to surfaces is necessary for many of their functions such as production of toxic molecules or survival against shear forces of flowing blood in small veins. In addition, the initial attachment of bacteria to surfaces is essential for many of the operations they are involved in such as infection of host cells (62), biofilms formation (63, 64), corrosion of water transfer pipes, and contamination of water source supplies (65). Therefore and as illustrated by the aforementioned examples, understanding the mechanism by which bacteria adhere to surfaces is very important. The attachment of bacteria to surfaces can occur via specific interactions such as those between bacterial cell ligands and receptors on epithelial cells (66) or via nonspecific interactions (48).

AFM can investigate bacterial interactions to surfaces and the factors affecting the adhesion via qualitative imaging, as will be described in this section and quantitative force measurements as will be described later. AFM imaging of bacterial adhesion is usually done in the following manner. Bacteria are usually allowed to macroscopically attach to the surface of interest under specific environmental conditions. After a certain period of time, the process terminates by withdrawing the surface from the bacterial solution. The surface is then rinsed thoroughly and imaged via AFM to investigate bacterial attachment to that surface. This process has been applied for many different applications in the literature. One of the main applications investigated is the effective use of antimicrobial coatings for preventing bacterial attachment. For example, the use of rifampicin coated silicon was shown to deform *Staphylococcus epidermidis* 35984 upon attachment (Figure 4) (67). A list of examples on the use of AFM to investigate bacterial adhesion to different surfaces is given in Table I.

Force Measurements between Bacteria and Surfaces

AFM is unique among current techniques used in bacterial studies in its ability to image bacteria in liquid and to measure interaction forces between

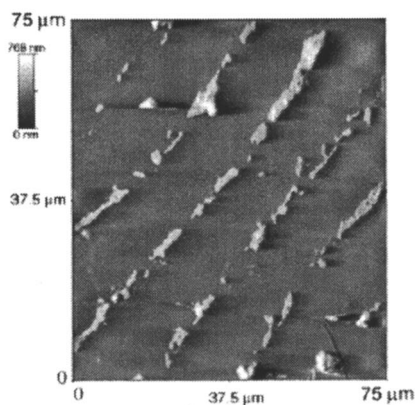


Figure 3. *S. mutans* attached on the patterned lines of pNIPAAm brushes after final incubation of cells at 4 °C. [Reprinted from de las Heras Alarcon, C.; Farhan, T.; Osborne, V. L.; Huck, W. T. S.; Alexander, C., *Bioadhesion at micro-patterned stimuli-responsive polymer brushes*. *Journal of Materials Chemistry* 2005, 15, 2089. (61) Copyright (2006), with permission of the Royal Society of Chemistry.]

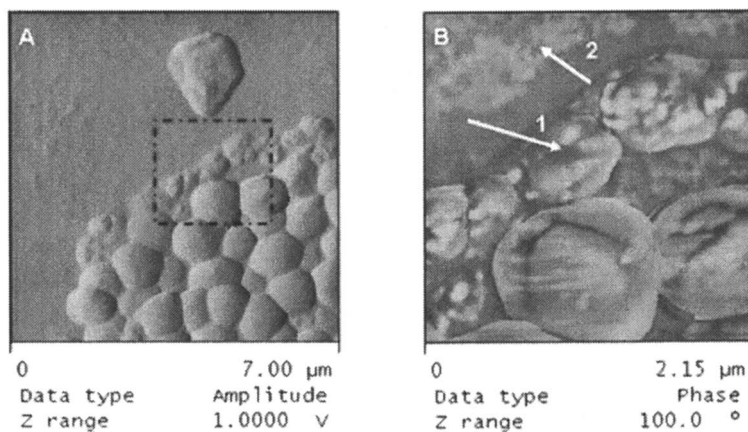


Figure 4. Amplitude image (A) and phase image (B) of *S. epidermidis* 35984 on rifampicin-coated silicon surfaces. The arrows in image B point to deformed bacterial cells. [Reproduced from Liang, X.; Wang, A.; Cao, T.; Tang, H.; McAllister, J. P. I.; Salley, S. O.; Ng, K. Y. S., *Effect of cast molded rifampicin/silicone on S. epidermidis* biofilm formation. *J. Biomed. Mater. Res.* 2006, 76A, 580. (67) Copyright (2006) with permission of Wiley Science.]

Table I. Examples on Studies that Investigated Bacterial Adhesion to Surfaces via AFM Imaging

<i>Bacteria Type</i>	<i>Surface</i>	<i>Env. Conditions</i>	<i>Variables Investigated</i>	<i>Ref.</i>
<i>D. geothermalis</i>	Stainless steel and glass	Water or air	RPM, T, time	(68)
<i>S. epidermidis</i>	Polyethylene oxide	Air	Time	(69)
<i>P. sp.</i> Aerobic soil microbes	Hydrous Fe(III) oxides	Air	Time	(70)
<i>L. crispatus</i>	Poly-L-lysine covered glass slides	10 mM KH_2PO_4 , 20 °C, pH = 7	Scan rate, scan size	(71)
<i>L. helveticus</i>				
<i>L. johnsonii</i>				
<i>P. aeruginosa</i>	Poly(hydroxy methylsiloxane)(PHMS)	Air	NA*	(72)
<i>L. oenus</i>	Polyurethane	PBS	NA*	(73)
<i>S. epidermidis</i> 35984	Silicon	Air, 22°C	Scan rate, rifampicin	(67)

*NA: No variables were investigated

bacteria and surfaces. In general, AFM measures forces between bacteria and a surface in a cycle. The cycle usually consists of measuring the interactions between bacteria and the surface upon the probe approaching the surface (upper schematic, Figure 5); the curves recorded in this part are called approach curves. The second part of the cycle represents the forces measured when the cantilever moves away from a surface and is called retraction curves (lower schematic, Figure 5). Approach curves often represent repulsive forces that can be used to characterize bacterial surface compliance, estimate the height of bacterial surface biopolymers, estimate the grafting density of the biopolymer brush, and measure the steric interactions (Figure 5A). Retraction curves are usually analyzed to quantify and characterize bacterial adhesion events. In a retraction curve, at least one, but often multiple adhesion events are usually observed, which represents an attachment between the AFM silicon nitride tip and a bacterial surface biopolymer (or biopolymers) (Figure 5B). Each adhesion event is characterized by a pull-off distance and a pull-off force as represented by the circles in Figure 5B. The pull-off force is equivalent to the adhesion force and represents the sum of all interaction forces between the bacterial surface biopolymers and the AFM cantilever.

AFM force measurements provide a wealth of information on the nature of interactions between bacteria and surfaces and an estimation of bacterial surface properties such as elasticity. A discussion of the AFM force measurements in

these perspectives is given below with special attention to bacterial adhesion measurements.

Bacterial Adhesion to Surfaces Quantified with Force Measurements

AFM offers a way to estimating bacterial adhesion at the molecular level. AFM can measure very small interactions forces between bacteria and surfaces in liquid media at high resolutions (picoNewton forces). Fundamental understanding of the adhesion phenomenon at the molecular level is necessary to better control macroscopic bacterial adhesion. The importance of the fundamental understanding of the phenomenon is well understood by the research community; the matter that is leading to continuous research efforts to investigate bacterial interactions at a fundamental level. The research efforts directed in this area are focused mainly upon two main streams. The first stream is directed towards the fundamental understanding of the bacterial adhesion phenomenon (41, 48, 74, 75); while the second stream is directed towards better understanding of the processes and applications affected by bacterial adhesion from a molecular point of view (76, 77).

Bacterial adhesion is usually affected by the properties of both bacteria and the surface they adhere to, in addition to the effect of the environmental condition in which the adhesion process is taking place (78). AFM can be used to investigate the effects of these different factors on bacterial adhesion phenomenon. To study the effect of different environmental factors on the adhesion process, bacteria are usually attached to the substrate and the AFM probes are used as model surfaces or can be chemically modified to mimic the surface chemistry of interest (79). To study the adhesion of bacteria to surfaces that are difficult to mimic with functionalized AFM probes, bacteria are usually attached to the probe instead of the substrate. Some examples are the interaction of bacteria with epithelial cells (57), biomedical devices (80), and biofilms (52). Table II lists examples of the use of the two types of AFM force measurements to quantify bacterial adhesion. The following sections will cover the effects of environmental factors, bacterial surface properties, and substrate effects on molecular measurements of bacterial adhesion phenomenon.

The Effect of Environmental Factors on Bacterial Adhesion to Surfaces

AFM was used to investigate the effects of different environmental factors on the adhesion of bacteria to surfaces. Among the factors investigated are solution properties such as pH (88), ionic strength (41, 83, 87), polarity (47), and solution type and concentration (77). The environmental factors directly affect

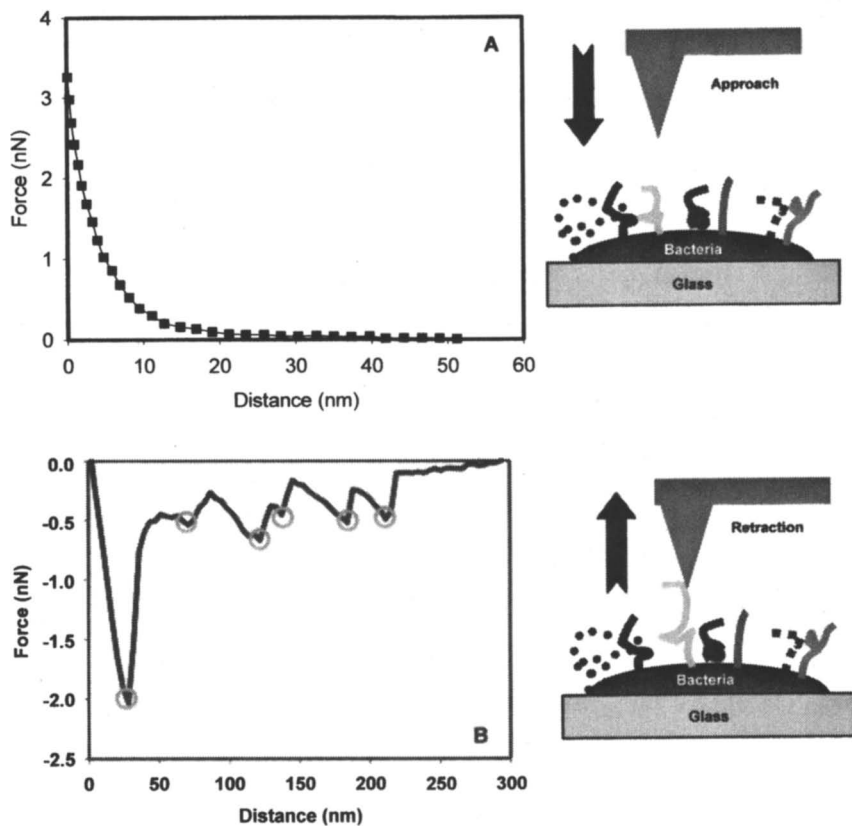


Figure 5. The cycle of force measurements in AFM. *A)* Upon approach of the cantilever to the surface. *B)* Upon retraction of cantilever from the surface, the curve shows several adhesion events marked with circles. The schematics to the side of the figures illustrate the approach and retraction parts of AFM force measurements.

Table II. Examples on AFM Studies that Investigated Bacterial Adhesion to Surfaces via Force Measurements

<i>Bacteria Type</i>	<i>Surface</i>	<i>Media</i>	<i>Adhesion Force (nN)</i>	<i>Ref.</i>
<i>E. coli</i> HB101	Si ₃ N ₄	5 % Cranberry juice	0 to 1.6	(77)
<i>L. crispatus</i>	Si ₃ N ₄	10 mM KH ₂ PO ₄ , 20 °C, pH = 7	No adhesion ~ 0.5	(71)
<i>L. johnsonii</i>	Filtration membrane	air	147.15	(81)
<i>E. coli</i>				
<i>E. faecalis</i> OGIX	Positively charged glass	PBS	1.3 ± 0.5	(7)
<i>S. mitis</i>	Si ₃ N ₄	Water	1.3 ± 0.6	(82)
		0.01 M KCl	0.5 ± 0.4	
<i>L. acidophilus</i>	OH thiol	10 mM KCl	0.11 ± 0.02	(83)
<i>L. casei</i>	OH thiol	10 mM KCl	2.0 ± 0.3	
<i>L. acidophilus</i>	CH ₃ thiol	10 mM KCl	1.3 ± 0.2	(41, 84)
<i>L. casei</i>	CH ₃ thiol	10 mM KCl	0.9 ± 0.1	
<i>L. lactis</i>	Si ₃ N ₄	Water	0.5 ± 0.2	(85)
<i>S. epidermidis</i> RP62A	<i>S. epidermidis</i> biofilm	PBS	0 to > 14	(85)
<i>E. coli</i>	Silicon	1 mM TRIS solution	22.75 ± 3.19	(86)
		OTS	9.91 ± 2.54	
		FAS	7.35 ± 2.31	
<i>E. coli</i> JM109	Si ₃ N ₄	Water	1.35 ± 1.24	(47, 78)
		Methanol	1.74 ± 1.1	
		Formamide	1.17 ± 0.76	
<i>P. putida</i> KT2442	Si ₃ N ₄	Water	0.33	(74, 87)
		0.01 M KCl	0.46	
		0.1 M KCl	0.66	
		1.0 M KCl	1.85	
Sulfate reducing bacteria (SRB)	8 hours SRB biofilms	Air	6.81 ± 0.53	(52)

the strength of interactions between bacteria and surfaces, the conformation of the bacterial surface biopolymers, and the integrity of cells. For example, changing the solution pH values from 4.75 to 8.67 increased the brush height of *Pseudomonas putida* KT2442 biopolymers from 230 nm to 750 nm. Similarly, when the solution pH increased from 2.2 to 7.0, the brush height of *Burkholderia cepacia* G4 increased from 350 nm to 1040 nm. The increased brush height for both strains as the pH of solution increased was associated with a reduction in the adhesion forces measured between the bacterial cells and silicon nitride cantilevers (75).

The effect of ionic strength on bacterial adhesion was the subject for many studies. When the ionic strength was varied over a range that extends from that of water to a value of 1 M KCl solution, the adhesion of *Pseudomonas putida* KT2442 to silicon nitride increased dramatically (Figure 6). This increase in adhesion was associated with the collapse of the bacterial surface biopolymers (87).

Similarly in another study, the adhesion of *Lactobacillus lactis* to a hydrophilic substrate increased from 0.11 nN to 2.1 nN upon increasing the KCl concentration from 10 mM to 100 mM. The trend was exactly the opposite when the adhesion of *Lactobacillus casei* (a mutant of *L. lactis* that lacks the S-layer

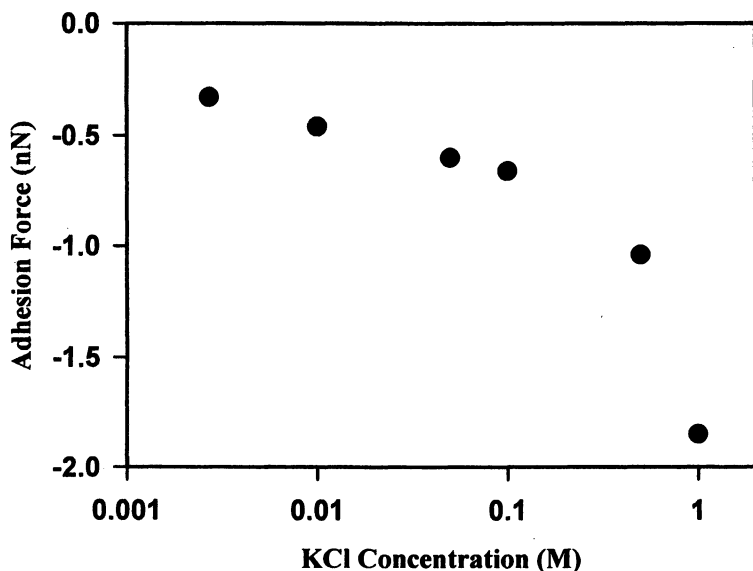


Figure 6. The average adhesion force measured with AFM between *Pseudomonas putida* KT2442 biopolymers and silicon nitride cantilever as a function of KCl solution ionic strength.

present on the bacterial surface) to a hydrophilic substrate was considered. The adhesion decreased from 2 nN to 0.5 nN upon the increase of KCl concentration from 10 mM to a 100 mM (83). These studies performed on the effect of pH and ionic strength point towards the important role played by environmental factors on controlling bacterial adhesion to surfaces.

In addition to ionic strength and pH, specific solvents might have great effects on bacterial adhesion. For example, cranberry juice has long been believed to play a role in prevention and treatment of urinary tract infections. In a recent study, the effect of cranberry juice concentration on the adhesion of two types of *E. coli* strains (HB101 that has no fimbriae and HB101pDC1 that express P-fimbriae) to silicon nitride was quantified (77). The study concluded that the use of cranberry juice at a concentration between 0 – 5% decreased the adhesion of fimbriated *E. coli* bacteria to the model surface (77).

The Effect of Substrate Properties on Bacterial Adhesion to Surfaces

The attachment of bacteria to surfaces equally depends on the chemical and physical properties of the substrate as well as on the bacterial surface properties. Therefore, many research efforts were focused on investigating how different substrate properties such as hydrophobicity or charge affect bacterial attachment at a microscopic level. To investigate substrate properties on bacterial adhesion with AFM, the AFM probe is usually coated with bacterial cells; such a probe is called the microbial probe (Figure 7).

Microbial probes are very useful for measuring interactions between bacteria and surfaces of interest that are hard to mimic with an AFM probe. The attachment of *E. coli* to a variety of biomaterials was investigated in several studies (76, 89, 90). Poly(ethylene glycol), polystyrene, and Teflon were some of the biomaterials studied. The interactions between bacterial cells and the different biomaterials were of variable magnitudes. The interactions between *Pseudomonas aeruginosa* and *P. aeruginosa* biofilms were investigated using similar approaches (91). In another example, the effect of substrate hydrophobicity on the interactions between *E. coli* JM109 and modified silicon surfaces in 1 mM TRIS buffer was investigated via microbial probe AFM measurements (86). The study demonstrated that varying substrate hydrophobicity can be used as a means to prepare antimicrobial surface coatings with great efficiency (86).

The Effect of Bacterial Surface Biopolymers Properties on Adhesion to Surfaces

Bacterial surface macromolecules play an essential role in bacterial attachment to substrates. Their involvement in the attachment process occurs

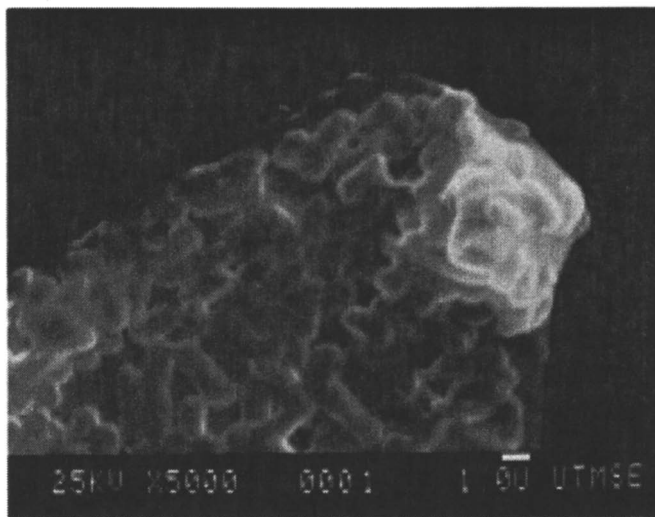


Figure 7. An SEM micrograph of a silicon nitride AFM probe coated with E. coli D21 cells. [Reprinted from Ong, Y.-L.; Razatos, A.; Georgiou, G.; Sharma, M. M. Adhesion Forces between E. coli Bacteria and Biomaterial Surfaces. Langmuir, 1999, 15, 2719. (89) Copyright (2006) with permission from American Chemical Society].

sometimes via a very specific method (ligand – receptor binding) such as that of bacterial attachment to epithelial cells (57). They can also affect the magnitude of the specific and non-specific forces that contribute to the bacterial attachment to substrates (48). In the text of this review, bacterial surface molecules will be referred to as the biopolymer brush consisting of surface lipopolysaccharides, extracellular polysaccharides, proteins, flagella, and pili.

Heterogeneity of Bacterial Surface Biopolymers

The bacterial surface is composed of many types of molecules that distribute through the surface in a heterogeneous way. The wide spread of the distribution of the bacterial surface molecules results in a charge distribution on the surface. The heterogeneity in the bacterial surface biopolymers makes it difficult to predict bacterial adhesion. AFM was used extensively to investigate the effect of bacterial surface biopolymers heterogeneity on the adhesion of *Pseudomonas putida* KT2442 to silicon nitride (92). Substantial heterogeneity was observed in the force-distance curves measured at different locations on a single bacterium and also when comparing force measurements made on

different bacterial cells from a single population. This heterogeneity in the bacterial surface biopolymers is the observed trend in many AFM studies (Figure 8) and usually is reflected in a large standard deviation in the adhesion forces measured (Table II). Statistical representation of measured adhesion forces with AFM might be the method to reduce the heterogeneity effect (48, 78).

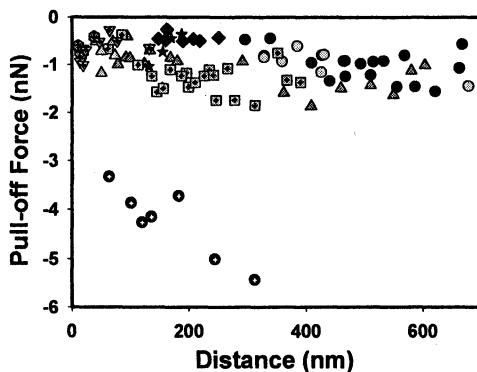


Figure 8. A summary of all adhesion events measured between 10 different *E. coli* JM109 cells and silicon nitride in water. Each symbol represents measurements on an individual cell.

Bacterial Surface Lipopolysaccharides (LPS) and Extracellular Polysaccharides (EPS)

LPS and proteins in the outer membrane of Gram-negative bacteria as well as EPS for some strains are the molecules that influence bacterial adhesion. The effect of these molecules on adhesion is of extreme importance since they are the first part of a bacterium to interact with a surface. The bacterial surface usually consists of multiple types of molecules. For example, the surface of *E. coli* JM109 consists of 75% LPS and 25% proteins (46). The ratio of different types of molecules on the surfaces changes as a function of bacterial growth phase (84). The role of these molecules on adhesion was always a focus of macroscopic research efforts. To investigate the role of a specific molecule or a set of molecules, mutants of bacteria that vary in their composition of one or more of the surface molecules are generally used (78). In a similar way, however, with a fundamental focus, AFM was employed to investigate the role of surface molecules on adhesion.

The effect of the chain length of LPS molecules present on the surface of *E. coli* on its adhesion to silicon nitride was investigated via AFM. Three *E. coli* mutants that varied in the length of their LPS length were used in the study (93).

The AFM measurements concluded that the LPS length was not the sole determinant of the adhesion process and that AFM measurements alone cannot predict the adhesion phenomenon (93). In another study, 80% of the *E. coli* JM109 surface LPS were removed via treatment with 100 mM of ethylenediaminetetraacetic acid (EDTA). The effect of the removal of the LPS on the adhesion of *E. coli* JM109 to silicon nitride was investigated with AFM. The EDTA treatment resulted in a significant reduction in the adhesion affinity of the bacterium to silicon nitride. The adhesion between untreated cells and silicon nitride was 2.1 ± 1.8 nN compared to 0.4 ± 0.36 nN for the treated cells, all measured in water (Figure 9) (78).

Although the aforementioned examples focused on the general effect of LPS on adhesion, other studies focused on the specific role of a single bacterial polysaccharide molecule type on the adhesion of bacteria to a surface. For example, the effect of colonic acid expopolysaccharide (CPS) on the adhesion of *E. coli* strains to hydrophobic glass was investigated via AFM. Two mutants that differ in their CPS content were used in the study. The outcome of this study suggested that CPS molecules do not enhance the adhesion of the pathogenic bacteria to inert surfaces but rather block the specific binding events (94).

In another effort, the effect of the removal of cellulose by cellulase enzymatic treatment from the surface of *Pseudomonas putida* KT2442 was investigated via AFM. The removal of cellulose was found to adjust the adhesion behavior of the bacterium to silicon nitride surface. The cellulase treatment decreased the adhesion to approximately half that of untreated cells (49). Similarly, the specificity of the interactions between two strains of *Enterococcus faecalis* with and without aggregation molecules and silicon nitride cantilevers were studied with AFM (7). The results indicated that the bacterial strain that expresses aggregation molecules had two fold higher adhesion than the strain lacking the expression of aggregation molecules (7). To conclude, the contribution of certain types of molecules on the bacterial surface to the adhesion strength of the bacteria to a surface might be of extreme significance in some cases.

In addition to the importance of the types of LPS molecules on adhesion, the properties of these molecules are equally important. LPS change their conformation and elasticity in order to adapt to environmental conditions in a reversible manner. For example, the biopolymers of *P. putida* KT2442 were found to be stiffer as the polarity of solvents increased from that of methanol to that of formamide. The elasticity of the biopolymers was quantified using a statistical thermodynamic freely jointed chain model (74). Similarly, the flexibility of the biopolymers of the same bacterium increased as the ionic strength increased from that of water to 1 M KCl (87).

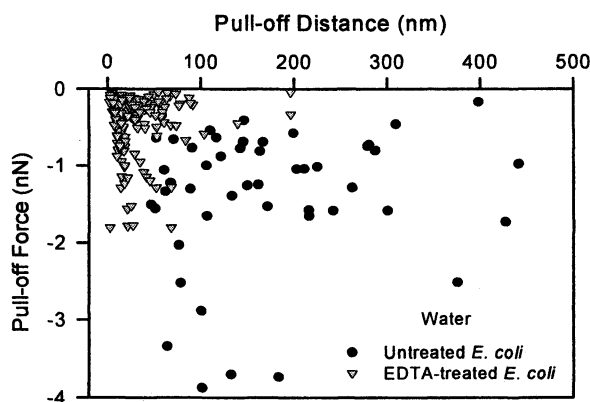


Figure 9. Adhesion forces measured between *E. coli* and silicon nitride in water, with and without treatment with 100 mM EDTA.

Bacterial Pili

Bacterial pili or fimbriae are thin, hair like appendages that are present on the surfaces of many types of microorganisms. Pili are important for adhesion, motility, and biofilm formation of *Pseudomonas aeruginosa* (95). By attaching bacteria to AFM tips, it was possible to fasten the bacteria to mica surface by pili tethers. Force measurements showed that the pili tethers are easily broken at 95 pN forces (95).

Specificity of the Interactions between Bacteria and Surfaces

Interactions between bacteria and surfaces can be described as the combined contribution of specific and non-specific forces (48). Specific forces such as ligand-receptor interactions are usually present between bacterial receptors and ligand on human cells. Non-specific interactions are usually a fixed contributor in all bacterial interactions with surfaces. AFM force measurements can be used to investigate both types of interactions, decouple the magnitudes of the interactions, and image the distribution of specific molecules on the bacterial surface. In general, the output of AFM measurements is the total adhesion force (specific and non-specific) unless specific experiments were designed to measure specific interactions. Decoupling of AFM forces into their specific and non-specific components is very important. In an effort to decouple these forces, Poisson statistical analysis of AFM forces measured between *E. coli* JM109 and silicon nitride surface in water was used (48). According to the analysis, both

short range specific forces and long range colloidal non-specific forces contributed significantly to the measured adhesion forces (48).

To measure specific interactions between bacteria and other cells, the AFM micro-cantilever is usually modified with specific receptors to the bacteria of interest. For example, specific interactions between live *Mycobacteria bovis* BCG and heparin modified tips were measured using force-volume mapping mode of AFM (20, 96). In localized regions, force maps revealed higher adhesion magnitudes due to the presence of the heparin complementary specific ligands called haemagglutinin adhesion (HBHA) (Figure 10).

Bacterial Surface Treatment

AFM force measurements of bacteria require immobilization onto surface. Prior to final immobilization, cultivation of bacteria from the growth media is necessary. The cultivation step consists of multi-physical treatment processes such as centrifugation and filtration. The effect of these different treatments on the bacterial adhesion is a legitimate concern. To address the effect of centrifugation on the adhesion of *Pseudomonas putida* KT2442 to silicon nitride, nanoscopic force measurements were performed on untreated cells and on cells after single or multiple centrifugation cycles (49). The study concluded that whether cells centrifuged once or multiple times, the adhesion forces varied very little (49). Chemical fixation of *E. coli* cells with glutaraldehyde changed the bacterial cell elasticity significantly. The bacterial cells became stiffer upon chemical treatment. These studies suggest the importance of the chemical and physical treatment of bacterial cells on the properties of these cells and eventually on bacterial adhesion to surfaces.

Bacterial Wall Surface Elasticity Estimated from AFM Indentation Measurements

Measuring bacterial properties is another avenue of approach for AFM force measurements. The use of AFM to characterize the elasticity of bacterial cell walls is one example. Cellular elasticity can be estimated as a Young's modulus value by direct fitting of Hertz model of non-contact mechanics to the indentation-force data. Hertz model describes the indentation of a non-deformable conical or parabolic indenter (AFM tip) or into an infinitely deformable elastic half space (bacterial cell) by:

$$F_{cone} = \frac{2}{\pi} \tan(\alpha) E^* \delta^2 \quad (1)$$

$$F_{\text{Parabolic}} = \frac{4}{3} E^* R^{0.5} \delta^{1.5} \quad (2)$$

$$E^* = \frac{E}{1 - \nu^2} \quad (3)$$

where F_{cone} or $F_{\text{Parabolic}}$ is the theoretical value of the force between the indenter (tip) and the bacterium, α is the half opening angle of the conical indenter, E^* is the surface elastic constant of the bacterium, δ is the indentation value, R is the radius of the parabolic indenter, E is the Young's modulus of the bacterium and ν is the Poisson ratio of the bacterium (47).

The Hertz model has been applied to AFM indentation-force data measured on bacterial cells in several studies in the literature. Elasticity of *E. coli* JM109 cells were probed in solvents with different polarities (47). The Young's modulus of the bacterial cells was found to increase as the polarity of the solvents decreased. In another study, the Young's modulus of the Gram-negative bacterium *Shewanella putrefaciens*, was measured from AFM experiments at pH values of 4 and 10 in 0.1 M potassium nitrate solutions (97). By fitting the Hertz model to the AFM data, Young's moduli were estimated to be 0.21 MPa at pH 4 and 0.037 MPa at pH 10. The authors suggested that variations in the Young's modulus as a function of solvent pH were due to the bacterial ultrastructure responding to solvent properties, and thus the nanomechanical properties of the cells could adapt to the different solvent conditions (97).

Bacterial Softness

AFM force curves can be employed to compare bacterial cells softness under different conditions. Force curves measured on bacteria consist of a nonlinear regime and a linear regime called the constant compliance region. Figure 11 shows a force curve measured on *Pseudomonas putida* KT2442 in 0.5 M KCl solution. The slope of the constant compliance regime is significantly less than that of a solid surface and can be used as a measure to bacterial cell softness (98). Several examples on the use of AFM to quantify bacterial softness will be discussed.

The softness of *P. putida* KT2442 cells was estimated from AFM force curves as a function of ionic strength. The cells' softness indicated by the slope of constant compliance regime was increased from 0.014 in water to 0.114 in 1 M KCl solution. The increase in the slope indicates that the bacterial cells became stiffer as the ionic strength increased (87).

Another example is the increase in the stiffness of *E. coli* JM109 cells upon treatment with glutaraldehyde (98). The slope obtained on the cells increased as the glutaraldehyde concentration increased, indicating stiffer cellular structures

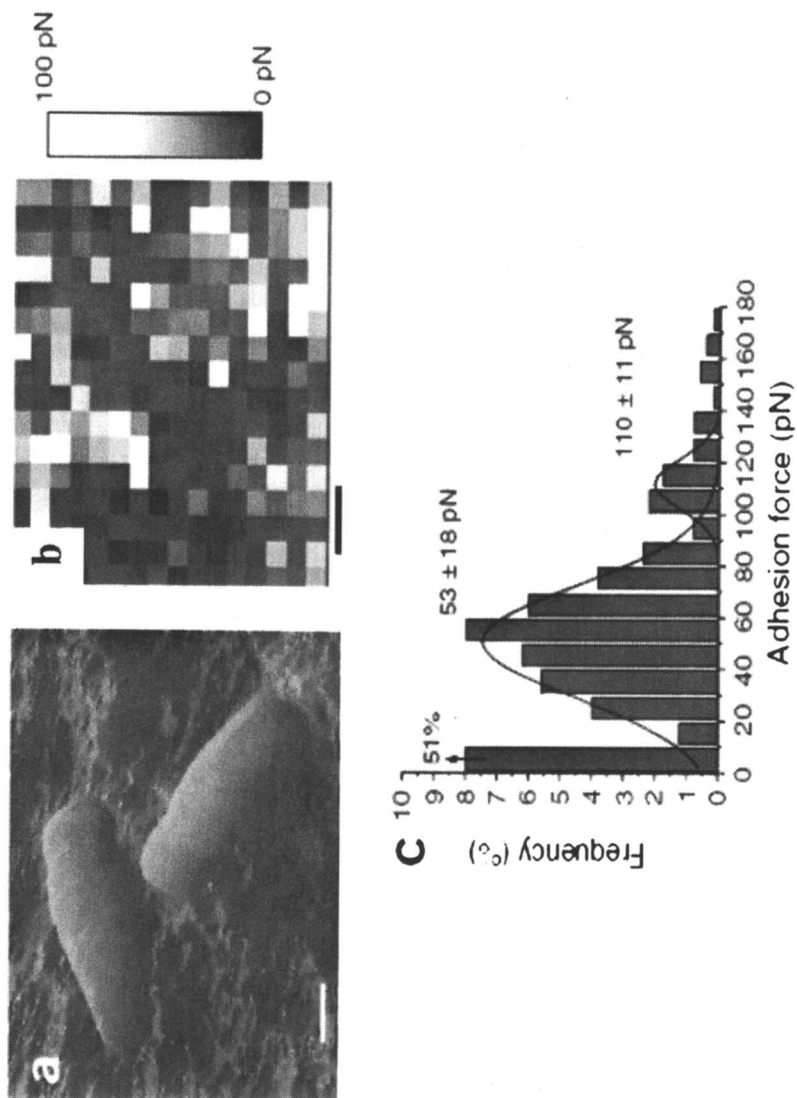


*Figure 10. Mapping molecular recognition events on live Mycobacteria bovis BCG using a heparin modified tip. The image represents two M. bovis BCG cells on a polymer substrate in PBS. The clear pixels in the adhesion map reveal localized adhesion events between heparin and adhesion proteins referred to as heparin-binding haemagglutinin adhesin (HBHA). The histogram represents adhesion forces recorded with the heparin tip at 10,000 pN/s and at interaction time of 500 ms. The 53 pN adhesion forces reflect the detection of single HBHA monomers while the 110 pN forces may correspond to single dimmers or two monomers. Scale bars are 1 μm (left) and 50 nm (right). [Reprinted from Dupres, V.; Menozzi, F. D.; Locht, C.; Clare, B. H.; Abbott, N. L.; Cuenot, S.; Bompart, C.; Raze, D.; Duffrene, Y. F., Nanoscale mapping and functional analysis of individual adhesins on living bacteria. *Nature Methods* 2005, 2, 515(96). Copyright (2006) from Nature Publishing Group.]*

(98). The stiffness of *E. coli* EAEC grown on agar plates are significantly stiffer than those grown in broth, as estimated from AFM curves (99). The softness of fibrillated *Streptococcus salivarius* HB and non-fibrillated *S. salivarius* HBC12 were compared. The fibrillated cells were twice as soft as the non fibrillated cells according to AFM force measurements (100).

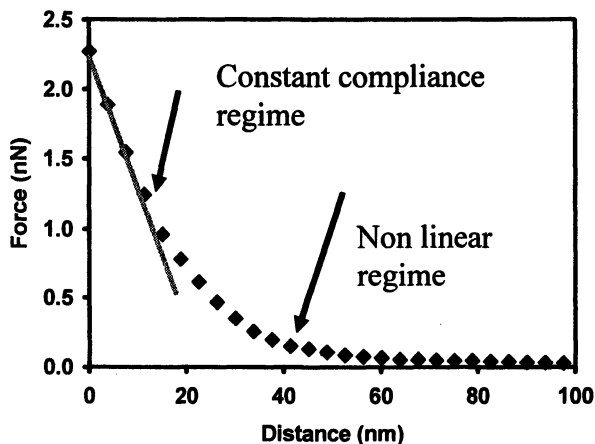


Figure 11. The different regimes of an AFM force curve. The solid line represents the tangent to the constant compliance regime with a slope that can be used to estimate cell softness.

Conclusions

For a long time, characterizing cells and biomacromolecules was difficult in their native environment. However, with the invention of AFM in 1986, cellular and molecular investigations in liquid media became possible. Since then, researchers have used AFM for many biological applications that extend from that of DNA investigations to complex multi cellular interactions. The context of this review is focused on AFM use to investigate live bacteria. Examples of the power of AFM in imaging bacterial cells and their ultrastructure in liquid media were discussed. The importance of imaging in characterizing bacterial surface properties and interactions was also discussed. Finally, the use of AFM to uncover the details of bacterial attachment to surfaces and to investigate the effects of individual factors on bacterial adhesion phenomenon was discussed.

References

1. *Biology: The Unity of Life*. Sixth ed.; Starr, C.; Taggart, R.; Wadsworth Publishing Company: Belmont, 1992; Vol. 1, p 260.
2. *Essential Biology*; Campbell, N. A.; Reece, J. B., Benjamin Cummings: San Francisco, 2001.
3. *Can Bacteria Cause Cancer? Alternative medicine confronts big science*; Hess, D. J., New York University Press: New York and London, 1997; p 234.
4. Morton, D. J.; Bakaletz, L. O.; Jurcisek, J. A.; VanWagoner, T. M.; Seale, T. W.; Whitby, P. W.; Stull, T. L. *Microbial Pathogenesis* **2004**, *36*, 25.
5. Casani, S.; Leth, T.; Knochel, S. *Food Control* **2006**, *17*, 540.
6. Perez-de-Mora, A.; Burgos, P.; Madejon, E.; Cabrera, F.; Jaeckel, P.; Schloter, M. *Soil Biology & Biochemistry* **2006**, *38*, 327.
7. Waar, K.; van der Mei, H. C.; Harmsen, H. J. M.; de Vries, J.; Atema-Smit, J.; Degener, J. E.; Busscher, H. J. *Microbiology (Reading, United Kingdom)* **2005**, *151*, 2459.
8. Farber, P. A.; Long, W. K. *Oral surgery, oral medicine, and oral pathology* **1983**, *55*, 463.
9. Dufrière, Y. F. *Micron* **2001**, *32*, 153.
10. Tsuneda, S.; Aikawa, H.; Hayashi, H.; Hirata, A. *Journal of Colloid and Interface Science* **2004**, *279*, 410.
11. Chen, G.; Zhu, H. *Colloids and Surfaces, B: Biointerfaces* **2005**, *44*, 41.
12. Tong, M.; Li, X.; Brow, C. N.; Johnson, W. P. *Environmental Science and Technology* **2005**, *39*, 2500.
13. Ubbink, J.; Schaer-Zammaratti, P. *Micron (Oxford, England: 1993)* **2005**, *36*, 293.
14. Binning, G.; Quate, C. F.; Gerber, C. *Physical Review Letters* **1986**, *6*, 930.
15. Smith, P. R.; Bradford, A. L.; Schneider, S.; Benos, D. J.; Geibel, J. P. *American Journal of Physiology-Cell Physiology* **1997**, *41*, C1295.
16. Abu-Lail, N. I.; Camesano, T. A. *Journal of Microscopy-Oxford* **2003**, *212*, 217.
17. Nunez, M. E.; Martin, M. O.; Chan, P. H.; Duong, L. K.; Sindhurakar, A. R.; Spain, E. M. *Methods in Enzymology* **2005**, *397*, 256.
18. Wong, J.; Chilkoti, A.; Moy, V. T. *Biomolecular Engineering* **1999**, *16*, 45.
19. Hansma, H. G.; Oroudjev, E.; Baudrey, S.; Jaeger, L. *Journal of Microscopy-Oxford* **2003**, *212*, 273.
20. Hinterdorfer, P.; Dufrière, Y. F. *Nature Methods* **2006**, *3*, 347.
21. Hansma, H. G.; Pietrasanta, L. I.; Golan, R.; Sitko, J. C.; Viani, M. B.; Palocz, G. T.; Smith, B. L.; Thrower, D.; Hansma, P. K. *Journal of Biomolecular Structure & Dynamics* **2000**, 271.
22. Giro, A.; Bergia, A.; Zuccheri, G.; Bink, H. H. J.; Pleij, C. W. A.; Samori, B. *Microscopy Research and Technique* **2004**, *65*, 235.

23. Fay, M. J.; Walter, N. G.; Burke, J. M. *Rna-a Publication of the Rna Society* **2001**, *7*, 887.
24. Lee, M. H.; Leng, C. H.; Chang, Y. C.; Chou, C. C.; Chen, Y. K.; Hsu, F. F.; Chang, C. S.; Wang, A. H. J.; Wang, T. F. *Biochemical and Biophysical Research Communications* **2004**, *323*, 845.
25. Tasker, S.; Matthijs, G.; Davies, M. C.; Roberts, C. J.; Schacht, E. H.; Tendler, S. J. B. *Langmuir* **1996**, *12*, 6436.
26. van der Aa, B. C.; Asther, M.; Dufrene, Y. F. *Colloids and Surfaces B-Biointerfaces* **2002**, *24*, 277.
27. Yamada, T.; Arakawa, H.; Okajima, T.; Shimada, T.; Ikai, A. *Ultramicroscopy* **2002**, *91*, 261.
28. Abrams, G. A.; Schaus, S. S.; Goodman, S. L.; Nealey, P. F.; Murphy, C. J. *Cornea* **2000**, *19*, 57.
29. Malkin, A. J.; McPherson, A.; Gershon, P. D. *Journal of Virology* **2003**, *77*, 6332.
30. Dufrene, Y. F.; Muller, D. J. *Microbial Imaging* **2005**, *34*, 163.
31. Abu-Lail, N.; Camesano, T. In *Dekker Encyclopedia of Nanoscience and Nanotechnology*, James A. Schwarz; Cristian I. Contescu; Karol Putyera Eds. Taylor & Francis Group, LLC: 2004; 119.
32. You, H. X.; Yu, L. *Methods in Cell Science* **1999**, *21*, 1.
33. Dufrene, Y. F. *Abstracts of Papers of the American Chemical Society* **2002**, *224*, U397.
34. Simon, A.; Durrieu, M.-C. *Micron* **2006**, *37*, 1.
35. Lehenkari, P. P.; Charras, G. T.; Nesbitt, S. A.; Horton, M. A. *Expert Reviews in Molecular Medicine* **2000**, 1.
36. Bolshakova, A. V.; Kiselyova, O. I.; Yaminsky, I. V. *Biotechnology Progress* **2004**, *20*, 1615.
37. Dufrene, Y. F. *Journal of Bacteriology* **2004**, *186*, 3283.
38. Kumar, S.; Chaudhury, K.; Sen, P.; Guha, S. *Journal of Nanobiotechnology* **2005**, *3*, 1.
39. Doktycz, M. J.; Sullivan, C. J.; Hoyt, P. R.; Peletier, D. A.; Wu, S.; Allison, D. P. *Ultramicroscopy* **2003**, *97*, 209.
40. Camesano, T. A.; Natan, M. J.; Logan, B. E. *Langmuir* **2000**, *16*, 4563.
41. Dufrene, Y. F.; Boonaert, C. J. P.; van der Mei, H. C.; Busscher, H. J.; Rouxhet, P. G. *Ultramicroscopy* **2001**, *86*, 113.
42. Touhami, A.; Jericho, M. H.; Beveridge, T. J. *Journal of Bacteriology* **2004**, *186*, 3286.
43. Wu, A. G.; Wei, G.; Li, Z. *Chinese Journal of Analytical Chemistry* **2004**, *32*, 1538.
44. Wright, M.; Revenko, I. *Veeco Application Notes* **2004**.
45. Boonaert, C. J. P.; Toniazzo, V.; Mustin, C.; Dufrene, Y. F.; Rouxhet, P. G. *Colloids and Surfaces B-Biointerfaces* **2002**, *23*, 201.
46. Amro, N. A.; Kotra, L. P.; Wadu-Mesthrige, K.; Bulychev, A.; Mobashery, S.; Liu, G. Y. *Langmuir* **2000**, *16*, 2789.

47. Abu-Lail, N. I.; Camesano, T. A. *Colloids and Surfaces B-Biointerfaces* **2006**, *51*, 62.
48. Abu-Lail, N. I.; Camesano, T. A. *Langmuir* **2006**, *22*, 7296.
49. Bell, C. H.; Arora, B. S.; Camesano, T. A. *Environmental Engineering Science* **2005**, *22*, 629.
50. Gad, M. *New Egyptian Journal of Microbiology* **2005**, *12*, 208
51. Bolshakova, A. V.; Kiselyova, O. I.; Filonov, A. S.; Frolova, O. Y.; Lyubchenko, Y. L.; Yaminsky, I. V. *Ultramicroscopy* **2001**, *86*, 121.
52. Fang, H. H.; Chan, K. Y.; Xu, L. C. *Journal of Microbiological Methods* **2000**, *40*, 89.
53. Pelling, A. E.; Li, Y.; Shi, W.; Gimzewski, J. K. *Proceedings of the National Academy of Sciences of the United States of America* **2005**, *102*, 6489.
54. Fu, J.; Ji, J.; Yuan, W.; Shen, J. *Biomaterials* **2005**, *26*, 6684.
55. Anderson, A. J.; Britt, D. W.; Johnson, J.; Narasimhan, G.; Rodriguez, A. *Water Science and Technology* **2005**, *52*, 21.
56. Lee, I.; BGreenbaum, E.; Budy, S.; Hillebrecht, J. R.; Brige, R. R.; Stuart, J. A. *J. Phys. Chem. B* **2006**, *110*, 10982.
57. Ahmed, K.; Nakagawa, T.; Nakano, Y.; Martinez, G.; Ichinose, A.; Zheng, C. H.; Akaki, M.; Aikawa, M.; Nagatake, T. *Microbial Pathogenesis* **2000**, *28*, 203.
58. Cross, S. E.; Kreth, J.; Zhu, L.; Qi, F. X.; Pelling, A. E.; Shi, W. Y.; Gimzewski, J. K. *Nanotechnology* **2006**, *17*, S1.
59. Abu-Lail, N. I.; Kaholek, M.; LaMattina, B.; Clark, R. L.; Zauscher, S. *Sensors and Actuators B-Chemical* **2006**, *114*, 371.
60. Cunliffe, D.; de Alarcon, C.; Peters, V.; Smith, J. R.; Alexander, C. *Langmuir* **2003**, *19*, 2888.
61. de las Heras Alarcon, C.; Farhan, T.; Osborne, V. L.; Huck, W. T. S.; Alexander, C. *Journal of Materials Chemistry* **2005**, *15*, 2089.
62. Abdel-Latif, M. M. M.; Windle, H.; Terres, A.; Ni Eidhin, D.; Kelleher, D.; Reynolds, J. V. *Journal of Gastrointestinal Surgery* **2006**, *10*, 551.
63. Beech, I. B.; Smith, J. R.; Steele, A. A.; Penegar, I.; Campbell, S. A. *Colloids and Surfaces, B: Biointerfaces* **2002**, *23*, 231.
64. Senechal, A.; Carrigan, S. D.; Tabrizian, M. *Langmuir* **2004**, *20*, 4172.
65. Arnold, J. W.; Boothe, D. H.; Suzuki, O.; Bailey, G. W. *Journal of Microscopy-Oxford* **2004**, *216*, 215.
66. Yan, L.; Liang, S. H.; Mao, Y. F.; Li, L. W.; Li, S. P. *World Journal of Gastroenterology* **2003**, *9*, 2240.
67. Liang, X.; Wang, A.; Cao, T.; Tang, H.; McAllister, J. P. I.; Salley, S. O.; Ng, K. Y. S. *J. Biomed. Mater. Res.* **2006**, *76A*, 580
68. Kolari, M.; Schmidt, U.; Kuismanen, E.; Salkinoja-Salonen, M. S. *Journal of Bacteriology* **2002**, *184*, 2473.
69. Marsh, L. H.; Coke, M.; Dettmar, P. W.; Ewen, R. J.; Havler, M.; Nevell, T. G.; Smart, J. D.; Smith, J. R.; Timmins, B.; Tsibouklis, J.; Alexander, C.

- Journal of Biomedical Materials Research, Part B: Applied Biomaterials* **2002**, *61*, 641.
70. Maurice, P.; Forsythe, J.; Hersman, L.; Sposito, G. *Chemical Geology* **1996**, *132*, 33.
 71. Schaer-Zamaretti, P.; Ubbink, J. *Ultramicroscopy* **2003**, *97*, 199.
 72. Satriano, C.; Messina, G. M. L.; Carnazza, S.; Guglielmino, S.; Marletta, G. *Materials Science and Engineering* **2006**, *C26*, 942.
 73. Hayden, O.; Bindeus, R.; Dickert, F. L. *Measurement Science & Technology* **2003**, *14*, 1876.
 74. Abu-Lail, N. I.; Camesano, T. A. *Langmuir* **2002**, *18*, 4071.
 75. Camesano, T. A.; Logan, B. E. *Environmental Science & Technology* **2000**, *34*, 3354.
 76. Razatos, A.; Ong, Y.-L.; Boulay, F.; Elbert, D. L.; Hubbell, J. A.; Sharma, M. M.; Georgiou, G. *Langmuir* **2000**, *16*, 9155.
 77. Liu, Y.; Black, M. A.; Caron, L.; Camesano, T. A. *Biotechnology and Bioengineering* **2006**, *93*, 297.
 78. Abu-Lail, N. I.; Camesano, T. A. *Environmental Science & Technology* **2003**, *37*, 2173.
 79. Salerno, M. B.; Logan, B. E.; Velegol, D. *Langmuir* **2004**, *20*, 10625.
 80. Emerson, R. J.; Camesano, T. A. *Ultramicroscopy* **2006**, *106*, 413.
 81. Whisman, N.; York, D.; Manning, L.; Brant, J.; Dyer, R.; Childress, A.; Marchand, E. A.; Adams, J. D. *Review of Scientific Instruments* **2003**, *74*, 4491.
 82. Vadillo-Rodriguez, V.; Busscher, H. J.; Norde, W.; de Vries, J.; van der Mei, H. C. *Langmuir* **2003**, *19*, 2372.
 83. Vadillo-Rodriguez, V.; Busscher, H. J.; Van der Mei, H. C.; De Vries, J.; Norde, W. *Colloids and Surfaces B-Biointerfaces* **2005**, *41*, 33.
 84. Boonaert, C. J. P.; Dufrene, Y. F.; Derclaye, S. R.; Rouxhet, P. G. *Colloids and Surfaces B-Biointerfaces* **2001**, *22*, 171.
 85. Chaw, K. C.; Manimaran, M.; Tay Francis, E. H. *Antimicrobial Agents and Chemotherapy* **2005**, *49*, 4853.
 86. Cao, T.; Tang, H.; Liang, X.; Wang, A.; Auner, G. W.; Salley, S. O.; Ng, K. Y. S. *Biotechnology and Bioengineering* **2006**, *94*, 167.
 87. Abu-Lail, N. I.; Camesano, T. A. *Biomacromolecules* **2003**, *4*, 1000.
 88. Camesano, T. A.; DeSantis, A. A.; Baygents, J. C.; Logan, B. E. *Abstracts of Papers of the American Chemical Society* **1999**, *218*, U440.
 89. Ong, Y.-L.; Razatos, A.; Georgiou, G.; Sharma, M. M. *Langmuir* **1999**, *15*, 2719.
 90. Razatos, A. P.; Ong, Y. L.; Sharma, M. M.; Georgiou, G. *Evaluating the interaction between bacteria and biomaterial surfaces using atomic force microscopy*, 216th ACS National Meeting, Boston, 1998; Boston, 1998.
 91. Emerson, R. J.; Camesano, T. A. *Applied and Environmental Microbiology* **2004**, *70*, 6012.
 92. Camesano, T. A.; Abu-Lail, N. I. *Biomacromolecules* **2002**, *3*, 661.

93. Burks, G. A.; Velegol, S. B.; Paramonova, E.; Lindenmuth, B. E.; Feick, J. D.; Logan, B. E. *Langmuir* **2003**, *19*, 2366.
94. Hanna, A.; Berg, M.; Stout, V.; Razatos, A. *Applied and Environmental Microbiology* **2003**, *69*, 4474.
95. Touhami, A.; Jericho, M. H.; Boyd, J. M.; Beveridge, T. J. *Journal of Bacteriology* **2006**, *188*, 370.
96. Dupres, V.; Menozzi, F. D.; Locht, C.; Clare, B. H.; Abbott, N. L.; Cuenot, S.; Bompard, C.; Raze, D.; Dufrière, Y. F. *Nature Methods* **2005**, *2*, 515.
97. Gaboriaud, F.; Bailet, S.; Dague, E.; Jorand, F. *Journal of Bacteriology* **2005**, *187*, 3864.
98. Velegol, S. B.; Logan, B. E. *Langmuir* **2002**, *18*, 5256.
99. Beckmann, M. A.; Venkataraman, S.; Doktycz, M. J.; Nataro, J. P.; Sullivan, C. J.; Morrell-Falvey, J. L.; Allison, D. P. *Ultramicroscopy* **2006**, *106*, 695.
100. van der Mei, H. C.; Busscher, H. J.; Bos, R.; de Vries, J.; Boonaert, C. J. P.; Dufrière, Y. F. *Biophysical Journal* **2000**, *78*, 2668.

Chapter 10

Immobilizing Bacteria for Atomic Force Microscopy Imaging or Force Measurements in Liquids

Yatao Liu and Terri A. Camesano

Department of Chemical Engineering, Worcester Polytechnic Institute,
Worcester, MA

The atomic force microscope (AFM) is a powerful microbiological tool that allows for high resolution imaging or force measurements on intact microbes in liquid. In order to take advantage of this benefit, the microbes must be immobilized with minimal alterations to their surface properties. This study investigates the feasibility and application of three immobilization methods, namely bacterial attachment through covalent bonding, electrostatic forces, and mechanical trapping. Special focus is given to the zero-length cross-link covalent bonding reaction commonly used for protein and bacterial immobilization. Based on comparing AFM images obtained with the three immobilization methods, experimental conditions were optimized through modifications in cell washing, sonication, and substrate selection, to achieve the easiest, most reproducible, and artifact-free cell immobilization. In addition, the strengths of the immobilization methods were evaluated.

Introduction

Overview of Microscopy Techniques used in Microbiology

Life scientists have long been trying to understand whether function determines form or function follows form. Regardless, direct observation of morphology can usually greatly promote the understanding of the function. An excellent example is the discovery of the three-dimensional structure of the DNA double helix, which created a revolution in biology and created whole new branches of genetic science and engineering.

Microbial research as an important life science branch has been important since the earliest microscopy studies to observe living cells in the late 17th century. Better understanding of function creates new questions to be answered in microbiology, which then require better imaging techniques that can reach to molecular and sub-molecular levels. Fluorescence microscopy can be combined with stains that target DNA or can be used to determine cellular viability, or fluorescent tags for proteins, thus extending the power of optical microscopy (1). Confocal microscopy, which improves the fluorescence microscope by exclusively collecting the fluorescence from the focus point, can be used to construct 3-D images of microbes or biological samples by scanning many continuous thin sections of the sample with the help of a computer. This technique has been quite useful for imaging microbial biofilm structures (2).

Based on the same theory as the optical microscope, transmission electron microscopy (TEM) and scanning electron microscopy (SEM) utilize electrons as the "light source" which have much shorter wavelengths, thus allowing for high resolution imaging at the nanoscale, since resolution is proportional to wavelength. However, the complex sample preparation, operation in vacuum and requirement of dried samples somewhat limit the application of TEM and SEM in microbiology. Cryo-TEM attempts to image "liquid samples" by freezing the sample rapidly to form an amorphous solid. This method produces detailed images of surface morphology and even internal structures, with careful application (3).

Based on an entirely different principle of operation, atomic force microscopy (AFM) derives topographic images by probing the surface with an ultrasharp tip, at the end of a cantilever. The subtle deformation of the cantilever is amplified and monitored by a laser lever collected by a photodetector. The piezo sensor is used to manipulate and record the AFM tip motion in three dimensions. AFM can image samples with nanometer resolution in the X-Y dimensions, with forces ranging from several picoNewtons to hundreds of nanoNewtons, a range that is well suited for imaging microbes without damage. A key advantage for microbiological studies is that the AFM can image samples

both in air and in liquid, enabling the observation of microbes in their natural environment. Another unique advantage of AFM is that it can be used to directly measure the interaction forces between bare or functionalized probes and the substrates, such as biomaterials, proteins or other cells, under conditions very similar to their real environments. In addition to gaining surface structure information, one can quantify the adhesion forces between microbes and uroepithelial cells, proteins, receptors, etc. as reviewed in Ref. (4).

Preparing Bacteria for AFM Imaging and Force Measurements

When microbes are imaged in air, immobilization of samples on substrata (usually glass slide, membrane filters or mica) can be spontaneously accomplished with adsorption of the microbes to the surface. An issue that must be addressed under this circumstance is how to wash the microbes properly to remove residue of the culture medium and products secreted by the microbes, all without damaging the native bacterial surfaces.

Examining bacteria under liquid solutions usually requires further steps in the preparation process due to the hydrophilicity of most microbes and the forces exerted on the cells during the AFM probing. Several techniques have been applied in this context.

One commonly used technique is to employ covalent bonding between bacterial cells and molecules attached to a glass slide. For several Gram-negative bacterial strains, the EDC/NHS zero-length cross-linking reaction has been applied to couple carboxylic groups on the bacterial surfaces with amino groups on 3-aminopropyl-trimethoxysilane treated glass slides (5-7). This covalent immobilization method has also been used for small biologically active molecules such as DNA, proteins and enzymes, etc. (8). However, for some microbes with fewer carboxylic groups or with strong hydrophilicity such as *Pseudomonas aeruginosa* PAO1, the covalent bonds may be not strong enough to withstand the hydrophilic forces between microbes and the liquid. A modification of this method is needed. In this study, we demonstrate how to reversibly apply the EDC/NHS zero-length cross-link reactions and successfully immobilize microbes that cannot be bonded through the original reaction scheme, broadening the application of this method.

A second commonly used methodology is to bond bacteria to a substrate based on electrostatic interactions. Poly-L-Lysine (PLL) and polyethylene imide (PEI) are agents frequently used to create a positively charged surface on glass (9, 10), mica (11, 12) or tapered fiber (13), in order to physically adsorb negatively charged microbes to the substrates. One study reported that gelatin solution was superior to PLL in immobilizing bacterial cells grown on Luria broth (LB) agar plates, in terms of the number of absorbed cells and the affinity

of immobilization (12). Due to non-specific interactions, electrostatic forces can be used to immobilize many cells or biomolecules at once. The strength of the physical bonding compared to the covalent attachment method has not been evaluated.

A third method we have evaluated is that of mechanically trapping bacterial cells. Most mechanical trap experiments are done via an isopore filter membrane, although one study immobilized bacteria in 40-45° molten agar. For example, yeast cells *Saccharomyces cerevisiae* were immobilized in agar for AFM imaging that would allow the observation of cell growth and division over a 6-7 hour period (14).

Kasas et. al. first reported the anchoring of round-shaped cells via filter membranes with comparable pore size with bacteria dimension (15). This simple method has been mostly applied to round bacteria i.e. Gram-positive cells such as *Lactococcus lactis* (16), *Staphylococcus aureus* (17) and *Streptococcus salivarius* (18), usually with an 0.8- μ m isopore polycarbonate (Millipore) filter membrane. However, trapping microbes by a filter membrane has not been successfully and widely applied to rod-shaped Gram-negative bacteria. An exception was the trapping of rod-shaped *Klebsiella terrigena* by a filter membrane (9). In the present study, we attempt to apply this method to more examples of rod-shaped Gram-negative bacteria and evaluate the effect of filtering on the morphology of the cells.

Methods and Materials

Bacteria Cultures and Harvesting

Three bacterial strains were used in this study. *Escherichia coli* HB101, a Gram-negative bacterium, was purchased from the American Type Culture Collection (ATCC 33694). It is a plasmid-free, non-fimbriated strain (19). *Pseudomonas aeruginosa* PAO1, a Gram-negative bacterium, was kindly provided by Professor Gerald Pier (Channing Laboratory, Department of Medicine, Brigham and Women's Hospital, Harvard Medical School, Boston, MA, USA). *Staphylococcus epidermidis*, a Gram-positive bacterium, was a gift from Professor Stephen Heard (Department of Anesthesiology, University of Massachusetts Medical School, Worcester, MA, USA). Bacterial cells were precultured in 30 g/L Tryptic Soy Broth (TSB) (Sigma, St. Louis, MO) at 37 °C overnight. Next, 0.5 ml bacteria solution from the preculture was added into ~30-50 ml fresh TSB and cultured in a water shaker bath at 37 °C. Bacterial growth was monitored by the absorbance at 600 nm using a spectrophotometer. Bacterial cells were harvested in the middle exponential phase, corresponding to absorbance measurements of 0.7-0.8 for *E. coli* HB101, 0.8-0.9 for *P.*

aeruginosa PAO1, and 0.5-0.6 for *S. epidermidis*. Cells were collected by centrifuging at 1400 g for 15 min (Fisher Scientific Model 225 Benchtop Centrifuge, Pittsburgh, PA, USA). Bacterial cells were washed three times with PBS buffer, unless otherwise specified, following a procedure described previously (20). In some cases, bacteria were not washed, so that the effect of not washing the cells on trapping and immobilization could be studied. Final bacterial concentrations were adjusted to 2×10^7 cells/ml in 0.1 M sodium phosphate (pH=7.1). Bacterial solutions were sonicated in an ultrasonic bath (40 KHz, 130 W) (Branson, Model 2510, USA) for ~5 min to break up any aggregates.

Immobilization Methods

(1) Covalent Bonding Immobilization

The covalent bonding reaction could be applied in two ways, depending on whether we wanted to target carboxylic groups or amine groups on the bacterial surfaces (Figure 1A-C).

To attach bacteria to substrates based on targeting the bacterial carboxyl groups, we followed a protocol developed previously (21), with some modifications (Figure 1A). The substrate could be glass or mica. Glass slides were acid cleaned before use, as described in (5) followed by 15 min sonication in ultrapure water, and rinsing with copious amounts of pure ethanol and analytical grade methanol (Fisher Scientific, Fair Lawn, NJ, USA), to remove all residual water from the glass slides. For mica substrates, Ruby red mica sheets (Electron Microscopy Science, Washington, PA, USA) were freshly cleaved immediately prior to use, but were not cleaned with any chemical agents.

Glass slides or mica sheets were immersed in 10-50 v/v% 3-aminopropyl-trimethoxysilane (Aldrich, Steinheim, Germany) in analytical grade methanol for 10-60 min. Slides were rinsed with excess methanol (>50 ml/slide) followed by ultrapure water (> 50ml/slide). After this step, amine groups have been attached to the glass or mica.

EDC (1-Ethyl-3-(3-dimethylaminopropyl) carbodiimide HCl) and Sulfo-NHS (N-Hydroxysulfosuccinimide) (Pierce, Rockford, IL, USA) were stored at -20°C in an airtight container to prevent contact with moisture. EDC and Sulfo-NHS were dissolved in 0.1 M sodium phosphate (pH=7.1) to form stock solutions with final concentrations at 0.5 M and 0.1 M, respectively, and stored at 4°C for short-term use (< 1 week).

EDC and Sulfo-NHS stock solutions were simultaneously added to bacterial solution (2×10^7 cells/ml), to reach final concentrations of 50 mM and

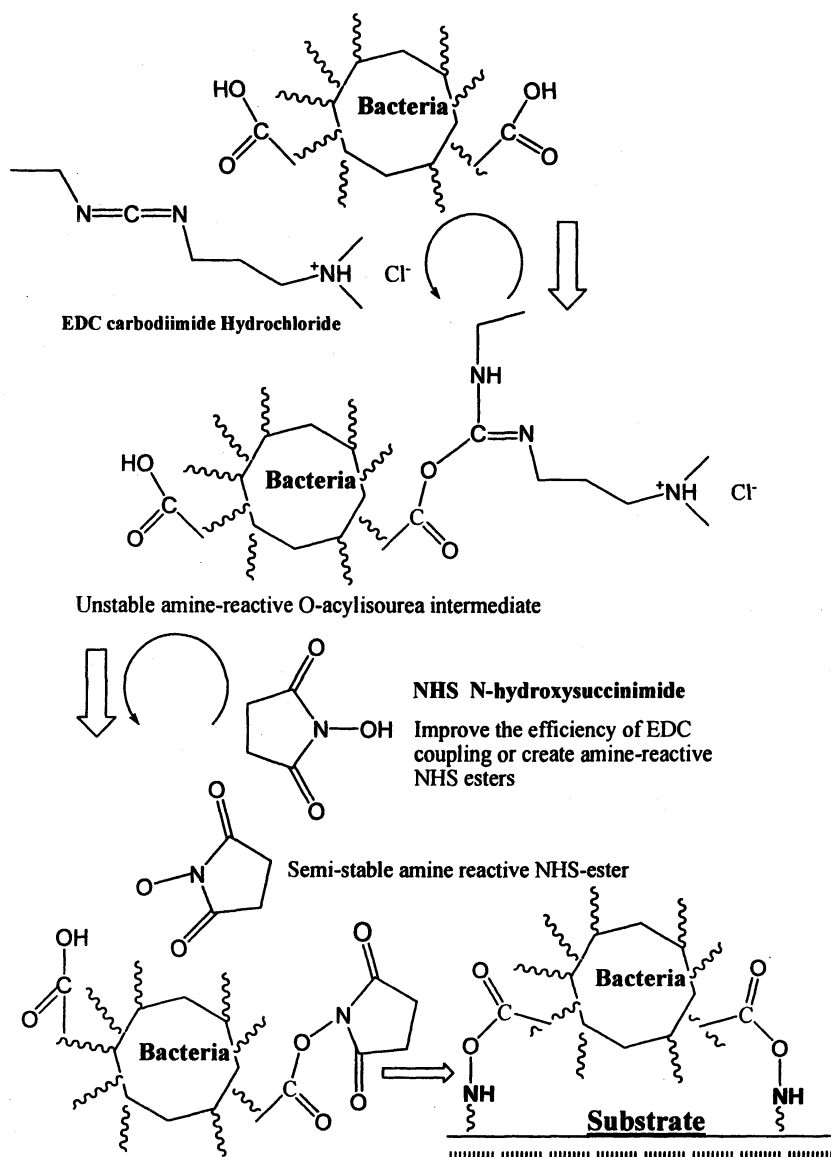


Figure 1A. Schematic of reaction used to immobilize bacterial cells via EDC/NHS covalent bonding, shown for $-\text{COOH}$ rich *E. coli* HB101 and *S. epidermidis* immobilized on glass slides treated with aminosilane.

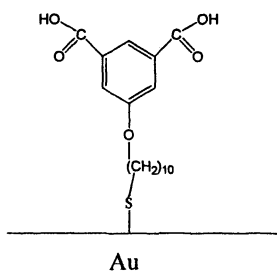


Figure 1B. Isophthalic acid attached to gold-coated glass slide to impart carboxyl functionality to surface

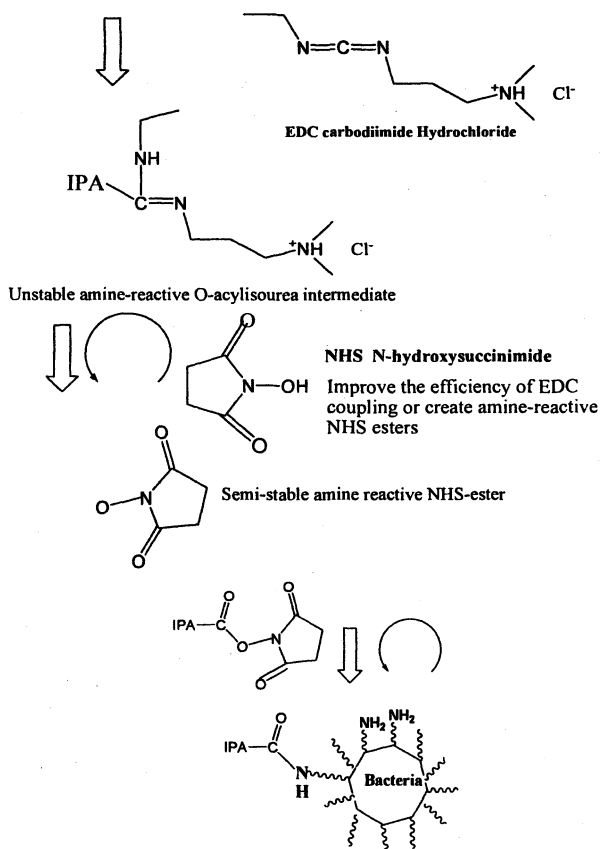


Figure 1C. Schematic of reaction to immobilize -NH_2 rich *Pseudomonas aeruginosa* PAO1 on EDC/NHS-treated IPA slide.

20 mM, respectively. The resulting solution was mixed on a rotator at ~70-125 rpm for 10-30 min. The solution was added to the prepared glass or mica substrates, followed by gentle shaking at ~125 rpm for 6-8 hours (21). During the entire reaction process, the system pH was around 7, since EDC, Sulfo-NHS and bacteria were all dissolved in 0.1 M sodium phosphate buffered solution. In order to bond bacteria covalently through a reaction that used the amine groups on their surfaces, the EDC/NHS procedure was again applied, but with using modified glass slides whose surfaces expressed carboxyl group functionalities (Figures 1B and 1C). Glass slides with gold coating were then prepared with an isophthalic acid compound, in order to aid in attachment of bacteria to these surfaces. The preparation and characterization of IPA slides was described previously (22). Briefly, commercially available gold-coated slides (Evaporated Metal Films; Ithaca, NY) were acid cleaned in piranha solution (70% sulfuric acid and 30% hydrogen peroxide) for 10 min, followed by ultrapure water rinse, ethanol rinse, and drying under nitrogen. Slides were immersed in 1 mM IPA ethanolic solution for 24 hours to form self-assembled monolayers (SAMs) on the substrates. A second ultrapure water/ethanol rinse and drying procedure was applied.

EDC and Sulfo-NHS solutions were added to the IPA-slides to form final concentrations of 100 mM and 40 mM, respectively, and agitated for 30 min at 125 rpm. Next, bacterial solution was added, followed by gentle shaking for >2 hours at 125 rpm, to allow the zero-length cross-link reactions to complete. Incubation times of 4-6 hours yielded the best immobilizations.

After applying either of these covalent immobilization procedures, slides were removed from solution and rinsed with ultrapure water to remove any loosely attached cells or other chemicals.

(2) Bacterial Immobilization through Electrostatic Forces

Poly-L-Lysine (PLL) (MW: 150,000-300,000) solution (0.1% w/v, in water) (Sigma, St. Louis, MO, USA) was used to create a positively charged surface on glass and mica. Glass slides and mica sheets were cleaned or cleaved, as described above. Then the slides were coated with PLL solution in a covered petri dish. When the slides were dry, a thin film of bacteria solution was deposited on top of the PLL-treated glass or mica. After 30-40 min, the slides were gently rinsed with ultrapure water.

During each of these immobilization processes, bacterial cells remained hydrated, even while briefly exposed to air. Bacteria can retain their residual moisture for several hours, as has been demonstrated through contact angle experiments (20).

(3) Mechanical Immobilization

Based on the size of *E. coli* HB101 and *P. aeruginosa* PAO1 cells, 0.22 and 0.6- μm isopore polycarbonate filter membranes were used for the mechanical trapping experiments (Millipore Corp., Billerica, MA, USA). In order to form a bacterial monolayer on the filter membrane, 100 μl bacteria solution (2×10^7 cells/ml) was diluted into 1-3 ml solution and was captured onto the filter at times ranging from 10 sec to 1 min, using a vacuum filtration pump. The membranes were attached to glass slides using double-sided tape.

AFM Imaging

All AFM images were acquired in ultrapure water at room temperature. AFM (Digital Instruments Dimension 3100 with Nanoscope IIIa controller) was operated in tapping mode unless specified. Rectangular silicon cantilevers (NSC36/AIBS, cantilever type C) (MikroMasch, Wilsonville, OR, USA) with a nominal tip curvature <10 nm and a nominal spring constant of 0.6 N/m were employed. The optical microscope was used to roughly select an area to engage the AFM tip. Images were acquired at a scan rate of 1.0 Hz, with 512 samples/line.

Atomic Force Microscopy Force Profiles

As a further way to characterize how the immobilization technique affected the bacterial surface and interfacial properties, AFM force profiles were obtained for some samples. After immobilization via covalent bonding or the electrostatic forces method, individual *E. coli* HB101 bacterial cells were probed by triangular AFM Si_3N_4 tip (DNPS, Digital Instruments). These tips have an average spring constant of 0.06 ± 0.03 N/m, calibrated according to the method of Cleveland et al (23, 24). Data from the approach and retraction portions of the AFM profiles was analyzed as described (6). Briefly, a steric model was employed to analyze approach profiles and characterize the surface polymers on the bacterial cell (25, 26). Two parameters can be generated from application of the steric model, the equilibrium length which corresponds to the outer membrane polymer and protein extension distance from the cell surface, and the density of outer membrane polymers and proteins. The adhesion forces were collected from the retraction data and statistical analyses and histograms were used to compile and compare the data. At least 5 bacterial cells were probed for force measurements under each condition and at least 8 force curves per cell were recorded.

Results and Discussion

For the chemical bonding and electrostatic immobilization of bacteria, the protocols were tested on all three bacterial strains. Mechanical trapping was not performed for *S. epidermidis*, since that technique is already well established for round-shaped Gram-positive bacteria and yeasts, but our aim was to extend its application to Gram-negative bacteria.

Covalent Bonding EDC/NHS Protocol

When the bacterial cells have enough carboxylic terminal groups, the EDC/NHS reaction can be used to attach bacteria, forming semi-stable amine reactive NHS-esters, followed by conjugation with the amine terminals on the substrate via firm amide bonds. This strategy worked well for *E. coli* HB101 (Figure 2A), *S. epidermidis* (Figure 2B), and has been successful in the past with other bacterial strains (5, 6, 21). However, if the carboxylic terminals are inadequate, this reaction does not work well, as we observed for *P. aeruginosa* PAO1 (no images could be obtained since the cells were not attached to the slides). Since PAO1 has many proteins present on its surface (27, 28), we instead chose to target the bacterial amine terminal groups, bonding them with carboxyl groups formed on IPA-coated slides. Thus, the reverse form of the EDC/NHS immobilization method (Figure 1C) was successfully applied for *P. aeruginosa* (Figure 2C). The advantage of using the IPA SAM is that a high density of carboxyl groups can be created, with all of the terminal molecules already in the correct orientation to be able to react with the bacterial amine groups.

In some previous studies using the EDC/NHS reaction, there was concern that the molecules to be immobilized would be altered through the reaction process. For example, Vermette and Meagher studied the impact of concentration of EDC/NHS on the coupling of poly(acrylic acid) (PAAC) onto thin films of n-heptylamine (8). Since PAAC contains many carboxylic groups in different orientations, the thickness of the films measured differed depending on the ratio and concentration of EDC/NHS used. With higher concentrations, more PAAC could bind to the films. The results show that the EDC/NHS reaction can yield different efficiencies under varying conditions. On the other hand, there are important differences to consider between how this set of reactions was applied and the way we apply it for bacterial bonding. The bacterial binding to glass occurs on the underside of the bacteria, while the AFM can only probe the top of the cell surfaces. The remaining functional groups on the bacterial surface that did not participate in the EDC/NHS reaction will rapidly revert to their original carboxylate form if they cannot contact the

amine groups on the substrate, because the intermediate compounds are too unstable to remain in this state (both the O-acylisourea intermediate and the semi-stable amine-reactive NHS-ester). Thus, the exposed surfaces of the immobilized bacterial cells retain their intact biological activity. The same logic is true for the reverse application of the EDC/NHS reaction, because the same unstable intermediates also form. The hydrolysis rate constant is only 2-3 sec⁻¹ for the active ester at pH 4.7 (29). The rate constant should be fairly stable since the reaction activity does not differ significantly when pH is increased to 7.5.

The application of similar bonding methods has shown that the chemicals used for the EDC/NHS reaction do not alter biological activities (30, 31). Wissink et al. compared the effects of different crosslinking agents such as formaldehyde, glutaraldehyde and EDC/NHS on endothelial cell seeding. The first two agents can cause cytotoxic reactions, while EDC/NHS does not have such side effects. Furthermore, the EDC/NHS linking method significantly increased the proliferation of seeded endothelial cells without causing morphological changes or other abnormal biological activities (30).

Our results show that the covalent bonding procedure works well for Gram-negative and Gram-positive bacteria. It is simple to construct substrates that have desired functional groups, with either carboxyl or amine-group terminations. When applying this reaction scheme to different strains of bacteria, the method can be applied in one of two ways, depending on whether carboxyl groups or amine groups dominate the bacterial surface. The only drawback of this method is that the bacterial cells can sometimes become aggregated due to the exposure to EDC and NHS. Therefore, it may be difficult to discern individual bacterial cells if sonication is not applied (discussed below).

Immobilization on Glass and Mica via Electrostatic Interactions

The chemical PLL was used to help bacteria attach to glass and mica. This method is practically universal, and worked well for *E. coli*, *S. epidermidis*, and *P. aeruginosa* (Figures 3A-C).

Glass slides and mica are the most commonly used substrates for microbe immobilization. Mica sheets are easier to prepare than glass slides, but for whole cell imaging or force measurements, there are no great differences between the two substrates. Due to the smoothness of mica, it can provide a better background when imaging fine structures such as the EPS and LPS associated with *P. aeruginosa* PAO1 (Figure 4). Although both Figure 3C and Figure 4 show strain PAO1 immobilized using the PLL method under identical conditions, the differences in the underlying substrate's smoothness do affect the resolution of the features on the bacteria that can be observed. Fine

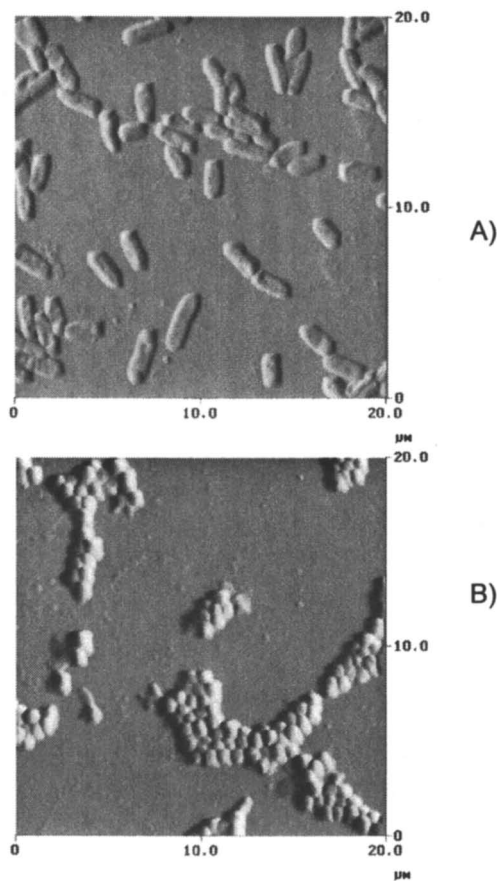


Figure 2. Examples of bacterial immobilization using the covalent bonding (EDC/NHS) reaction pathway. A) *E. coli* HB101 immobilized on glass slide using method shown in Figure 1A, where bacterial carboxyl groups are coupled with amine groups from an aminosilane compound; B) *S. epidermidis* immobilized on glass slide using same method as in 2A; C) *P. aeruginosa* PAO1 immobilized on glass slide that was treated with IPA to impart carboxyl functionality, for coupling with bacterial amine groups using method described in Figure 1C. All images in ultrapure water. Continued on next page.

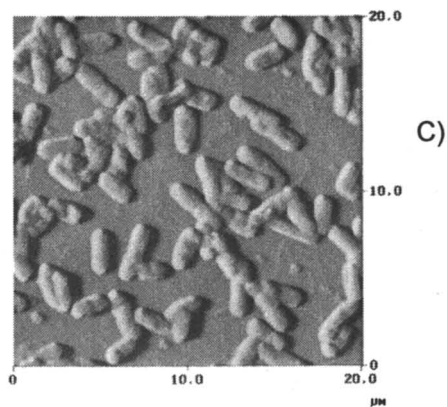


Figure 2. Continued.

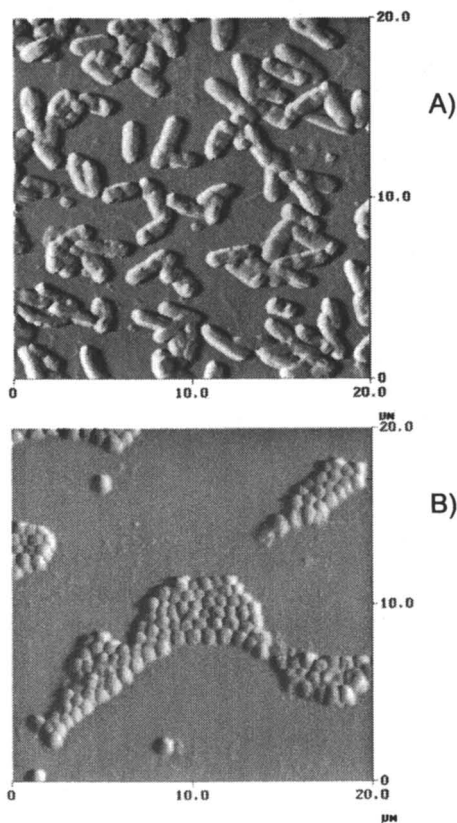


Figure 3. Bacteria immobilized on PLL-coated glass slides.
 A) *E. coli* HB101; B) *S. epidermidis*; C) *P. aeruginosa* PAO1
 All images acquired in ultrapure water. Continued on next page.

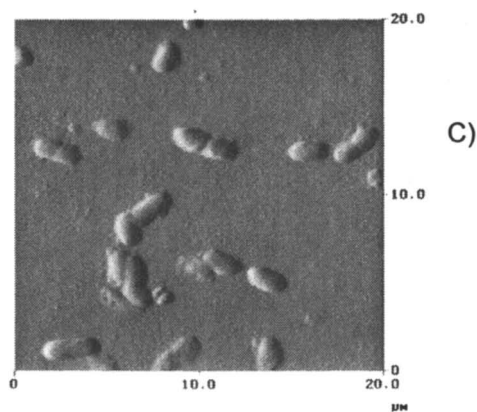


Figure 3. Continued.

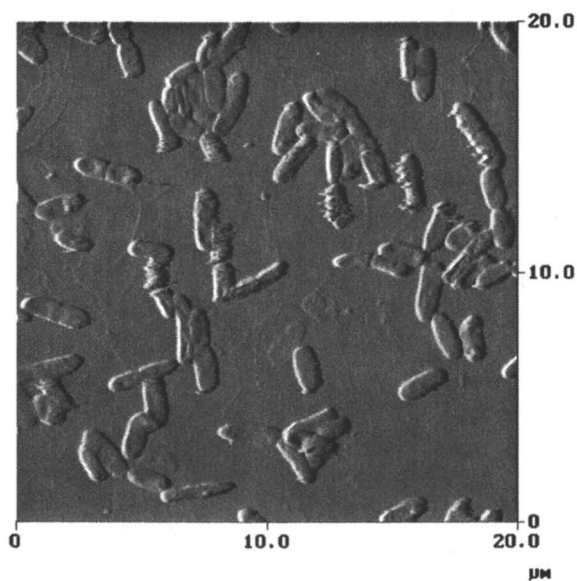


Figure 4. P. aeruginosa PAO1 immobilized on mica slide via PLL method, imaged in ultrapure water. (In comparison with Figure 3C, fine LPS structures can be appreciated on mica slide.)

molecules on the bacterial surface, which may include flagella, lipopolysaccharides, and polysaccharides, can be better appreciated for the bacteria attached to mica.

The drawback of using mica is that the sheet is thin and provides poor mechanical strength, sometimes deteriorating the image quality. To avoid this, multiple layers of mica sheet are preferred.

Breakup of Bacterial Aggregates through Sonication

A potential complication of using chemicals to aid in bacterial bonding is that after treatment with PLL or EDC/NHS, the bacterial cells may become sticky and aggregate. Therefore, we have incorporated sonication into our methodology, to help break up bacterial aggregates. For example, all of the images shown in Figures 2 and 3 were of sonicated bacteria. When this step was not performed, bacteria were always in aggregates. This was true regardless of whether glass or mica was the substrate, and for either the EDC/NHS or PLL immobilization techniques. Examples are shown of cells that were not sonicated, for *E. coli* HB101 (Figure 5A) and *P. aeruginosa* PAO1 (Figure 5B). By comparison with Figure 2A and 3C for *E. coli* HB101 and *P. aeruginosa* PAO1, respectively, it is clear that sonicating the cells for 5 min improved the clarity of the images that could be obtained by decreasing aggregation.

Gram-positive bacteria behave differently and always tend to aggregate. Sonication was not able to break up the aggregates of *S. epidermidis* (Figures 2B and 3B), and images of cells that were not sonicated were identical to the sonicated ones (images not shown).

Sonication appears to provide a benefit for the imaging of bacterial morphology for Gram-negative bacteria. Previous studies have shown that the duration and dose of sonication used in this study disperses bacterial aggregates without affecting bacterial viability or morphology (20).

Effect of Bacterial Cell Washing on Immobilization

In previous work, we showed that proper washing steps are necessary to reveal the bacterial surface's true morphology (20). This is especially important for physicochemical characterizations of bacterial surfaces, such as measuring the contact angles to determine the surface energies, or probing with AFM. Crystallization of materials from the culture medium and residue of molecules secreted during bacterial growth can easily mask the true cell surface. Washing cells has not been considered necessary for investigations of bacteria in liquids since it was assumed that the soluble molecules from the culture medium would be dissolved in liquid and hence unable to cover the bacterial surface. However, the materials produced by the bacteria, such as extracellular polymeric

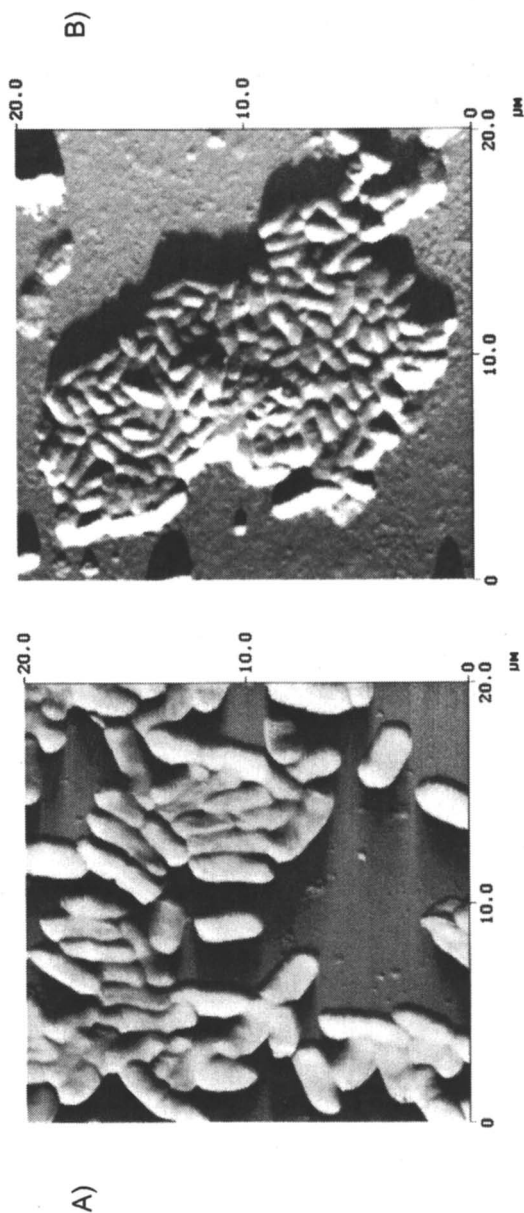


Figure 5. Representative examples of bacterial cells that were not sonicated in solution to break up aggregates. A) *E. coli* HB101 immobilized on glass slide via EDC/NHS; B) *P. aeruginosa* PAOI immobilized on glass via electrostatic forces (PLL). All images obtained in ultrapure water.

substances (EPS) or ornithine-derived lipids produced by *P. aeruginosa* PAO1 under growth in rich medium (32), remain on the bacterial surface, especially adsorbing to surface appendages such as LPS, flagella, fimbriae, and polysaccharides. After introducing the immobilization agents such as EDC/NHS or PPL, these materials can cover the bacterial surfaces (Figures 6A and 6B). Excess EPS can interact with the AFM probe, which was especially problematic using PLL immobilization method. Figure 6B represents a poor image with many scan lines due to EPS remaining on the *P. aeruginosa* PAO1 cell surfaces. These types of artifacts were not observed when the cells were washed (i.e. Figures 2C and 3C), following a protocol discussed previously (20).

Immobilization Strength and Duration

Generally, a researcher must spend several hours or longer to image bacteria or obtain force measurements with AFM. Therefore, the duration that the immobilization reaction endures must be investigated. Either form of the EDC/NHS reaction provides stable bacterial immobilization for at least five hours, without notable bacteria dissociation from the slides. However, immobilization via PLL started to break down after two hours, as shown for *E. coli* HB101, although similar results were obtained with all bacteria investigated (Figure 7). Due to the weak nature of non-specific interactions (electrostatic forces) compared to covalent bonds, and the water solubility of PLL, this chemical was not able to immobilize bacteria for as long as the covalent bonding methods.

Optimal Immobilization Conditions

In some studies, a greater density of bacteria must be immobilized onto the substrates. For example, bonding of bacteria to a specific receptor can be investigated if the receptor is coated to an AFM tip. Modified tips may not provide very sharp images or may become altered by repeated scanning, so for certain types of studies, it is preferable to have a complete lawn of bacteria, ensuring that the tip will probe bacteria regardless of the location the tip makes contact with the surface. We discuss a few potential approaches to help increase the immobilization.

(1) Increase the Dose of EDC/NHS and of the Aminosilane Compound

Excess EDC or NHS does not boost the immobilization efficiency, since the amounts typically used are ten-fold molar excess over the amount of the target

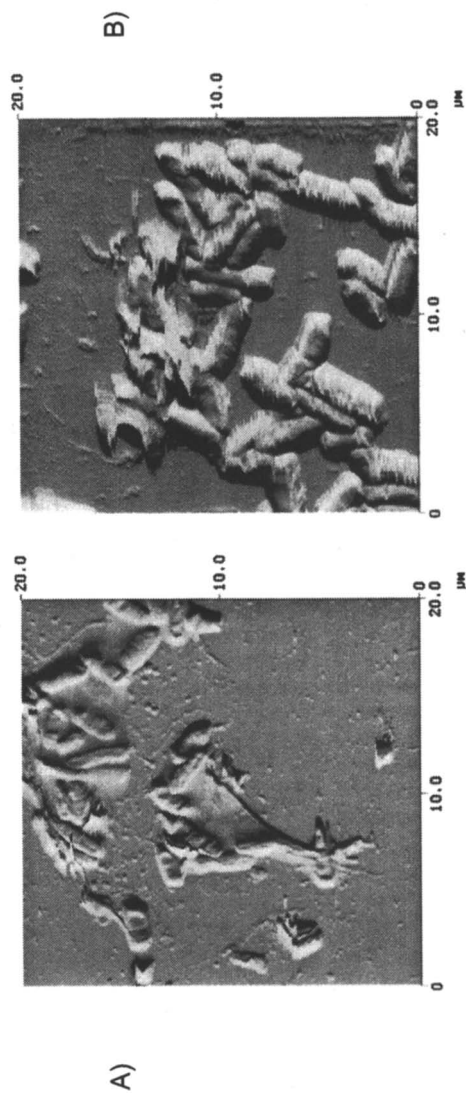


Figure 6. *Necessity of washing bacterial cells, even for AFM investigations in liquids. Some representative examples are shown of bacteria that were not washed. A) P. aeruginosa PAO1 immobilized on IPA-coated glass slide via EDC/NHS, without washing; B) P. aeruginosa PAO1 immobilized on PLL-coated glass slide, without washing. All images obtained in ultrapure water.*

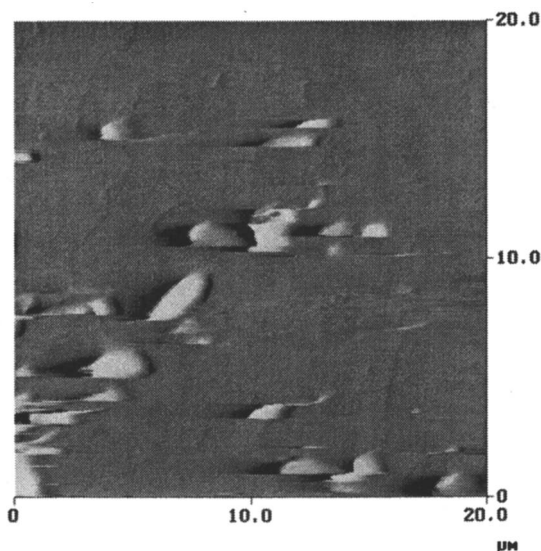


Figure 7. E. coli HB101 immobilized on glass slide via PLL method, imaged for two hours. After the two hour period, weakly immobilized bacterial cells could be displaced by the friction forces of the AFM cantilever. All images obtained in ultrapure water.

molecules such as proteins present (29). This amount should already be sufficient to react with the carboxylic functional groups on the bacterial surface.

Therefore, the controlling step is the limitation in the number of equivalent amine groups on the substrate. We found that both using a higher silane concentration and leaving the aminosilane in contact with the slide for longer can help, but using a higher concentration had a more substantial effect. Sometimes, leaving the aminosilane solution on the glass slide for too long led to drying and crystallization of the molecules, which obscured the substrate in later images. After several optimization experiments, we found that concentrations ≤ 50 v/v % aminosilane solution for one hour contact time was optimal.

(2) Lowering EDC/NHS Reaction System pH

The optimal reaction pH range for the EDC/NHS reaction is between 4.7 and 6, but research has suggested that the carbodiimide reaction remains effective up to pH 7.5 without significant loss of yield (29). Lowering the pH may not be possible when taking into account the integrity of the bacteria. Also, care must be taken to ensure that components in the buffer system do not

interfere with the reaction. Previous research determined that 0.1 M MES [2-(N-morpholino) ethane sulfonic acid] can be used at low pH (pH 4.7-6.0) and 0.1 M phosphate buffer is suitable for neutral pH reactions (pH 7.3) (29). Therefore, no pH adjustments are needed during the course of reactions.

(3) Combination of EDC/NHS and PLL Methods

The immobilization methods of covalent bonding combined with electrostatic forces were applied simultaneously, to create a surface completely covered with bacteria, as demonstrated for *E. coli* HB101 on mica (Figure 8; note that similar results can be obtained on glass). The procedures used were the same as described above when the reactions were treated individually, with 50 v/v % aminosilane solution and a 1 hour incubation time. Although the mica surface was fully covered by *E. coli* HB101, we expect this surface to remain stable for only 2-3 hours due to the solubility of PLL and its relatively weaker ability to adhere bacteria to the substrate.

Another possibility we tested was to increase the bacterial concentration. This did not improve the number of cells attaching to any appreciable degree, because the limiting step in this reaction is the relatively weaker attractive forces between the bacterial cells and the substrate. Simply increasing the bacterial concentration did not attract more cells to the substrate because the bacterial concentration was already high enough that availability of attachment sites was not the concern.

Mechanical Immobilization

Bacteria immobilized by mechanical trapping in a filter were the final group investigated. To mechanically trap bacterial cells into a pore, the pore size should be slightly smaller than the bacterial dimension. This method is usually limited to round-shaped bacteria (15-18). The pore size selection for rod-shaped bacteria should be based on the bacterial width. Figure 9 represents an attempt to trap *E. coli* HB101 with a 0.22- μm filter membrane, but no cells could be found even after examining multiple areas of the filter surface. While the average pore size should be 0.22 μm , in some areas, several pores merged together to form openings much larger than the average size, even reaching a size of 1.2 μm (near center of Figure 9). The width of this bacterium was previously shown to be $0.5 \pm 0.2 \mu\text{m}$ (20). Filters were examined in both right side up and upside down orientations, and failed to display any bacterial cells.

The 0.6- μm filter membrane was found to be capable of trapping *E. coli* (Figure 10), but this was possible only through several trials. We could not consistently and easily trap rod-shaped Gram-negative bacteria in any of the

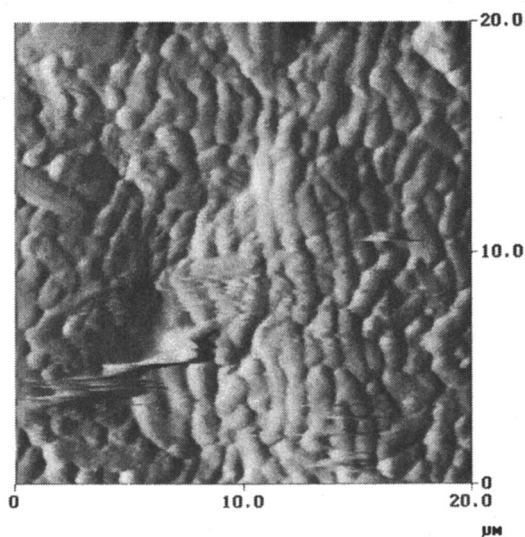


Figure 8. E. coli HB101 immobilized on mica via both EDC/NHS reactions and PLL method applied simultaneously, imaged under ultrapure water.

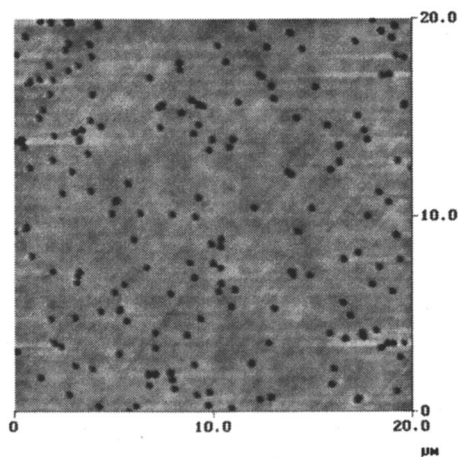


Figure 9. Isopore polycarbonate membrane filter (pore size of 0.22 μm), where we had attempted to immobilize E. coli HB101, imaged in ultrapure water.

filter membranes tested. For spherical Gram-positive bacterial cells, filter trapping may be a suitable method of immobilization. However, besides the experimental difficulties, there may be other reasons why mechanical trapping is not well-suited for rod shaped bacteria. Trapping of rod-shaped cells exposes only the ends for AFM investigation, while the middle part of the cells can have different physical and mechanical properties. It is generally the “center” of rod-shaped bacteria that are probed with AFM, since previous research has shown that artifacts could be caused by measuring force profiles of *E. coli* K12 strains at the edges of the cells (33). Further, the charge properties of *E. coli* K12 strains were found to be different at the ends compared to the center (34). Using differential electrophoresis, Jones et al. showed that polystyrene preferentially adhered to the tips of *E. coli* compared to the middle portion, with the authors proposing the existence of nanodomains on the *E. coli* tips that could cause different charge properties.

Role of Immobilization Method on AFM Force Profiles

As a more quantitative method of comparing how the different immobilization methods affected bacterial properties, we captured force profiles on the bacteria and analyzed the approach and retraction portions of these cycles. Since only a few *E. coli* HB101 cells could be mechanically trapped with our protocol, we could not make force measurements for this condition.

The analysis of force profiles from the AFM data demonstrated that quite different force profiles were obtained depending on whether *E. coli* were immobilized by covalent bonding or through electrostatic forces (Figure 11). Figures 11A and B show the distributions of pull-off distances and adhesion forces acquired from the summation of all retraction curves. The PLL-immobilized cells had longer pull-off distances and greater adhesion forces with the bare Si_3N_4 tip compared to the EDC/NHS immobilized cells.

The application of the steric model to the approach curve data also demonstrated differences for the two methods. With the EDC/NHS method, the average equilibrium polymer length was 32 ± 10 nm and the average polymer density was $(5.27 \pm 1.62) \times 10^{16} \text{ m}^{-2}$. With the PLL method of immobilization, the equilibrium length extended to 169 ± 47 nm and the polymer density decreased to $(1.32 \pm 0.26) \times 10^{16} \text{ m}^{-2}$.

We believe the changes are caused by PLL adsorbing also to the top of the bacterial cells and altering some of their chemical structures. So when we probed the PLL-immobilized bacteria, we may have also collected small amounts of PLL on the AFM tip, leading to higher adhesion forces and longer pull-off distances. The presence of PLL could also have accounted for the longer equilibrium lengths we predicted based on the steric model. These results show that even for washed bacteria, some PLL can remain on top of the

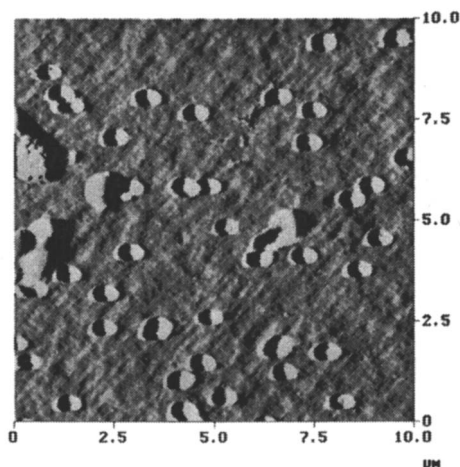


Figure 10. Isopore polycarbonate membrane filter (pore size of $0.60\ \mu\text{m}$), a few *E. coli* HB101 cells have been immobilized. Image obtained in ultrapure water.

bacterial cells and can produce artifacts in the observed profiles. Although the PLL is water soluble, it appears that some residual PLL may remain on the bacterial surface when the force measurements are obtained. The force profiles for either condition are equally reproducible, so that may indicate that the small amount of PLL that does remain on the bacterial cells is difficult to remove and will always be present when prepared in the same way.

Vadillo-Rodriguez et al. were the first to note that bacteria immobilized by physical adsorption (using poly(ethylene)imide) produced different AFM force profiles than bacteria mechanically trapped in a filter, using *Klebsiella terrigena* as the test organism (9). The authors did not compare these force profiles with that of bacteria covalently bound to a substrate.

Conclusions

Three commonly used microbial immobilization methods were introduced and compared. The zero-length cross-link technique was broadened to utilize the amine groups present on bacterial surfaces instead of carboxylic groups, extending the number of bacterial strains that can be immobilized. Due to the instability of the intermediates during the carbodiimide reaction, the intermediates on the surface of the cells which do not contact with the substrate will revert back to the original carboxylic groups or amine groups after undergoing a swift hydrolysis reaction.

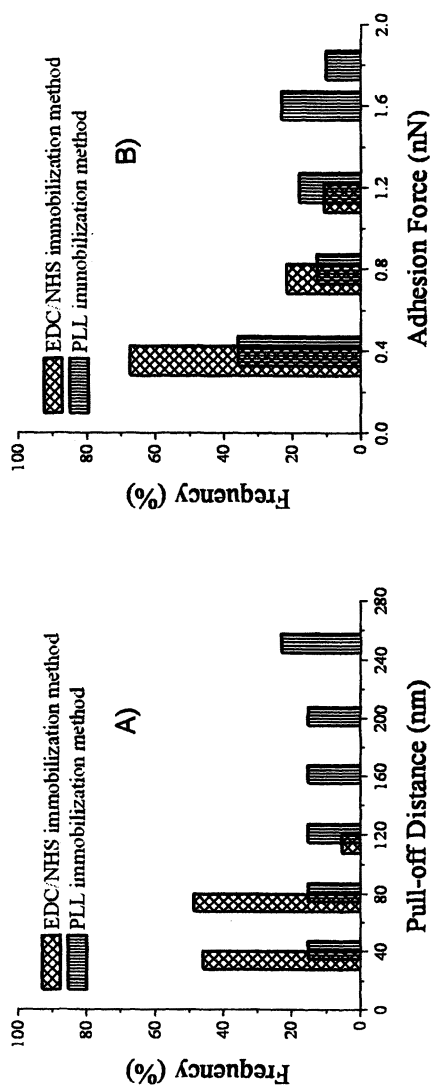


Figure 11. Force measurements data analysis and comparison between covalent bonding method and electrostatic forces method based on E. coli HB101 A) Histogram of pull-off distances distribution; B) Histogram of adhesion forces distribution.

Overall, the covalent bonding method can provide highly efficient immobilization with minimal alteration to the bacterial cell surfaces. This method appears to be well-suited to immobilizing a range of types of bacterial cells for AFM imaging and force measurements in liquid.

References

1. Bouvier, T. and P.A. del Giorgio. *FEMS Microbiology Ecology* **2003**, *44*, 3.
2. Yang, Y.; P.K. Sreenivasan; R. Subramanyam, and D. Cummins. *Applied and Environmental Microbiology* **2006**, *72*, 6734.
3. Beveridge, T.J. *Molecular Microbiology* **2006**, *62*, 1.
4. Dufre ne, Y.F. *Future Microbiology* **2006**, *1*, 387.
5. Abu-Lail, N.I. and T.A. Camesano. *Biomacromolecules* **2003**, *4*, 1000.
6. Liu, Y.;M.A. Black; L. Caron, and T.A. Camesano. *Biotechnol Bioeng* **2006**, *93*, 297.
7. Camesano, T.A.; M.J. Natan, and B.E. Logan. *Langmuir* **2000**, *16*, 4563.
8. Vermette, P. and L. Meagher. *Langmuir* **2002**, *18*, 10137.
9. Vadillo-Rodriguez, V.; H.J. Busscher;W. Norde; J. De Vries; R.J. Dijkstra;I. Stokroos, and H.C. Van Der Mei. *Appl Environ Microbiol* **2004**, *70*, 5441.
10. Velegol, S.B. and B.E. Logan. *Langmuir* **2002**, *18*, 5256.
11. Bolshakova, A.V.; O.I. Kiselyova; A.S. Filonov; O.Y. Frolova; Y.L. Lyubchenko, and I.V. Yaminsky. *Ultramicroscopy* **2001**, *86*, 121.
12. Doktycz, M.J.; C.J. Sullivan; P.R. Hoyt;D.A. Pelletier; S. Wu, and D.P. Allison. *Ultramicroscopy* **2003**, *97*, 209.
13. Maraldo, D.; P.M. Shankar, and R. Mutharasan. *Biosensors & Bioelectronics* **2006**, *21*, 1339.
14. Gad, M. and A. Ikai. *Biophysical Journal* **1995**, *69*, 2226.
15. Kasas, S. and A. Ikai. *Biophysical Journal* **1995**, *68*, 1678.
16. Boonaert, C.J.P.; V. Toniazzo; C. Mustin; Y.F. Dufrene, and P.G. Rouxhet. *Colloids and Surfaces, B: Biointerfaces* **2002**, *23*, 201.
17. Touhami, A.; M.H. Jericho, and T.J. Beveridge. *J Bacteriol* **2004**, *186*, 3286.
18. Van der Mei, H.C.; H.J. Busscher; R. Bos; J. De Vries; C.J.P. Boonaert, and Y.F. Dufrene. *Biophysical Journal* **2000**, *78*, 2668.
19. Goodacre, R.B., Roger C. W.; Beringer, John E. *Journal of Analytical and Applied Pyrolysis* **1991**, *22*, 19.
20. Gallardo-Moreno, A.M.; Y. Liu; M.L. Gonz lez-Mart n, and T.A. Camesano. *Journal of Scanning Probe Microscopy* **2006**, *1*, 63.
21. Camesano, T.A. and B.E. Logan. *Environmental Science and Technology* **2000**, *34*, 3354.

22. Emerson, R.J.; T.S. Bergstrom; Y. Liu; E.R. Soto; C.A. Brown; W.G. McGimpsey, and T.A. Camesano. *Langmuir* **2006**, *22*, 11311
23. Cleveland, J.P.; S. Manne; D. Bocek, and P.K. Hansma. *Review of Scientific Instruments* **1993**, *64*, 403.
24. Emerson, R.J. and T.A. Camesano. *Ultramicroscopy* **2006**, *106*, 413.
25. Butt, H.-J.; Kappl, M.; Mueller, H., and Raiteri, R. *Langmuir* **1999**, *15*, 2559.
26. de Gennes, P.G. *Advances in Colloid and Interface Science* **1987**, *27*, 189.
27. Doyle, T.B.; A.C. Hawkins, and L.L. McCarter. *Journal of Bacteriology* **2004**, *186*, 6341.
28. Zaidi, T.S.; G.P. Priebe, and G.B. Pier. *Infection and Immunity* **2006**, *74*, 975.
29. Hermanson, G.T., *Bioconjugate Techniques*. Academic Press: San Francisco, CA, 1996.
30. Wissink, M.J.B.; M.J.A. Van Luyn; R. Beernink; F. Dijk; A.A. Poot; G.H.M. Engbers; T. Beugeling; W.G. Van Aken, and J. Feijen. *Thrombosis and Haemostasis* **2000**, *84*, 325.
31. Lee, J.M.; H.H.L. Edwards; C.A. Pereira, and S.I. Samii. *Journal of Materials Science: Materials in Medicine* **1996**, *7*, 531.
32. Lewenza, S.; R.K. Falsafi; G. Winsor; W.J. Gooderham; J.B. McPhee; F.S.L. Brinkman, and R.E.W. Hancock. *Genome Research* **2005**, *15*, 583.
33. Velegol, S.B. and B.E. Logan. *Langmuir* **2002**, *18*, 5256.
34. Jones, J.F.; J.D. Feick; D. Imoudu; N. Chukwumah; M. Vigeant, and D. Velegol. *Applied and Environmental Microbiology* **2003**, *69*, 6515.

Chapter 11

Binding Forces Associated with *Staphylococcus aureus* Biofilms on Medical Implants

Ruchirej Yongsunthon¹, Vance G. Fowler, Jr.,²
and Steven K. Lower¹

¹The Ohio State University, 125 South Oval Mall, 275 Mendenhall
Laboratory, Columbus, OH 43210

²Duke University Medical Center, Box 3824, Durham, NC 27710

Staphylococcus aureus is one of the most frequently isolated bacteria from infected medical implants. *S. aureus* has the capacity to adhere to the surface of an implant where it forms a biofilm. We used atomic force microscopy to probe binding forces between a fibronectin-coated tip and isolates of *S. aureus*, which were obtained from either patients with infected prostheses or healthy humans. A unique force-signature was observed for binding events between the tip and the cells. There is a statistically significant difference in the binding force-signature observed for *S. aureus* isolated from the infected vs. healthy populations. This observation suggests a fundamental correlation between nanometer scale binding forces and the clinical outcome of patients with implanted medical devices.

Introduction

Surgical implants significantly improve the quality of life for many humans but also place these same patients at risk for life-threatening infections by bacteria (1). *Staphylococcus aureus* is the most frequently isolated microorganisms from such devices (1, 2). Mortality attributable to such *S. aureus* infections can be as high as 60% (3, 4).

S. aureus colonize the surface of an implant by forming bonds with host ligands, such as fibronectin (Fn), which commonly coat a prosthetic device (5, 6). This type of bond is mediated by MSCRAMMs (microbial surface components that recognize adhesive matrix molecules) located on the cell wall of *S. aureus* (5, 7-12). A predominant MSCRAMM on *S. aureus* is the fibronectin-binding protein (FnBP). Figure 1 illustrates the structures of Fn and FnBP, and highlights the several binding sites along each protein.

We and others have used atomic force microscopy (AFM) or optical tweezers to probe the fundamental binding forces associated with type-strains or laboratory-derived strains of *S. aureus* (e.g., 13-16). These previous studies have been very useful, but they do not explore the binding mechanisms of the strains of *S. aureus* that actually cause complications in humans or "real world" clinical settings.

Therefore, we have used AFM to measure binding forces between a simulated prosthetic device and several clinical isolates of *S. aureus*, which were obtained from either patients with an infected device or healthy subjects. These data suggest an intriguing correlation between the nanometer-scale forces at the bacterium-material interface and the clinical outcome of patients with implanted medical devices. This chapter provides a concise description of this work. An extended version of this study can be found in Yongsunthon et al. (17).

Methods and Materials

Collection of *S. aureus* Isolates and Growth of Cells for AFM Experiments

Invasive isolates of *S. aureus* were collected at Duke University Medical Center from the bloodstream of patients with a confirmed infection of a prosthesis. The control isolates came from the anterior nares of healthy subjects. All isolates were obtained from individuals in the same geographic area to account for strain variation.

Growth cultures were started from cryogenically preserved samples. Each isolate was cultured to exponential stage at 37 °C in tryptic soy broth containing 0.25% dextrose (18). Approximately 1 mL of cell suspension was washed three

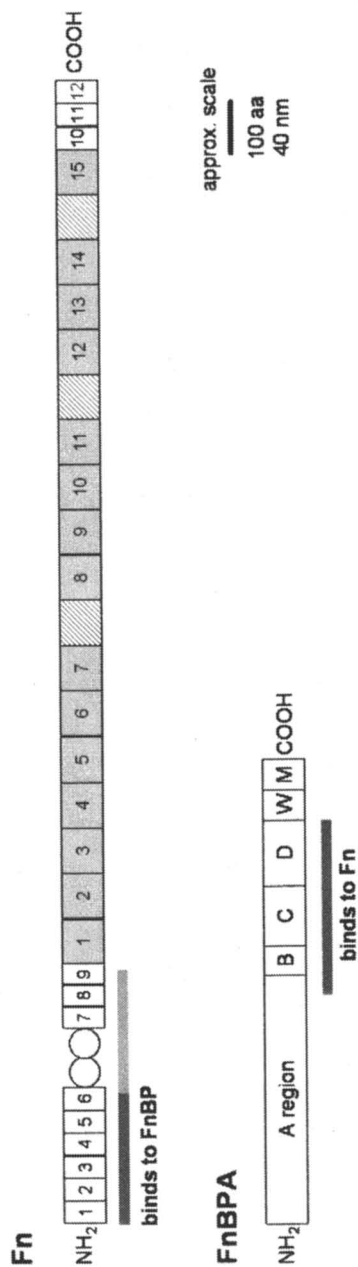


*Figure 1. (Top) Structure of fibronectin (Fn), which is a human protein that commonly coats the surface of implanted devices. Fn is mainly composed of three domains FnI (white boxes; 45 amino acids, aa), FnII (circles; 60 aa), and FnIII (gray boxes; 90 aa). (Bottom) Structure of fibronectin binding protein A (FnBPA), which is exposed on the outer cell wall of *S. aureus*.*

times in saline solution, dropped onto a glass cover slip, and allowed to sit without drying for 5 min. Loose cells were rinsed off with phosphate buffered saline (PBS; 0.01 M with 0.85% NaCl, pH 7.2), which was also the solution used in AFM experiments. It is worth mentioning that the glass cover slips were used as supplied by the manufacturer (Corning, Inc.). We found that the bacteria did not adhere very well to clean cover slips, presumably because the cleaning process removed the manufacturer's proprietary coating.

AFM Force Measurements

Force measurements were conducted with a Bioscope AFM (Veeco) mounted on an Axiovert 200M inverted optical microscope (Zeiss). The AFM's z-piezoelectric scanner was calibrated with two NIST certified calibration gratings. The tips used in these experiments were coated with Fn using a slightly modified version of a method developed by Oberdorfer et al. (19). Briefly, silicon nitride tips were cleaned in a piranha solution (20), rinsed with MilliQ water (18.2 M Ω -cm), and then immersed in a 100 μ g/mL Fn (Sigma-Aldrich) PBS solution for 45 minutes.

Force measurements were carried out as described in (17). Briefly, an inverted optical microscope was used to position an AFM tip over *S. aureus* cells that were sitting on a glass coverslip. A Fn-coated probe was brought into contact with a bacterium, pushed against the cell wall until the cantilever flexed 50-100 nm, and then pulled away from the bacterium. This approach-retraction cycle took 1 second (i.e., 1 Hz scan rate) and the vertical travel distance of the z-piezoelectric scanner was 2.7 μ m. The AFM cantilevers had a spring constant of 0.02 nN nm⁻¹ as determined by the hydrodynamic drag method (21). The theoretical loading rate (i.e., product of the spring constant and velocity of tip) was \sim 50 nN sec⁻¹. All force data were acquired within \sim 60-75 min of the initial harvesting of cells.

Results and Discussion

When collecting force measurements, it is a bit challenging to ensure that the AFM tip is positioned directly over a bacterium rather than the substrate that is supporting the cell. There are a couple of ways to locate a cell. A cell may be "found" by using the tip to collect an AFM image of the sample prior to collecting force curves. However, the imaging process may contaminant the tip.

Therefore, we used a different method to locate cells. An inverted optical microscope was used to position the tip over an *S. aureus* cell, which was usually a part of a binary fission pair. Figure 2 shows the positions of a Fn-coated tip and *S. aureus* cells on a glass cover slip in PBS solution. Because of the

resolution of an optical microscope, several practice runs were necessary before we were able to achieve competence with this method of alignment.

In our practice trials, the inverted optical microscope was used to position the tip over the glass substrate $\sim 2 \mu\text{m}$ away from a cell. We collected force measurements on the glass substrate and then, with the aid of the inverted optical microscope, used the x - or y -piezos to move the sample stage under the tip at

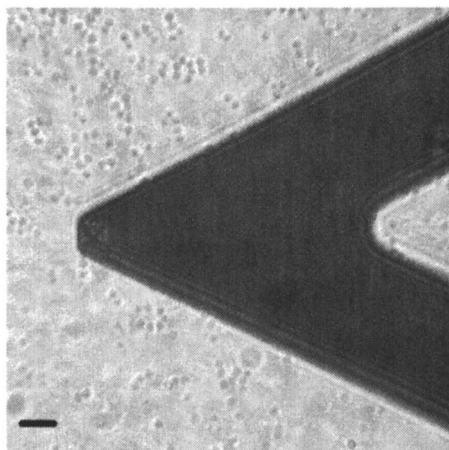


*Figure 2. Optical micrograph that shows the positions of the AFM cantilever and tip, as well as coccus-shaped *S. aureus* cells on a glass cover slip. The cells are blurred because the plane of focus is on the AFM tip. The scale bar is $\sim 4 \mu\text{m}$.*

intervals of a few nanometers. The resulting force curves, particularly the region of contact and retraction data, were significantly different for the cell versus the substrate. In this fashion, for this particular AFM and optical microscope, we were able to develop an effective strategy for coming down directly on top of a bacterium without the need to collect an AFM image of the cells beforehand.

Force profiles from all isolates of *S. aureus* demonstrated repulsion upon approach of the Fn-probe towards a bacterium. Figure 3 shows randomly selected approach curves collected on the 8 control and 7 invasive isolates of *S. aureus*. The magnitude and range of repulsion is consistent with electrosteric forces between *S. aureus* and a Fn-coated substrate (15). However, such repulsion is contrary to the common clinical observation of infectious *S. aureus*-biofilms on cardiac device implants. This inconsistency can be explained by examining the retraction force-profiles.

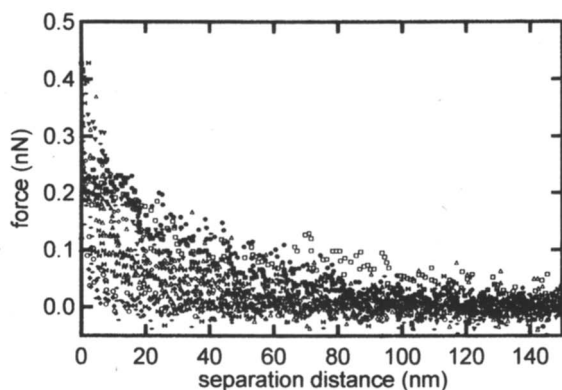


Figure 3. Force curves for a fibronectin-coated probe approaching the cell wall of the control strains of *S. aureus* (solid symbols) or the invasive isolates of *S. aureus* (open symbols). Positive force values indicate repulsion. All force data were collected in a PBS buffer solution.

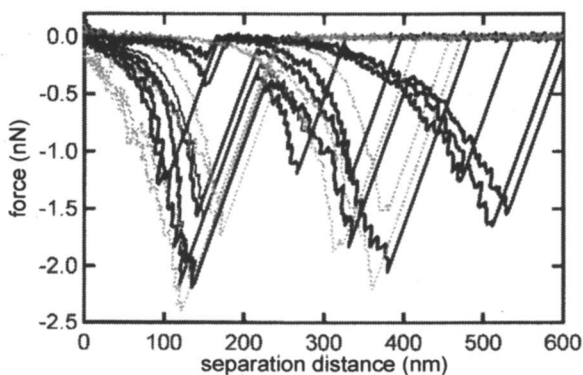


Figure 4. Force curves for a fibronectin-coated probe as it is pulled from contact with the cell wall of the control stains of *S. aureus* (dotted lines) or the invasive strains of *S. aureus* (solid lines). Negative force values indicate repulsion. All force data were collected in a PBS buffer solution. Modified after Yongsunthon et al. (17).

Retraction data often revealed an attractive bond as the Fn-coated probe was pulled away from a bacterium's cell wall. This attraction manifested itself as discrete sawtooth-shaped force signatures in the retraction profile (Figure 4). The sawtooth shape is consistent with the unfolding of a protein and suggests a specific binding event (22).

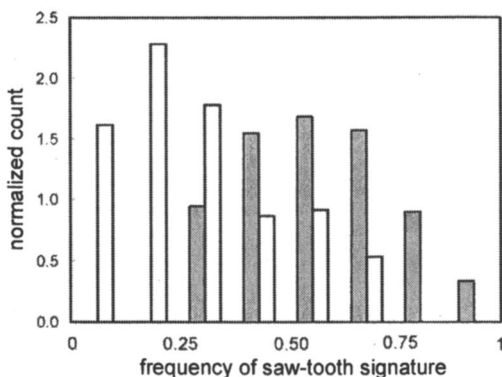
For each of the 15 *S. aureus* isolates, the frequency of specific binding events was determined by counting retraction curves that exhibited the sawtooth signature(s) and normalizing by the total number of curves for that isolate. The results are shown in Table I. Relative to the control isolates, the invasive isolates exhibited higher frequencies of adhesion and also tended to yield more force profiles with multiple sawtooth signatures (17).

Table I. Frequency of observing a specific binding event for each control isolate (label begins with "C") and invasive isolate (label begins with "I").

<i>Isolate</i>	<i>Frequency*</i>
C55	0.12±0.01
C67	0.14±0.02
C59	0.20±0.02
C52	0.26±0.02
C57	0.36±0.02
C58	0.40±0.02
C68	0.42±0.02
C53	0.44±0.02
I141	0.42±0.02
I306	0.46±0.02
I221	0.52±0.02
I399	0.55±0.02
I1066	0.57±0.03
I386	0.72±0.03
I1790	0.73±0.03

*average ± Poisson standard deviation.

After determining the average adhesion frequency for each isolate (Table I), the results were grouped according to whether the *S. aureus* was from the invasive or control population. These two groupings are shown in Figure 5. Each isolate's data were normalized such that it contributed a total count of one. For example, the sum of the control bars shown in Figure 5 is eight, which equals the number of control isolates analyzed with AFM. In spite of the spread resulting from individual cell differences (Table I), isolates from the invasive and control



*Figure 5. Histograms of the binding frequencies for the control (open bars) vs. the invasive (solid bars) strains. The distributions include retraction data for every cell probed and are normalized so that each of the *S. aureus* strains contributes a count of one. Modified after Yongsunthon et al (Modified from reference 17. Copyright 2007 American Chemical Society.)*

populations form very distinct distributions. The frequency means of the invasive and control populations are 0.57 ± 0.05 and 0.29 ± 0.05 , respectively. Using a Student T-test, we found that this difference is significant at the 99% confidence level.

Conclusion

In summary, this study presents an intriguing correlation that spans nine orders of magnitude from force measurements at the length scale of a bond to clinical studies of human patients with prosthetic implants. Our observations reveal that microorganisms of the exact same phylogeny (i.e., genus species classification) may be classified by the force-signatures of their binding proteins. This discovery could have a positive impact on health care as it bridges the disconnect between macroscopic, clinical investigations and nanometer-scale forces ultimately responsible for biofilms on implanted prosthetic devices.

References

1. Darouiche, R. O., *New Eng. J. Med.* **2004**, *350*, 1422.
2. Chamis, A. L.; Peterson, G. E.; Cabell, C. H.; Corey, G. R.; Sorrentino, R.

- A.; Greenfield, R. A.; Ryan, T.; Reller, L. B.; Fowler, V. G., *Circulation* **2001**, *104*, 1029.
3. Mylonakis, E.; Calderwood, S. B., *New Eng. J. Med.* **2001**, *345*, 1318.
 4. El-Ahdab, F.; Benjamin, D. K.; Wang, A.; Cabell, C. H.; Chu, V. H.; Stryjewski, M. E.; Corey, G. R.; Sexton, D. J.; Reller, L. B.; Fowler, V. G., *Amer. J. Med.* **2005**, *118*, 225.
 5. Greene, C.; McDevitt, D.; Francois, P.; Vaudaux, P. E.; Lew, D. P.; Foster, T. J., *Mol. Microbiol.* **1995**, *17*, 1143-1152.
 6. Foster, T., *Staphylococcus*. In *Medical Microbiology*, 4th ed.; Baron, S., Ed. The University of Texas Medical Branch at Galveston: Galveston, TX, 1996; Chapter 12.
 7. Kuusela, P., *Nature* **1978**, *276*, 718.
 8. Proctor, R. A.; Mosher, D. F.; Olbrantz, P. J., *J. Biol. Chem.* **1982**, *257*, 14788.
 9. Foster, T. J.; Hook, M., *Trends Microbiol.* **1998**, *6*, 484.
 10. Wann, E. R.; Gurusiddappa, S.; Hook, M., *J. Biol. Chem.* **2000**, *275*, 13863.
 11. Massey, R. C.; Kantzanou, M. N.; Fowler, T.; Day, N. P. J.; Schofield, K.; Wann, E. R.; Berendt, A. R.; Hook, M.; Peacock, S. J., *Cell. Microbiol.* **2001**, *3*, 839.
 12. Schwarz-Linek, U.; Werner, J. M.; Pickford, A. R.; Gurusiddappa, S.; Kim, J. H.; Pilka, E. S.; Briggs, J. A. G.; Gough, T. S.; Hook, M.; Campbell, I. D.; Potts, J. R., *Nature* **2003**, *423*, 177.
 13. Prince, J. L.; Dickinson, R. B., *Langmuir* **2003**, *19*, 154.
 14. Simpson, K. H.; Bowden, G.; Hook, M.; Anvari, B., *J. Bacteriol.* **2003**, *185*, 2031.
 15. Yongsunthon, R.; Lower, S. K., *Adv. Appl. Microbiol.* **2006**, *58*, 97.
 16. Yongsunthon, R.; Lower, S. K., *J. Elec. Spectro. Rel. Phenom.* **2006**, *150*, 228.
 17. Yongsunthon, R.; Vance G. Fowler, J.; Lower, B. H.; Vellano, F. P.; Alexander, E.; Reller, L. B.; Corey, G. R.; Lower, S. K., *Langmuir* **2007**, *23*, 2289.
 18. Gross, M.; Cramton, S. E.; Gotz, F.; Peschel, A., *Inf. Imm.* **2001**, *69*, 3423.
 19. Oberdorfer, Y.; Fuchs, H.; Janshoff, A., *Langmuir* **2000**, *16*, 9955.
 20. Lo, Y. S.; Huefner, N. D.; Chan, W. S.; Dryden, P.; Hagenhoff, B.; Beebe, T. P., *Langmuir* **1999**, *15*, 6522.
 21. Craig, V. S. J.; Neto, C., *Langmuir* **2001**, *17*, 6018.
 22. Lower, B. H.; Yongsunthon, R.; Vellano, F. P.; Lower, S. K., *J. Bacteriol.* **2005**, *187*, 2127.

Chapter 12

Characterization of the Outer Membrane of *M. Tuberculosis* with Atomic Force Microscopy Methods

Matthew T. Basel¹, Katharine Janik¹, Michael Niederweis²,
and Stefan H. Bossmann¹

¹Department of Chemistry, Kansas State University, 111 Willard Hall,
Manhattan, KS 66506 (sbossman@ksu.edu)

²Department of Microbiology, University of Alabama at Birmingham,
Birmingham, AL 35294-2170 (mnieder@uab.edu)

The mycobacterial cell envelope forms an exceptionally strong barrier rendering mycobacteria naturally impermeable to a wide variety of antimicrobial agents. An integral part of the cell envelope is a giant macromolecule consisting of peptidoglycan, arabinogalactan and long-chain, 2-alkyl-3-hydroxy fatty acids, the so-called mycolic acids. Physisorbed at this cell-wall skeleton are a large variety of other lipids, presumably forming the outer leaflet of a unique bacterial outer membrane. Atomic force microscopy (AFM) using contact-mode measurements in air at 293K and 50% relative humidity indicated that *Mycobacterium tuberculosis* has a very smooth surface. However, the adhesion between individual *M. tuberculosis* cells as well as between the cells and the hydrophilic mica-surface was surprisingly strong. We were unable to detach the mycobacteria from each other, the mica-surface or to damage the cell surface of *M. tuberculosis* applying shear-forces using the AFM in the contact mode. The geometry of the AFM tip, in combination with the spring constant, were used to calculate the associated force for the lower bound of the resistance of the cell wall to shearing forces. It was found to be 9.38×10^{-6} N. This finding offers a

new explanation how the formation of biofilms by mycobacteria can occur. Furthermore, we were able to demonstrate that the oxidation of clustering *M. tuberculosis* by H_2O_2 is an efficient method to destroy the cells and, therefore, also the mycobacterial biofilms. The implications for the disinfection of surfaces are apparent.

Introduction

Mycobacterium tuberculosis causes more deaths than any other single bacterial organism (i). Approximately one third of the world's population is already infected. More than 2,000,000 associated deaths occur annually. During the last two decades, multi-resistant strains have appeared due to the discontinuing treatment of tuberculosis in many countries, threatening all countries that experience immigration (1). A successful treatment of a multi-resistant case of tuberculosis (MDR-TB) requires up to 6 different antibiotics and 18-24 months of continuing care. In the United States, the typical costs per patient with MDR-TB are approximately \$200,000. Since no new TB drug has been developed in the past 40 years using classical methods, it is believed that new strategies are required for TB drug discovery (ii). Our approach aims to understand the fundamental basis of drug transport that often limits the efficiency of existing drugs against *M. tuberculosis*. To this end, we describe the biophysical characterization of the cell surface of *M. tuberculosis*. It is envisioned that current and new TB treatment strategies will profit from these results. Mycobacteria are known to possess an extremely stable and unique outer membrane that has an extremely low permeability and plays a crucial role in the intrinsic drug resistance and in the survival of mycobacteria under harsh conditions. Therefore, the aim of this study was to analyze the outer membrane of *M. tuberculosis* by AFM.

Biological background: Mycobacteria form a Unique Outer Membrane

Mycobacteria produce mycolic acids that are α -branched β -hydroxy fatty acids consisting of up to 90 carbon atoms and are the longest fatty acids known in nature (iii). Minnikin originally proposed that the mycolic acids, which are covalently bound to the arabinogalactan-peptidoglycan copolymer, form the inner layer of a unique outer membrane (OM) (Figure 1)(iv). In addition, the mycobacterial cell envelope contains a fascinating diversity of other lipids, many of which are unique to mycobacteria (v). Some of these extractable lipids were

shown to be an important part of the OM and are assumed to form the outer leaflet of this unique OM (e.g. TDM (trehalose dimycolate)) (2). Thus the mycobacterial OM resembles a supported asymmetric lipid bilayer and provides an extraordinarily efficient permeability barrier, which is 100 to 1000-fold less permeable than that of *E. coli* (vi). The existence of an additional lipid bilayer requires a set of dedicated OM proteins. *E. coli* uses more than 60 proteins to functionalize its OM (vii), many of which are channel proteins to permeabilize the membrane for nutrient transport. The observation, discovery (viii) and structural analysis of mycobacterial porins (ix) provided the first conclusive example that functionally similar, but structurally completely different OM proteins also exist in mycobacteria. Whereas the porins determine the permeability of the mycobacterial OM for hydrophilic substances, the extremely hydrophobic and covalently bound mycolic acids form the so-called cell-wall-skeleton. Mycobacteria are able to synthesize a fascinating variety of mycolic acids, of which more than 500 different structures are known to date (x). Together they form an almost impenetrable cell wall, as we will demonstrate in this report.

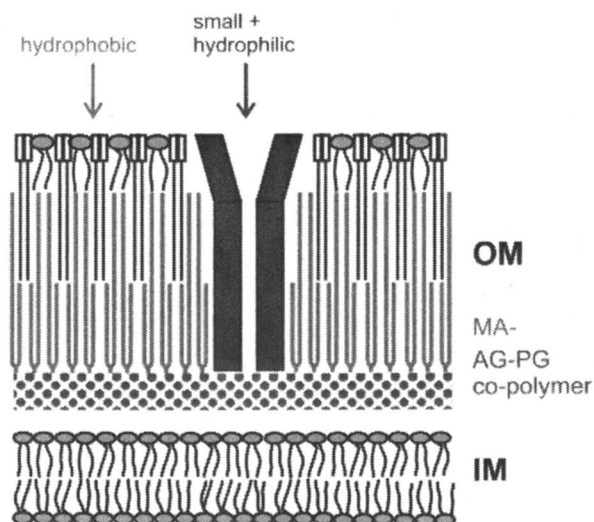


Figure 1. Schematic representation of the mycobacterial cell envelope, based on the model proposed by Minnikin (4). The inner leaflet of the outer membrane (OM) is composed of mycolic acids (MA), which are covalently linked to the arabinogalactan (AG) – peptidoglycan (PG) copolymer. The inner membrane (IM) of mycobacteria consists of a double-layer.

Experimental

M. tuberculosis cells:

Inactivated *Mycobacterium tuberculosis* cells (H37Rv) were obtained from the Mycobacteria Research Laboratories (MRL) at Colorado State University through the "TB Vaccine Testing and Research Materials" contract (HHSN266200400091C). These cells were produced by growing *M. tuberculosis* to late-log phase (day 14) in glycerol-alanine-salts (GAS) medium. The bacilli were harvested by filtration washed with PBS pH 7.4, pelleted by centrifugation and frozen at -80°C . For inactivation, the cell pellet was exposed to 2.4 mRads of ionizing gamma irradiation using a ^{137}Cs source. Confirmation of inactivation was performed using the Alamar Blue Assay. The inactivated cell pellets were then stored at -80°C . This procedure kills *M. tuberculosis* to a 10^{20} degree of certainty while maintaining 93-95% of their enzymatic activity (xi).

Sample Preparation and AFM-measurements:

Inactivated *M. tuberculosis* cells were diluted in 100mM Brij-58 in butanol (as well as optionally with 5M urea and 3% wt/wt H_2O_2) to reduce cell to cell lipid and protein interaction.

A typical procedure was as follows: Solution I: 1.0g of *M. tuberculosis* was diluted to 50mL with 0.1% phosphate buffer at pH 7.0; Solution II: 0.10 M Brij-58 in n-butanol. 900 μL of solution 2 and 100 μL distilled water was added to a 1.5mL Eppendorf vial. The solution was sonicated for 5 minutes in a low power sonicator bath. The mixture was then spin coated (2000rpm) onto freshly cleaved mica. The layer on mica was allowed to dry in an environmental chamber at 50 rel.% humidity at 293K for 24h. All AFM measurements were carried out under these conditions as well. The deposition conditions have been optimized prior to the AFM measurements. In the absence of *M. tuberculosis* cells in the buffer mixture, there were no discernible structures or residues on mica.

Contact AFM using a Nanoscope IIIa multimode AFM (Digital Instruments employing Si_3N_4 -tips (NP-1 tip A from Veeco Nanoprobe)) was performed on the samples employing an AFM setpoint voltage of 2V in order to provide an initial image. The approach voltage was then systematically raised in 2V steps and rescanned (xii). The final approach voltage was 16V and no change in the cell morphology was noted. The geometry of the AFM, in combination with the spring constant, was used to calculate the associated force for the lower bound of the resistance of the cell wall to shearing forces. The calculated lower bound was 9.38×10^{-6} N. Considering the tip geometry, this correlates to 7.47×10^9 N/m². Note that the *M. tuberculosis* cells have been imaged using the Tapping Mode of the Nanoscope IIIa as well. A typical result is shown in Figure 2. Principally, the same topology, resulting from the presence of the *M. tuberculosis* cells on mica, can be discerned from both contact and Tapping Mode measurements. Although we cannot completely rule out the occurrence of capillary forces between the

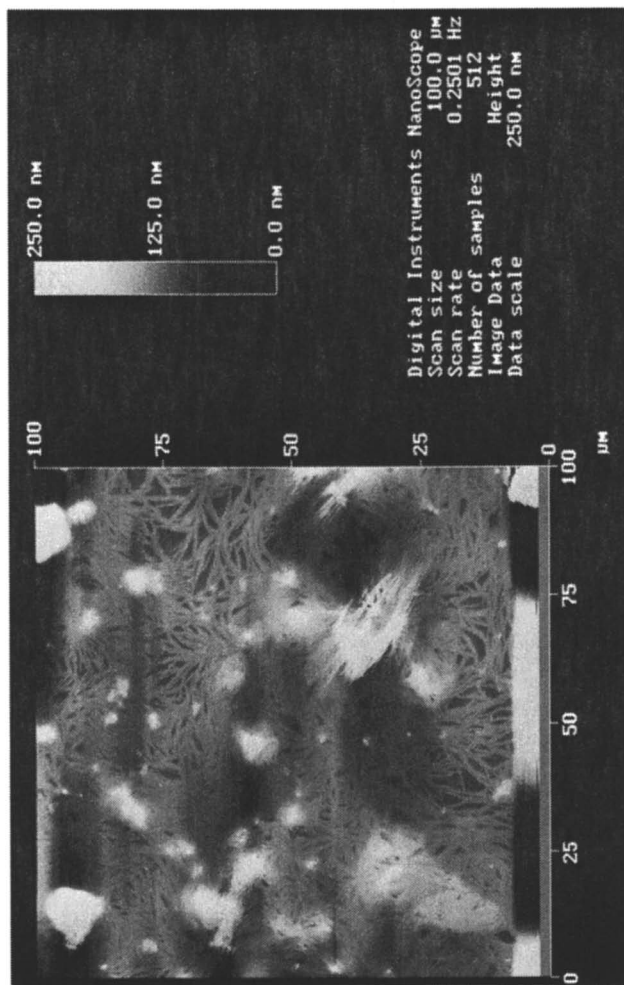


Figure 2. M. tuberculosis on mica, imaged by Tapping Mode AFM

AFM-tip and the *M. tuberculosis* cells, the comparison between the results obtained from both AFM-modes indicates that the shear-forces are dominating in our contact mode AFM measurements.

Results and Discussion

AFM as Method to Study Mycobacterial Surfaces

Due to the pathogenicity and resistance to treatment of tuberculosis and other mycobacterial diseases, a better understanding of the structure and biophysical properties of mycobacteria would be useful. One particularly interesting property of mycobacteria is their outer cell membrane (OM), because the OM acts as a shield against many antibiotics. Furthermore, the unusual hydrophobicity of the OM may play an important role in the biofilm formation, which is regarded as a major pathway of infection in hospitals (*xiii*). In Figure 3, typical mycolates are shown, which are responsible for the unusual hydrophobicity of the OM. In this study, atomic force microscopy (AFM) was used to quantify the strength of the cell wall of *M. tuberculosis* by its resistance to shearing forces. *M. tuberculosis* was chosen, because it clearly represents the greatest threat to humankind of all mycobacteria (*l*).

Our approach also permits the direct measurement of the adhesive forces of individual mycobacteria, which form either a cluster or a biofilm. We have chosen to work with inactivated *M. tuberculosis* cells, because they do not put as many restrictions on method development as live cells do. It quickly became clear from our AFM-measurements that gamma-radiation did not damage the outer cell wall of *M. tuberculosis*, which appeared as smooth as previously seen by using electron microscopy (*xiv*).

Mycobacterial Cells and Residues on Mica

In Figure 4A, we see the same kind of organic residue on the mica slate in spite of the spin-coating procedure being performed with 3000rpm instead of 2000rpm. In Figure 4B, the AFM-image of *M. tuberculosis* on mica is shown. A cluster of several individual cells of 10 - 20 μm x 1 μm in size is discernible beside some smaller organic structures. Our conclusion that this substance is organic is based on the following reasoning: A) Inorganic salts such as Na_2HPO_4 or NaCl are easily discernible when imaging with AFM due to their distinct shapes (*xv*). Furthermore, they are water-soluble and can be easily washed off the mica-slate. B) We have also tested Brij-58, n-butanol and PBS-buffer separately and combined, but in the absence of *M. tuberculosis* cells using the same

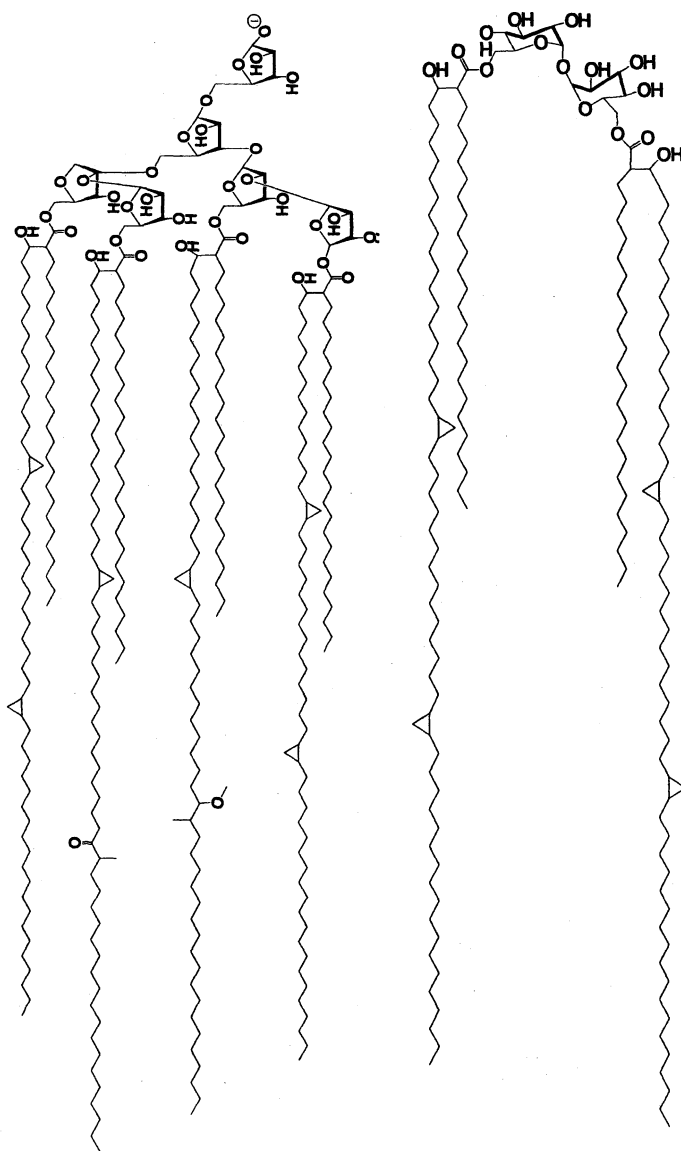


Figure 3. Schematic representation of the mycobacterial cell envelope, based on the model proposed by Minnikin (4). *A: (Left) Typical mycolic acids, covalently bound to AG-PG. B: (Right) A variety of extractable lipids presumably form the outer leaflet of the OM exists. Shown is trehalose dimycolate (TDM), a typical extractable lipid from the OM of mycobacteria (xvi).*

spin-coating procedure. The presence of Brij-58 did not help to disaggregate the cell clusters. Under no conditions were we able to obtain the typical residue, except when cells were present in the mixture that was spin-coated onto mica.

Because we did not find any evidence for ruptures or leaks of the mycobacterial outer membranes resulting from radiation treatment, we assume that the organic residue found on mica originates from the cell surface of *M. tuberculosis*. One molecule that can form such structures is lipoarabinomannan (LAM) (see Figure 4C). Mannosylated lipoarabinomannans (ManLAMs) are found in the cell wall of pathogenic mycobacteria and are considered a virulence factor of *M. tuberculosis* contributing to the entry and persistence in host cells (xvii). ManLAMs are released by *M. tuberculosis* into the supernatant (5). Recently, it was shown that ManLAMs in solution can self-assemble to micelle-like supramolecular structures (xviii). We further speculate that LAMs are a major component of the “glue” between individual *M. tuberculosis* cells that is responsible for the observed clustering. We have devised the following experimental procedure to either confirm or disprove this hypothesis.

M. tuberculosis cells were treated with the surfactant Brij-58 (I), Brij-58 and urea (II) and Brij-58, urea and hydrogen peroxide (III). Brij-58 is known to disrupt hydrophobic clustering. If the hydrophobic interaction between *M. tuberculosis* cells would be solely responsible for the observed clustering, the presence of a sufficient concentration of Brij-58 (as well as n-butanol) would disaggregate them and they would appear as single cells in the AFM image. However, if the aggregation of surface proteins of *M. tuberculosis* would lead to the observed clustering, it should be sensitive to high concentrations of urea, which denatures most proteins.

Finally, H₂O₂ was added to this mixture to target possible sugar-moieties that could contribute to the observed clustering. This approach is inspired by the hypothesis that LAMs could be indeed responsible for cell-cell adhesion with each other. The oxidation of the sugars would destroy the backbone of these very complex sugar-lipid assemblies and thus decrease their ability to interconnect the *M. tuberculosis* cells.

A Demonstration of Force

AFM contact mode was performed to convey defined shear forces on the samples. The measurement started with using normal parameters (approach of 2V) in order to provide an initial picture. Equation (1) was derived using geometric considerations and permits the calculation of the shear force F (N) in dependence of the applied voltage V .

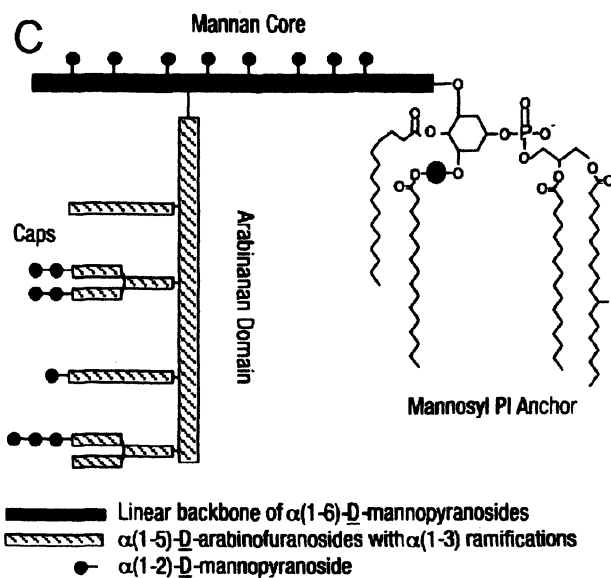
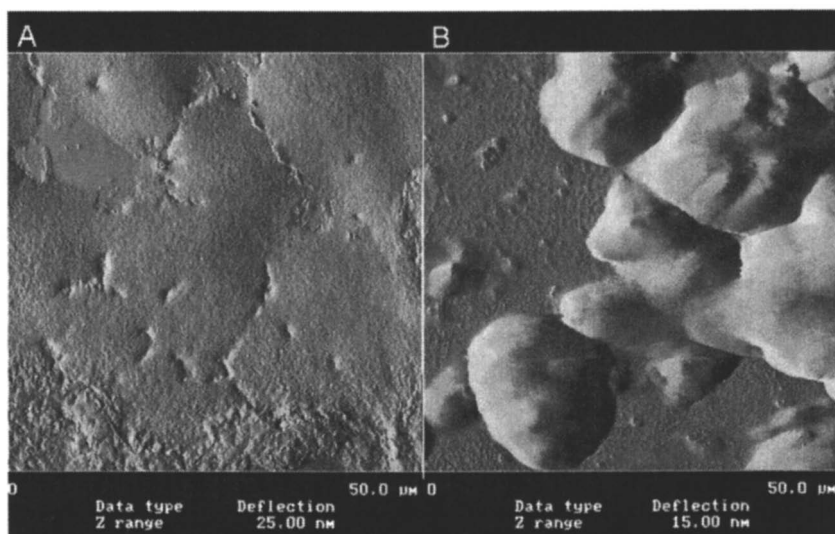


Figure 4. A: Residue from *M. tuberculosis* on mica after spinning at 3000 rpm. B: *M. tuberculosis* on mica, imaged by contact-AFM after spinning at 2000 rpm. C: Lipoarabinomannan (LAM), a highly viscous candidate for the amphiphilic residue shown in A.

$$F = 0.0413(V/109000 + 8.021 \times 10^{-5}) \quad (1)$$

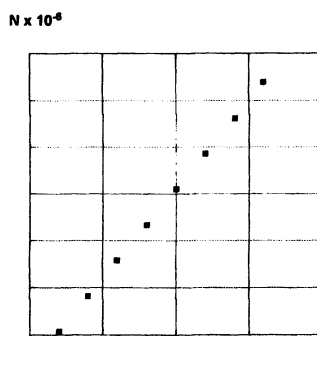
The voltage was raised in 2V steps during the approach and rescanned. This was performed systematically until the final approach voltage reached 16V and we found that the cell morphology showed no change. The geometry of the AFM was used to calculate the associated force for the lower bound of the resistance of the cell wall to shearing forces. The lower bound was calculated to be 9.38×10^{-6} N. Taking the tip geometry into consideration, this correlated to 7.47×10^9 N/m². In Table I, the shear forces conveyed by the AFM-tip are provided together with the applied voltage (see Figure 5).

In Figure 6, a series of six images of the same site comprising six clustering *M. tuberculosis* cells on mica is shown. As it becomes apparent, the series of imaging events in the AFM-contact mode with step-wise increasing mechanical-forces was not able to inflict any damage to the cell membrane or to disaggregate two or more *M. tuberculosis* cells. In Figure 6A-F, the AFM-image of the same region, imaged by applying a series of shear-forces, is provided. Although the resolution suffers from the greatly increasing shear-forces in the series A-E, it becomes clear that Figure 6F (again 2V applied) is essentially the same image as Figure 6A. From the comparison of this image and Figure 4B, it becomes clear that the cells remain indeed undamaged by the imaging force.

Table I. Shear Forces and Applied Forces as calculated according to eqn. 1

Voltage (V)	Shear Force (N)	Applied Force (N/m ²)
2	4.07×10^{-6}	3.24×10^9
4	4.83×10^{-6}	3.85×10^9
6	5.58×10^{-6}	4.44×10^9
8	6.34×10^{-6}	5.05×10^9
10	7.10×10^{-6}	5.65×10^9
12	7.86×10^{-6}	6.25×10^9
14	8.62×10^{-6}	6.86×10^9
16	9.38×10^{-6}	7.47×10^9

Figure 5. Plot: Shear Force vs. Voltage



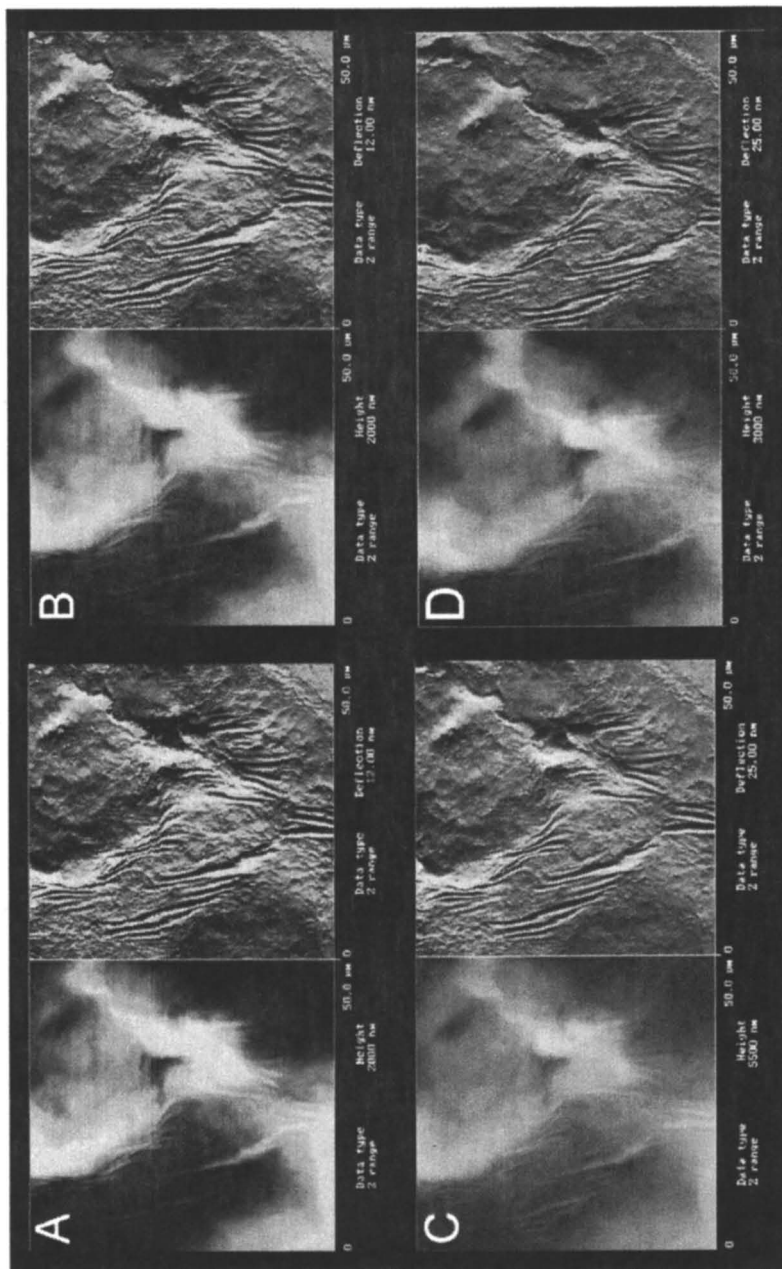
It is safe to assume that the upper limit of the shear-force during AFM-contact can be regarded as the lower limit for three processes: A) adhesion of *M. tuberculosis* on mica, B) adhesion between *M. tuberculosis* cells and C) damage of the cell surface of *M. tuberculosis*. All three processes require greater forces than can be applied by using the Atomic Force Microscopes available to us (Nanoscope IIIA and SPM 2000). However, this study shows that the strength of the cell wall can be quantified and that the cell surface of *M. tuberculosis* can withstand extremely strong mechanical forces. This may be attributed to the unusual composition of the mycobacterial cell wall that contain extremely long chain fatty acids that are covalently linked to the peptidoglycan polymer.

But how strong is a pressure of $7.47 \times 10^9 \text{ Nm}^{-2}$ really? In order to provide a suitable comparison, let's turn to some not so recent events in American history. One F1-engine of the Saturn 1C booster stage (first stage of the moon rocket Saturn-5) (xix) is able to generate 690,000 kilograms (of force, kgf) of thrust at sea level. That is equal to 6,766,563 N (xx). Considering the surface area of 24.63 m^2 at the end of the nozzle, the applied pressure is $274,729 \text{ N m}^{-2}$. Compared to the shear forces that we are able to convey by means of the AFM-tip in the contact mode, the force per square meter generated by the F1-engine is surprisingly low. The highest value for the AFM-tip, as obtained from our calculations (eqn. (1)), exceeds that of the F1-engine by a factor of 27,190! Of course, we are aware that the very small geometric extensions are working in favor of the AFM-tip, but nevertheless, this large factor is really surprising. This comparison emphasizes how stable the mycobacterial cell wall is. Furthermore, it may serve as an example, how great the forces exerted by an AFM-tip really can be.

Carbohydrates but not proteins appear to play a major role in cell-cell interactions of *M. tuberculosis*

Addition of 5M urea did not visibly change the cell-cell interactions of *M. tuberculosis* (Fig. 6). Note that the concentration of 5M is above the threshold for denaturation of many surface proteins (xxi). Based on these findings, it is concluded that a significant contribution of surface proteins to the observed cell-cell adhesion of *M. tuberculosis* is not likely. This conclusion is consistent with the AFM-image shown in Figure 4B, because the surface of *M. tuberculosis* appears to be smooth and does not display any structures larger than the spatial resolution of the AFM in the scanning mode of approximately 10 nm. It cannot be excluded, however, that smaller and very stable surface proteins contribute to the interactions between *M. tuberculosis* cells.

Finally, 3% wt/wt of hydrogen peroxide was added to the buffer containing the inactivated *M. tuberculosis* cells. As it becomes apparent in Figure 7, the



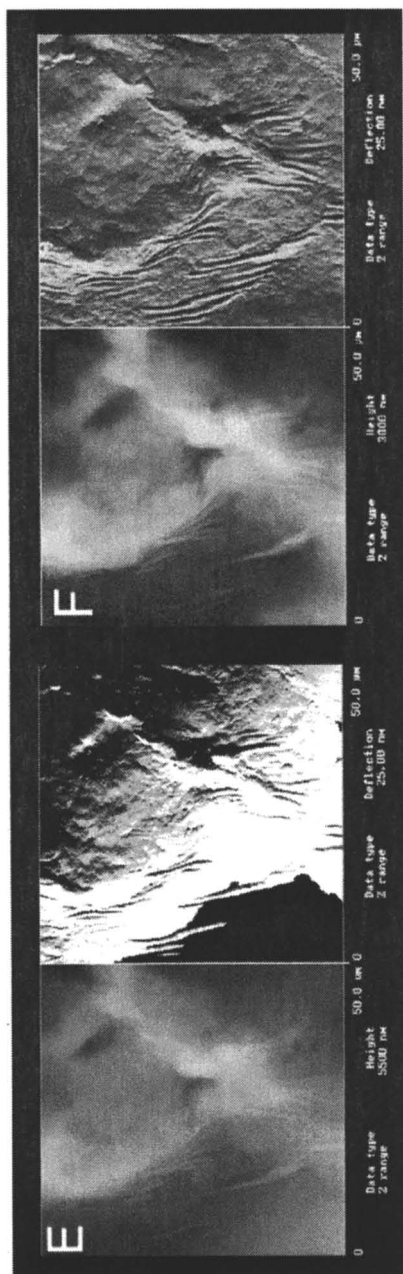


Figure 6. (left: topography, right: phase image) A: 2V applied, B: 6V, C: 10V, D: 14V, E: 16V (maximum), F: 2V

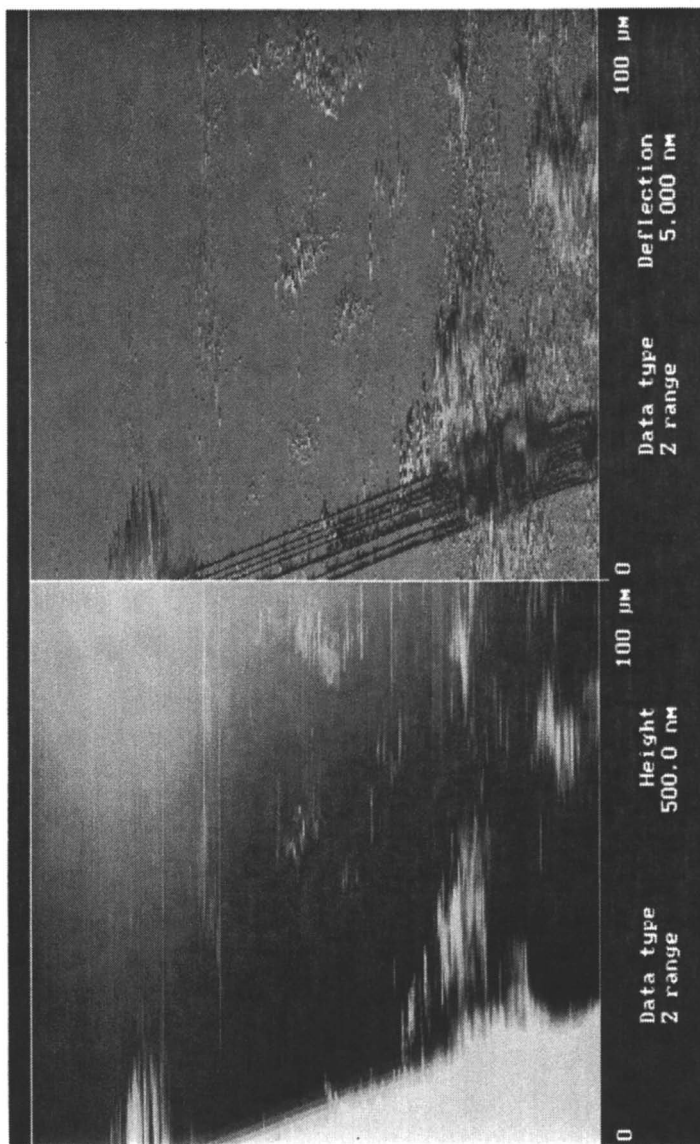


Figure 7. (left: topology, right: phase image) AFM-image (contact mode) after adding 3% wt/wt of H_2O_2 before performing the standard deposition procedure on mica. No more cell structures can be discerned!

addition of H₂O₂ had a dramatic effect: no more cells are visible in the AFM (contact mode). This means that the shear forces conveyed by AFM are sufficient to disintegrate the cell walls of *M. tuberculosis* when an oxidant is present that can decompose sugar moieties of the cell-wall skeleton of mycobacteria. The addition of H₂O₂ has a profound influence on all three observable processes: clustering of TB-cells, adhesion on mica and the strength of individual cell walls. Note that the result shown in Figure 7 is typical for the addition of 3% wt/wt of H₂O₂ to *M. tuberculosis* cells. We have reproduced this rather surprising finding five times and could not discern “surviving” cells any of those experiments. The remaining layer after oxidation is somewhat similar to the layer of (most likely) organic material shown in Figure 4A. We have attempted to follow the H₂O₂-induced process of cell decomposition by AFM, but failed. 3% wt/wt of H₂O₂ appears to be the threshold when the decomposition of *M. tuberculosis* cells happens very quickly. Below this concentration, notable effects could not yet be imaged. At this point, our hypothesis is that the remaining (organic) material on mica is resulting from the oxidative breakdown of the cells and the added urea and Brij-58.

Note that we have thoroughly checked that the *M. tuberculosis* cells were not simply spun off by imaging the boundary regions of droplets put on mica before, during and after evaporation of the employed buffer mixture. We could not obtain any indication for the presence of *M. tuberculosis* cells under our experimental conditions. Therefore, it is safe to assume that oxidative damage is weakening the structural integrity of inactivated *M. tuberculosis* cells substantially. This observation suggests a molecular explanation for the damaging effects of reactive oxygen and nitrogen intermediates which are produced by macrophages to kill *M. tuberculosis* inside phagosomes (xxii).

Conclusion

We have demonstrated that contact mode AFM is a suitable method to probe the surface of previously inactivated *M. tuberculosis* with defined mechanical-forces. The aim of our experiments is the quantitative understanding of the surface properties of *M. tuberculosis*, which are believed to be important for clustering and biofilm formation of *M. tuberculosis* (xxiii). These processes contribute to the spread of tuberculosis, especially in hospitals and other urban environments. The surface of *M. tuberculosis* appeared very smooth. However, they form very strong cell-cell and cell-mica aggregates. The force for the lower^{xxiv} bound of the resistance of the cell wall to shearing forces was calculated to 9.38×10^{-6} N, indicating that the biofilms formed by *M. tuberculosis* are indeed very resistant. Hydrogen peroxide weakened the cell wall of *M. tuberculosis* so much that the forces conveyed during contact-AFM imaging were sufficient to

completely disrupt the cells. Thus, we have identified the oxidation of cell wall components, most likely carbohydrates, as an important mechanism to prevent cell-cell adhesion of *M. tuberculosis*.

References

1. Statistics from the World Health Organization (<http://www.who.int>)
2. Mitchison, D. A. *Front. Biosci.* **2004**, *9*, 1059-1072.
3. Barry, C. E., 3rd; Lee, R. E.; Mdluli, K.; Sampson, A. E.; Schroeder, B. G.; Slayden, R. A.; Yuan, Y. *Prog. Lipid. Res.* **1998**, *37*, 143-179.
4. Minnikin, D. E. in *Lipids: Complex lipids, their chemistry, biosynthesis and roles.*; Ratledge, C. Stanford, J.; Academic Press, London, 1982.
5. Brennan, P. J.; Nikaïdo, H. *Annu. Rev. Biochem.* **1995**, *64*, 29-63.
6. Chambers, H. F.; Moreau, D.; Yajko, D.; Miick, C.; Wagner, C.; Hackbarth, C.; Kocagoz, S.; Rosenberg, E.; Hadley, W. K.; Nikaïdo, H. *Antimicrob. Agents Chemother.* **1995**, *39*, 2620-2624.
7. Molloy, M. P.; Herbert, B. R.; Slade, M. B.; Rabilloud, T.; Nouwens, A. S.; Williams, K. L.; Gooley, A. A. *Eur. J. Biochem.* **2000**, *267*, 2871-2881.
8. Niederweis, M.; Ehrst, S.; Heinz, C.; Klöcker, U.; Karosi, S.; Swiderek, K. M.; Riley, L. W.; Benz, R. *Mol. Microbiol.* **1999**, *33*, 933-945.
9. Faller, M.; Niederweis, M.; Schulz, G. E. *Science* **2004**, *303*, 1189-1192.
10. Barry, C. E., 3rd; Lee, R. E.; Mdluli, K.; Sampson, A. E.; Schroeder, B. G.; Slayden, R. A.; Yuan, Y. *Prog. Lipid Res.* **1998**, *37*, 143-179.
11. TB Vaccine Research and Materials Contract, Colorado State University (<http://www.cvmb.colostate.edu/microbiology/tb/subcell.htm>).
12. Dupres, V.; Menozzi, F. D.; Loch, C.; Clare, B. H.; Abbott, N. L.; Cuenot, S.; Bompard, C.; Raze, D.; Dufrene, Y. F. *Nature Methods* **2005**, *2*, 515-520.
13. Knoell, T.; Safarik, J.; Cormack, T.; Riley, R.; Lin, S. W.; Ridgway, H. *Journal of Membrane Science* **1999**, *157*, 117-138.
15. Mailaender, C.; Reiling, N.; Engelhardt, H.; Bossmann, S.; Ehlers, S.; Niederweis, M. *Mol. Biol.* **2004**, *150*, 853-864.
16. The method used is described in: Sukhorukov, G. B.; Susa, A. S.; Davis, S.; Loporatti, S.; Donath, E.; Hartmann, J.; Moehwald, H. *Journal of Colloid and Interface Science* **2002**, *247*, 251-254.
14. Brennan, P. J. *Tuberculosis* **2003**, *83*, 91-97.
17. Briken, V.; Porcelli, S. A.; Besra, G. S.; Kremer, L. *Mol. Microbiol.* **2004**, *53*, 391-403.
18. Riviere, M.; Moisand, A.; Lopez, A.; Puzo, G. *J. Mol. Biol.* **2004**, 907-918.
19. Smithsonian National Air and Space Museum : Saturn V Rocket (<http://www.nasm.si.edu/exhibitions/ATM/nojs/rm.br.s5.1.html>).

20. The unit newton ($\text{kgm}^{-1}\text{s}^{-2}$) is equal to about 0.101972 kilograms of force (kgf).
21. Pace, C. N.; Grimsley, R., G.; Scholtz, J. M. *Protein Folding Handbook* **2005**, *1*, 45-69.
22. North, R. J.; Jung, Y. J. *Annu. Rev. Immunol.* **2004**, *22*, 599-623.
23. Ojha, A.; Anand, M.; Bhatt, A.; Kremer, L.; Jacobs, W. R., Jr.; Hatfull, G. F. *Cell* **2005**, *123*, 861-873.

Chapter 13

Directly Measuring Adhesive and Elastic Properties of Bacteria Using a Surface Force Apparatus

Joan E. Curry^{1,2}, Cheol Ho Heo¹, and Raina M. Maier^{1,2}

¹Department of Soil, Water, and Environmental Science, University of Arizona, Tucson, AZ 85721

²BIO5 Institute, University of Arizona, Tucson, AZ 85721

Bacteria are increasingly being employed as components in biosensors and biofilm reactors. It is important to understand the material properties of bacteria in dry conditions for these applications. For a decade, Atomic Force Microscopy (AFM) has been the primary tool used to study the adhesion and elastic properties of individual bacteria. In this work we show it is possible to use a Surface Forces Apparatus (SFA) to measure elastic and adhesive properties of small collections of surface bound bacteria. The measurements are conducted with submonolayer, patterned bacterial films and we have developed a protocol to image the contact area with AFM after the experiment. Using the SFA, we measured the force profile between a *Pseudomonas aeruginosa* PAO1 film and a bare mica surface. *Pseudomonas aeruginosa* PAO1 is a ubiquitous gram-negative soil bacterium and is also an opportunistic pathogen. We repeated the measurement in the same contact position for a number of days to determine the effect of desiccation on the film material properties.

Bacterial adhesion is the first step in biofilm formation which impacts numerous environmental, industrial and medical processes. Examples of undesirable consequences of biofilm formation include metal rust, sewage sludge and bacteria-related diseases. Desirable consequences are biofiltration and bioremediation. Bacteria are resilient and can survive in harsh environments. A severe stress is desiccation since dehydration can damage DNA and change the properties of proteins. Some bacteria protect against dehydration by accumulating sugars such as sucrose and trehalose while others undergo a transformation from an active to a dormant state. Evaporative deposition of bacteria on a surface shows that some bacteria aggregate to form two dimensional patterns which may be important for nutrient sharing and survival in dry conditions (1). Bacterial attachment and survival on surfaces is important for understanding biofilm formation, transport of pathogens in the subsurface and disease transmission. Consequently, many groups (2-11) have worked to understand the mechanisms responsible for bacterial adhesion to surfaces. Individual bacterial cells can be probed with atomic force microscopy (AFM). Recently, Abu-Lail and Camesano (11) directly measured the force between AFM cantilevers with silicon nitride (Si_3N_4) tips and bacteria covalently attached to flat glass substrates. We have used a Surface Forces Apparatus (SFA) to measure forces between an incomplete bacterial monolayer and a mica surface. The force profiles are used to discuss changes in the film due to desiccation.

Evaporative Deposition of Bacterial Films for use in the SFA

The experiments were carried out using a modified Mark IV interferometric SFA (12) with two muscovite mica surfaces mounted as facing, crossed cylinders. One surface is coated with a bacterial film as described below. The lower surface is mounted on a flexible double cantilever spring [$k \sim 147 \text{ N m}^{-1}$], and the upper surface is mounted on a cylindrical piezoelectric crystal, the expansion of which controls the surface separation with an accuracy of 0.1 nm. Coarse surface separation was controlled directly with a DC motor on the translation stage attached to the lower surface, and fine control was achieved with the piezoelectric device attached to the upper surface. In order to form the interferometer (12) the mica (S & J Trading, NY) which had been cleaved into molecularly flat sheets (2-6 μm thick) was back silvered (50 nm thick film) using evaporative deposition and glued to cylindrically polished silica disks using an epoxy resin (Epon 1004, Shell Chemical Co.). The interferometer formed by the back-silvered surfaces transmits only certain discrete wavelengths that are passed through a diffraction grating and observed directly with an eyepiece as fringes of equal chromatic order at the exit slit of the spectrometer. The fringes allow measurements of the surface separation and refractive index

of the medium between the surfaces (12). Before coating one surface with bacteria, the contact fringe positions of the untreated mica surfaces were recorded for reference.

Pseudomonas aeruginosa PAO1 was chosen for these experiments because it is genetically well-characterized, is a ubiquitous soil microorganism and is an opportunistic pathogen. The organism was precultured in 30 ml R2B (Difco Laboratories, Detroit MI) at 24 °C in ambient air for 24 hours. The preculture was used to inoculate a second culture, which was grown for a further 24 hours. The bacteria were harvested between late exponential and early stationary phase. The cells were centrifuged for 15 minutes at 10,000 RPM (Beckman, model J2-21 Centrifuge). The solution used to coat a mica surface for use in the SFA was prepared by first washing the cells in 15 ml of a minimal salts media (MSM, 0.15g NH₄H₂PO₄, 0.1g K₂HPO₄, 0.00041g FeSO₄·7H₂O, 0.05g MgSO₄·7H₂O in 100 mL water) to remove extracellular material and organic media components. The cells were then centrifuged and resuspended in an additional 15 ml of MSM. The ionic strength and pH of the MSM were 0.061 M and 6.6 respectively. The MSM did not contain a carbon source in order to eliminate growth related changes in the bacteria during the force measurements. The concentration of cells in the deposition solution was 10⁸ cfu/ml. One of the mica samples was placed in the bacterial solution for 1 hour, carefully removed and dried on an incline in a laminar flow hood with the cylindrical axis oriented in the direction of the incline. The three phase contact line moved from the top to the bottom of the surface depositing bacteria at the drying front. In order to increase the speed of the contact line and hence the deposition rate a Kimwipe was gently placed into contact with the side of the silica disc at the lower edge of the surface thus employing capillary action to remove excess bacterial solution. The total drying time was approximately 1 minute. This procedure produces incomplete patterned monolayer bacterial films which are more generally known as cellular or honeycomb films (13, 14). Figure 1 shows a portion of a film prepared for use in an SFA experiment. Complete bacterial films substantially reduce light passage and are not optimal for SFA experiments. At the end of the experiment, the bacteria coated sample was removed from the SFA and with the aid of a digital picture of the contact area obtained in the SFA the contact area was imaged using AFM.

Film Formation

Figure 1 shows a portion of a typical incomplete bacterial film used in SFA experiments. The bacteria appear light and the mica surface appears dark. Individual bacteria (~1 μm length) are not visible in this image. The entire surface is covered by the cellular pattern which is deposited at the three phase contact line during drying. The size of the holes in the film is on the order of 50

μm . On close inspection with AFM it is found that the film consists of a connected network of bacteria deposited as a monolayer with nominal thickness of ~ 400 nm. The very bright spots in the image are either salt precipitates originating from the deposition solution or bacterial aggregates. Fortunately it is possible to find a suitable contact position and to avoid interference from these protrusions since the distance between the protrusions is large enough.

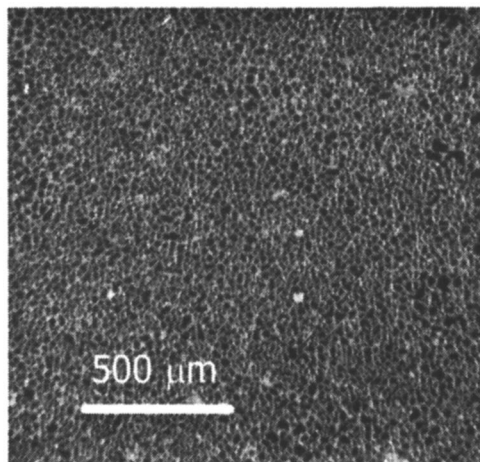


Figure 1. Optical microscope image of a patterned cellular film produced for use in an SFA experiment.

Force Measurements

After the bacteria coated surface is inserted in the SFA chamber the system is allowed to equilibrate for ~ 24 hours. Following equilibration, the force as a function of the separation between the mica surfaces is measured at 25°C in ambient humidity. The measured humidity was very low ($10 \pm 3\%$) due to the desert climate and was not externally controlled. Variations in humidity did not noticeably affect the measured forces. The force measurement begins with the surfaces out of contact. As the surfaces approach the force increases indicating contact between the bacterial film and the bare mica surface. The measured distance is the absolute distance between the mica surfaces and in the non-zero force region this corresponds to the thickness of the bacterial layer at the center of the contact zone. The film is compressed slightly as the separation continues to decrease and then the process is reversed as the surfaces are pulled apart. Adhesion is measured as a negative force as the surfaces are separated.

Figure 2 shows force profiles as a function of time for a 10 day experiment, where closed and open symbols denote “advancing” and “receding”, respectively. The legend notes the time of the measurement relative to the beginning of the experiment in terms of days (d) and hours (h). The force curves shift to the left with time, indicating the bacterial film thickness decreases. One explanation for this is that water is removed from the film through compression and natural evaporation processes. Another explanation is that the film undergoes a rearrangement and a locally thick region (~450 nm) collapses to the thickness of the remainder of the film (~350) after the 3rd day. The film thickness as determined by the closest separation at an applied force of 2 mN/m was 335 - 340 nm for days 4 through 10.

For the first two days, the adhesive force was very strong but then decreased as a function of time. The large adhesive forces at 1d 8hr and 2d 4hr suggest that capillary forces contribute to the adhesion and support the idea that water loss occurs over several days as the sample dries and is subjected to compression measurements. With time the adhesive force decreased but increased again in the 10d 6hr measurement. This is likely due to the formation of a conditioning film on the bare mica surface which should increase the adhesive force. Conditioning films mediate bacterial adhesion and promote biofilm formation in aqueous systems. The composition of the conditioning film is unknown but is likely comprised of bacterial associated polymers which are transferred from the bacterial monolayer.

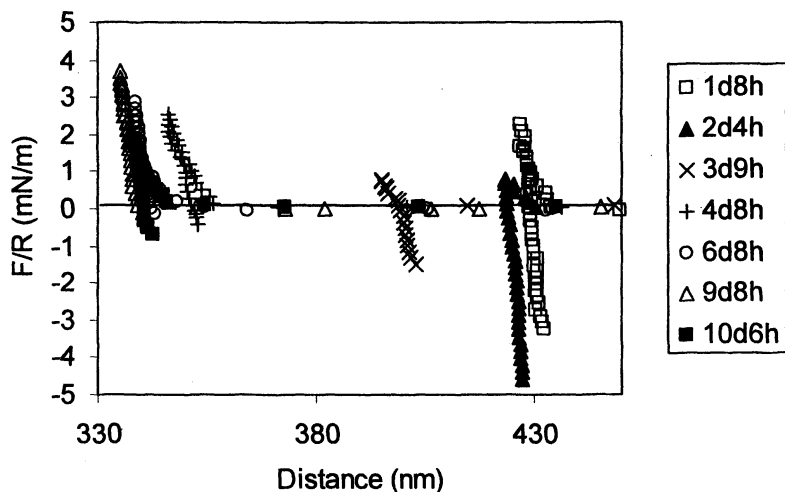


Figure 2. Advancing and receding forces measured in the same contact area over a 10 day period.

Figure 3 shows the adhesive forces measured for three different experiments as a function of time in the SFA chamber. With the exception of experiment 1 contact #1 the adhesive force is initially close to zero and then increases with time in the chamber and number of contacts. Repeated contacts likely result in a conditioning film on the opposing surface, which increases adhesion. At very long times the bacteria die and lyse, thus changing the surface dramatically and resulting in significantly increased adhesion. For experiment 1 contact #3 a conditioning film could be seen with the naked eye after the experiment definitely showing that the bacteria were no longer intact. The following factors are expected to influence the adhesive force: applied force, capillary condensation, bacterial surface coverage, bacterial film roughness, bacterial healthiness and age. While little is known about the specific changes in *P. aeruginosa* PAO1 under drying conditions Yao et al. (15) found that this species could be dried on a filter for four days and then rehydrated successfully.

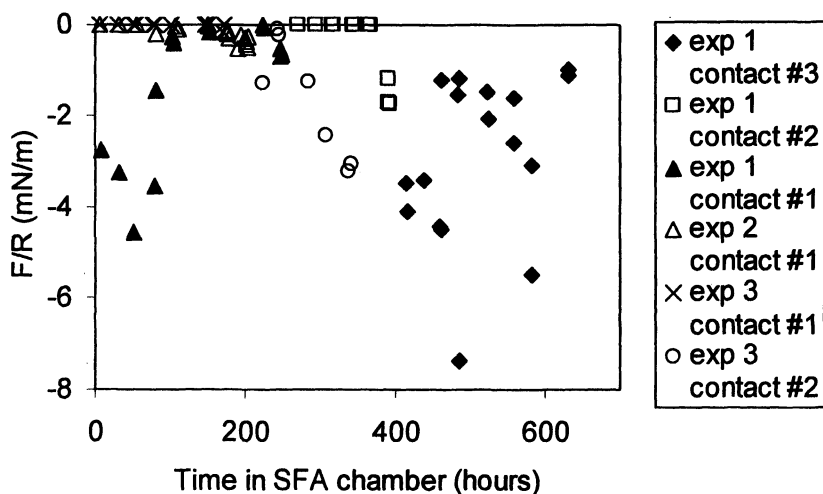


Figure 3. Adhesive force as a function of time for three different bacteria coated samples and a total of six contact areas.

In a subsequent experiment the contact zone was located and imaged with AFM as shown in Figure 4. On the left is the digital image obtained while the surfaces are in the SFA chamber. The bright background associated with the contact zone is easily seen inside the circle overlaid on the figure. The center of the contact zone is located by viewing Newton's rings with monochromatic light when the surfaces are in contact. The AFM image of the contact zone is shown

on the right. Representative heights of the bacterial patches obtained from the AFM image are noted for comparison with force profiles shown in Figure 5.

Advancing and receding force profiles were obtained in the same contact position beginning 29 hours after the sample was introduced into the SFA chamber and continuing over a period of six days. Figure 5 shows the first two complete force profiles measured at 29 and 37.5 hours. There is little difference in the advancing profiles. The shift to the left in the receding profile at 37.5 hours can be attributed to the higher compressive force applied in that run. A comparison of the receding profiles shows no adhesion at 29 hours while there is a small adhesion at 37.5 hours. In contrast to the experiment discussed in the previous section little adhesion is observed throughout this experiment due to the low density of bacteria and significant surface roughness as verified by AFM. Advancing profiles are shown in Figure 6 for the entire experiment. The onset of the repulsion resulting from compression of the bacteria correlates well in general with the measured heights of the bacteria obtained with AFM as noted in Figure 4. On careful inspection it is seen that the profiles are not smooth but rather contain small discontinuities due to the surface roughness. As the surfaces are pressed together the number of actual contact regions increases and the discrete regions of the film which are in contact are compressed. In effect the advancing profile records the collective height distribution of the roughness features.

In the third measurement at 52 hours, the force curve is shifted to the right by ~ 10 nm. This suggests an increase in film thickness and is likely due to a physical modification of one or more regions of the contact zone. The advancing curves for 37.5 (filled circles) and 52 (filled squares) hours are compared in Figure 7. A small jump-in at a distance of 475 nm is prominent in both cases suggesting that this surface feature is not changed substantially during these two measurements. Figure 7 also shows the 52 hour curve shifted along the y-axis by -0.8 mN/m to coincide with the 37.5 hour curve (open squares). The two curves are very similar with the major difference being an additional feature in the 52 hour curve at 490 nm which has the effect of shifting the overall curve to the right. This suggests that one or more of the higher features which are subjected to the most pressure during the compression at 37.5 hours is slightly modified in such a way that its height is increased. With this additional barrier it is then necessary to apply more force in the subsequent force run to reach the same film thickness.

In addition to physical modification which may produce shifts in the force profiles to the left or the right it is also possible that the film thickness uniformly decreases due to water loss as the bacteria respond to the desiccating conditions. This will result in a shift of an identifiable force profile feature to the left to a smaller distance. This is the case for the profile at 102 hours which appears to the left of the profile at 89 hours (see Figure 8). Alignment of the profiles was achieved by shifting the 102 hour curve to the right by 5 nm and up by 0.12 mN/m. The agreement is particularly good at separations between 440 and 470

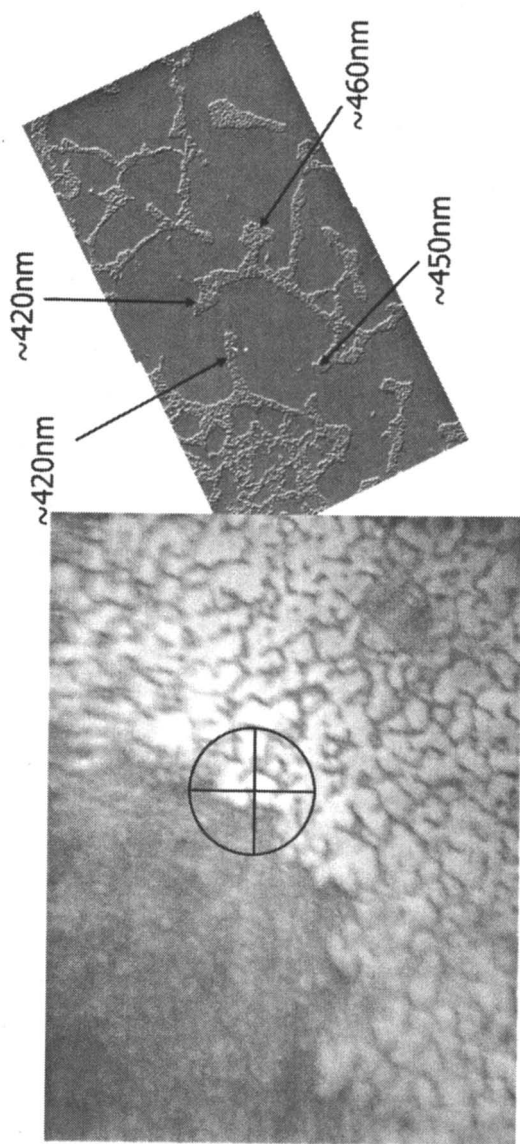


Figure 4. Optical image of the contact zone viewed in the SFA (left). AFM image of the contact zone obtained at the end of the experiment after the surfaces had been removed from the SFA chamber (right).

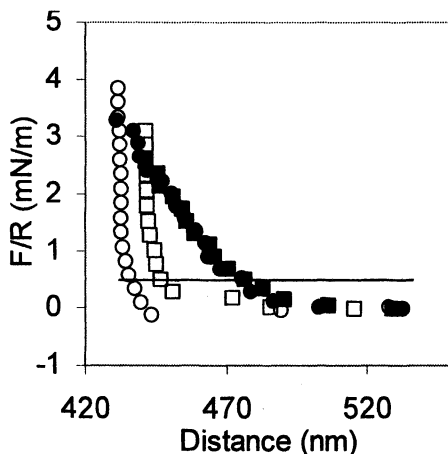


Figure 5. Advancing (closed symbols) and receding (open symbols) forces between the bacterial film and a mica surface for 29 hr (squares) and 37.5 hr (circles). Forces are normalized by the radius of curvature of the mica surfaces, R , which is 2 cm.

nm. The small vertical shift indicates that surface modification also takes place during the 89 hour measurement. At 485 nm there is an increased repulsion indicating the presence of a surface protrusion. This increased repulsion is much reduced in the 102 hour measurement.

This technique of aligning sequential force curves was attempted for all force measurements in this experiment. It was possible to align force profiles in the early measurements with good confidence that identifiable surface features were preserved between measurements as illustrated in the two examples above. At later times it was not possible to identify features in the force profile that were unambiguously preserved thus no conclusions could be drawn concerning the separate effects of physical modification and overall film shrinkage in these cases. It is possible that a number of modifications occur at the same time thus obscuring more isolated changes that are identifiable in earlier measurements. For the cases where alignment was shifted in discrete units horizontally and vertically the distance and force shifts are plotted as a function of time (Figure 9). The data suggest that surface modification is important in force measurements. Additionally, it appears it is possible to separate contributions from physical modification and overall film shrinkage by comparing sequential force curves. Shifts along the x-axis to smaller separations correspond to film shrinkage. It is possible the shrinkage is the result of water loss due to either mechanical perturbations resulting from the compressive force or equilibration processes in the film due to desiccation. Shifts along the y-axis appear to

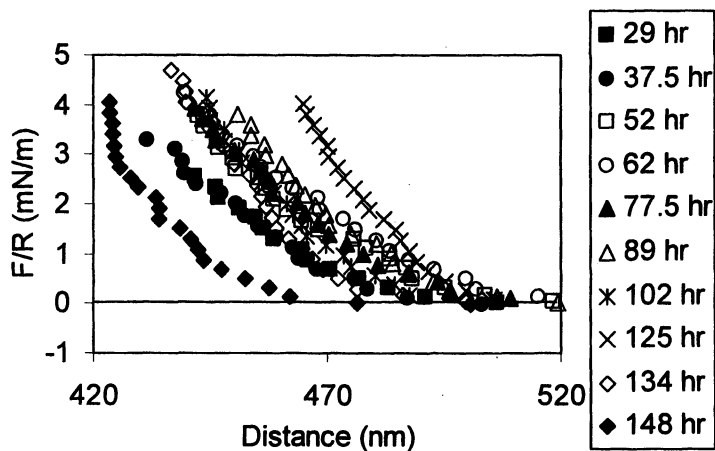


Figure 6. Advancing forces for days 1 to 6.

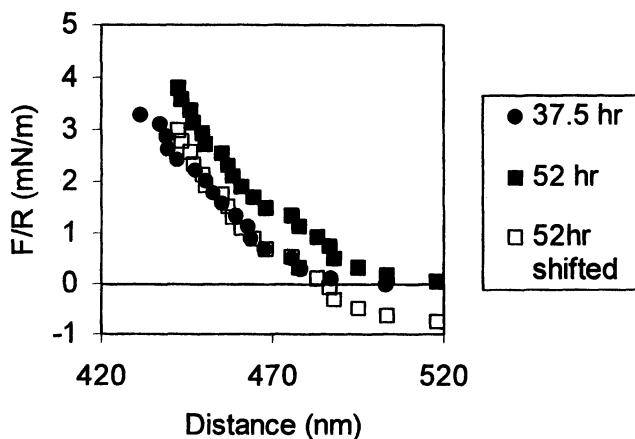


Figure 7. Comparison of advancing profiles at 37.5 and 52 hours. Open symbols show a mathematical vertical shift of the 52 hour curve by -0.8 mN/m.

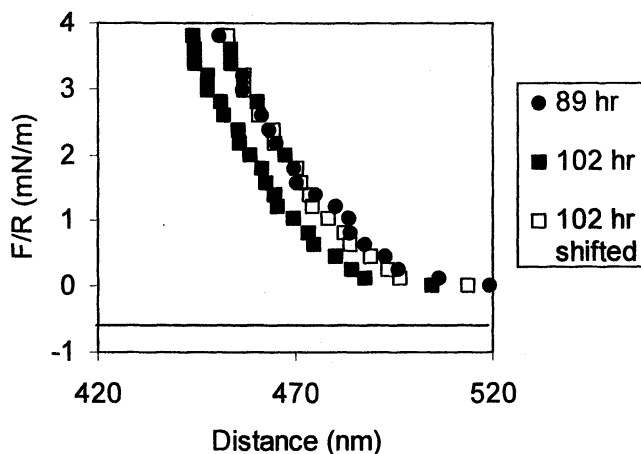


Figure 8. Comparison of advancing profiles at 89 and 102 hours. Open symbols show a mathematical horizontal shift of the 102 hour profile by 5 nm as well as an upward vertical shift of 0.12 mN/m.

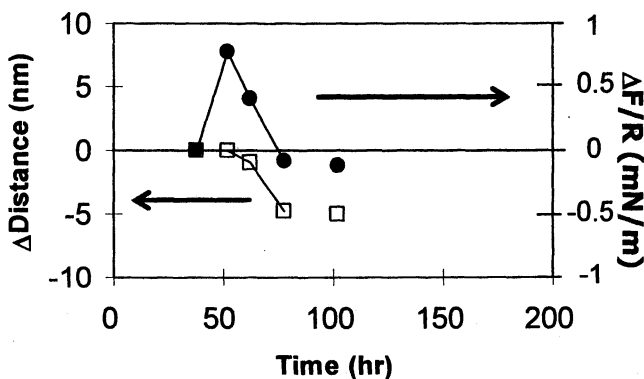


Figure 9. Shifts along the distance axis and the F/R axis required to align sequential force profiles. A negative shift along the distance axis indicates film shrinkage whereas a shift on the F/R axis corresponds to physical modification of the bacterial surface.

correlate with physical modifications of the film. This suggests the possibility of using force measurements to separate film changes resulting from physical modification due to mechanical perturbation from those due to water loss as the film responds to desiccating conditions.

AFM is used widely to measure adhesive (6, 7, 10, 11) and more recently elastic properties (15) of single bacterial cells. As a next step towards understanding the growth and development of biofilms it will be necessary to study the properties of small clusters of surface associated bacteria under controlled conditions. This work represents a first effort in this direction and demonstrates the possibility that the SFA can be used for this purpose. It is anticipated that AFM studies of single cells and SFA studies of multiple cell samples will be used together to obtain more information on surface associated bacteria and ultimately provide an improved understanding of biofilm formation and degradation.

Conclusions

A protocol to use SFA to study bacterial adhesion and elasticity has been developed. In these initial studies force profiles were measured on patterned *Pseudomonas aeruginosa* PAO1 monolayer bacterial films. The force profile reflects the height distribution of roughness features. Changes in the force profile with successive measurements in the same contact location can be attributed separately to physical modification and uniform shrinkage likely caused by water loss. Further work to link force profiles with the surface roughness distribution as detected with AFM will allow quantitative determination of elasticity properties of monolayer bacterial films.

Acknowledgements

Srinivas Manne and Mary Liddelw are thanked for the AFM imaging. This project was supported by National Research Initiative Competitive Grant No. 2003-35107-13770 from the USDA Cooperative State Research, Education, and Extension Service.

References

1. Potts, M. *Microbiol. Rev.* **1994**, *58*, 755.
2. Paul, J. H.; Jeffrey, W. H. *Appl. Environ. Microbiol.* **1985**, *50*, 431.
3. van Loosdrecht, M. C. M.; Lyklema, J.; Norde, W.; Schraa, G.; Zehnder, A. J. B. *Appl. Environ. Microbiol.* **1987**, *53*, 1898.

4. Grasso, D.; Smets, B. F.; Strevett, K. A.; Machinist, B. D.; van Oss, C. J.; Giese, R. F.; Wu, W.; *Environ. Sci. Technol.* **1996**, *30*, 3604.
5. Bruinsma, G. M.; Rustma-Abbing, M.; Van der Mei, H. C.; Busscher, H. J. *J. Microbiol. Methods.* **2001**, *45*, 95.
6. Ong, Y. L.; Razatos, A.; Georgiou, G.; Sharma, M. M. *Langmuir.* **1999**, *15*, 2719.
7. Velegol, S. B.; Logan, B. E. *Langmuir.* **2002**, *18*, 5256.
8. Vigeant, M. A. S.; Wagner, M.; Tamm, L. K.; Ford, R. M. *Langmuir.* **2001**, *17*, 2235.
9. Klein, J. D.; Clapp, A. R.; Dickinson, R. B. *J. Colloid Interface Sci.* **2003**, *261*, 379.
10. Emerson, R. J.; Camesano, T. A. *Appl. Environ. Microbiol.* **2004**, *70*, 6012.
11. Abu-Lail, N. I.; Camesano, T. A. *Langmuir*, **2006**, *22*, 7296.
12. Israelachvili, J. N. *J. Colloid Interface Sci.* **1973**, *44*, 259.
13. Nguyen V. X.; Stebe, K. J. *Phys. Rev. Lett.* **2002**, *88*, 164501.
14. Martin, C. P.; Blunt, M. O.; Moriarty, P. *Nano Lett.* **2004**, *4*, 2389.
15. Yao, X.; Walter, J.; Burke, S.; Stewart, S.; Jericho, M. H.; Pink, D.; Hunter, R.; Beveridge, T. J. *Coll. Surf. B* **2002**, *23*, 213.

Chapter 14

Measuring the Strength of Bacterial Adhesion by Micromanipulation

Guanglai Li and Jay X. Tang

Physics Department, Brown University, Providence, RI 02912

We introduce a two-micropipette method to measure the strength of bacterial adhesion. In this method, the bacterium is allowed to adhere to a flexible glass micropipette. A stiff suction micropipette is then used to grab and pull the cell in a direction perpendicular to the axis of the flexible one, ultimately detaching the cell. The adhesion force is calculated from the deflection of the flexible micropipette when the cell is detached. This method was successfully used to measure the adhesion force of *Caulobacter crescentus*. This technique is capable of measuring very large adhesion forces on the μN scale, which is beyond the range of applicability of many other methods.

Introduction

Bacteria in their natural environment are typically found attached to surfaces as individual cells or as part of a biofilm (1). Bacterial biofilms may cause the biofouling in implanted catheters, in water distribution systems, or on the hull of ships. The strong attachment of single bacterial cells provides the critical first step in the biofouling of a surface. Understanding the detailed mechanisms by which bacteria attach to surfaces, in addition to the nature, biosynthesis, and properties of the adhesives that mediate their attachment, is essential for a full understanding of the mechanisms of biofilm formation.

The development of bacterial adhesion is usually divided into two stages: a reversible adhesion followed by an irreversible adhesion (2). The reversible adhesion is a result of the competition between the attractive van der Waals force and the repulsive electrostatic force. The cells are trapped at a distance very close to the surface, which can be estimated by Derjaguin-Landau-Verwey-Overbeek (DLVO) theory and measured by total internal reflection microscopy (3). The cells are not in direct contact with the surface at this stage. The cell continues to move laterally near the surface and may swim or diffuse away from the surface at any point. The attractive force is very small, typically on the order of pN, during this reversible stage. Even this small force, however, significantly increases the amount of time the cell stays close to the surface, called the dwell time. This increase in the dwell time causes an increase in the probability of the cell to make contact with the surface and develop into an irreversible adhesion. The irreversible adhesion is usually mediated by the extracellular fibers, such as exopolysaccharide, pili, and flagellar filaments (4-6). Cells become immobilized on the surface in this stage and a strong adhesion develops after the irreversible stage.

Several methods have been developed to measure bacterial adhesion forces. Traditionally, adhesion strength was studied by flow chamber experiments for a population of cells by counting the number of cells that remained attached after a hydrodynamic shear stress was applied (7). A popular method to measure the adhesion force of a single cell is to use atomic force microscopy (AFM). There are two strategies for this type of measurement. One technique has the AFM tip approach and retract from a cell permanently attached to the substrate and the adhesion force is measured when the tip breaks apart from the cell (8). The other technique is to attach the cell permanently on the AFM tip and approach and retract the cell from a substrate, thus measuring the adhesion force between the cell and the substrate (9). In either case, the adhesion is not completely developed and the measured adhesion force is on the order of nN. The AFM tip has also been used to push laterally, scraping off single cells from the surface. The resulting forces were up to 200 nN in magnitude (10). The adhesion forces of single cells have also been measured with micropipette techniques (11). In this method, a bent micropipette was used to trap and pull the cell from the

substrates. The forces were measured from the deflection of the pipette tip. Finally, in a separate chapter of this book, J. E. Curry describes direct measurements of adhesive and elastic properties of bacteria using a surface force apparatus.

In this chapter we introduce a method employing two micropipettes for measuring the adhesion force of single bacterial cells, with the ability to measure forces in the μN range. We have used the method to measure the adhesion force of *Caulobacter crescentus* on a glass substrate. We found the adhesion force of a single *C. crescentus* cell to be on the order of μN , the largest ever measured for single bacterial cells (12). Here we describe the method in details, which may facilitate further application of the technique.

Methods

The Two-Micropipette Method

Two micropipettes were used to measure the adhesion force. As shown in Figure 1, a bacterial cell is attached to a flexible micropipette. A second stiff pipette is brought to the location of the cell. Suction is applied so that the cell body becomes trapped in the narrow opening of the stiff pipette. The suction micropipette pulls the cell in a direction perpendicular to the flexible micropipette until the cell is detached from the flexible one. The adhesion force can be calculated from the displacement of the flexible micropipette at the position the cell is detached. The force constant of the flexible micropipette is individually calibrated by causing a certain amount of bending with a known force (detailed in the subsection below). In this method, the flexible micropipette serves as the force sensor. Its force constant can be tuned simply by changing the length and diameter of the pipette. The flexible micropipette can be made very thin, with a diameter comparable to the cell size. It is also easy to locate a cell on a thin micropipette using a light microscope. In addition, the light microscope makes it possible to easily follow the deflection of the flexible micropipette. No piezoelectronic controller is needed as is typical in the single micropipette method (11).

A modification of this configuration for measuring strong adhesion is shown in the inset of Figure 1. Limited by the strength of the cell wall, the suction pipette may not be able to apply a very large suction force on the cell without damaging it. If the adhesion is very strong, the cell will slip away from the suction pipette before the cell is detached. In an effort to get around this problem, the cell is drawn into the suction micropipette parallel to the flexible one. The cell is therefore bent 90° with respect to the pulling direction allowing

the suction pipette to apply a large pulling force without applying a large suction pressure.

The micropipettes were fabricated using a Sutter Micropipette Puller P-97 (Sutter Instrument) from borosilicate glass tubes with a 1.0 mm outer diameter and a 0.5 mm inner diameter. The flexible micropipette was made with one step heating and pulling. The length and thickness of the tip were controlled by regulating the heating temperature and pulling force. A typical flexible micropipette has a long thin tapered tip of ~15 mm in length and ~2 μm in diameter at the end. Suction micropipettes were produced differently, with 3 steps of programmed heating and pulling to produce an opening comparable to the size of a *C. crescentus* cell at 0.5-2 μm . The suction micropipette is many times stiffer compared to the flexible one and its deformation is negligible during the pulling of the cell.

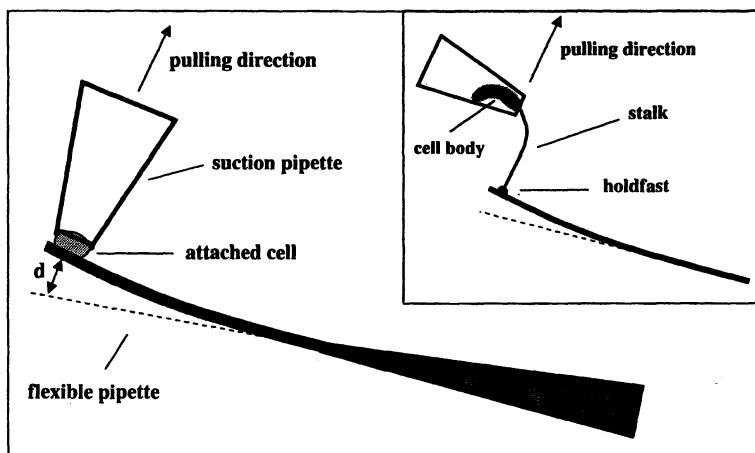


*Figure 1. Two-micropipette method for the measurement of bacterial adhesion force. Inset is a modification of the method specifically for elongated cells such as the stalked cells of *Caulobacter crescentus*.*

Determining the Force Constant of the Flexible Micropipette

An AFM (Dimension 3100, Digital Instruments) is employed to measure the force constant of the flexible micropipette in contact mode. In the measurement, a tipless calibration cantilever (#CLFC, Veeco Probe) with known force constant, $k_{\text{cantilever}}$, is pushed against the flexible micropipette. Only the very end of both the flexible micropipette and the AFM cantilever are in contact, as shown in Figure 2A. An AFM force curve is then acquired. At equilibrium,

the cantilever and the micropipette have deflections of $d_{\text{cantilever}}$ and d_{pipette} respectively and the force of the thin flexible micropipette is balanced by the elastic force of the cantilever $k_{\text{pipette}} \cdot d_{\text{pipette}} = k_{\text{cantilever}} \cdot d_{\text{cantilever}}$. The deflections of the pipette, d_{pipette} , and cantilever, $d_{\text{cantilever}}$, are generated by the AFM's piezoelectric tube traveling a distance d_{tube} . For small deflections, $d_{\text{tube}} = d_{\text{cantilever}} + d_{\text{pipette}}$. The traveling distance of the AFM tube, d_{tube} , and the deflection of the cantilever, $d_{\text{cantilever}}$, can be read from the force curve. With a known force constant of the cantilever, $k_{\text{cantilever}}$, we then obtain the force constant of the pipette, k_{pipette} , which is $k_{\text{pipette}} = k_{\text{cantilever}} s / (1 - s)$, where $s = d_{\text{cantilever}} / d_{\text{tube}}$ is the absolute value of the slope of the approaching force curve after the cantilever makes contact with the micropipette, as shown in Figure 2B.

Case Application: Measuring the Adhesion Force of *Caulobacter crescentus*

Caulobacter is a Gram-negative bacterium that is widely present in aquatic environments, including fresh water, soil and underground water (13). It is among the first colonizers of submerged surfaces, initiating the process of biofouling (14). *C. crescentus* has a dimorphic life cycle with a motile swarmer cell stage, followed by a non-motile stalked cell stage. Adhesion is developed during the swarmer cell stage (6). The pili and motility of the swarmer cell are both required for efficient attachment. Motility may increase the occurrence of contacts between the cell and a surface, and/or provide the force that is necessary to overcome the repulsive barrier near the surface. The presence of the pili and flagellum may also help break this repulsive barrier. A typical adhesion process for *Caulobacter* is shown in Figure 3. After the initial reversible adhesion on the surface, the irreversible adhesion develops during which the pili make contact with the surface and then retract. This retraction of pili brings the pole where the adhesive holdfast is located into close proximity with the surface, and helps ensure that the cell orientation is optimal for the subsequent adhesion by the holdfast. The holdfast then cements the attachment to the surface.

Attachment of *Caulobacter* cells to a surface in the irreversible adhesion stage is extremely strong. Even strong jets of water cannot wash them away. (15). We set out to measure this strong adhesion force using the two-micropipette method.

A two-step growth method was employed to reproduce *Caulobacter* cells on the flexible micropipette. *Caulobacter* CB15 wild type cells were first grown in a peptone yeast extract (PYE) medium (16) at 30°C overnight without agitation in a Petri dish. A flexible micropipette was placed in the Petri dish while the cells were growing. Cells were observed by light microscopy, confirming that

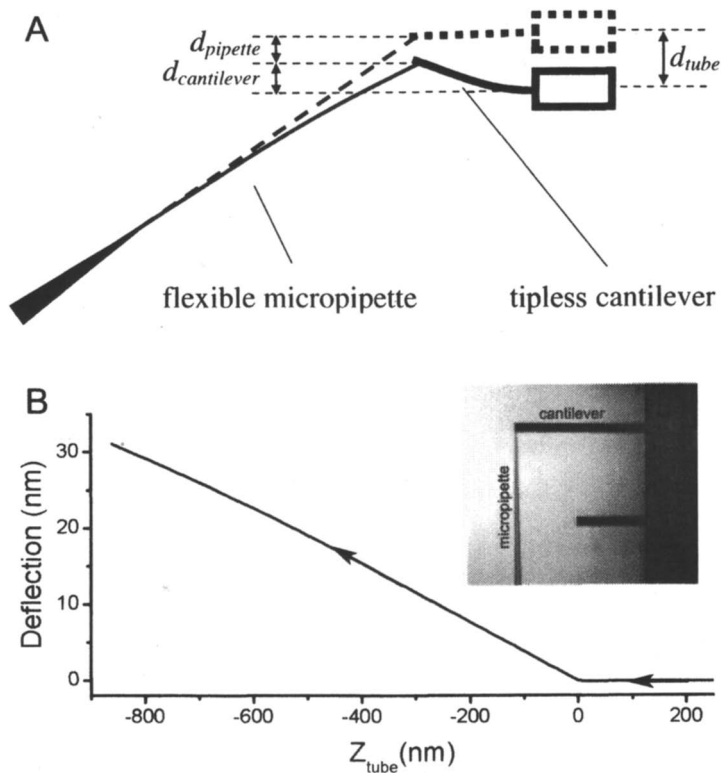


Figure 2. (A) A schematic drawing of the determination of the force constant of the flexible micropipette aided by a tipless AFM cantilever. (B) A typical AFM force curve. The cantilever approaches from above ($Z_{\text{tube}} > 0$ nm) and makes contact with the micropipette at $Z_{\text{tube}} = 0$ nm. The cantilever is deflected when pushing against the micropipette ($Z_{\text{tube}} < 0$ nm). The inset is a picture showing the calibration cantilever and the flexible micropipette under the AFM.

they had attached to the micropipette. After the overnight growth, the medium was changed to Hutner imidazole glucose glutamate (HIGG) medium (17) and the cells on the micropipette were grown for an additional two days. The HIGG medium contained a reduced phosphate concentration of 0.03 mM, which promoted the elongation of the stalks (18). To monitor the cells with fluorescence microscopy, we diluted the NanoOrange protein quantitation reagent (component A of Kit N-666, Molecular Probes Inc.) 500 times in the HIGG growth medium. The cell was visible under fluorescence microscopy while there is no background fluorescence since NanoOrange reagent is essentially non-fluorescent in aqueous solution but becomes strongly fluorescent when bound to proteins.

The adhesion force was measured with the method shown in the inset of Figure 1. Due to the large force required, the cell body had to be sucked into the suction micropipette, which was then bent away from the pulling direction. The suction pipette was mounted on a NanoControl micromanipulator (Kleindiek Nanotechnik), which moves in incremental steps of 50 nm to 1 μm . Suction pressure was produced by a Stoelting 51222 Manual Microsyringe Driver with a Hamilton 710LT 100 μl Syringe. The operation was monitored under a Nikon TE-2000U inverted microscope with a 100 \times objective designed for phase contrast and fluorescence imaging. When observing in phase contrast mode, the suction pipette approached a cell and held the cell in place just inside the tip of the suction pipette. The microscope was then switched to the fluorescence mode and the suction pipette was moved perpendicular to the flexible micropipette until the cell was detached. The process was recorded using a Marshall V-1070 B/W CCD camera and a Sony GV-D800 Digital Video Recorder. Through analysis of the series of fluorescence images, we were able to determine whether the cell remained inside of the suction micropipette, or whether it had slipped out.

Figure 4 shows an example of successive frames of a pulling operation. The deflection of the micropipette when the cell was detached was measured directly from the frame as shown in Figure 4E. Successful pulls were performed on fourteen individual *Caulobacter* cells. The force constant of the flexible micropipette ranged from 0.012 to 0.026 N/m and the deflection from 5 to 176 μm . The adhesion force ranges from 0.11 μN to 2.26 μN , with an average of 0.59 ± 0.62 μN (standard deviation). To our knowledge, this was the largest adhesion force of a single bacterium ever measured (12). This example demonstrates that the two-micropipette technique is capable of measuring very large forces in fully developed adhesions.

Conclusions

A two-micropipette method was developed to measure the bacterial adhesion force. In this method, a bacterial cell was attached to a flexible

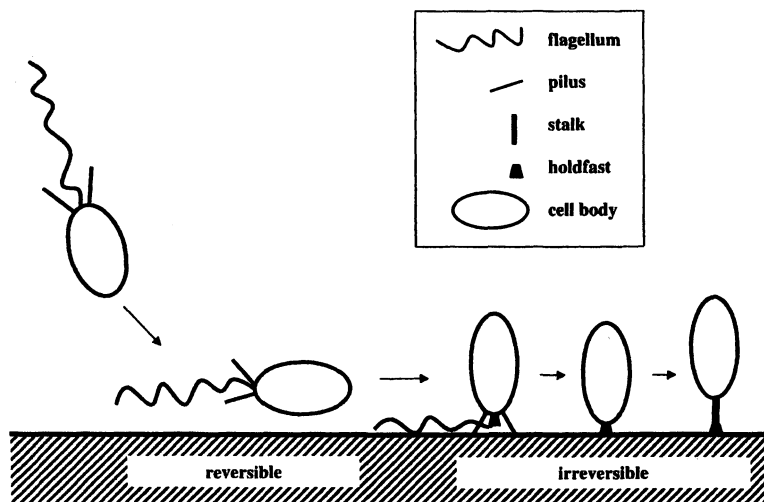


Figure 3. Diagram of the stages of Caulobacter adhesion. From left to right, a swarmer cell approaches a substrate and swims near the surface (reversible adhesion). The pili then bind to the surface and retract, bringing the adhesive holdfast in contact with the surface (irreversible adhesion). The attached cell grows a stalk, which is a long and thin cylindrical extension of the cell wall capped by the holdfast.

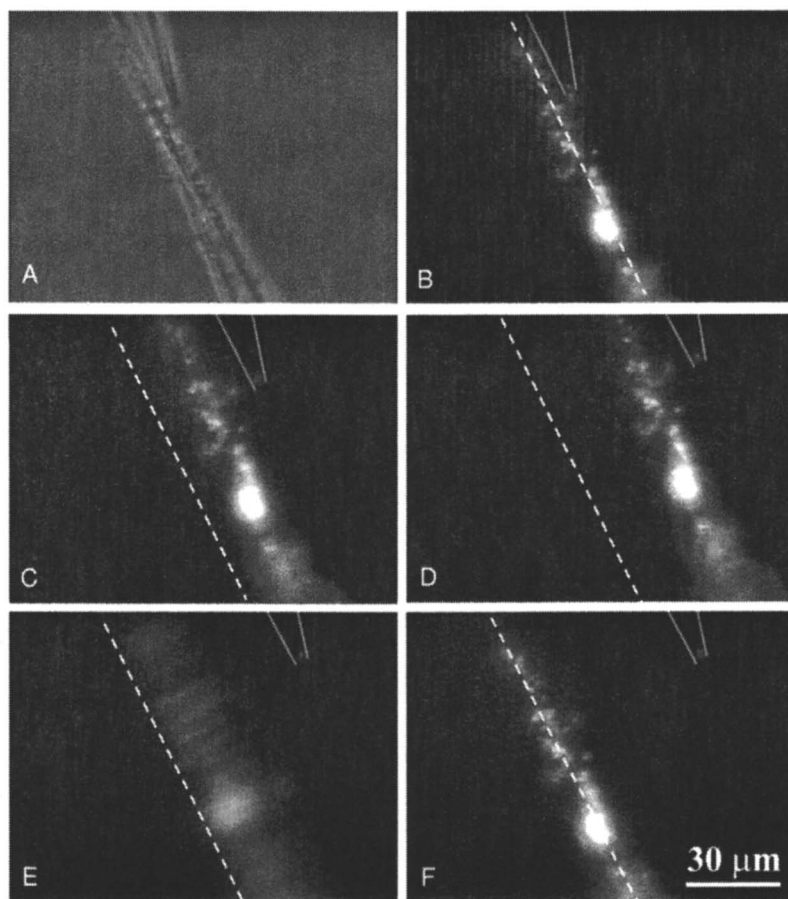


Figure 4. Successive frames of a pulling operation. (A) Phase contrast image showing the tip of a suction pipette holding a *Caulobacter* cell in place. (B-F) Fluorescence images. The dashed lines indicate the rest position of the flexible micropipette and the two solid lines depict the position of the suction micropipette. There is a cell in the mouth of the suction pipette. The cell is pulled and the flexible micropipette increasingly deviates from its original position. (D) The instant right before the cell is pulled off from the flexible micropipette. (E) The cell is pulled off the flexible micropipette. The movement of the pipette is easily seen from the blurring in the image. (F) The thin flexible pipette has returned to its original position.

micropipette and a stiff micropipette trapped and pulled the cell until the cell was detached from the flexible micropipette. The adhesion force was calculated from the deflection of the flexible micropipette. The motion of the suction pipette was controlled by a micromanipulator and the operation was monitored and recorded under a light microscope. The deflection was measured directly from the video. This method was applied to the *Caulobacter crescentus* to measure the force of adhesion between the bacteria and the glass surface. We found that the *Caulobacter* had an adhesion force on the order of μN . This result shows that the two-micropipette method is suitable for measuring very large adhesion forces. Indeed, a wide range of adhesion forces can be measured with this method by choosing a flexible micropipette with an appropriate force constant. This technique, therefore, might be widely applicable to the study of interactions between microbes and surfaces.

References

1. Donlan, R.M., Biofilms: microbial life on surfaces. *Emerg. Infect. Dis.*, **2002**, *8*, 881-889.
2. Marshall, K.C., *Mechanisms of bacterial adhesion at solid-water interfaces*, in *Bacterial adhesion: mechanism and physiological significance*, D.C. Savage and M.M. Fletcher, Editors. 1985, Plenum: New York. p. 133-161.
3. Vigeant, M.A.S., Ford, R.M., Wagner, M., and Tamm, L.K., Reversible and irreversible adhesion of motile *Escherichia coli* cells analyzed by total internal reflection aqueous fluorescence microscopy. *Appl. Environ. Microbiol.*, **2002**, *68*, 2794-2801.
4. Sutherland, I.W., Biofilm exopolysaccharides: a strong and sticky framework. *Microbiology*, **2001**, *147*, 3-9.
5. Otto, K., Norbeck, J., Larsson, T., Karlsson, K.-A., and Hermansson, M., Adhesion of type 1-Fimbriated *Escherichia coli* to abiotic surfaces leads to altered composition of outer membrane proteins. *J. Bacteriol.*, **2001**, *183*, 2445-2453.
6. Bodenmiller, D., Toh, E., and Brun, Y.V., Development of surface adhesion in *Caulobacter crescentus*. *J. Bacteriol.*, **2004**, *186*, 1438-1447.
7. Burmeister, J.S., Vraný, J.D., Reichert, W.M., and Truskey, G.A., Effect of fibronectin amount and conformation on the strength of endothelial cell adhesion to HEMA/EMA copolymers. *J. Biomed. Mater. Res.*, **1996**, *30*, 13-22.
8. Fang, H.H., Chan, K.Y., and Xu, L.C., Quantification of bacterial adhesion forces using atomic force microscopy (AFM). *J. Microbiol. Methods.*, **2000**, *40*, 89-97.

9. Ong, Y.L., Razatos, A., Georgiou, G., and Sharma, M.M., Adhesion Forces between *E. coli* Bacteria and Biomaterial Surfaces. *Langmuir*, **1999**, *15*, 2719-2725.
10. Sagvolden, G., Giaever, I., Pettersen, E.O., and Feder, J., Cell adhesion force microscopy. *Proc. Natl. Acad. Sci. USA*, **1999**, *96*, 471-476.
11. Francis, G., Fisher, L., Gamble, R., and Gingell, D., Direct measurement of cell detachment force on single cells using a new electromechanical method. *J. Cell Sci.*, **1987**, *87*, 519-523.
12. Tsang, P.H., Li, G., Brun, Y.V., Freund, L.B., and Tang, J.X., Adhesion of single bacterial cells in the micronewton range. *Proc. Nat. Acad. Sci. USA*, **2006**, *103*, 5764-5768.
13. Poindexter, J.S., The *Caulobacters*: ubiquitous unusual bacteria. *Microbiol. Rev.*, **1981**, *45*, 123-179.
14. Corpe, W.A., *Microfouling: the role of primary film forming marine bacteria.*, in *Proceedings of the Third International Congress on Marine Corrosion and Fouling*, R.F. Acker, et al., Editors. 1972, Northwestern University Press: Evanston, Ill. p. 598-608.
15. Smith, C.S., Hinz, A., Bodenmiller, D., Larson, D.E., and Brun, Y.V., Identification of genes required for synthesis of the adhesive holdfast in *Caulobacter crescentus*. *J. Bacteriol.*, **2003**, *185*, 1342-1442.
16. Poindexter, J.S., Biological properties and classification of the *Caulobacter crescentus* group. *Bacteriol. Rev.*, **1964**, *28*, 231-295.
17. Poindexter, J.S., Selection for nonbuoyant morphological mutant of *Caulobacter crescentus*. *J. Bacteriol.*, **1978**, *135*, 1141-1145.
18. Gonin, M., Quardokus, E.M., O'Donnol, D., Maddock, J., and Brun, Y.V., Regulation of stalk elongation by phosphate in *Caulobacter crescentus*. *J. Bacteriol.*, **2000**, *182*, 337-347.

Chapter 15

Modeling Bacterial Adhesion and Transport in the Environment: Surface Free Energy Relationships in Interpreting Bacterial Deposition in Porous Media

Gang Chen, Amy Chan Hilton, and Mitch Williams

Department of Civil and Environmental Engineering, FAMU-FSU,
College of Engineering, Tallahassee, FL 32310

Bacterial transport in the subsurface has received considerable attention either because of possible contamination of drinking water supplies, or their roles in *in-situ* bioremediation. Bacterial transport is governed by their adherence propensity to soil matrices, which is determined by their surface physicochemical properties and influenced by transport conditions such as solution chemistry, i.e., pH and ionic strength. Bacterial strains with different cell surface properties show different adhesion kinetics and affinity for soil matrices. It has been proven that the initial adhesion of bacteria to soil matrices plays an important role in bacterial transport, which can be explained in terms of bacterial interaction free energy with soil matrices. Using laboratory column or field experiments, researchers investigated bacterial transport in porous media and fitted bacterial transport breakthrough curves with the advection-dispersion equation. The fitted bacterial deposition is related to the interaction free energy between bacterial cells and media surfaces, which can be described by the Derjaguin-Landau-Verwey-Overbeek (DLVO) theory.

Introduction

Interest in predicting the fate and transport of bacteria in the subsurface is motivated by either a concern that bacteria can contaminate drinking water supplies or their role in bioremediation (1). Bacterial transport is affected by a variety of factors, including cell propensity for sorption to the soil matrix (2, 3). Model calculations with support of numerical simulation techniques have aided in the identification of the key processes that govern the bacterial transport and sorption, which makes it possible to evaluate bacterial adsorption mechanisms more effectively. The recently developed two-site and two-region transport models, which well define solute transport, have also been introduced to describe bacterial transport. These models assume that the solid phase can be partitioned into kinetic and equilibrium sorption sites or the liquid phase can be partitioned into mobile (flowing) and immobile (stagnant) regions. Mass exchange exists between the two sites or the two regions. Based on the two-site model, bacteria are assumed to deposit on kinetically controlled adsorption sites only. Based on the two-region transport model, bacterial attachment to porous media is assumed to be composed of two processes: bacterial transfer from the mobile region to the immobile region owing to the concentration gradient and bacterial deposition in the immobile region owing to attractive interactions between bacteria and the media.

Traditional and extended DLVO theories have been successfully introduced in describing bacterial surface thermodynamics (2, 4, 5). Assuming that bacteria behave as inert particles and that bacterial adhesion can be understood by a physicochemical approach, DLVO theory can be used in describing bacterial adsorption in porous media. In the early eighties, van Loosdrecht (6) reported the applicability of the DLVO theory for the interpretation of bacterial adhesion to glass as well as more practical surfaces (Rhine river sediment and protein-coated surfaces). Further, by assuming that bacteria can be modeled as spheres, van Loosdrecht *et al.* (7) demonstrated that the DLVO theory could be used to calculate the interaction Gibbs free energy between a cell and a surface as a function of the separation distance. More recently, researchers have linked the DLVO theory to bacterial transport observations (8, 9, 10).

Bacterial Surface Thermodynamic Properties

Over the past decade, efforts have been made to characterize bacterial surfaces as well as their attachment to abiotic surfaces thermodynamically using the DLVO theory (11). According to DLVO theory, bacterial surfaces can be described by their surface thermodynamic parameters of van der Waals component of surface tension (γ^{LW}), electron-acceptor parameter (γ^+) and

electron-donor parameter (γ^-) of Lewis acid/base component of surface tension and surface potential (ψ). Bacterial thermodynamic components can be determined independently, and used to calculate microbe-substratum interactions. These interactions are very well understood and formulated in mathematical equations. Bacterial initial adhesion on abiotic surfaces can thus be evaluated using the total free energy of these interactions calculated based on their surface thermodynamic properties.

Bacterial surface thermodynamic properties can be obtained through contact angle measurements using the van Oss-Chaudhury-Good equation (12):

$$(1 + \cos\theta)\gamma_L = 2(\sqrt{\gamma_S^{LW}\gamma_L^{LW}} + \sqrt{\gamma_S^+\gamma_L^-} + \sqrt{\gamma_S^-\gamma_L^+}) \quad (1)$$

where γ_L is the surface tension of the liquid that is used for the measurement; γ^{LW} is the Lifshitz-van der Waals component of surface tension (subscript S for solid and L for liquid); γ^+ is the electron-acceptor parameter and γ^- is the electron-donor parameter of Lewis acid/base component of surface tension. In addition, liquid surface tension γ_L can be expressed in terms of Lifshitz-van der Waals and Lewis acid/base components of surface tension γ_L^{LW} , γ_L^+ and γ_L^- :

$$\gamma_L = \gamma_L^{LW} + 2\sqrt{\gamma_L^-\gamma_L^+} \quad (2)$$

For the determination of bacterial surface thermodynamic properties, i.e., γ_S^{LW} , γ_S^+ and γ_S^- , three contact angle measurements (with three different liquids) are needed.

Bacterial contact angles are measured by depositing bacterial cells on a flat surface, growth of cells on a flat solid (nutrient) media, or suction-filtrating cell suspensions onto a flat filter (4, 8, 9). As a certain amount of moisture is required during contact angle measurements to maintain a smooth and measurable surface, the measured bacterial surface thermodynamic properties depend on lawn moisture contents.

Bacterial Interaction Quantification

Bacterial interactions with porous media are correlated with bacterial outer surface physicochemical properties (9, 13, 14). Interactions of bacteria with different cell surface properties can be characterized and quantified differently in terms of their overall surface thermodynamic properties (15 - 17). Qualitatively, the traditional DLVO theory has been developed to explain the attachment trends in terms of electrolyte concentrations (18 - 22). When the traditional DLVO theory fails in explaining bacterial adhesion, hydrophobic or hydration forces have been suggested to account for the discrepancy (11, 12, 23 - 25). Under

many conditions, hydrophobic or hydration forces have been shown to be important in bacterial interactions, especially at high ionic strength when electrostatic interactions are not important.

Assuming bacteria can be modeled as a sphere having a radius that is at least one order of magnitude less than that of media grains, a sphere-flat plate configuration can be adopted to simplify the description of interactions between bacteria and the media. The distance-dependent Lifshitz-van der Waals interactions between a spherical microbe, 1, and a flat plate media grain, 2, immersed in water, 3, are given by (12):

$$\Delta G_{132}^{LW} (\text{sphere} - \text{plate}) = \frac{A}{6} \left[\frac{2R^2}{y(4R+y)} + \frac{2R^2}{(2R+y)^2} + \text{Ln} \frac{y(4R+y)}{(2R+y)^2} \right] \quad (3)$$

where y is the distance between the bacterial surfaces (sphere) and the media matrix (flat plate) measured from the outer edge of the sphere; R is the radius of the bacterium and A is the Hamaker constant, which can be obtained from the Gibbs free energy at the equilibrium distance, i.e.,

$$A = 12\pi y_0^2 \Delta G_{y_0}^{LW} \quad (4)$$

where y_0 is the equilibrium distance of 1.57 Å, which was obtained by comparison of a sizable number of liquid and solid compounds (12); $\Delta G_{y_0}^{LW}$ is the van der Waals interaction free energy of two parallel plates, 1 and 2, immersed in water 3 at y_0 and can be calculated based on bacterial and porous media surface thermodynamic properties (18):

$$\Delta G_{y_0}^{LW} = -2(\sqrt{\gamma_3^{LW}} - \sqrt{\gamma_2^{LW}})(\sqrt{\gamma_3^{LW}} - \sqrt{\gamma_1^{LW}}) \quad (5)$$

where $\gamma_{1,W}$ is the Lifshitz-van der Waals component of surface tension and subscript 1, 2 and 3 denote bacteria, porous media and water, respectively.

The Lewis acid/base interaction free energy ΔG_{132}^{AB} decays exponentially from the Gibbs free energy value at the equilibrium distance (18):

$$\Delta G(y)_{132}^{AB} = 2\pi R y_0 \Delta G_{y_0}^{AB} e^{(y_0 - y)/\lambda} \quad (6)$$

where λ is the water decay length (0.6 nm for pure water) (12) and $\Delta G_{y_0}^{AB}$ is the Lewis acid/base interaction free energy of two parallel plates, 1 and 2, immersed in water 3 at the equilibrium distance (18):

$$\Delta G_{y_0}^{AB} = 2[(\sqrt{\gamma_1^+} - \sqrt{\gamma_2^+})(\sqrt{\gamma_1^-} - \sqrt{\gamma_2^-}) - (\sqrt{\gamma_1^+} - \sqrt{\gamma_3^+})(\sqrt{\gamma_1^-} - \sqrt{\gamma_3^-}) - (\sqrt{\gamma_2^+} - \sqrt{\gamma_3^+})(\sqrt{\gamma_2^-} - \sqrt{\gamma_3^-})] \quad (7)$$

where γ^+ and γ^- are electron-acceptor and electron-donor parameters of Lewis acid/base component of surface tension.

The electrostatic interaction free energy $\Delta G_{132}^{\text{EL}}$ can be evaluated by (constant potential approach valid for $\kappa y > 10$) (12):

$$\Delta G(y)_{132}^{\text{EL}} = \pi \epsilon \epsilon_0 R [2 \psi_{01} \psi_{02} \text{Ln} \left(\frac{1 + e^{-\kappa y}}{1 - e^{-\kappa y}} \right) + (\psi_{01}^2 + \psi_{02}^2) \text{Ln} (1 - e^{-2\kappa y})] \quad (8)$$

where ϵ and ϵ_0 are the relative dielectric permittivity of water (78.55 for water at 25°C) and permittivity under vacuum (8.854×10^{-12} C/V·m) respectively; $1/\kappa$ is the Debye-Hückel length that is also an estimation of the effective thickness of the electrical double layer (26); and ψ_{01} , ψ_{02} are the potentials at the bacterial and media surfaces, which can be calculated by:

$$\psi_0 = \zeta(1 + z/r) \exp(\kappa z) \quad (9)$$

where ζ is the zeta potential measured at the slipping plate; z is the distance from the particle surface to the slipping plate; and r is the radius of the particle.

The DLVO theory can be verified by direct measurement of the interaction forces by means of atomic force microscopy (AFM) measurements. AFM measurements probe molecular interactions and surface physicochemical properties, which contribute to our knowledge of cell surface functions and provide new insight into the structure-function relationships of bacterial surfaces (27). The development of AFM or scanning probe microscopy has opened the door for researchers to obtain topographical images and force measurements on living cells. In recent years, AFM has been applied to measure intermolecular forces for a variety of systems, including van der Waals, electrostatic, solvation, hydration, and steric/bridging forces (28). The main advantages of AFM over other techniques are that images and force curves can be obtained *in-situ* and can provide quantitative morphological information and direct interaction measurements.

Bacterial Transport Model

Saturated Bacterial Transport

Under saturated conditions, bacterial transport is controlled by bacterial adsorption to media matrices, which is typically classified as a kinetic adsorption process (29 - 35). Experimentally, model calculations have made it possible to evaluate bacterial transport effectively with support of numerical simulation techniques to characterize the adsorption processes (36). Practically, two-site models have been developed to account for both equilibrium and kinetic adsorption processes with an assumption that bacterial adsorption only occurs at

kinetic sorption sites (37). Two-site models provide better descriptions of bacterial transport to account for the complications arising from the potential of bacteria to react with different components of the media matrices at different rates and with varying intensities. These two-site models consist of an expression for an equilibrium isotherm which can be used to describe bacterial retention at the fraction of the adsorption sites that are equilibrium controlled, combined with an expression for a kinetic rate law that can be used to describe bacterial adhesion at the remaining fraction of the adsorption sites that are assumed to be kinetically controlled. Adsorption at equilibrium sites is assumed to be instantaneous and can be represented using either linear or nonlinear adsorption isotherms, while adsorption at kinetic sites is usually assumed to exhibit a time-dependent, first-order irreversible reaction (37):

$$\left(1 + f \frac{\rho_b K_d}{\theta}\right) \frac{\partial C}{\partial t} = D \frac{\partial^2 C}{\partial x^2} - v \frac{\partial C}{\partial x} - \omega \frac{\rho_b}{\theta} [(1-f)K_d C - S_k] \quad (10)$$

$$\frac{\partial S_k}{\partial t} = \omega [(1-f)K_d C - S_k] - \mu_{s,k} S_k \quad (11)$$

where C is the bacterial concentration in the liquid phase; t is the elapsed time; f is the fraction of exchange sites that are assumed to be in equilibrium with bacteria; ρ_b is the bulk density of the porous media; K_d is the partitioning coefficient of bacteria between the porous media and the aqueous phase; θ is the media porosity; D is the longitudinal dispersion coefficient; x is the position coordinate parallel to the direction of flow; v is the pore-water velocity; ω is the mass transfer rate coefficient; S_k is the bacterial concentration on the solid phase; and $\mu_{s,k}$ is the bacterial deposition rate coefficient on the kinetic adsorption sites of the porous media.

Based on the filtration theory, bacterial deposition rate coefficient $\mu_{s,k}$ in packed-bed systems (e.g., subsurface geological formations) can be expressed as (38):

$$\mu_{s,k} = \frac{3}{2} \frac{(1-\theta)}{d_c} \alpha \eta^* v \quad (12)$$

where d_c is the diameter of the porous media grain; α is the collision efficiency factor; and η^* is the single collector efficiency. The collision efficiency factor, α , represents the probability of bacteria to attach upon reaching the collector surface and is a function of fractional surface coverage, ϕ if monolayer sorption is assumed (39):

$$\alpha = \alpha_0 (1 - B\phi) \quad (13)$$

where α_0 is the clean bed collision efficiency; B is the blocking factor; and ϕ is the fractional surface coverage with bacterial cells, which represents the

percentage of the bacterial surface that is covered or attached with bacterial cells.

The single collector efficiency, η^* , represents the ratio of the rate at which bacteria strike the collector to the rate at which bacteria approach the collector. Disregarding effects of gravitational forces in deposition (an assumption that should be true for bacterial cells because the cell density is close to that of water) and also disregarding effects of straining (an assumption that should also be valid because bacterial cells are so much smaller than the media grain), η^* due to interception alone is given by (29, 40):

$$\eta^* = 4A_s^{(1/3)} N_{pe}^{(-2/3)} \quad (14)$$

where

$$A_s = 2(1 - p^5)/(2 - 3p + 3p^5 - 2p^6) \quad (15)$$

$$N_{pe} = 3\pi\mu_b d_c v/(kT) \quad (16)$$

where $p=(1-\theta)^{1/3}$; μ is the fluid viscosity (1.002×10^{-3} N·s/m² for water at 20°C); d_b is the bacterial diameter; k is the Boltzmann constant (1.38048×10^{-23} J/K); and T is the absolute temperature. It should be noted that new expressions have been proposed for the calculation of η^* , though further validation is required (41).

Unsaturated Bacterial Transport

Bacterial transport in unsaturated porous media has often been found to correspond to the mobile-immobile region concept (42):

$$(\eta_m + f\rho_b K_d) \frac{\partial C_m}{\partial t} = \eta_m D_m \frac{\partial^2 C_m}{\partial x^2} - J_m \frac{\partial C_m}{\partial x} - \omega(C_m - C_{im}) \quad (17)$$

$$[\eta_{im} + (1 - f)\rho_b K_d] \frac{\partial C_{im}}{\partial t} = \omega(C_m - C_{im}) - \eta_{im} \mu_{L,im} C_{im} - (1 - f)\rho_b K_d \mu_{s,im} C_{im} \quad (18)$$

where C_m and C_{im} are bacterial concentrations in the mobile and immobile region of the liquid phase, respectively; η_m and η_{im} are mobile and immobile volumetric water content; D_m is the longitudinal hydrodynamic dispersion coefficient in the mobile region; ω is the mass transfer coefficient governing the rate of bacterial exchange between the mobile and immobile regions of the liquid phase; $\mu_{L,im}$ and $\mu_{s,im}$ are the bacterial capturing rate coefficient at the air-water interface and deposition rate coefficient at the media surface from the immobile liquid phase.

It is assumed that bacterial retention in the system is either captured at the solid-liquid interface by physicochemical deposition or captured at the air-water interface owing to capillary forces or captured in small pore throats at the air-water-solid three phase interface due to physical constrains. Bacterial deposition at the solid-liquid interface is similar to that of saturated transport. Bacterial attachment to the air-water interface is usually assumed to be irreversible and the attachment is determined by the bacterial surface physicochemistry. Film straining is the special case of bacterial attachment at the air-water interface and occurs when the thickness of the water film is smaller than the diameter of bacteria (43). Even at high water saturation, film straining is still likely to occur as water film thickness distribution is uneven within the system owing to the heterogeneity of porous media surfaces. At regions where water film thickness is greater than the bacterial diameter, bacteria can be captured at the solid-liquid interface by physicochemical deposition or captured at the air-water interface owing to capillary forces. If bacteria do not attach at the air-water interface, in most cases, they do not deposit at the solid-liquid interface either. Physical constraints occur when bacteria are entrapped in pore throats at the air-water-solid three phase interface that are too small to allow the bacteria to pass through. Physical constrains are greatly effected by the bacterial size and media size distribution as well as water saturation (44, 45).

DLVO Theory in Describing Bacterial Adhesion

The strength of the initial adhesion of bacteria to abiotic substrate is of special interest, as the following biological process can proceed only if initial adhesion occurs (46). During the initial adhesion process, the density of bacterial cells is almost the same as that of the bulk media, making the gravitational settling of the cells of minor importance. Bacterial deposition in porous media is projected in the following discription: when bacterial cells get close to porous media surfaces owing to solute transport, molecular diffusion or Brownian movement, they first encounter the strong repulsive electrostatic interactions. At this stage, the free energy of attractive van der Waals and Lewis acid/base interactions is much smaller as compared to those of repulsive electrostatic interactions. With decreasing in separating distance, the free energy of repulsive electrostatic interactions decreases. On the other hand, attractive van der Waals and Lewis acid/base interactions increase with the decrease of separation distance. Once bacteria are in close proximity to media surfaces, Lifshitz-van der Waals and Lewis acid/base interactions begin to dominate over electrostatic interactions. Lifshitz-van der Waals and Lewis acid/base interactions as the driving forces for bacteria adhesion on media surfaces can be quantified at the equilibrium distance where physical contact between bacteria

and media matrices occurs. Eventually, bacteria have a net attractive free energy with the porous media when they are close enough to the media. Only those that have enough energy to overcome the repulsive barrier can reach the porous media and attach.

Bacterial initial adhesion on abiotic surfaces can be evaluated using the total free energy of interactions between bacteria and substrate as a function of separation distance ($\Delta G_{132}^{\text{TOT}}$), which is the sum of van der Waals interaction free energy ($\Delta G_{132}^{\text{LW}}$), Lewis acid/base interaction free energy ($\Delta G_{132}^{\text{AB}}$) and electrostatic interaction free energy ($\Delta G_{132}^{\text{EL}}$) (25). $\Delta G_{132}^{\text{LW}}$ and $\Delta G_{132}^{\text{AB}}$ are usually negative, which contribute attractions between bacteria and abiotic substrate. $\Delta G_{132}^{\text{EL}}$ is usually positive because both bacteria and substrate are commonly negatively charged. Using column experiments, transport of typical Gram-negative and Gram-positive bacterial strains of *E. coli*, *P. aeruginosa*, *P. fluorescens*, *P. putida*, *P. sp* and *B. subtilis* was performed and their transport was simulated using bacterial transport models (Figure 1) (9). Bacterial transport parameters was linked to their interaction free energy with the porous media. Figure 2 shows bacterial deposition as a function of the maximum free energy of electrostatic interactions between *E. coli*, *P. fluorescens* and silica sand and Figure 3 shows bacterial deposition as a function of the free energy of Lifshitz-van der Waals interactions evaluated at the equilibrium distance. The deposition coefficient of both *E. coli* and *P. fluorescens* decreases exponentially with these two interactions. By comparing the effects of these two interactions, electrostatic interactions play a more important role than Lifshitz-van der Waals interactions in determining bacterial deposition in the porous media according to the fact that the slope of the deposition coefficient versus electrostatic interaction free energy curve is much steeper than versus Lifshitz-van der Waals interaction free energy (Figure 4).

More specifically, the clean bed collision efficiency, α_0 is found to be an exponential function of the total interaction free energy between bacteria and the porous media (Figure 5) (9):

$$\alpha_0 = f(e^{-\Delta G_{132}^{\text{TOT}} / kT}) \quad (19)$$

Since deposited bacterial cells on media surfaces alter interactions between bacteria and the media by changing the media surface properties, which impacts the consequent deposition of bacteria, the blocking factor, B is further proven to be a function of the total free energy of the cell-cell interactions (Figure 6) (9):

$$B = f\left(\frac{1}{e^{\Delta G_{131}^{\text{TOT}} / kT}}\right) \quad (20)$$

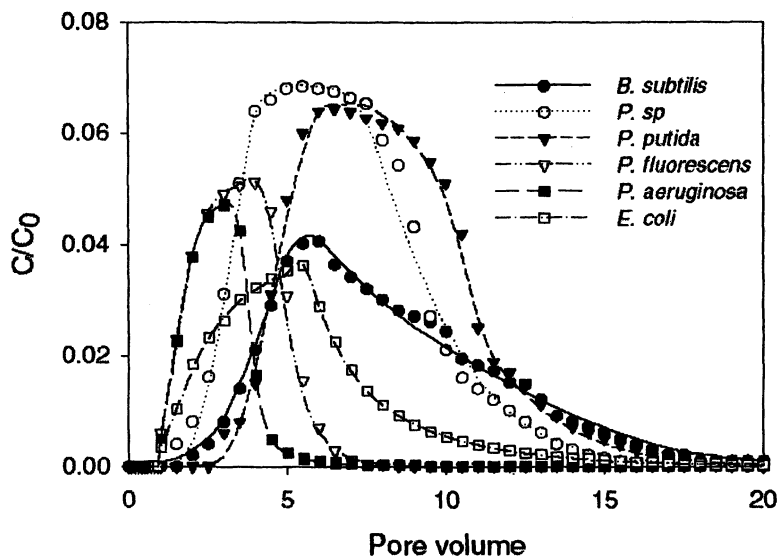


Figure 1. Bacterial breakthrough curves and model simulations (Symbols are observations and lines are model simulations) (Reproduced with permission from reference 9. Copyright 2003.)

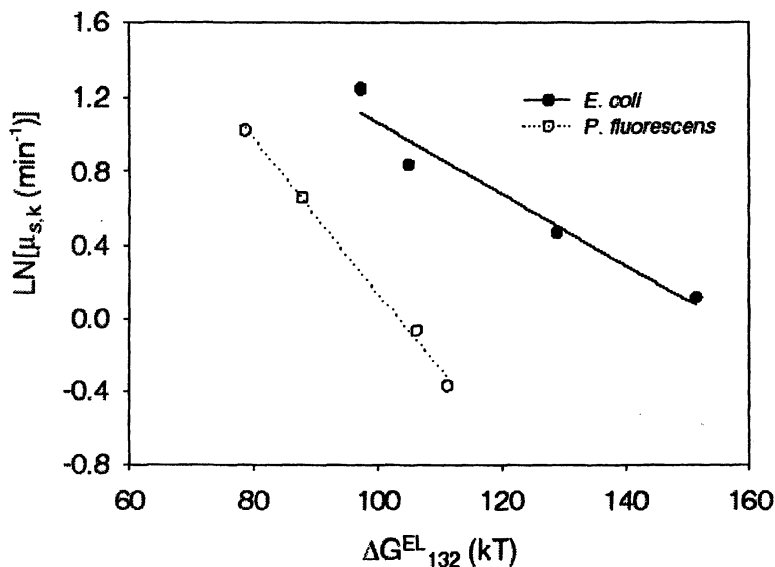


Figure 2. Deposition coefficient as a function of maximum electrostatic interaction free energy (Reproduced with permission from reference 10. Copyright 2004.)

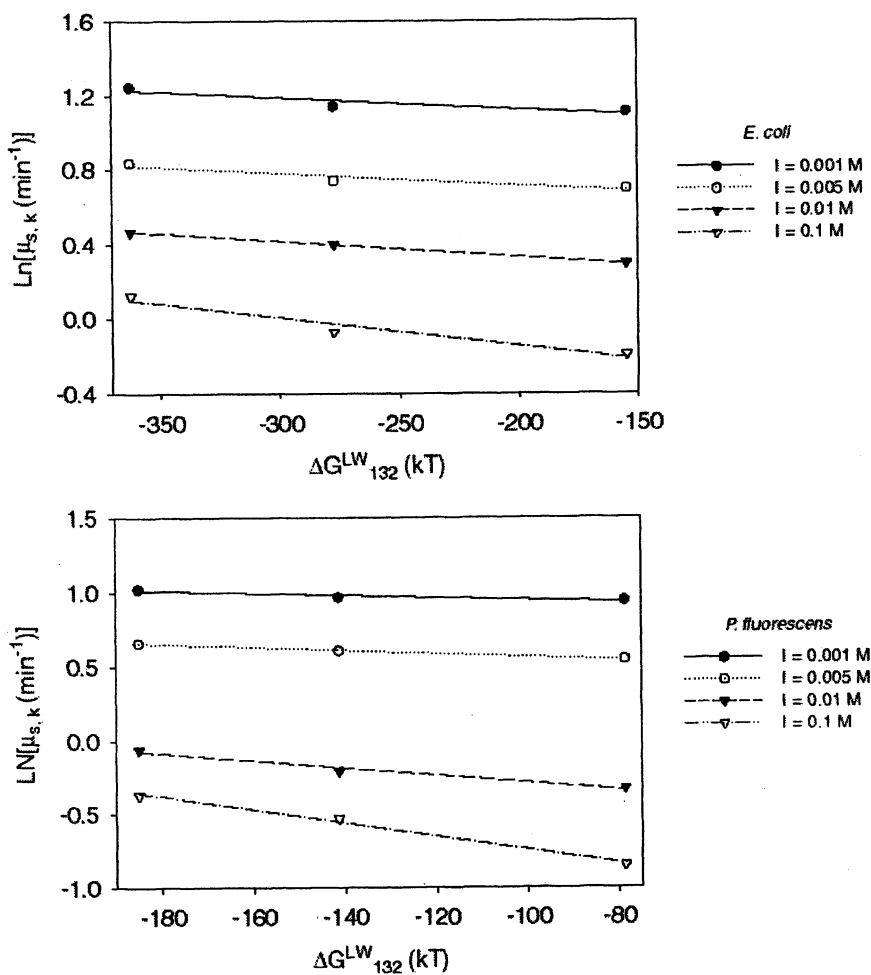


Figure 3. Deposition coefficient as a functions of Lifshitz-van der Waals interaction free energy evaluated at equilibrium distance (Reproduced with permission from reference 10. Copyright 2004.)

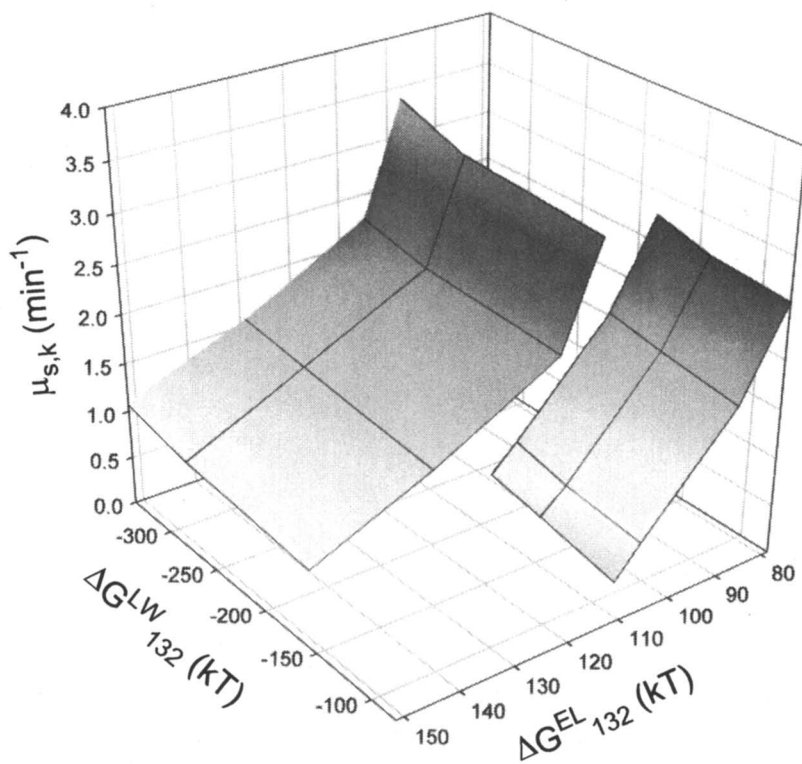


Figure 4. Deposition coefficient as a functions of maximum electrostatic interaction free energy and Lifshitz–van der Waals interaction free energy evaluated at equilibrium distance (Left image denotes E. coli and right one denotes P. fluorescens) (Reproduced with permission from reference 10. Copyright 2004.)

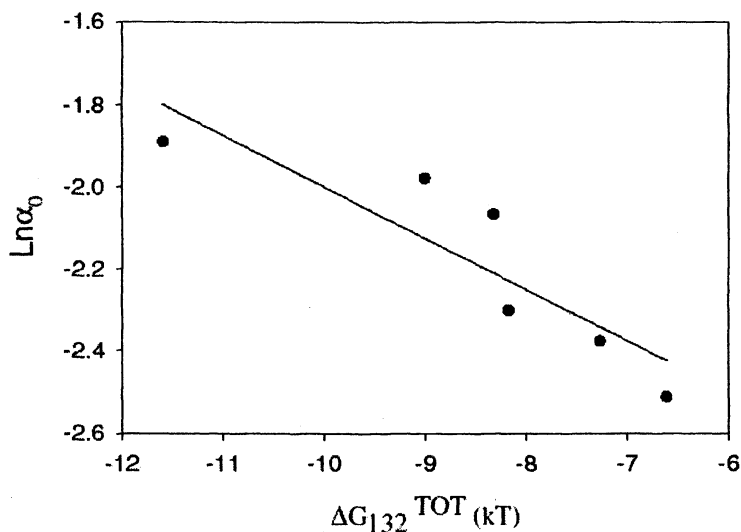


Figure 5. Exponential function of α_0 as a function of total interaction free energy between bacteria and porous media (Reproduced with permission from reference 9. Copyright 2003.)

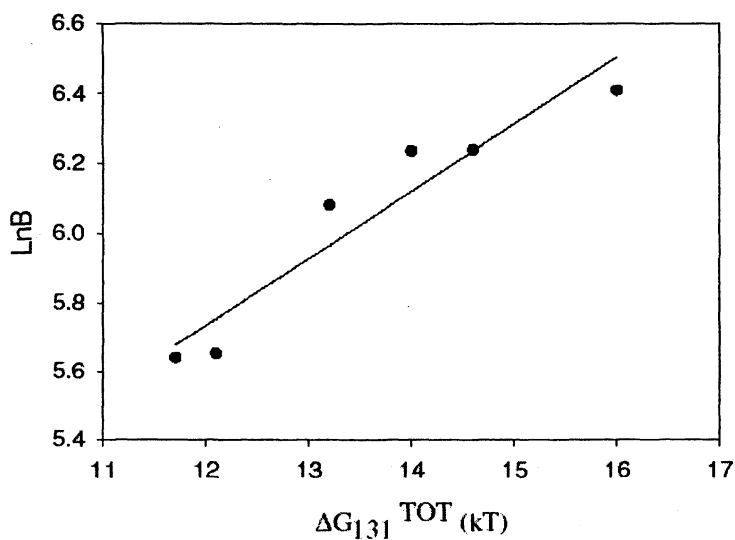


Figure 6. Exponential function of B as a function of total interaction free energy between deposited bacterial cells and suspended bacterial cells (Reproduced with permission from reference 9. Copyright 2003.)

Summary

The application of natural attenuation of organic contaminants or *in-situ* bioremediation is severely limited by the understanding of bacterial migration in the subsurface. Biological, chemical, and hydrologic factors all impact bacterial transport in the subsurface. It is well accepted that bacterial transport in the subsurface is governed by their adherence propensity to soil matrices, which is determined by their surface physicochemical properties. To date, much work has been done in describing how physical and chemical variations in the subsurface result in changes in bacterial migration, and yet, further insights into the subsurface as a habitat for microorganisms requires the understanding of bacteria and media interactions. This review summarizes the usage of the traditional and extended DLVO theories in describing bacterial sorption processes by linking bacterial transport to their interactions with the porous media. The application of DLVO theory in describing bacterial subsurface transport provides a rational forecasting framework for engineered *in-situ* bioremediation by applying fundamental science principles to facilitate the development of engineering strategies. Bacterial surface thermodynamic theory has the potential to work as a bridge to connect micro-scale bacterial interactions with macro-scale biological functions. With the help of bacterial surface thermodynamic theory, bacterial fate and transport in the subsurface can be predicted and controlled, which is of great interest for engineering practices. With its easy measurements and important functions, bacterial surface thermodynamics is becoming an important microbial physical and biological parameter.

References

1. Fontes, D.E.; Mills, A. L.; Hornberger, G. M.; Herman, J. S. *Appl. Environ. Microbiol.* **1991**, *57*, 2473.
2. Smets, B. F.; Rittmann, B. E.; Stahl, D. A. *Appl. Environ. Microbiol.* **1993**, *59*, 3430.
3. Karickhoff, S. W.; Brown, D. S.; Scott, T. A. *Water Res.* **1979**, *13*, 241.
4. Grasso, D.; Smets, B. F.; Strevett, K. A.; Machinist, B. D.; van Oss, C. J.; Giese, R. F.; Wu, W. *Environ. Sci. Technol.* **1996**, *30*, 3604.
5. Chen, G.; Strevett, K. A. *Environ. Microbiol.* **2001**, *3*, 237.
6. van Loosdrecht, M. C. M. *Ph. D. thesis*; Wageningen Agricultural University, the Netherlands, 1988.
7. van Loosdrecht, M. C. M.; Lyklema, J.; Norde, W.; Zehnder, A. J. B. *Microb. Ecol.* **1989**, *17*, 1.

8. Chen, G.; Strevett, K. A. *J. Environ. Eng.* **2002**, *128*, 1.
9. Chen, G.; Strevett, K. A. *Environ. Engr. Sci.* **2003**, *20*, 237.
10. Chen, G.; Zhu, H. *Res. Microbiol.* **2004**, *155*, 467.
11. Hermansson, M. *Colloids Surf. B: Biointerf.* **1999**, *14*, 105.
12. van Oss, C. J. *Interfacial Forces in Aqueous Media*; Marcel Dekker: New York, 1994.
13. Briandet, R.; Meylheuc, T.; Maher, C.; Bellon-Fontaine, M. *Appl. Environ. Microbiol.* **1999**, *65*, 5328.
14. Gallardo-Moreno, A. M.; Méndez-Vilas, A.; González-Martín, M. L.; Nuevo, M. J.; Bruque, J. M.; Garduño, E.; Pérez-Giraldo, C. *Langmuir* **2002**, *18*, 3639.
15. Israelachvili, J. N. *Intermolecular and Surface Forces*; Academic Press: London, 1991.
16. van der Mei, H. C.; van de Belt-Gritter, B.; Doyle, R. J.; Busscher, H. J. *J. Colloid Interface Sci.* **2001**, *241*, 327.
17. Bakker, D. P.; Busscher, H. J.; van der Mei, H. C. *Microbiol-SGM.* **2002**, *148*, 597.
18. Meinders, J. M.; van der Mei, H. C.; Busscher, H. J. *J. Colloid Interface Sci.* **1995**, *176*, 329.
19. Bos, R.; van der Mei, H. C.; Busscher, H. J. *FEMS Microbiol. Rev.* **1999**, *23*, 179.
20. Gottenbos, B.; Grijpma, D. W.; van der Mei, H. C.; Feijen, J.; Busscher, H. J. *J. Antimicrob. Chemoth.* **2001**, *48*, 7.
21. Gottenbos, B.; van der Mei, H. C.; Busscher, H. J. *Method Enzymol.* **1999**, *310*, 523.
22. Gottenbos, B.; van der Mei, H. C.; Busscher, H. J. *J. Biomed. Mater Res.* **2000**, *50*, 208.
23. Drozd, C.; Schwartzbrod, J. *Appl. Environ. Microbiol.* **1996**, *62*, 1227.
24. Briandet, R.; Herry, J. M.; Bellon-Fontaine, M. N. *Colloids Surf. B: Biointerf.* **2001**, *21*, 299.
25. Sharma P. K.; Rao, K. H. *Adv. Colloid Interface* **2002**, *98*, 341.
26. Marshall, K. C.; Breznak, J. A.; Calleja, G. B.; Mcfeters, G. A.; Rutter P. R. *Bacterial Adhesion and Aggregation*; Springer-Verlag: New York, 1984.
27. Gad, M.; Ikai, A. *Biophys. J.* **1995**, *69*, 2226.
28. Dufrene, Y. F. *J. Bacteriol.* **2002**, *184*, 5205.
29. Harvey R.W.; Garabedian, S. P. *Environ. Sci. Technol.* **1991**, *25*, 178.
30. Gannon, J. T.; Manilal, V.B.; Alexander, M. *Appl. Environ. Microbiol.* **1991**, *57*, 2497.
31. Hornberger, G. M.; Mills, A. L.; Herman, J. S. *Water Res. Res.* **1992**, *28*, 915.
32. Rijnaarts, H. H. M.; Norde, W.; Bouwer, E. J.; Lyklema, J.; Zehnder, A. J. B. *Environ. Sci. Technol.* **1996**, *30*, 2869.

33. Rijnaarts, H. H. M.; Norde, W.; Bouwer, E. J.; Lyklema, J.; Zehnder, A. J. B. *Environ. Sci. Technol.* **1996**, *30*, 2877.
34. Bolster, C. H.; Hornberger, G. M.; Mills, A. L.; Wilson, J. L. *Environ. Sci. Technol.* **1998**, *32*, 1329.
35. Powelson, D. K.; Mills, A. L. *Soil Sci.* **1998**, *163*, 694.
36. Skinner, G. E.; Larkin, J. W.; Rodehamel, E. J. *J. Food Saf.* **1994**, *14*, 175.
37. Šimůnek, J. M.; van Genuchten, M. Th. *The Hydrus-2D Software Package for Simulating Two-Dimensional Movement of Water, Heat and Multiple Solutes in Variably Saturated Media, Version 2.0 IGWMC-TPS-53*; International Ground water Modeling Center, Colorado School of Mines: Golden, CO, 1999.
38. Rajagopalan, R.; Tien, C. *AIChE J.* **1976**, *22*, 523.
39. Meinders, J. M.; Noordmans, J.; Busscher, H. J. *J. Colloid Interface Sci.* **1992**, *152*, 265.
40. Tien, C.; Turian, R. M.; Pandse, H. *AIChE J.* **1979**, *25*, 385.
41. Tufenkji, N.; Elimelech, M. *Environ. Sci. Technol.* **2004**, *38*, 529.
42. van Genuchten, M. Th.; Wagenet, R. J. *Soil Sci. Soc. Am. J.* **1989**, *53*, 1303.
43. Wan, J.; Tokunaga, T. K. *Environ. Sci. Technol.* **1997**, *31*, 2413.
44. Harvey, R. W.; Kinner, N. E.; MacDonald, D.; Metge, D. W.; Bunn, A. *Water Resour. Res.* **1993**, *29*, 2713.
45. Bradford, S. A.; Yates, S. R.; Betahar, M.; Simunek, J. *Water Resour. Res.* **2002**, *38*, 1327, doi: 10.1029/2002WR001340.
46. *Bacterial Adhesion to Surfaces*; Bekeley, R. C. W.; Lynch, J. M.; Melling, J.; Rutter, P. R.; Vincent, B. Edts.; Ellis Horwood Limited: Chichester, 1980.

Chapter 16

Mechanistic Modeling of Bacterial Transport in Saturated Porous Media

Kirk E. Nelson

Department of Civil and Environmental Engineering, University of
California, One Shields Avenue, Davis, CA 95616

Successful prediction of bacterial transport and adhesion in saturated natural porous media requires a fundamental mechanistic understanding of the important processes involved. Colloid filtration theory (CFT) provides a convenient framework for attaining this understanding, but the classical CFT was developed for non-living colloids and is still widely applied to the case of bacterial colloids without consideration of the unique traits of bacteria. This chapter lays the groundwork for using CFT to further our mechanistic understanding of bacterial transport processes at the laboratory column scale and below. Included in this is a reexamination of some of the key assumptions of CFT, notably those implicit in the derivation of the so-called filtration equation. A new form of the filtration equation is proposed for more reliable testing of the CFT parameter η (the frequency at which colloids come into contact with porous media surfaces or energy barriers) against experimental data. Initial work applying CFT to the case of bacterial polymer interactions is also presented.

Predicting the fate and transport of bacteria in saturated natural porous media is a complex and challenging endeavor that requires a fundamental mechanistic understanding of the physicochemical and biological processes impacting transport at multiple length and time scales. Ultimately, the multiplicity of controlling processes and scales of interest will call for a modeling approach that aims to account for the intricate coupling between all of the individual processes. The emerging body of work known as reactive transport modeling (c.f., 1, 2, 3) is such an approach that shows promise for providing a comprehensive accounting of all important processes and their couplings over all the relevant scales. However, a prerequisite, still requiring much work, for the successful application of reactive transport modeling to field-scale subsurface bacterial transport problems is a solid understanding and scientifically validated mechanistic description of the important individual processes.

This chapter discusses use of the conceptual framework provided by the colloid filtration theory (CFT) to acquire the requisite mechanistic understandings. CFT is based on an analysis of particle transport within an idealized pore space surrounding a single grain of the porous medium. The classical CFT translates this pore-scale analysis to the scale of a deep bed filter via a one-dimensional (1-D) mass balance. CFT was originally developed in the 1970's to tackle the problem of predicting particle deposition rates in deep-bed filtration. The use of CFT for modeling bacterial transport in groundwater aquifers was first suggested (4) in the late 1980's, and in the early 1990's it was implemented in an aquifer (5) and in laboratory column experiments (6). These initial applications of CFT to bacterial transport in saturated porous media assume that bacterial transport is controlled by the same processes as the inorganic colloids for which the classical CFT was formulated. This assumption is based on the fact that bacterial cells, having a diameter of about 1 μm , fall within the size range of colloids and, thus, as biocolloids, they experience the same physical transport mechanisms that are accounted for by CFT (convection by Stokes flow, hydrodynamic retardation, gravitational sedimentation, Brownian diffusion, and transport near solid surfaces induced by DLVO forces). However, it has been noted (7) that biological processes such as active adhesion/detachment, chemotaxis, and metabolic activity also influence bacterial transport.¹ Thus, there is a clear need to incorporate biological processes into CFT to further the theory's contribution to our understanding of subsurface

¹ In this chapter, the phrase "bacterial transport" implicitly includes the adhesion process as well, because the extent to which cells adhere to solid surfaces and the degree to which this adhesion is reversible are directly linked to the degree of transport that results. When "transport" is used by itself, it refers to the transport of a cell from the aqueous medium to the solid surface of the porous media grain in the pore-scale analysis.

bacterial transport. This chapter presents a critical review of the theoretical underpinnings of CFT and presents some initial work that has been completed towards the incorporation of biological processes. The scope of the discussion here is limited to the goal of attaining a mechanistic understanding of bacterial transport at the sub-pore, pore, and laboratory column scales.

Basic Parameters of CFT

CFT describes the deposition of suspended particles onto porous media grains as a two-step process. The first step – transport to the grain surface – is quantified by the collection efficiency (η), the frequency at which particles in the aqueous phase arrive at the surface of the solid phase (i.e., the “collector”). The second step – attachment to the grain surface – is quantified by the sticking efficiency (α), the frequency at which the particles arriving at the surface of the collector actually attach to it. In equation form, these definitions are:

$$\eta = \frac{r_S}{r_F} \quad (1)$$

$$\alpha = \frac{r_A}{r_S} \quad (2)$$

where

r_S = number of particles striking the collector per unit time

r_F = number of particles flowing towards the collector per unit time

r_A = number of particles attaching to the collector per unit time

It can be seen that the product $\alpha\eta$ gives the fraction of particles flowing towards the collector that become attached to it. It is important at this point to discuss the meaning of the phrases “striking the collector” in the definition of r_S and “arrive at the surface” in the definition of η preceding equation (1). Mathematically, the occurrence of “striking” or “arrival” has been defined as either a surface-to-surface separation distance of zero (δ) or the closest approach allowed by Born repulsion, taken to be 5 Å (ρ). In either case, this separation distance could not be reached under conditions in which electrostatic repulsion creates a significant energy barrier to the approach. Thus, the value of η can be thought of as representing either the frequency at which colloids arrive at the surface of the collector (within 5 Å or less) when electrostatic repulsion is

absent, or the frequency at which colloids arrive at the energy barrier when electrostatic repulsion is present.

In the initial development of CFT (10, 11), it was assumed that repulsive interactions were absent (i.e., α equals unity a priori). As researchers started to study systems with a significant energy barrier, a means for calculating α became necessary. The traditional approach for the application of CFT to real-world systems has been to calculate η a priori from the properties of the colloids, the flowing water, and the porous media grains. Then α is calibrated with the use of data from the actual filtration systems. Both η and α are assumed spatially constant. In the case of subsurface bacterial transport through aquifers, a common technique is to obtain parameters for field-scale transport models via lab-scale column transport experiments. The typical approach in such experiments has been to base the calibration of α on the effluent breakthrough concentrations. However, studies have also been reported in which the calculation of α is based on the fraction of retained particles in the column (12), as well as the measured profile of retained particles along the column (13, 14). In the studies using measured profiles, it has been found that the exponential decay of retained particles with distance predicted by the classical CFT² is exhibited when repulsive DLVO interactions are absent, but this spatial distribution is not exhibited when repulsive interactions are present. The important implication of this observation is that the assumption of a spatially constant α appears invalid for the case of an energy barrier.³ Researchers have also calibrated α based on field data (5). The η and α values (obtained via theory and calibration, respectively) are finally used in a macroscopic transport equation. In the case of subsurface bacterial (or in general, colloidal) transport, the transport equation is the advection-dispersion (also referred to as convective-diffusion or Smoluchowski) equation. In the case of deep-bed filtration, the transport equation is typically referred to as the filtration equation (which in its approximate form is equal to the solution of the steady-state Smoluchowski equation with diffusion neglected; the approximate and exact forms of the filtration equation are discussed in the section entitled "The Filtration Equation" below). The so-called filtration equation is also used for the calibration of α via column experiments.

² The reason for the predicted exponential decay is discussed in the section entitled "The Filtration Equation" below.

³ The lack of agreement between observed profiles when repulsive interactions are present and CFT predictions that assume a spatially constant α is an outstanding research question of relevance to both inorganic and biological colloids. As the focus of this chapter is incorporation of biological processes into the calculation of η , this issue is not discussed here, but the interested reader is referred elsewhere (c.f., 13-19).

The relevant quantities containing the product $\alpha\eta$ are k_{irr} , the irreversible adsorption constant for subsurface applications and λ , the filter coefficient for deep-bed filtration. Both of these quantities have the same mathematical definition and physical meaning: the rate of deposition per unit length of transport in the macroscopic porous medium. These deposition rate coefficients are derived from the filtration equation. The most commonly used formula for these rate coefficients is:

$$\lambda = k_{\text{irr}} = \frac{3(1-\varepsilon)}{2d_c} \alpha\eta \quad (3)$$

where ε is porosity and d_c is the collector (i.e., filter or aquifer grain) diameter. Later in this chapter, the filtration equation will be derived and alternate forms presented. One set of alternate forms stems from the choice of an approximate versus an exact characterization of the idealized macroscopic porous medium, and a second set of alternate forms stems from the way that r_f is defined in the model for η . It will be seen in the next section that the definition of r_f used by one of the principal studies in the CFT's development (11) requires a different expression for the deposition rate coefficients than that given by equation (3).

Equations for η

Several equations have been developed for predicting the parameter η as a function of system properties. The first such equation (10), referred to herein as the YHO equation, assumes that transport is controlled by interception⁴, diffusion, and sedimentation, and that these three mechanisms are independent, allowing for the summation of three analytical solutions to the Smoluchowski equation. Yao et al.'s analysis uses the isolated sphere model of porous media, which assumes the representative porous media grain (collector) is a spherical grain immersed in an unbounded aqueous medium. The YHO equation was improved upon by Rajagopalan and Tien (11) by including the following additional features: accounting of the constriction of flow due to neighboring grains via use of the Happel sphere-in-cell porous media model (20); use of the Happel model as a mapping between the idealized collector and pore space and the macroscopic porous medium; use of the Derjaguin-Verwey-Landau-

⁴ Interception refers to the deposition that occurs as a result of particle size and convective flow; a particle is said to be intercepted if it is being transported precisely on a streamline and the streamline comes within one particle radius of the collector surface.

Overbeek (DLVO) theory of colloidal stability to account for the effects of surface forces on particle trajectories at close approach distances; hydrodynamic retardation effect (for all mechanisms except diffusion) to account for increased viscous resistance to transport in the vicinity of the collector; use of a Lagrangian trajectory analysis in lieu of the convective-diffusion equation for all mechanisms except diffusion. The approximate closed-form solution for η (referred to herein as the RT equation) that resulted from their analysis has been the most commonly used means to calculate η for the past thirty years. The RT method for calculating η also provides the basic foundation for the simulation approach described later in this chapter for incorporation of biological processes into CFT.

The RT equation is based on Rajagopalan and Tien's trajectory analysis within the Happel sphere-in-cell porous media model (see Figure 1). To compute the trajectory of a particle suspended in the aqueous phase of the model porous medium, Rajagopalan and Tien performed a force and torque balance on the suspended particle. The forces and torques included in their deterministic analysis were gravity, the London van der Waals force, the convective force of the Happel flow field, and the drag forces and torques that result from the hydrodynamic retardation effect. Using their trajectory analysis, multiple computations of η were completed for the range of parameter values typical of deep-bed filtration ($0 \leq N_G \leq 10^{-1}$, $10^{-4} \leq N_R \leq 10^{-1}$, and $10^{-8} \leq N_{LO} \leq 10^{-1}$; see **Nomenclature** for definitions of the dimensionless numbers). Rajagopalan and Tien then performed a regression analysis on their numerical results to obtain an approximate closed-form expression for η . The component of η due to diffusion alone was added on separately (assuming that it acted independently of all deterministic forces) using the analytical solution of Levich (21) for the convective-diffusion equation with no external forces and interception neglected. This is the same analytical solution that was used in the YHO equation to represent diffusion as an independent mechanism.

The resulting RT equation was originally presented (11) as:

$$\eta \approx 0.72 A_S N_{LO}^{1/8} N_R^{15/8} + 0.0024 A_S N_G^{1.2} N_R^{-0.4} + 4 A_S^{1/3} N_{PE}^{-2/3} \quad (4)$$

where A_S is a porosity-dependent parameter accounting for the effects of neighboring collectors, N_{LO} is a dimensionless number describing the van der Waals attraction force, N_R is a dimensionless number describing the effect of particle and collector sizes, N_G is a dimensionless number describing the effect of gravitational sedimentation, and N_{PE} is a dimensionless number describing the effect of Brownian diffusion. The hydrodynamic retardation effect was considered in the development of the first two terms, but not the third term of equation (4). The first term of equation (4) characterizes the amount of collection that occurs due to the van der Waals attraction force (the inclusion of

which, it should be noted, is a mathematical necessity for nonzero η values due to the need for a mechanism to overcome hydrodynamic retardation). The second term of equation (4) characterizes the amount of collection that occurs due to gravitational sedimentation. The third term of equation (4) characterizes the amount of collection that occurs due to Brownian diffusion. The mechanism of interception is accounted for by the A_S and N_R factors.

An error in equation (4) has been noted (22, 23). The first two terms were derived by Rajagopalan and Tien's trajectory analysis which defines η based on the definition of flow through the Happel model (see Figure 1). This flow field was formulated such that the Happel sphere represents the entire filter bed (rather than an isolated sphere, or single collector, as in the YHO formulation), and this also ensures that η never exceeds unity (22). This is done by defining the total flux of particles approaching the collector (r_F) in terms of the concentric liquid envelope surrounding the collector instead of defining the total particle flux in terms of the projected area of the collector (as done by Yao et al.). The third term accounting for diffusion was developed using the Yao et al. definition of flux. Thus, the diffusion term must be transformed to the Happel definition of flow area. To do so, it can be multiplied by a factor equal to γ^2 where $\gamma = (1-\epsilon)^{1/3}$ and ϵ is the porosity. The first two terms of equation (4) have the γ^2 factor already incorporated for the particular value $\epsilon = 0.39$ (which Rajagopalan and Tien considered typical for deep-bed filtration). Multiplying the diffusion term by γ^2 and also extracting the hidden γ^2 out of the first two terms gives the following equation:

$$\eta \approx \gamma^2 [A_S N_{LO}^{1/8} N_R^{15/8} + 0.00338 A_S N_G^{1.2} N_R^{0.4} + 4 A_S^{1/3} N_{PE}^{-2/3}] \quad (5)$$

Equation (5) is what is referred to herein as the RT equation. In practice, the bracketed expression by itself has typically been used for calculating η , in which case the resulting η values are not consistent with Rajagopalan and Tien's definition of η for a packed bed (i.e., the definition of η that is based on the defined fluxes in the Happel model). In addition to being inconsistent with the definition of η given by equation (14) of the original paper (11), the form of the RT equation without γ^2 has the theoretical difficulty that it can result in η values greater than unity (22). This is because the quantity r_S in equation (1), the rate at which particles strike the collector, is taken from Rajagopalan and Tien's calculations that were based on the total flux of particles in the Happel sphere, whereas the quantity r_F in equation (1), the rate at which particles approach the collector, is taken as the flux from the projected area of the collector, which represents only part of the total flux of particles in the Happel sphere. Correct application of the RT equation for the purpose of studying the transport step

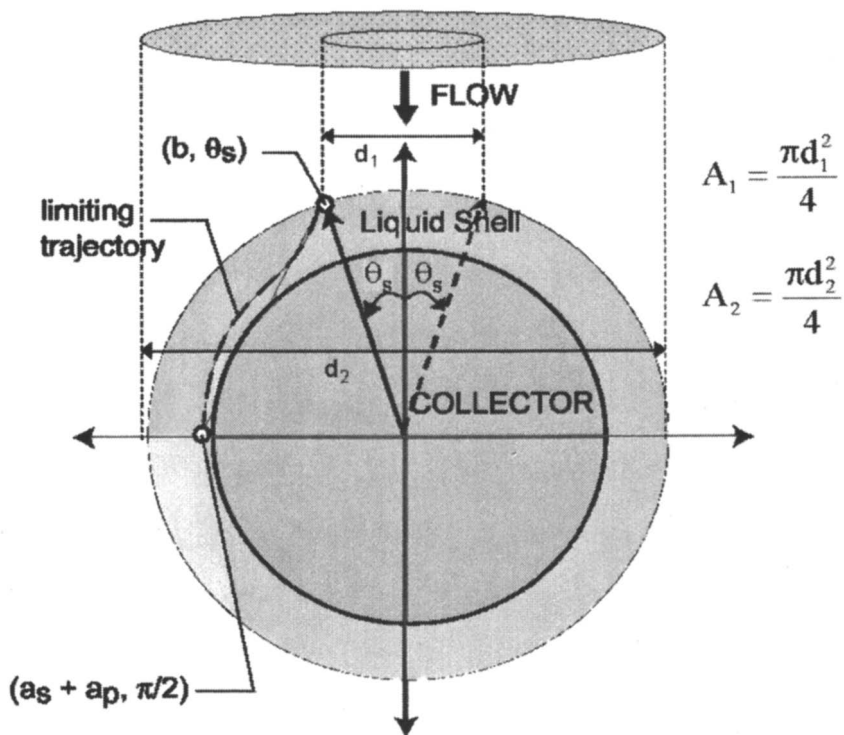


Figure 1. Happel's sphere-in-cell porous media model. When all forces are characterized deterministically, η is given by the ratio of area A_1 to area A_2 . (Reproduced from *Langmuir*, 2005, vol. 21, 2173. Copyright 2005 American Chemical Society.)

alone necessitates inclusion of the γ^2 factor in the formula for η (i.e., equation (5) exactly as written here).

Use of the RT equation without the γ^2 factor apparently stems from the presentation (23) of two alternatives for the use of the RT equation. The first alternative proposed, which will be referred to here as the "consistent collector choice", is to use the full form of equation (5) for calculation of η . Then, for calculation of α , the filtration equation of Yao et al. (10) is used in a modified form such that the coefficient in front of the term containing η is divided by γ^2 . How this modification comes about will be seen in the derivation of the filtration equation presented below (the section entitled "The Filtration Equation"). The second alternative proposed, which will be referred to here as the "inconsistent collector choice", is to calculate η only from the bracketed expression of equation (5). Then, the filtration equation of Yao et al. is used in

its original form. In effect, this second alternative consists of calculating η from the number of particles striking the Happel collector divided by the number of particles approaching the isolated collector (hence the term inconsistent collector choice). Since there are more particles flowing through the Happel model than the number flowing through the isolated sphere model, this approach can produce physically impossible η values (i.e., $\eta > 1$). The derivation of the filtration equation in the section entitled "The Filtration Equation" will further substantiate these interpretations of the two alternatives for applying the RT equation as a consistent collector choice and an inconsistent collector choice.

Recently, the first major development in the theory for calculating η since the RT equation has been presented. This new equation (8) is based on a numerical solution of the convective-diffusion equation in which hydrodynamic retardation and the van der Waals interaction force are incorporated. Additionally, the diffusion coefficient D_{BM} is allowed to be a function of separation distance, wherein the radial dependence is due to the hydrodynamic retardation effect. In this solution of the convective-diffusion equation, the flow field of the Happel model is used instead of the undisturbed Stokes flow field used for the YHO equation. However, in their definition of η , the approach rate of particles is based on the isolated collector model (the inconsistent collector choice). This can be seen directly from their equation (5):

$$\eta = \frac{I}{\pi a_c^2 U C_o} \quad (6)$$

where I is the overall rate of particle deposition onto the collector obtained by integration of the particle flux at the collector surface over the entire surface of the Happel collector (this is equivalent to r_s in equation (1)), and a_c is the radius of the Happel collector. Results were obtained by applying this solution technique to a wide range of parameter values typical of those found in both natural and engineered systems involving both inorganic and microbial colloids. They performed regression on the various dimensionless parameters and drew upon Yao et al.'s example of an additivity rule applying to the primary collection mechanisms, as well as another study (23) that lends support to the additivity assumption to obtain an approximate closed-form solution analogous to the RT equation.⁵ The resulting TE equation is:

⁵ It should be noted that while TE (8) cite the additivity assumption as a basis for their equation, it has been shown (9) that the TE equation possesses no mathematical dependence on this assumption (i.e., the equation assumes no independence between any of the transport mechanisms).

$$\eta = 2.4 A_S^{1/3} N_R^{-0.081} N_{PE}^{-0.715} N_{vDW}^{0.052} + 0.55 A_S N_R^{1.675} N_A^{0.125} + 0.22 N_R^{-0.24} N_G^{1.11} N_{vDW}^{0.053} \quad (7)$$

Comparisons made between this new formula and the RT equation show that the TE equation computes lower values of η for particles with diameters in the range $0.1 \mu\text{m} \leq d_p \leq 4 \mu\text{m}$ (i.e., particles covering the size range of bacterial cells and for which Brownian diffusion is significant). TE also compare the ability of the YHO equation, the RT equation, and the TE equation to reproduce experimental results for η (obtained in well-controlled experiments having chemical conditions such that α was close to unity). Their comparative analysis is presented as evidence that the TE equation is in fact more accurate than the RT equation. Each model's ability to reproduce experimental data was quantified by calculating the slope and y-intercept in plots of the measured versus theoretical values. The YHO equation yielded a slope of 0.34 (and y-intercept of 0.0007), the RT equation a slope of 0.74 (and y-intercept of 0.0004), and the TE equation a slope of 0.90 (and y-intercept of 0.0002). As a slope of one and y-intercept of zero would correspond to perfect agreement, this comparison ostensibly indicates the marked improvement made by RT over YHO and then further improvement by TE (a discussion of the validity of these comparisons with experimental data is presented later in this chapter). Tufenkji and Elimelech attribute the improved performance of TE over RT to their inclusion of the influence of hydrodynamic interactions and the van der Waals force on Brownian diffusion.

The TE equation's incorporation of hydrodynamic retardation effects and van der Waals forces on the collection due to Brownian diffusion indeed represents a significant theoretical advancement in the CFT. However, their use of the inconsistent collector choice warrants closer examination. As will be shown, the choice of collector models on which to base the filtration equation has implications not only for the theoretical calculations of η , but also for the experimental determination of η . Thus, the validation against experimental data presented by TE (8) must be re-examined. Results from a fully Lagrangian analysis for η (9) will be compared against some of the available experimental data to show that use of the two different definitions of η can lead to substantially different interpretations of a given model's ability to reproduce the data.

The Filtration Equation

It should be noted that all forms of the "filtration equation" presented here assume spatially constant η and α values. As noted previously, there is ample

evidence now that α is not spatially constant in systems with an energy barrier. However, the focus of this discussion is on the calculation of η and the experimental testing of theoretical η calculations. As such, the goal is the development of an expression suitable for testing theories for η . It still seems a tenable assumption that η will be spatially constant in a physically homogeneous porous medium under any chemical conditions (keep in mind that η is defined here as the frequency at which colloids arrive at either the collector surface in the absence of repulsive DLVO interactions, or the energy barrier in the presence of repulsive DLVO interactions). And for the purpose of testing η , it is possible to design experiments in the absence of an energy barrier such that α can be assumed equal to unity. Thus, examination of the filtration equation is worthwhile for the purpose of rigorous testing of η calculations.

The RT and TE equations for η both rely on the Happel Sphere-in-Cell porous media model to describe the flow field of the liquid surrounding the collector. However, only the RT equation (i.e., equation (5) exactly as written) utilizes the Happel model to fully describe the geometry of the collector grains and surrounding pore space. The TE equation uses the isolated sphere representation of the collector and pore space geometry. This is why the RT equation can be said to utilize a consistent collector choice, while the TE equation utilizes an inconsistent collector choice. To apply the commonly used Yao et al. filtration equation in conjunction with the RT equation for η , one must omit the γ^2 factor from the RT equation (i.e., transform the RT equation to the inconsistent collector choice definition). Thus, a different filtration equation is needed for the consistent collector choice definition of η as computed in the Happel Sphere-In-Cell porous media model. This filtration equation for the Happel model is now derived via mass balance on a representative filter. The mass balance that leads to the filtration equation will be performed using both a continuous and a discrete approach, the former leading to an approximate solution and the latter leading to the exact solution. In deriving the proper filtration equation for the Happel model, the difference with the isolated sphere derivation will be highlighted.

The Happel model makes use of an idealized sphere and pore space to represent the entire filter (see Figure 1). The concentric pore space around the spherical collector grain is formulated such that the porosity of the Happel sphere equals the porosity of the entire filter. This geometrical representation will be significant in the following derivation. Using the continuous approach, the filtration equation may be derived via a steady-state mass balance within the representative filter as follows. Consider a filter represented by the Happel Sphere-In-Cell porous media model. For an incremental control volume of thickness Δz within the filter, we can write the following balance of particle fluxes:

$$UAC(z) - UAC(z + \Delta z) = r_s \alpha N_c \quad (8)$$

where U is the velocity of the fluid (taken as the approach velocity in the Happel model), A is the cross-sectional area of flow through the filter, C is the number concentration of particles, r_s is the rate at which particles strike the collector, α is the sticking efficiency, N_c is the number of collectors in the control volume, and z is the vertical axis of flow with the sign convention that positive is downward.

As shown in equation (1), the generic definition of η can be stated as the rate at which particles strike the collector divided by the rate at which particles approach the collector. To obtain the appropriate expression for r_s , we must look at the geometrical definition of η . There is a significant difference between this definition for the Happel model and for an isolated sphere model. For the isolated sphere, the rate at which particles approach the collector is based on the volumetric flow rate given by the projected area of the collector. This definition leads to:

$$r_s = \eta UC \left(\frac{\pi}{4} \right) d_c^2 \quad (9)$$

Insertion of equation (9) into equation (8) will lead to the well-known filtration equation of Yao et al. (10).

The rate at which particles approach the collector in the Happel model is based on the volumetric flow rate given by the combined area of the collector and pore space (see equation (14) in RT, 11). This definition leads to:

$$r_s = \eta UC \left(\frac{\pi}{4} \right) d_H^2 \quad (10)$$

where d_H is the diameter of the combined collector and pore space. The different diameters used in equations (9) and (10) constitute the only difference between the mass balances for a filter represented by the isolated sphere as opposed to a filter represented by the Happel model.

Continuing the mass balance, we write the following expression for N_c :

$$N_c = \frac{A(1-\epsilon)\Delta z}{\left(\frac{\pi}{6} \right) d_c^3} \quad (11)$$

where ϵ is the porosity. We now insert equations (10) and (11) into equation (8) to obtain:

$$UAC(z) - UAC(z + \Delta z) = \left(\frac{3}{2}\right) \left(\frac{\alpha\eta UAC\Delta z}{d_c}\right) \left(\frac{d_H}{d_c}\right)^2 (1 - \epsilon) \quad (12)$$

The Happel model definition that the Sphere-In-Cell's porosity is equal to the filter bed porosity gives the identity $d_C/d_H = (1-\epsilon)^{1/3}$. Inserting this identity, dividing by $UAC\Delta z$, and rearranging gives:

$$\frac{C(z + \Delta z) - C(z)}{\Delta z} = - \left[\frac{3(1-\epsilon)^{1/3}}{2} \frac{\alpha\eta C}{d_c} \right] \quad (13)$$

Taking the limit as $\Delta z \rightarrow 0$ gives:

$$\frac{dC}{dz} = - \left[\frac{3(1-\epsilon)^{1/3}}{2} \frac{\alpha\eta C}{d_c} \right] \quad (14)$$

Separating variables and integrating over the length of the filter, L , gives the appropriate filtration equation for use with the RT equation for η (and also the TE equation if multiplied by γ^2), as defined in the Happel Sphere-In-Cell porous media model:

$$\frac{C}{C_0} = \exp \left[- \frac{3(1-\epsilon)^{1/3}}{2} \frac{\alpha\eta L}{d_c} \right] \quad (15)$$

The only difference between equation (15) and the filtration equation of Yao et al. (1971) is the power of $(1-\epsilon)$ equals unity in the Yao equation. When the mass balance through the filter is performed based on the Happel model, the power of $(1-\epsilon)$ is reduced by 2/3, relative to the isolated sphere filtration equation. The reason for this change is the Happel model formulation that Sphere-In-Cell porosity equals filter bed porosity. This definition of porosity for the concentric pore space results in the identity $d_C/d_H = (1-\epsilon)^{1/3}$. Using the notation $\gamma^2 = (1-\epsilon)^{2/3}$ shows that when η is calculated without the γ^2 factor (i.e., according to the isolated sphere geometry), the Yao et al. filtration equation is the appropriate one to use. Both alternatives give identical values for C/C_0 , α , λ , and k_{int} , but they of course give different values for η .

Although equation (15) represents the consistent collector choice for the Happel model, it is actually an approximation to the exact filtration equation⁶, owing to the continuous nature of the mass balance employed. In general, the approximation is adequate for most cases of practical relevance. However, it is possible that the approximation will become invalid for small values of L/d_c . The exact filtration equation can be derived as follows. Consider the path of a parcel of fluid as it travels through a filter as represented by either the Happel Sphere-In-Cell porous media model or the isolated sphere model. The relative concentration of effluent to influent can be expressed as:

$$\frac{C}{C_0} = (1 - \alpha\eta)^{N_L L} \quad (16)$$

where N_L is the number of collectors per unit length in the filter. In equation (16), the probability of a colloid passing through an individual collector's pore space is raised to the power of the number of collectors, because the exit concentration of one collector becomes the input concentration for the next collector (and since the mass balance is one-dimensional, the colloid suspension passes through every collector sequentially). The number of collectors per unit volume of the filter is:

$$N_v = \frac{\gamma^3}{(\pi/6)d_c^3} \quad (17)$$

where γ^3 is now being used to represent the fraction of solid material, $(1-\epsilon)$, within the filter. To proceed now for the Happel model specifically, we multiply equation (17) by the area of the entire Happel Sphere-In-Cell (collector plus liquid envelope) to obtain the number of Happel collectors per unit length of the path:

$$N_L = \left(\frac{3}{2}\right)(\gamma^3)\left(\frac{d_H^2}{d_c^3}\right) \quad (18)$$

Note that if we were writing the mass balance for the isolated sphere model, the diameter used for the area in the above expression would have been d_c .

Continuing for the Happel sphere, we can substitute γ for d_c/d_H giving:

⁶ RT (11) present both the exact and approximate form of the filter coefficient for the inconsistent collector choice.

$$N_L = \left(\frac{3}{2}\right) \frac{\gamma}{d_c} \quad (19)$$

Inserting equation (19) into equation (16) gives:

$$\frac{C}{C_o} = [1 - \alpha\eta]^{2d_c \frac{3\gamma L}{2d_c}} \quad (20)$$

Equation (20) is the *exact* filtration equation for the *consistent collector choice* formulation of the Happel Sphere-In-Cell porous media model in the CFT. Writing the result as an exponential gives:

$$\frac{C}{C_o} = \exp\left[\left(\frac{3}{2}\right) \frac{\gamma L}{d_c} \ln(1 - \alpha\eta)\right] \quad (21)$$

Noting that $\gamma = (1-\epsilon)^{1/3}$, one can see that equation (15) is an approximation of equation (21) that may become invalid for large values of $\alpha\eta$ when L/d_c is small. When the product $\alpha\eta$ is equal to unity, C/C_o should equal zero. Equation (21) satisfies this requirement and equation (15) does not. Thus, the continuous approach yields an approximation and the discrete approach yields the exact solution. This is because the conceptual model of CFT (whether the isolated or Happel sphere is employed) describes the change in particle concentration with respect to filter length as a discrete process. That is, the concentration changes by a fixed ratio (i.e., $1-\alpha\eta$) each time that a parcel of fluid passes a collector (i.e., after the discrete length of d_c is traversed). Casting the problem into the framework of a continuous function that gives the change in concentration for arbitrary distance traveled through the filter introduces the approximation. Figure 2 presents the results of both equation (21) and equation (15) for six values of L/d_c . It can be seen that the two equations are indistinguishable for large values of L/d_c , but the approximation gets worse for smaller values of the ratio L/d_c and that for any given L/d_c , the approximation gets worse for larger $\alpha\eta$.

Figure 3 plots the percentage error in α as a function of L/d_c for a range of C/C_o values. Figure 3 demonstrates that the errors incurred by the approximation in the commonly used form of the filtration equation may become significant only for experiments where η and α are both very large (resulting in very small C/C_o values) and the L/d_c ratio is small; e.g., on the order of 200 or less. This ratio corresponds to $L = 10$ cm and $d_c = 500$ μm . It is believed that the majority of column experiments do not meet these criteria for

significant errors. The experiments reported in Yao et al. (10), for example, used an L/d_c ratio of 353. However, it is possible to design an experiment with commonly available columns and glass beads that would correspond to the values where errors start to become significant. Therefore, one should exercise caution when using the approximate filtration equation for experiments using short columns, large collectors, and strongly adhesive colloids (e.g., bacteria).

Consistent vs. Inconsistent Collector Choice

The discussion now turns to the practical implications of the inconsistent collector choice for the η equations. A survey of the literature indicates that practitioners of the CFT typically use the inconsistent collector choice. However, to this author's knowledge there has never been an explanation or a justification for making this choice. This theoretical inconsistency therefore warrants closer examination. At times, this discussion will focus on the two alternatives that have been proposed (23) for use of the RT equation. However, the implications of collector choice apply equally to the TE equation.

When the RT η is used without the γ^2 factor, the original filtration equation of Yao et al. may be used for consistent calculations of α , λ , and k_{irr} (even though the values of η will be different). The equivalence of the collector choices for α , λ , and k_{irr} calculations can be easily seen when one conducts a careful inspection of the Yao et al. filtration equation, the Happel based filtration equation (equation (15) here), and the RT equation (equation (5) here). Therefore, if one is applying the CFT to model deposition rates in a filter or aquifer via λ or k_{irr} , or even if one is applying the CFT to assess the "stickiness" (e.g., bacterial adhesion properties) of a particular colloid via calibration of α , the decision to use the consistent collector choice or the inconsistent collector choice will be inconsequential. In this respect, it does not seem unreasonable that the inconsistent collector choice has been so widely used. However, it would seem that use of a flawed definition of η may lead to a flawed understanding of the transport step in the CFT. If the conceptual model of the CFT (i.e., sequential transport and attachment steps) is valid, then η provides us with a fundamental measure of the transport step and it is important to base the definition of η on a theoretically sound definition. In the following discussion, the terms "true η " and "true α " will be used to denote the actual physical quantities that we are trying to calculate.

If the true η approaches unity, an obvious problem occurs. Since the total number of particles striking the Happel collector is being divided by the total number of particles approaching the Happel collector multiplied by the factor γ^2 (which is always < 1), at some point the inconsistent collector choice will yield physically impossible η values (i.e., $\eta > 1$). As it turns out, though, the

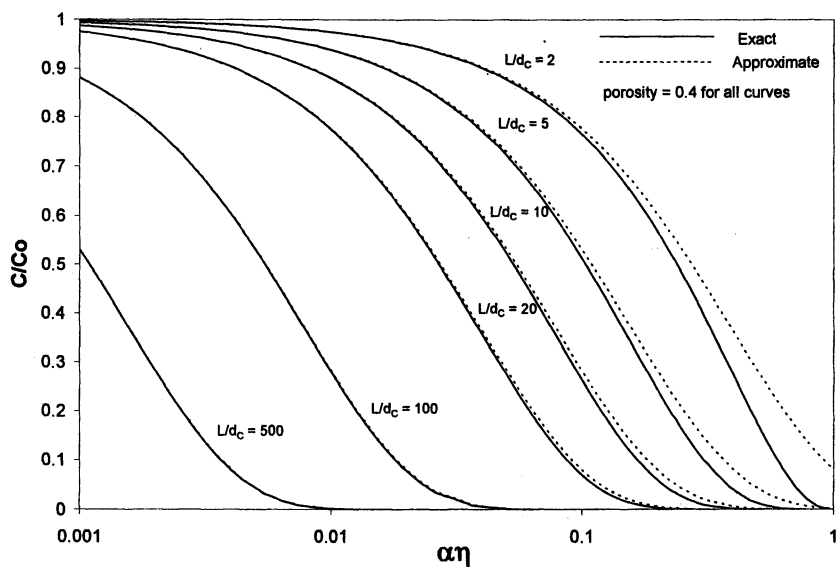


Figure 2. Comparison of exact and approximate filtration equations. The approximation breaks down as the product $\alpha\eta$ approaches unity and as the ratio of column length to collector diameter decreases.

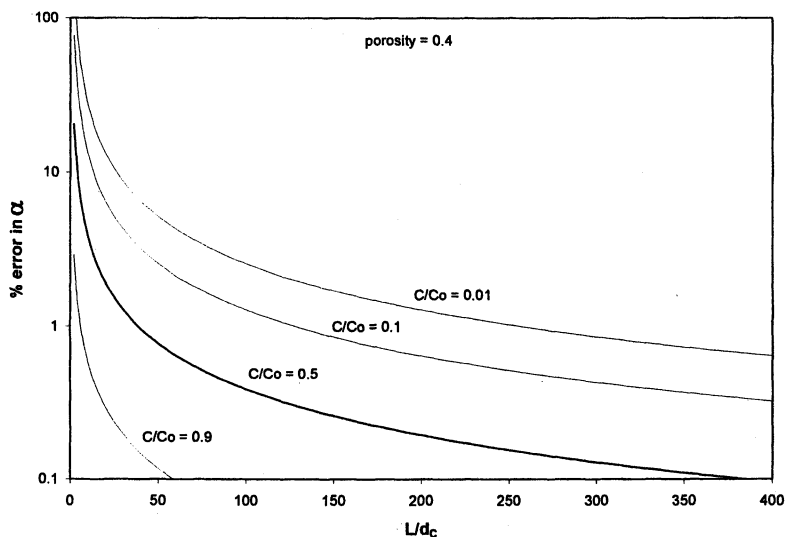


Figure 3. Errors in α due to use of the approximate filtration equation.

regression analyses used by both RT and TE to obtain *approximate* closed-form expressions for η result in the unity limitation being violated anyway at the very bottom of the colloidal diameter range. These unity violations occur only for the smallest colloidal particles ($\sim 1 - 10$ nm) transported under low flow rate conditions. In other words, the available regression equations for η predict values greater than unity for conditions under which Brownian diffusion is highly dominant. Using the inconsistent collector choice does make the violation occur for slightly larger particles, but the difference is small. However, the impact of the inconsistent collector choice is relevant not only for the case where physically impossible values are calculated; rather, it results in inaccuracies for all calculations of η .

A variety of plots are now presented to help visualize the implications of the inconsistent collector choice and the level of inaccuracy incurred for the calculation of η under different conditions. Figure 4 shows a comparison of where the RT and TE equations become > 1 for both of the collector choice options. It is reiterated that for the selected parameters used in this plot, only the smallest colloids (e.g., some viruses) attain η values > 1 .

For example, the TE equation yields $\eta > 1$ for particles of diameter ≤ 10 nm. Figure 5 shows η as calculated by the four equations for the full range of colloidal particle diameters. This plot demonstrates that the unity violation only occurs at the small end of the colloidal size range. Figure 6 shows the different η values resulting from the collector choice for the range of typical bacterial cell diameters. This plot shows that in the bacterial size range, the magnitude of the difference decreases with decreasing diameter. Figure 7 shows a comparison of the difference in η values that result from the collector choice with the difference in η that results from using the TE versus the RT equation. These differences are normalized by the consistent collector definition of η . It can be seen that the normalized difference in η that results from using the inconsistent collector definition (dashed line) stays constant for all particle sizes (this difference is the same whether calculated for the TE or the RT equation). The solid line shows the difference resulting from using the TE versus the RT equations for η when both are defined by either the inconsistent or the consistent collector model definitions. The signs of these differences have been retained with the TE η subtracted from the RT η . For the set of parameters used in these calculations, we have TE $\eta <$ RT η for all particle diameters (d_p) > 25 nm. For $d_p < 25$ nm, we have TE $\eta >$ RT η . The reason for the sign change is that as d_p decreases, the hydrodynamic retardation effect becomes weaker and the van der Waals attractive force becomes stronger. The largest difference between the two equations occurs at about $d_p = 1.3$ μm , right in the middle of the bacterial cell size range. It can be seen that for the majority of the bacterial size range, the difference in η due to using TE instead of RT is greater than the difference due to the collector choice in the filtration equation. However, for d_p

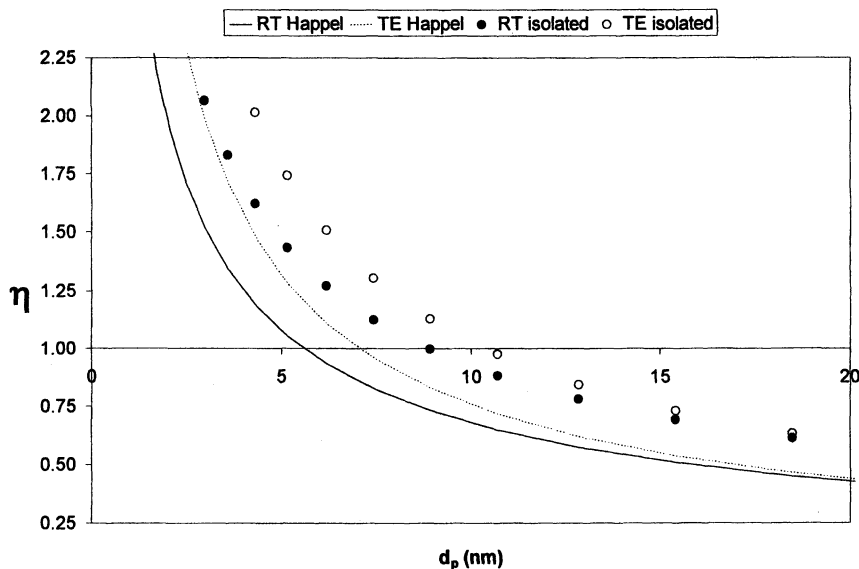


Figure 4. Calculation of physically impossible η values by different forms of the RT and TE equations. The TE equation based on the isolated sphere filtration equation is the first (as we go from larger to smaller particles) to calculate $\eta > 1$, followed by the TE equation based on the Happel filtration equation, the RT equation based on the isolated sphere filtration equation, and finally the RT equation based on the Happel filtration equation. For this set of parameters ($d_c = 300 \mu\text{m}$, $U = 1 \cdot 10^{-5} \mu\text{m/s}$, $\rho_p = 1100 \text{ kg/m}^3$, $\rho_f = 997 \text{ kg/m}^3$, $\mu = 8.9 \cdot 10^{-4} \text{ kg/m}^2\text{s}$, $T = 298 \text{ K}$, $A = 3.0 \cdot 10^{-21} \text{ J}$, $\varepsilon = 0.37$), all equations break the unity line only for extremely small particles, between about 5 and 10 nm. Some of the smallest viruses may fall in this size range. The polio virus is about 20 nm.⁷

$< 0.289 \mu\text{m}$ and $d_p > 3.54 \mu\text{m}$, the difference in η due to the collector choice is greater than the difference in η due to the TE equation. This comparison shows that the decision to use the inconsistent collector definition in the filtration equation results in differences in η that are of comparable magnitude as the improvement made by the TE equation in considering the effects of hydrodynamic retardation and van der Waals forces on D_{BM} . Furthermore, for both small and large colloids the difference in η values resulting from the inconsistent collector choice can be larger than the difference that results from the TE equation's more rigorous treatment of Brownian diffusion. To summarize the conclusions gleaned from Figures 4 through 7: (1) values of $\eta >$

⁷ This number was found at

http://www.hhmi.org/biointeractive/disease/pdf/microbe_size.pdf.

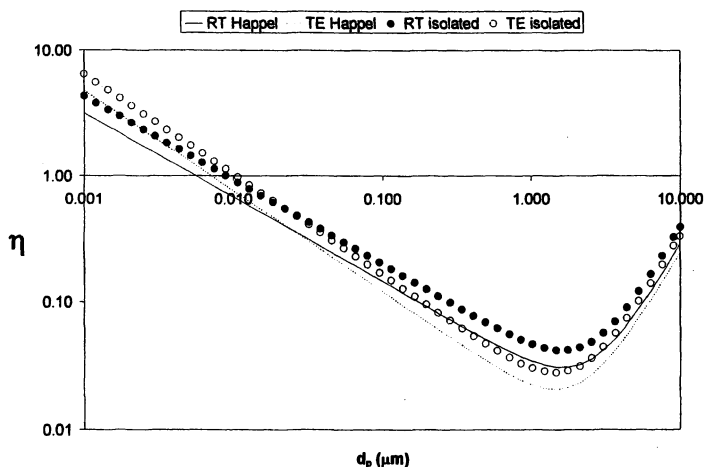


Figure 5. Comparison of η values given by different forms of the RT and TE equations. The curves labeled "isolated" represent the η values obtained when the Happel model is used to compute the rate at which particles strike the collector and the isolated sphere model is used to compute the rate at which particles approach the collector. The curves labeled "Happel" represent the η values obtained when the Happel model is consistently used to compute both rates.

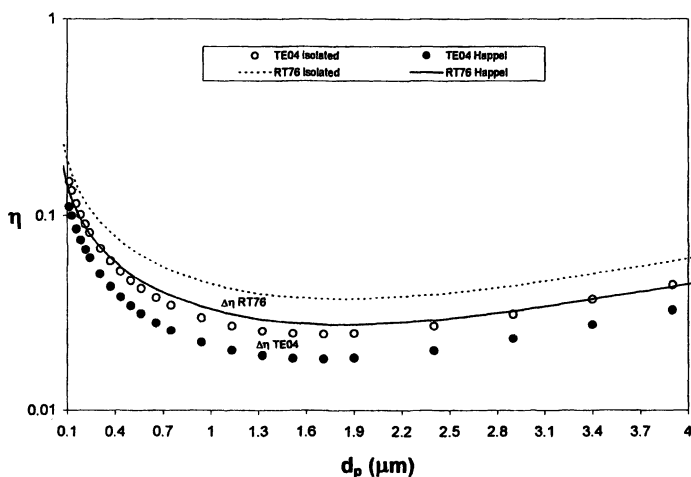


Figure 6. Different η values resulting from inconsistent choice of collector models for RT and TE equations. The curves labeled "isolated" represent the η values obtained when the Happel model is used to compute the rate at which particles strike the collector and the isolated sphere model is used to compute the rate at which particles approach the collector. The curves labeled "Happel" represent the η values obtained when the Happel model is consistently used to compute both rates.

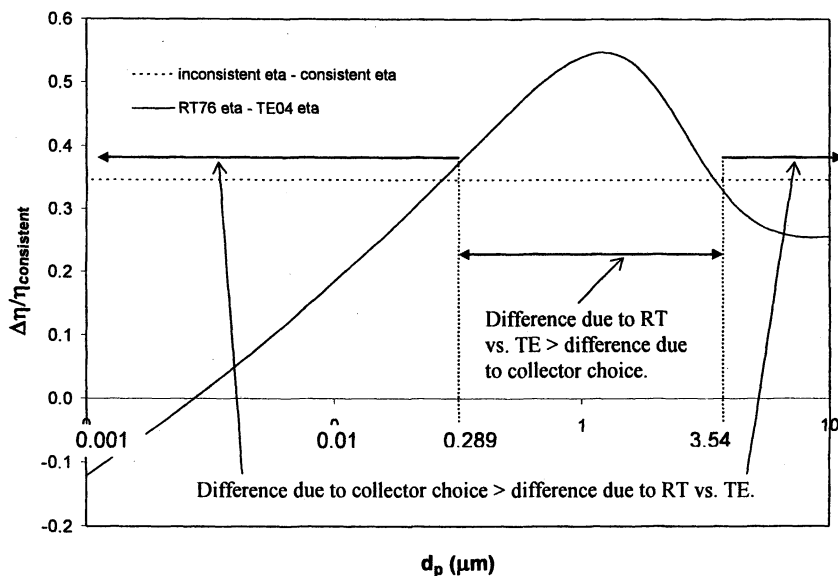


Figure 7. Comparison of the difference in η due to the inconsistent collector definition of the filtration equation and the difference in η due to using the TE vs. the RT equations. Both differences are normalized by the consistent collector η and plotted as a function of particle size.

unity could be a problem only for the very smallest of all colloidal particles; (2) the difference in computed η values resulting from the inconsistent collector choice is of comparable magnitude to the improvements made by the TE equation; (3) the importance of the collector choice on computed η values (relative to the difference in η values attributable to TE vs. the RT treatments of diffusion) becomes greater for colloids as they get smaller (starting from about the low end of bacterial sizes) and also as they get larger (starting from about the high end of the bacterial size range).

There is one other quantity of interest besides η that is not equivalent under the two collector choice scenarios. That is the product $\alpha\eta$. This does not turn out to be a problem if one is modeling the rate of deposition in a filter, because the missing factor γ^2 from the η equation is merely placed in front of η in the filtration equation. However, we might ask ourselves what if the true α equals one? In this case, the idea of equivalence between the two alternative ways of applying the RT equation (23) becomes more problematic. Within the conceptual model of CFT, there is no direct link between the values of α and η . That is, a colloid with a high α value may experience a wide range of η values depending on its own size and density, flow conditions, and properties of the filter within which it is traveling. Thus, if we have good reason to believe that α

has a value of one, this will give us no information about η . Imagine, then, that experiments are being conducted on a particularly sticky colloid, and further imagine that the purpose of the experiments is not to assess the rate of deposition in a deep-bed filter or aquifer, but rather the purpose is to assess the value of η (i.e., the rate at which particles are transported to collector surfaces) under certain conditions of flow, porosity, collector size, etc. This has in fact been pursued by several researchers (e.g., 10, 25-30). In these studies, it has been noted that for certain ideal colloids, we can expect that in high ionic strength solutions it is reasonable to assume an α close to unity. If we make this assumption, then the approximate form of the filtration equation for the Happel model becomes:

$$\frac{C}{C_0} = \exp\left[-\frac{3(1-\epsilon)^{1/3}}{2d_c}\eta L\right] \quad (22)$$

Solving for η gives:

$$\eta_{\text{Expt}} = -\frac{2}{3}\frac{d_c}{(1-\epsilon)^{1/3}L}\ln\left(\frac{C}{C_0}\right) \quad (23)$$

where the subscript has been added to emphasize that this is the expression for an experimentally determined η . If the filtration equation for the isolated sphere model is used, then the expression for the experimental η will be:

$$\eta_{\text{Expt}} = -\frac{2}{3}\frac{d_c}{(1-\epsilon)L}\ln\left(\frac{C}{C_0}\right) \quad (24)$$

Comparison of equations (23) and (24) indicates that the choice of whether to base the filtration equation on the Happel model or the isolated sphere model has a significant impact on experimentally obtained values of η . Figure 8 shows the difference between the two equations as a function of ϵ for $C/C_0 = 0.5$, $d_c = 200$ μm , and $L = 10$ cm. Figure 9 shows the percentage difference as a function of ϵ . For the fairly typical porosity value of 0.4, the percentage difference between the two formulas is 40%. One final plot is presented in Figure 10 to demonstrate the consequences of utilizing the Happel model for the flow field and the isolated sphere model for the macroscopic filter representation in the calculation of η . This plot compares the η values that result from the consistent collector choice and the inconsistent collector choice as a function of the overall rate of particle deposition on the Happel collector. It can be seen that the two approaches diverge as the rate of deposition increases (i.e., as η approaches unity).

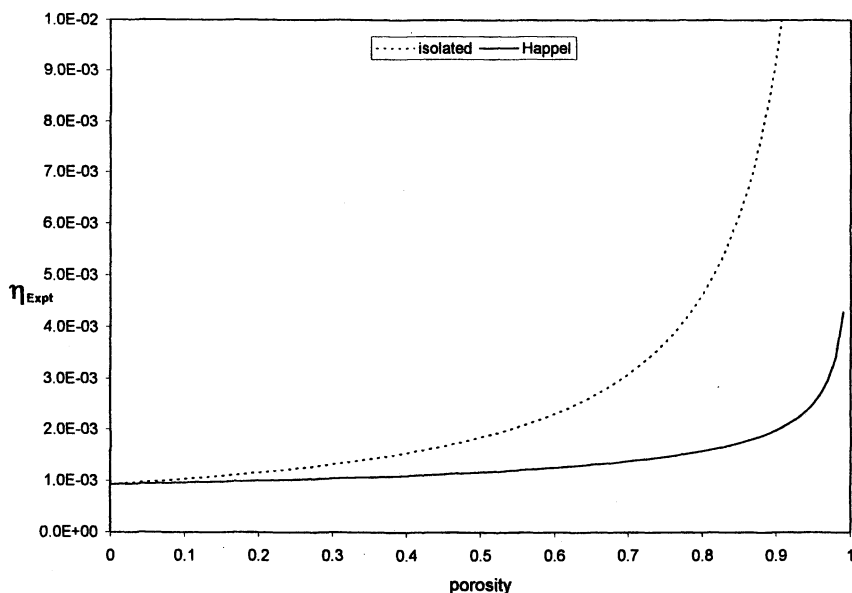


Figure 8. Different values of the experimental η computed using the isolated and the Happel filtration equations. The parameters used in these calculations were $L = 10$ cm, $C/C_0 = 0.5$, and $d_c = 200$ μm .

The question of collector choice has implications only for the analysis of the collection efficiency, η . If one is concerned with applying the available CFT formulas to predict deposition rates, then the two alternatives for application of the RT equation (23) will yield equivalent results. The choice is also inconsequential if one is focused on studying the attachment step, as both alternatives will yield the same values for α . However, if one is focused on studying the transport step of the CFT, then the collector choice for the filtration equation represents a significant decision. The choice of collector models for the filtration equation represents a decision on how to best represent an assemblage of collectors in the real world. That is, how do we translate the analysis within the Happel sphere to the overall transport behavior in a lab-scale column, a deep-bed filter, or even an aquifer? It appears that a tacit consensus has been reached that although the flow field of the Happel model is superior to the flow field of the isolated sphere model, the isolated sphere model is superior for representing the macroscopic assemblage of collectors. This choice of how to represent the macroscopic porous medium has a significant impact on the resulting values of η , whether evaluated theoretically or experimentally. If we accept that the classical CFT conceptual model of sequential transport and attachment steps has some validity and if we are interested in learning more

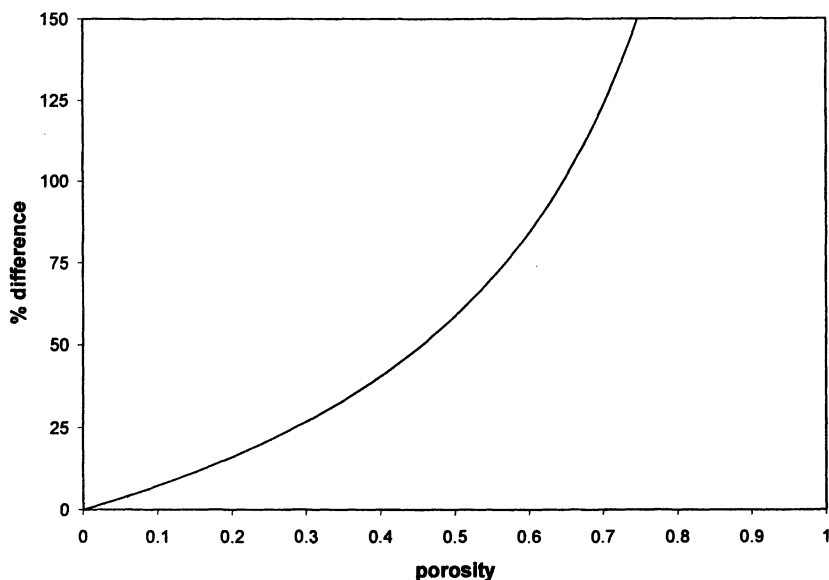


Figure 9. Percentage difference between the different values for experimental η as computed by consistent (Happel) and inconsistent (isolated) collector choices.

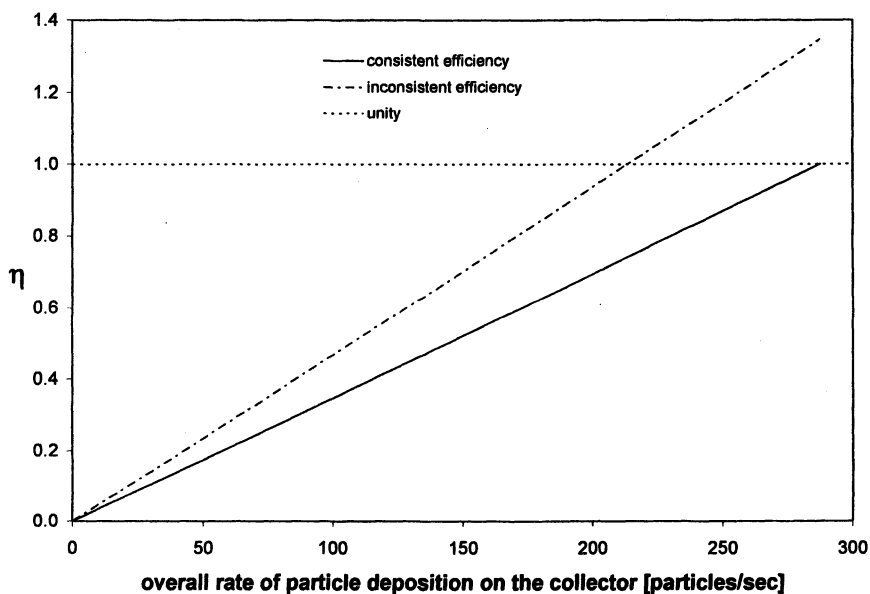


Figure 10. Difference between inconsistent collector choice and consistent collector choice definitions of η as function of particle deposition rate.

about the processes that carry a colloidal particle from the center of a pore to the surface of a porous media grain, then the choice of which collector model to use is an important one. The Happel model may not be the best possible representation of a macroscopic porous medium, but the fact that it maintains macroscopic porosity and ensures the calculation of physically possible values seems to favor it over the isolated sphere model.

To test the importance of the collector choice on comparisons of theoretical η calculations with experimental η values, calculations of η made via a fully Lagrangian method (9) were compared to some of the available experimental data (26, 28-30). Plots similar to those presented by TE (8) were created using both the isolated collector definition of the experimental η formula (equation (24)) and the Happel collector definition (equation (23)). These plots are presented in Figures 11 and 12, respectively. The theoretical values of η calculated by the simulations are on the x-axis, and the experimental values are on the y-axis. As expected, the simulation results obtained a better fit with the Happel definition (slope = 0.75) than with the isolated definition (slope = 0.55). This comparison gives another indication of the significant difference that will result from the two different η definitions. Moreover, if we assume the simulations reported here provide a reasonable representation of the physical transport processes in the experiments, the better fit with the Happel definition provides evidence that the Happel model gives a more accurate representation of the macroscopic filter than does the isolated sphere model.⁸

To reiterate the importance of the collector model that is chosen for the derivation of the filtration equation (and, thus, the formula for computing experimental η values when α is assumed ≈ 1), it is noted that constructing plots such as those in Figures 11 and 12 using the inconsistent collector choice for both the theoretical and experimental η values will not yield a plot equivalent to the one generated by using the consistent collector choice for both the theoretical and experimental η values. The idea of equivalence that applies to the calculation of α , λ , and k_{irr} does not apply here. This is because one must divide by γ^2 to convert the Happel based theoretical η to an isolated sphere based theoretical η . However, to convert the Happel based experimental η to an isolated sphere based experimental η , one must multiply by γ^2 . To demonstrate this lack of equivalence, a third comparison plot is presented in Figure 13, in which both the theoretical and experimental η values have been converted to the isolated sphere definitions. It can be seen that this plot gives the worst agreement (slope = 0.41). This type of plot (i.e., isolated sphere definition used for both theoretical and experimental η) is what has been presented by TE (8) for

⁸ It is believed that the simulations results used in these comparisons provide a reasonably rigorous representation of the transport processes in the cited experiments. However, it should be noted that the radial dependence of D_{BM} due to hydrodynamic retardation was omitted in these simulations.

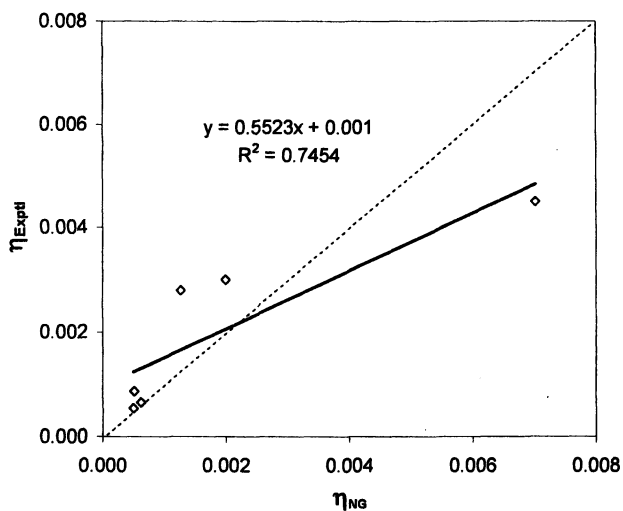


Figure 11. Comparison of simulations (Happel theoretical definition of η retained) against experimental data with η based on the isolated sphere model.

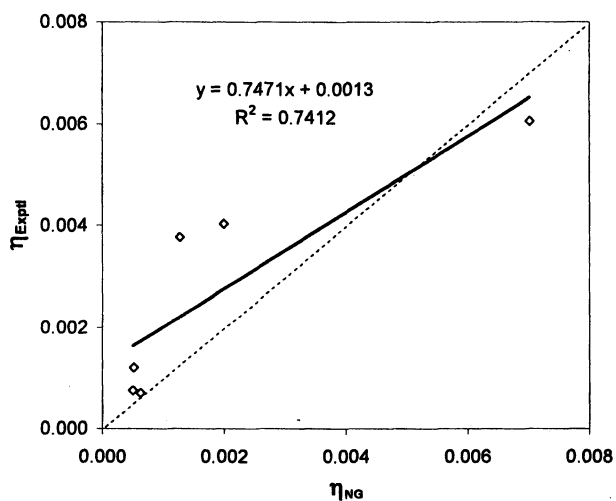


Figure 12. Comparison of simulations (Happel theoretical definition of η retained) against experimental data with η based on the Happel model.

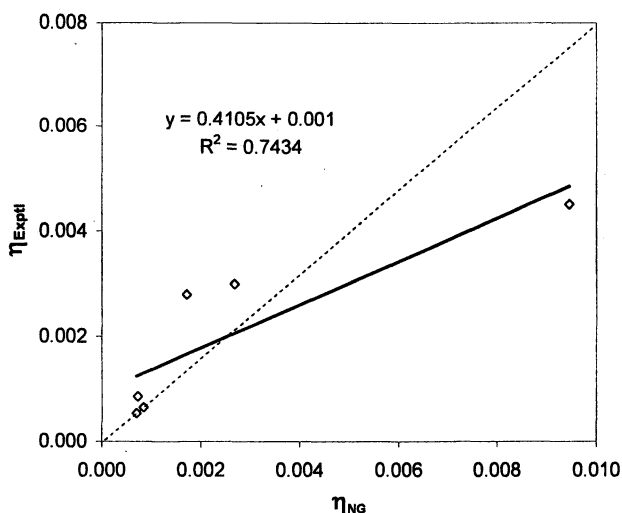


Figure 13. Comparison of simulations (with Happel theoretical definition of η converted to isolated sphere definition) against experimental data with experimental η based on the isolated sphere model.

their comparisons against experimental data. Given the theoretical advantages of the Happel definitions of η and the filtration equation (e.g., idealized sphere porosity = filter porosity, η is guaranteed not to exceed unity), it is believed that the type of plot presented in Figure 12 (i.e., Happel sphere definition used for both theoretical and experimental η) provides the most reliable comparison of the theoretical η calculations against the experimental data. Based on this comparison of the different ways to compare theoretical and experimental results for η , the degree to which the TE equation has improved upon agreement with experimental data (as shown in δ) is unclear.

Preliminary Work on Incorporation of Biological Processes

To incorporate biological processes into the pore-scale analysis of CFT, it is desirable to use an approach that considers all transport mechanisms (i.e., all mechanisms giving rise to particle motion) simultaneously. The method employed for the RT equation does not satisfy this requirement, because the deterministic mechanisms are treated separately from the stochastic process of Brownian diffusion. Two recent studies (8, 9) do consider all classical CFT transport mechanisms simultaneously, the former from an Eulerian perspective and the latter from a Lagrangian perspective. In most cases, the two approaches

(Eulerian and Lagrangian) should be equally applicable to the treatment of biological processes. However, in the event that a process exhibits hysteresis, the Eulerian approach might be problematic. The fully Lagrangian method for calculating η (9) follows the approach of RT, with the exception that diffusion is also treated in the Lagrangian trajectory analysis. This renders the trajectories stochastic in nature, and η is thus obtained from a stochastic Monte Carlo analysis using the following equation:

$$\eta = \int_0^{\pi/2} 2P_c(\theta_s) \sin(\theta_s) \cos(\theta_s) d\theta_s \quad (25)$$

where θ_s is the starting angle of a trajectory and $P_c(\theta_s)$ is the probability that a trajectory starting from θ_s will make contact with the collector (see Figure 1). Equation (25) reduces to $\eta = \sin^2(\theta_s)$, equation (14) in RT (11), when $P_c(\theta_s)$ equals one for all $\theta_s \leq \theta_{LT}$ and zero for all $\theta_s > \theta_{LT}$ (i.e., when the trajectories are deterministic). The function $P_c(\theta_s)$ is found from a large number of trajectory simulations in the Monte Carlo analysis. Equation (25) can be used to incorporate any stochastic biological process into the trajectory simulations for η . Recently, this approach was used to incorporate the random motility of *E. coli* cells (31).

The Lagrangian approach employing equation (25) may also be used to extend CFT to the modeling of interactions between bacterial cell surface structures and porous media surfaces. There is much recent and ongoing experimental work concerning the role of bacterial cell surface structures in the attachment of bacteria to surfaces. For example, many bacterial cell surfaces exhibit extracellular polymeric substances (EPS). These EPS may be able to form bridges that result in adhesion to surfaces (32-34). In addition to this attachment function, these EPS may play a role in the final moments of the transport step (i.e., at close separation distances). Several researchers have observed that the DLVO theory of colloidal stability (on which the close-separation interaction forces of CFT are based; specifically, CFT assumes that electrostatic repulsion is negligible yielding an interaction potential that is solely the van der Waals force) fails to describe the experimentally observed interaction forces that arise when bacterial cells approach a surface (e.g., 35, 36). It has been proposed that the presence of cell surface structures is the most likely explanation for the failure of DLVO (32, 36, 37). In one set of experiments with atomic force microscopy, the measured forces were very different from DLVO forces and were modeled successfully with a steric repulsion model (36).

Modeling the combined effects of Brownian motion and EPS interactions will likely require a rigorous, mechanistic modeling approach, such as the Lagrangian particle tracking employed in this study. Also, EPS interaction forces may exhibit hysteresis, which would preclude use of the convective-

diffusion equation, but would not be an obstacle for a Lagrangian approach. If the EPS interactions control the attachment step for some bacterial strains, then it may be possible (for conditions absent of repulsive DLVO interactions) to perform a priori calculations for the frequency with which aqueous colloids attach, i.e. an $[\alpha\eta]_{\text{theo}}$. Then, if desired, one could define a theoretical value for the sticking efficiency:

$$\alpha_{\text{theo}} = \frac{[\alpha\eta]_{\text{theo}}}{\eta} \quad (26)$$

where the numerator is the result given by the Lagrangian trajectory analysis with EPS interactions included, and the denominator is the result given by the Lagrangian trajectory analysis without EPS interactions (and ignoring other attachment processes). Given a sufficiently validated calculation of η , our result for α_{theo} could be compared to experimentally determined α values to assess the accuracy of EPS interaction models. It is believed that detailed characterization of bacterial surfaces with technologies like AFM, well-controlled laboratory transport experiments, and Lagrangian CFT trajectory analyses could be pursued jointly to further our understanding of the bacterial transport and attachment processes.

The repulsive effects of polymer interactions can be modeled by a steric interaction potential function. AFM measurements have been presented (36) in which the interaction forces between individual negatively charged bacteria (*P. putida* KT2442 and *Burkholderia cepacia* G4) and silicone nitride were represented well by a steric repulsion model based on the prior work (38, 39). This Alexander-deGennes potential was modified for a sphere-plate system (40). The resulting potential that successfully modeled the reported AFM data (36) is:

$$F^{\text{St}}(h) = 50kT a_p L_o \Gamma^{3/2} e^{-2\pi h/L_o} \quad (27)$$

where h is the surface-to-surface separation distance, k is the Boltzmann constant, T is absolute temperature, L_o is the equilibrium length of the polymer brush layer, and Γ is the grafted polymer density.

The attractive effects of polymer interactions can be represented by a polymer bridging model. The classical CFT assumption of irreversible adhesion may be appropriate for the phenomenon of polymer bridging, in which the cell is fixed to the solid surface by bridges formed between its extracellular polymers and the surface. If the total adhesion force of these bridges is strong enough to oppose the torque generated by the hydrodynamic shear force, then irreversible adhesion will result (barring any metabolic or other changes that could induce detachment). Force data presented in the literature (34) suggests that the adhesion force of a single KT2442 polymer bridge is sufficient to achieve irreversible adhesion at typical groundwater velocities.

Polymer bridging can be incorporated into CFT via the definition of where “collection” occurs, in which case the collection event now incorporates both the transport and attachment steps. A simple model based on the mean length and adhesion force of the cell polymers can be expressed in terms of the surface-to-surface separation distance as follows:

$$h_{\text{att}} = (l_m + a_p)[1 - (n_b/2\pi a_p^2 \Gamma)] - a_p \quad (28)$$

where h_{att} is the separation distance at which collection occurs, l_m is the mean polymer length, and n_b is the number of bridges required for adhesion. The parameter n_b is a function of the mean adhesion force of the cell polymers and the hydrodynamic shear force of the flowing water. This expression for h_{att} assumes all polymers have the same length and exhibit an equal adhesion force; given these assumptions, the formula is derived purely from the geometry of the simplified system. Figure 14 depicts the geometrical relationships that result in equation (28). Note that when $n_b > 1$ (and assuming all polymers are of length l_m), the effects of compression of polymers closer to the normal than the

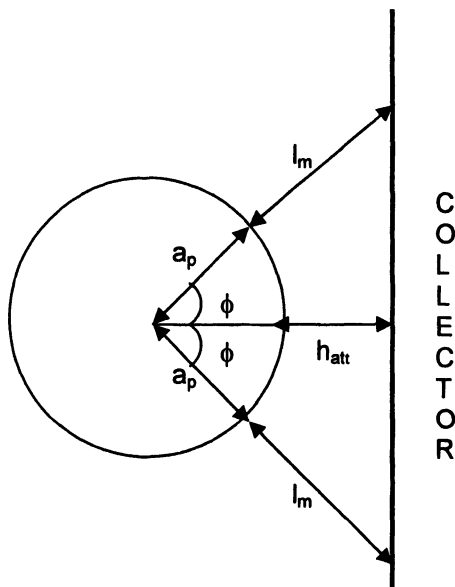


Figure 14. Geometrical determination of h_{att} . The mean polymer length, the number of polymer bridges required for attachment, and the density of polymers determine the separation distance required for attachment. The solid angle spanning all bridging polymers is equal to $2\pi a_p^2(1 - \cos\phi)$.

outermost attaching polymer are not taken into account explicitly by equation (28); however, the steric effects of this compression are incorporated via simultaneous simulation of equation (27) in the trajectory computations. If we allow for a distribution of both polymer lengths and adhesion forces, then h_{att} will be described by a bivariate frequency distribution.

If we have confidence that all significant transport mechanisms have been adequately incorporated into the Lagrangian trajectory analysis (note that motility will have to be incorporated for many bacterial strains), then we can compare the α_{theo} value obtained from equation (26) with experimentally determined α values⁹ to assess the accuracy of the EPS interaction modeling. If the simple model represented by equation (28) is inadequate, then more sophisticated polymer models, such as the freely jointed chain (41) or wormlike chain (42) models that provide representations of conformational behavior, may be incorporated into the polymer bridging simulations. Experimental data may also suggest new model forms that may be tested within the framework proposed here.

Conclusions

This chapter will conclude with some suggestions for applying CFT to the study of bacterial transport and adhesion mechanisms operating at scales ranging from interfacial to column. This methodology is based on the critical review of the theory that has been presented, which has noted some inconsistencies and possible sources of error in the conventional application of CFT. These observations are particularly relevant to the use of the CFT for furthering the scientific understanding of bacterial transport and adhesion mechanisms. First, a fairly minor (yet worthwhile) observation is that the commonly used filtration equation used for calculating λ , k_{irr} , and α is an approximation to the exact equation that is readily available. The approximate and exact forms of the filtration equation are indistinguishable for most (if not all) experimental conditions that have been reported in the literature for colloid deposition studies using laboratory columns. However, it is possible that experiments using short columns (e.g., $L \leq 10$ cm), large collectors (e.g., $d_c \geq 200$ μm), and strongly adhesive bacterial cells will incur significant errors when the approximate filtration equation is used.

The most fundamental inconsistency that has been observed is that it is common to calculate the rate of particle collisions with porous media grains based on the flow field of the Happel Sphere-In-Cell porous media model, but

⁹ It should be emphasized that if effluent breakthrough concentrations are being used to determine a spatially constant α value, the experiments should be conducted under “favorable conditions”, absent a DLVO energy barrier.

then to use the isolated sphere model for the definition of η . This results in a definition of η that is fundamentally flawed, because it can produce physically impossible η values that are greater than one. Even if the unity limit is never violated, it is clear that the flawed definition of η will give different values than the more theoretically sound Happel definition. The commonly used η definition diverges from the consistent Happel definition as the overall rate of particle deposition increases (i.e., as η approaches unity).

The most problematic aspect of the flawed η definition is its use in conjunction with experimental evaluations of η . Figures (11) through (13) show how use of the two different η definitions in the evaluation of experimental data can lead to substantially different interpretations. Based on the theoretical flaws in the isolated sphere definition of η , it is expected that continued use of the Yao et al. (10) definition of η for theoretical calculations of η along with equation (24) for experimental evaluations of η will yield inaccurate representations of the transport behavior of colloidal particles from the bulk fluid phase to collector surfaces. The hallmark of scientific endeavor is that theories can be tested in the laboratory or the field. However, if the analysis of experimental data is flawed, then this basic tenet of science is largely negated and the scientific process is not likely to succeed. In trying to comprehend the complex processes of bacterial transport and adhesion, it is imperative to apply the most fundamentally sound theory available.

Given all of the above, the following recommendations are made:

1. Calculations of η based on the Happel model should use the Happel definition of flux (i.e., r_F) in the definition of η .
2. The filtration equation used in conjunction with η values based on the Happel model should be derived based on the Happel model.
3. The exact form of the filtration equation should be used.
4. Formulas for the calculation of η should consider all relevant mechanisms simultaneously.
5. A new formula should be used for the experimental determination of η values from column breakthrough data. The suggested formula is based on the exact form of the filtration equation and on the macroscopic representation of the filter medium given by the Happel model. This formula is derived by setting $\alpha = 1$ and solving equation (20) for η which yields:

$$\eta_{\text{Expt}} = 1 - \left(\frac{C}{C_0} \right)^{\frac{2d_c}{3\gamma L}} \quad (29)$$

This formula is valid for determining η using column breakthrough data from experiments in which the influent is described by a continuous pulse boundary condition, the effluent concentrations have reached steady-state conditions, and no energy barrier is present ($\alpha = 1$). The above suggestions constitute a starting point for successful application of CFT towards improving our mechanistic understanding of bacterial transport and adhesion at the column scale and below.

Nomenclature

Symbols:

a_p = bacterial cell radius

a_s = collector radius

A_s = neighboring grains parameter = $2(1 - \gamma^5) / (2 - 3\gamma + 3\gamma^5 - 2\gamma^6)$

d_c = collector diameter

D_{BM} = Brownian diffusion coefficient = $kT / (6\pi\mu a_p)$

H = Hamaker constant = 10^{-20} J

k = Boltzmann constant = 1.38066×10^{-23} kg·m/sec²·K

N_G = dimensionless gravity number = $2a_p^2(\rho_p - \rho_f)g / (9\mu U)$

N_{LO} = dimensionless London van der Waals number = $H / (9\pi\mu a_p^2 U)$

N_{PE} = dimensionless Peclet number = $U(2a_s) / D_{BM}$

N_R = dimensionless relative size number = a_p / a_s

$P_c(\theta_s)$ = probability of trajectory with initial azimuthal coordinate θ_s contacting collector

T = absolute temperature

U = fluid approach velocity

Greek letters:

α = sticking efficiency

ε = porosity

$\gamma = (1 - \varepsilon)^{1/3}$

η = theoretical collection efficiency

η_{Expt} = experimental collection efficiency

μ = fluid viscosity

θ = azimuthal coordinate

θ_s = initial azimuthal coordinate of a trajectory

ρ_f = fluid density

ρ_p = bacterial density

References

1. Steefel, C.I.; MacQuarrie, K.T.B. *Rev. Mineral.* **1996**, *34*, 83.
2. Murphy, E.M.; Ginn, T.R., *Hydrogeol. J.* **2000**, *8*, 142.
3. Steefel, C.I.; DePaolo, D.; Lichtner, P.C. *Earth and Planetary Sci. Letters* **2005**, *240*, 539.
4. Matthes, G.; Pekdeger, A. *J. Cont. Hydrol.* **1989**, *2*, 171.
5. Harvey, R.W.; Garabedian, S.P. *Environ. Sci. Technol.* **1991**, *25*, 178.
6. Martin, R.E.; Bouwer, E.J.; Hanna, L.M. *Environ. Sci. Technol.* **1992**, *26*, 1053.
7. Ginn, T.R.; Wood, B.D.; Nelson, K.E.; Scheibe, T.D.; Murphy, E.M.; Clement, T.P. *Advances in Water Resources* **2002**, *25*, 1017.
8. Tufenkji, N.; Elimelech, M. *Environ. Sci. Technol.* **2004**, *38*, 529.
9. Nelson, K.E.; Ginn, T.R. *Langmuir* **2005**, *21*, 2173.
10. Yao, K-M; Habibian, M.T.; O'Melia, C.R. *Environ. Sci. Technol.* **1971**, 1105.
11. Rajagopalan, R.; Tien, C. *AIChE J.* **1976**, *22*, 523.
12. Gross, M.J.; Albinger, O.; Jewett, D.G.; Logan, B.E.; Bales, R.C.; Arnold, R.G. *Water Research* **1995**, *29*, 1151.
13. Albinger, O.; Biesemeyer, B.K.; Arnold, R.G.; Logan, B.E. *FEMS Microbiol. Lett.* **1994**, *124*, 321.
14. Li, X.; Scheibe, T.D.; Johnson, W.P. *Environ. Sci. Technol.* **2004**, *38*(21), 5616.
15. Redman, J.A.; Estes, M.K.; Grant, S.B. *Colloids Surf. A: Physicochem. Eng. Aspects* **2001**, *191*(1-2), 57.
16. Tufenkji, N.; Elimelech, M. *Langmuir* **2004**, *20*, 10818.
17. Li, X.; Johnson, W.P. *Environ. Sci. Technol.* **2005**, *39*(6), 1658.
18. Tong, M.; Li, X.; Brow, C.; Johnson, W.P. *Environ. Sci. Technol.* **2005**, *39*(10), 3888.
19. Tong, M.; Camesano, T.A.; Johnson, W.P. *Environ. Sci. Technol.* **2005**, *39*(10), 3679.
20. Happel, J. *AIChE J.* **1958**, *4*, 197.
21. Levich, V.G. *Physicochemical Hydrodynamics*; Prentice-Hall: Englewood Cliffs, NJ, **1962**.
22. Rajagopalan, R.; Tien, C.; Pfeffer, R.; Tardos, G. *AIChE J.* **1982**, *28*, 871.
23. Logan, B.E.; Jewett, D.G.; Arnold, R.G.; Bouwer, E.J.; O'Melia, C.R. *J. Environ. Eng.* **1995**, *121*, 869.
24. Prieve, D.C.; Ruckenstein, E. *AIChE J.* **1974**, *20*, 1178.
25. Fitzpatrick, J.A., Ph.D Dissertation, Harvard University, **1974**.
26. Elimelech, M.; O'Melia, C.R. *Langmuir* **1990**, 1153.
27. Elimelech, M., Ph.D Dissertation, The Johns Hopkins University, **1989**.
28. Elimelech, M. *J. Colloid Interface Sci.* **1991**, *146*, 337.

29. Elimelech, M. *J. Colloid Interface Sci.* **1994**, *164*, 190.
30. Elimelech, M. *Sep. Technol.* **1994**, *4*, 186.
31. Nelson, K.E.; Massoudieh, A.; Ginn, T.R. *Advances in Water Resources* in press.
32. Jucker B.A., Zehnder A.J.B., Harms H. *Environ. Sci. Technol.* **1998**, *11*, 33.
33. Ortiz, C.; Hadziioannou, G. *Macromolecules* **1999**, *32*, 780.
34. Camesano, T.A.; Abu-Lail, N.I. *Biomacromolecules* **2002**, *3*, 661.
35. Ninham, B.W. *Adv. Colloid Interface Sci.* **1999**, *83*, 1.
36. Camesano, T.A.; Logan, B.E. *Environ. Sci. Technol.* **2000**, *34*, 3354.
37. Otto, K.; Elwing H.; Hermansson, M. *Colloids Surf B: Biointerfaces* **1999**, *15*, 99.
38. Alexander, S. *Le Journal de Physique.* **1977**, *38*:983.
39. de Gennes, P.G. *Adv. Colloid Interface Sci.* **1987**, *27*, 189.
40. Butt, H.-J.; Kappl, M.; Mueller, H. & Raiteri, R. *Langmuir* **1999**, *15*, 2559.
41. Flory, P.J.; *Statistical Mechanics of Chain Molecules*; Interscience Publishers, New York, **1969**.
42. Debye, P. *J. Chem. Phys.* **1946**, *14*, 636.

Chapter 17

Mechanisms of Retention of Biological and Non-biological Colloids in Porous Media

Wedging and Retention in Flow-Stagnation Zones in the Presence of an Energy Barrier to Deposition

William P. Johnson

Department of Geology and Geophysics, University of Utah, Salt Lake City, UT 84112

This chapter reviews recent findings that have revolutionized our understanding of the processes governing the retention of microbes and non-biological colloids in porous media under environmentally relevant conditions. The recent shift in our understanding of colloid retention in porous media is driven both by experimental findings and mechanistic simulations. The experimental data indicate previously unaccounted for influences of fluid drag and pore domain geometry on retention of biological and non-biological colloids in porous media. The mechanistic simulations are able to capture these processes when the pore domain geometry is altered to reflect the presence of grain-to-grain contacts and zones of flow stagnation in the porous media. These findings lay the foundation for improved theory to predict the retention of biological and non-biological colloids in porous media under environmentally-relevant conditions.

This review focuses on the mechanisms governing colloid transport in porous media in the presence of an energy barrier to deposition. Here the term colloid is used to refer to “particles” in the size range between 10 nm and 10 μm regardless of origin (biological or non-biological), and the term “energy barrier” refers to repulsion between the colloid and surrounding surfaces, as is typical of environmental contexts. The goal is to emphasize that colloid retention in porous media is driven by equivalent mechanisms in both the absence and the presence of an energy barrier to deposition, whereas the influences of the pore domain geometry and fluid flow field become paramount in the presence of an energy barrier. In both the absence and presence of an energy barrier to deposition, colloids experience forces from fluid drag, innate energy (diffusion), colloid-surface interaction, and gravity. Under conditions absent an energy barrier, colloids attach upon collision with the grain surface, which occurs somewhat randomly across the porous media surface, wherever the flow field first brings them into contact the surface. In the presence of an energy barrier to deposition, colloid collision with the surface is prevented, and colloids that closely approach surfaces will translate along these surfaces without retention, except under three circumstances: 1) colloids intercept local heterogeneity where the energy barrier is eliminated, and they attach; 2) colloids become confined between two or more bounding surfaces which then force them to overcome one of the bounding energy barriers, and they attach; 3) colloids intercept zones where fluid velocities are sufficiently weak, or secondary energy minimum interactions are sufficiently strong, such that they are retained without attachment. Experimental evidence indicates that the first mechanism can be minor relative to the other two, as described below.

The upshot of the review that follows is that deposition of colloids (biological and non-biological) in porous media is a much more dynamic process than has been traditionally considered. Conditions that reduce colloid deposition and promote colloid re-entrainment include decreased ionic strength, and increased fluid velocity, both of which can be expected to occur during high runoff events. The dynamic nature of colloid deposition also yields distributions of retained colloids that are non log-linear, e.g. hyper-exponential or non-monotonic, and which may migrate with elution, challenging our ability to predict colloid transport distances in the field. The observation that the majority of colloid deposition occurs near the riverbed during riverbank filtration has previously led to the conclusion that the riverbed material is a critical component of the filtration system. However, accumulated experimental results indicate that colloid deposition may occur dominantly near the source regardless of whether or not riverbed material is present.

The recent progress made in identifying the mechanisms responsible for colloid retention in porous media in the presence of an energy barrier leads to the possibility that correlation equations will soon be available for easy

prediction of colloid transport distances in the presence of an energy barrier. The variability of the profiles of retained colloids in the presence of an energy barrier promises to complicate prediction of transport distances; however, identification of mechanisms of retention, and development of correlation equations for the collector efficiency in the presence of an energy barrier, constitute important steps toward meeting this challenge.

Similarities of Biological and Non-Biological Colloids

Biological colloids (e.g. viruses, bacteria, and protozoa) and non-biological colloids (e.g. microspheres and mineral colloids) differ fundamentally in terms of potential physiological controls on the transport of biological colloids in porous media. For example, the attachment and detachment behaviors of microbes may vary due to physiologic processes or features such as growth (1-5), starvation (1), polymer secretion (6, 7), and the presence of appendages, e.g. flagella (8-10). Even when these differences are neutralized (e.g. by starvation); biological and non-biological colloids may differ in terms of the contribution of polymeric materials to their surface characteristics (11-21). Despite these important differences between biological and non-biological colloids, their transport behaviors in environmental porous media share important similarities; the most fundamental among them being that they undergo deposition in porous media even when existing theory suggests otherwise; i.e. their interaction energies with the porous media indicate that direct attachment to the surface should be prevented by a formidable energy barrier. Recent experiments highlight additional similarities in the transport behavior of biological and non-biological colloids that have increased our understanding of the mechanisms driving their retention in porous media in the presence of an energy barrier. The observations include:

- 1) Profiles of retained colloid concentrations as a function of distance in porous media show hyper-exponential or non-monotonic deviation from the log-linear shape expected from classic filtration theory, demonstrating that deposition rate coefficients are, in effect, not spatially constant.
- 2) Colloid deposition rates decrease, and re-entrainment rates increase, with increasing fluid velocity, demonstrating that fluid drag mitigates colloid deposition and drives colloid re-entrainment.
- 3) Colloid deposition rates increase with increasing colloid:collector size ratio for ratios greater than about 0.005, demonstrating that the size of the colloid relative to the collector is a major governor of deposition above this threshold.
- 4) Re-entrainment of a large fraction of the retained colloid population in

porous media occurs when the system is perturbed by a pulse of low ionic strength water, demonstrating that a large fraction of the retained population may be loosely associated with surfaces via secondary energy minima.

- 5) Colloid deposition efficiencies and re-entrainment rates are much higher in porous media relative to flat surfaces, demonstrating that the geometry of the pore domain is a major governor of colloid deposition in porous media.

These common attributes of the deposition behaviors of biological and non-biological colloids in the presence of an energy barrier indicate processes underlying deposition that occur independently of the characteristics of the particular biological or mineral colloid. The above phenomena demonstrate that fluid drag and pore-domain geometry are major governors of colloid deposition and re-entrainment in the presence of an energy barrier. Existing models of transport, including filtration theory, do not yet incorporate processes that yield the above phenomena, calling for development of new transport models to guide characterization of transport potential. This document reviews the state of existing models of colloid deposition in porous media, the experimental evidence that suggests the need for development of new models, and the state of development of these new models.

Issues Outside the Scope of this Review

Biological and non-biological colloid transport behaviors in porous media are controlled by a deceptively short list of processes: advection, dispersion, deposition, and re-entrainment, which are governed by complex characteristics of the subsurface and the colloid. Advection and dispersion are dominantly controlled by macro- to micro-scale physical characteristics of porous media, specifically, by permeability and permeability contrasts in the subsurface (22-31). Deposition and re-entrainment are controlled by a larger set of characteristics of the system that range from the micro- to the nano-scale, that include both physical and chemical characteristics (32, 33), and that shift in response to perturbations in fluid velocity and solution chemistry (34-40). Although advection and dispersion are extremely important processes in colloid transport, understanding these processes is largely an issue of characterization of the subsurface. The issues of preferential flow paths and initiation of flow in subsurface pore domains are strongly tied to the field; and hence, are tied to the particular porous media and hydrologic setting of interest. This review recognizes the importance of these issues, but focuses on processes that are general to colloid transport regardless of environmental context.

The review that follows does not consider important complications presented by unsaturated flow conditions, and conditions where subsurface preferential flow paths exist. Since transient wetting events and subsurface field-

scale heterogeneity present major challenges to maintenance of groundwater quality, it is worthwhile to mention here some of the considerations related to these topics. These topics are not entirely separable since unsaturated soils and sediments tend to be structured, containing macropores through which the majority of flow may pass (e.g. 41, 42). In settings where preferential flow paths dominate, e.g. karst settings, storm events may re-suspend colloids and particulates previously stored in the system (43), whereas preferential flow paths may yield rapid transport of colloids regardless of previous storage (44, 45). Hence, the potential inclusion of physically heterogeneous units in the flow field during high discharge events is a major concern for groundwater quality.

A more general concern associated with high runoff events is the potential initiation of flow in previously unsaturated units, which constitutes an important means of mobilizing colloids (biological and non-biological) (e.g. 46-49). Colloid mobilization under unsaturated flow conditions appears to be largely driven by capillary forces which bind the colloids to the air-water interface, and which are larger than the DLVO forces between colloids, or between the colloids and the air-water interface (50-55), although hydrophobic interactions also play a role (56, 57), and this role may increase with increasing water content (55, 58).

Existing Theory

Filtration Theory

In this section, the fundamental processes controlling colloid deposition (biological and non-biological) in porous media are reviewed in the context of classic filtration theory. In classic filtration theory, colloid deposition is mediated by two primary processes: 1) transport of colloids to porous media grain surfaces; and 2) colloid-surface interaction, which is governed by forces that may allow or prevent direct attachment of the colloid with the grain surface. The probability that a colloid will approach close to a grain surface is estimable on the basis of the physical properties of the system, as enveloped in filtration theory (59-61). This probability is estimated from an easily implemented expression (62, 63) composed of dimensionless parameters representing properties of the colloid and the porous media. These so-called correlation equations were developed via correlation to mechanistic numerical simulations of colloid transport to an idealized spherical collector (porous media grain), as shown in Figure 1.

The spherical collector and a surrounding sheath of fluid (together referred to as the Happel sphere-in-cell model) (64) represent the porous media by using collector and fluid sheath diameters that preserve the porosity of the porous

medium. The transport model accounts for advection of colloids on streamlines within the porous media flow field, some of which will allow the colloid to closely approach the collector surface. The model also accounts for colloid crossing of streamlines via diffusion and gravitational settling (which serve to enhance the probability of close approach), as well as hydrodynamic retardation (which serves to decrease the probability of close approach). The probability of close approach to porous media grain surfaces (which yields attachment under ideal conditions), is referred to as the collector efficiency (η). From the collector efficiency, a colloid deposition rate coefficient (k_f) can be determined (63):

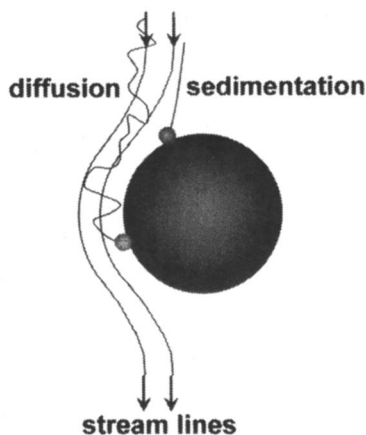


Figure 1. Schematic of Happel sphere-in-cell unit collector.

$$k_f = \frac{3}{2} \frac{(1-\theta)^3}{d_c} v \eta \quad (1)$$

where θ is the porosity of the porous media, d_c is the porous media grain diameter, and v is the fluid velocity. Note that the above expression assumes the absence of an energy barrier, obviating the inclusion of a deposition efficiency (α), as described below. Deposition occurs upon close approach if there is no significant colloid-surface repulsion that prevents deposition, as described in detail below. Deposition, together with advection, dispersion, and re-entrainment, describes colloid transport in porous media:

$$\frac{\partial C}{\partial t} = -v \frac{\partial C}{\partial x} + D \frac{\partial^2 C}{\partial x^2} - k_f C + k_r \frac{\rho_b}{\theta} S \quad (2)$$

where C is the aqueous colloid concentration, v is the interstitial velocity, D is the dispersion coefficient of the colloid, and k_r is the re-entrainment rate coefficient. Re-entrainment is possible for the reversibly deposited fraction of the deposited population (S), where S is typically a subset of the overall deposited population S_{total} . The terms θ and ρ_b represent the porosity and the bulk density of the sediment, respectively.

By assuming steady state transport, negligible dispersion relative to deposition, and negligible detachment, the following equation can be derived, which predicts a log-linear decrease in the concentration (C) of suspended (and retained) colloids as a function of distance (x) from the source.

$$\ln \frac{C}{C_0} = -\frac{k_f}{v} x \quad (3)$$

where C_0 is the concentration at the source.

Interaction Forces

Filtration theory (prediction of η and k_f) is a highly useful construct that has been demonstrated to predict accurately the collector efficiency and log-linear distribution of colloid concentrations with distance from the source in ideal systems, that is, systems where the net interaction forces between the colloid and the grain surfaces are not significantly repulsive. The interaction forces between colloids and porous media are classically estimated based on the respective contributions from electric double layer and van der Waals interaction energies, as described in DLVO theory (65, 66). In DLVO theory, the electric double layer interaction energy is repulsive when the colloid and the grain surfaces are like-charged, and the distance over which this repulsion extends is inversely related to solution ionic strength. In contrast, the van der Waals interaction is attractive for the vast majority of surfaces, and is typically considered to be independent of solution ionic strength. These two classic interactions decay with colloid-surface separation distance at distinct rates, such that van der Waals attraction may greatly dominate at small separation distances, electric double layer repulsion may dominate at intermediate separation distances, and van der Waals attraction may slightly dominate at greater separation distances. These attributes are demonstrated in Figure 2, where the net interaction energy (ΔG_{total}) is strongly negative (attractive) at colloid-surface separation distances less than a

few nm (the so-called primary energy minimum) due to the dominance of van der Waals attraction (Figure 2). At intermediate separation distances, ranging from a few to tens of nm, ΔG_{total} may be strongly positive (repulsive) for like-charged surfaces, yielding an energy barrier to deposition with magnitude inversely proportional to solution ionic strength. At even greater separation distances, weak van der Waals attraction may exceed weak electric double layer repulsion, yielding an attractive secondary energy minimum (Figure 2, right).

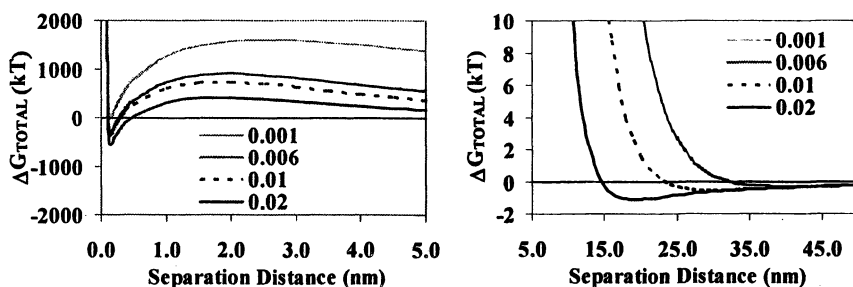


Figure 2. (140) Example DLVO interaction energy profiles at various ionic strengths for $1.1 \mu\text{m}$ carboxylate modified latex microspheres, for separation distances within 5 nm (left), and between 5 and 50 nm (right) from the collector surface. Note that repulsive energies greater than 10 kT are maintained at separation distances greater than 50 nm at 0.001 M ionic strength condition.

The energy barrier to deposition is absent when the colloid and grain surfaces are oppositely charged, or when the ionic strength is sufficiently high to compress the electric double layer repulsion to short separation distances. Under conditions absent an energy barrier (e.g. oppositely-charged colloid and collector surfaces), the concentrations of mobile and retained colloids are observed to decrease exponentially with distance from the source, as expected from a spatially invariant k_f . As well, in the absence of an energy barrier, the re-entrainment of colloids from porous media is negligible. Finally, in the absence of an energy barrier, filtration theory predicts well the magnitude of colloid deposition during transport through porous media (e.g. 67).

Presence of Energy Barriers

In the presence of a significant energy barrier to deposition (e.g. $> 10 \text{ kT}$), the explicit numerical models of colloid deposition based on the Happel sphere-

in-cell model predict that no colloid deposition will occur (e.g. 67). However, the prevalence of colloid deposition in environmental systems despite the presence of significant energy barriers to deposition is well demonstrated; for example, by the general success of filtration as a water treatment technology and by the generally higher quality of ground water relative to surface water. The ratio of the collector efficiency (η) in the presence relative to the absence of an energy barrier to deposition has been referred to as the collision efficiency or deposition efficiency (α). It should be stressed that α has no physico-chemical basis other than to represent the degree by which the collector efficiency is changed in the presence relative to the absence of an energy barrier. Although many researchers have ascribed α to represent the chemical properties of the system, this definition does not wholly encompass the range of influences that come into play in the presence of an energy barrier, as described below. Early attempts to predict α used correlation of dimensionless parameters to experimental results to develop predictive empirical correlation equations (68-72), with some success under the experimental conditions considered. The drawback of such an approach is, of course, the inability to generalize the empirical correlations among different biological and non-biological colloids and different porous media settings.

Geochemical Heterogeneity

Surfaces of environmental colloids (biological and non-biological) and porous media tend to display overall like charge (negative), yielding overall repulsive electric double layer energies between them. The overall negative surface charge emanates from acidic functional groups, which dominate the surfaces of biological colloids and the surfaces of silicate mineral grains under most environmentally relevant groundwater conditions (e.g. pH 6-9) (73, 74).

Some of the minor mineral phases in porous media, such as iron oxides, may display positive surface charge at environmental pH conditions. One can characterize the bulk of subsurface media as being negatively charged, but with varying extents of surface charge heterogeneity arising from mineral phases such as iron oxides (75-78). Iron oxyhydroxide coatings have been shown to increase bacterial attachment in natural (35) and model sediments (79), due to electrostatic attraction between negatively charged bacteria and the positively charged iron oxyhydroxides (lack of an energy barrier between the colloid and the surface). The same has been demonstrated for bacteriophage (80-82). This conclusion is also based on the observation that bacterial attachment in iron oxyhydroxide coated sand is sensitive to increases in pH that result in charge reversal of the iron oxyhydroxide coatings (35). Even in the absence of discrete metal oxide phases, nano-scale defects in mineral structures can confer charge

heterogeneity or otherwise influence the extent of repulsion from otherwise negatively charged surfaces. Hence, colloid deposition onto overall like-charged surfaces (relative to the colloid) can result from localized nano-scale patches of attractive surface charge (67, 75, 76, 78) and surface roughness (32, 33) which act to locally reduce or eliminate the energy barrier to deposition.

The prevalence of natural organic matter in the environment results in masking of positive surface charges by adsorbed natural organic matter, which carries negative charge derived from carboxylic and phenolic functional groups (73, 74, 83). Sorption of natural organic matter to iron oxyhydroxide-coated sediment has been shown to decrease deposition of bacteria (35, 79) and viruses (82), and to lower sensitivity of bacterial attachment to variations in pH (35). These results are consistent with masking of positively charged iron oxyhydroxide surfaces with negatively charged natural organic matter. Natural organic matter in the mobile phase (under conditions of negligible sorption to porous media) has also been demonstrated to yield decreased deposition of *Cryptosporidium parvum* oocysts (84). Non-ionic surfactants have also recently been demonstrated to influence the interaction energies measured between bacteria and quartz surfaces (85); however, the specific influence (increase or decrease) could not be generalized.

In a geochemically heterogeneous porous media, one can expect colloids (biological and non-biological) to deposit onto zones of the surface that are oppositely charged relative to the colloid. If the porous media is heterogeneous at the grain scale, the heterogeneity is thus evenly distributed at larger scales through the media, and a patch-wise model may be used to estimate deposition in the presence of an energy barrier (78, 86). In this model, the overall deposition efficiency is a linear combination of two individual deposition efficiencies; unity and near-zero for the oppositely charged and like-charged surfaces, respectively. The individual deposition efficiencies are weighted according to their surface area fractions in the porous medium. Abudalo et al. (87) found that the removal of bacteriophage PRD1 agreed well with the patch-wise model, whereas removal of *Cryptosporidium parvum* oocysts agreed poorly with the patch-wise model, demonstrating that the model does not accurately portray the complexities of physicochemical filtration for all organisms. Further demonstrating the complexity of filtration is a recent study by Hijnen et al. (88) which demonstrated that the removal of bacteriophages, bacteria, spores, and protozoan oocysts increased with increasing organism size in a relatively coarse-grained "gravel soil", whereas removal did not follow this trend in a relatively fine-grained calcareous sand. Furthermore, removal was greater in the coarser media relative to the finer media (88), which a trend that is opposite to expectations of existing theory.

The noted discrepancies with existing theory may relate to non-DLVO surface characteristics of the colloids and the media. In addition to electrostatic and van der Waals considerations, bacterial surfaces may display significant

hydrophobicity, an attribute that increases bacteria-grain and bacteria-bacteria attachment to greater extents than would be predicted based on electrostatic and van der Waals consideration alone (89-91). DLVO theory has been extended to include this hydrophobic force component (92). The adhesion of two bacterial strains (*Streptococcus mitis* and *Lactobacillus casei*) during batch equilibration with silica and goethite-coated silica agreed well with expectations from extended DLVO theory (93). However, as will be stressed later, the dynamic of colloid deposition in packed porous media differs greatly from that on flat surfaces, and can be expected to differ even more significantly from that of batch systems, where the issue of geometry is neutralized by mixing (e.g. 94).

It should also be noted that the energy barrier to deposition is not necessarily strictly electro-osmotic or hydrophobic in origin, but rather may result from steric interactions emanating from extracellular polymers on microbial surfaces, e.g. bacterial surfaces (e.g. 19-21, 95), and surfaces of *Cryptosporidium parvum* oocysts (96-101).

Given the complexities involved in mechanistic understanding of filtration, some researchers have turned toward correlation of deposition rate coefficients to porous media properties such as hydraulic conductivity (102, 103). This approach can be justified by the fact that in many porous media, the dominance of grain mineralogy by metal oxides that promote colloid attachment is inversely correlated with grain size (e.g. 104), and this approach can be successful in the context for which the correlation was developed (102, 103). The drawback of this approach is that one cannot generalize the correlations among different colloids, microbes, and even bacterial strains. Nor is it likely that one can generalize this approach across different porous media settings.

Experimental Results Driving New Models

Deviation from Existing Filtration Theory

An important discrepancy between filtration theory predictions and experimental observations is provided by the observed distribution of retained colloids as a function of transport distance. In the presence of an energy barrier, the profiles of retained colloids deviate from the log-linear behavior expected from classic filtration theory (Equation 3 above). Specifically, the colloid concentrations decrease faster than log-linearly (hyper-exponentially) with distance from the source. This result was originally observed in the bacterial transport literature, and was ascribed to heterogeneity among the bacterial population (105-112); the practical implication being that classic filtration theory underestimates microbial transport distances, since the colloidal population becomes less sticky with increasing distance of transport. This observation was

quickly extended to virus transport (81, 113-115), and was demonstrated in a recent compilation of field data (116), where the observed “filtration factors” decreased greatly over significant transport distances (117).

Recently, deviation from classic filtration theory has been recognized as a general aspect of colloid filtration in the presence of an energy barrier to deposition (118-120); it occurs regardless of whether the colloid is biological or non-biological. Furthermore, the deviation is not always hyper-exponential, but may also be non-monotonic, e.g. apparent increases in the deposition rate coefficient with transport distance at relatively short distances, followed by apparent decreases in the deposition rate coefficient with increasing transport distance (121, 122). For example, the profiles of retained bacteria in glass beads (adhesion deficient *Comamonas* sp.) examined by Tong et al. (122) transitioned from hyper-exponential to non-monotonic in concert with increased ionic strength from 0.006 M to 0.02 M (Figure 3). Although overall deposition increased with increasing ionic strength (as expected from DLVO considerations), the profile became non-monotonic, and the center of mass was observed to move down-gradient with increasing time of elution, signaling loose association of the cells with the porous media surface (122). Notably, the adhesion of functionalized microspheres to protein-coated surfaces has been demonstrated to decrease with increasing ionic strength (123), indicating that the conformation of cell surface molecules may mediate the reversibility of adhesion and perhaps the development of non-monotonic retained profiles of microbes. Non-monotonic retained profiles have been observed for biological and non-biological colloids, and for both cases the profiles have been considered to reflect loose initial association with the surface (e.g. 121, 122, 124).

To test the hypothesis that hyper-exponential deviation from classic filtration theory reflects the preferential removal of relatively sticky individuals in the colloid population, experiments were recently performed to examine the profiles of retained carboxylate latex microspheres in columns in series to determine whether the shapes of the profiles changed with distance of transport (125). The experiments demonstrated that the standard deviation and mean value of the distribution of deposition rate coefficients decreased with increasing transport, as indicated by a flatter and lower retained profile in the down-gradient column relative to the up-gradient column and relative to a parallel column with colloid concentrations matching those of the down-gradient column (Figure 4). This result indicates that the heterogeneity in the colloid population drives deviation from classic filtration theory under the conditions of the experiments (125), and corroborates similar observations by others (109).

Influence of Fluid Drag

Another important aspect of colloidal transport in the presence of an energy barrier to deposition is the slow steady re-entrainment of colloids (extended

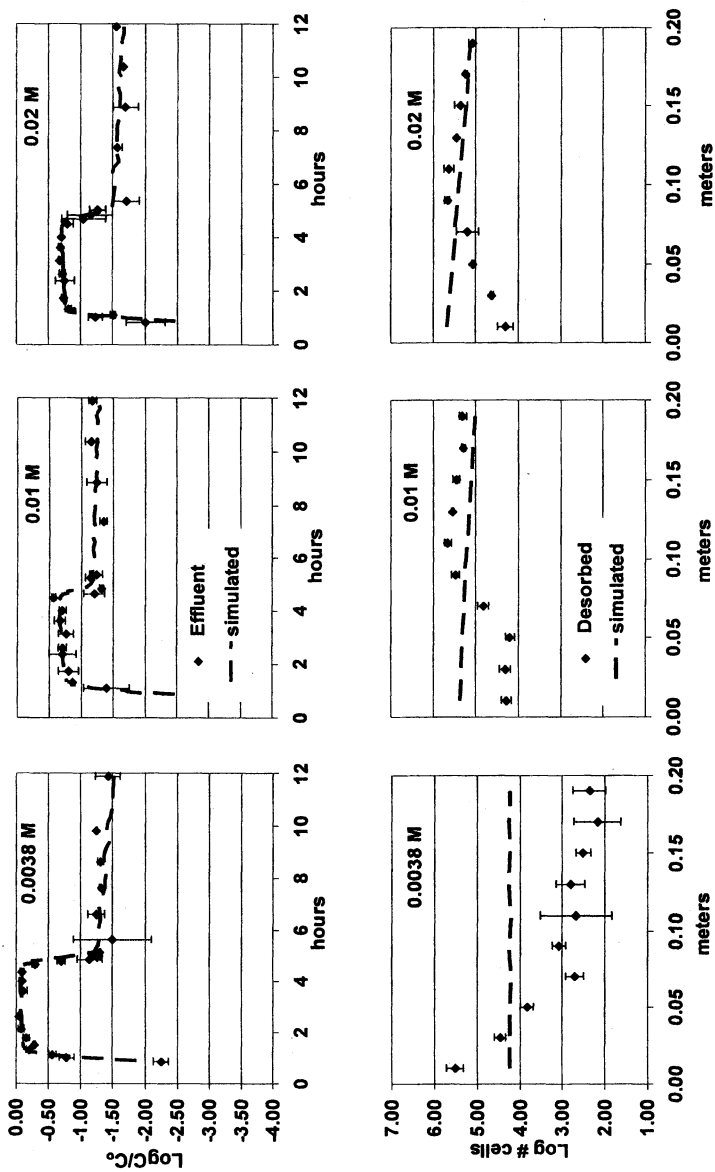


Figure 3. (122) Ionic strength series for DA001 at flow rate = 4 m-day⁻¹, showing effluent breakthrough-elution curves (top), and retained (desorbed) profiles (bottom). Error bars show standard deviations from replicate experiments (n = 2-4). Simulations (dashed) are from a kinetic model using a single deposition rate coefficient (k_d).

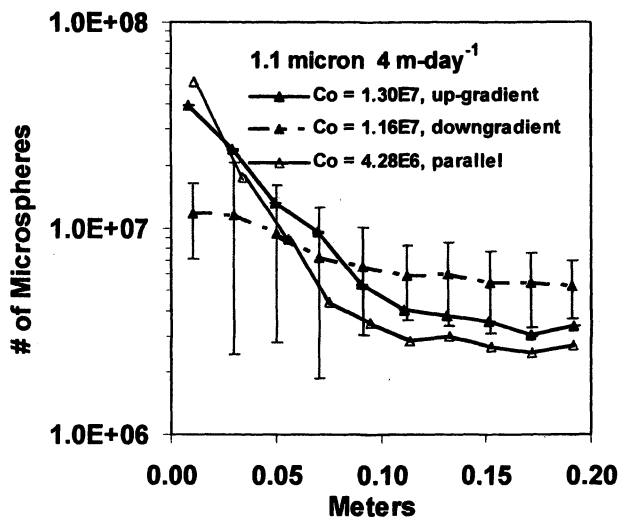


Figure 4. (125) Retained profiles for 1.1 μm microspheres at ionic strength = 0.01 M and pH=6.72 at fluid velocity of 4 $\text{m}\cdot\text{day}^{-1}$

tailing), which is observed ubiquitously for both biological and non-biological colloids in laboratory and field contexts. Extended tailing has been observed in laboratory experiments involving carboxylated latex microspheres (126-128), mineral colloids (129, 130), bacteria (34, 131-135), and protists (1, 136). Extended tailing has also been well-observed in field transport of mineral colloids (137), bacteria (1, 35, 105, 112) and bacteriophage (39, 114, 138).

Re-entrainment is typically dwarfed by deposition, and so can often be neglected when predicting transport distances of the overall population. The significance of re-entrainment is that it may potentially yield low concentrations of colloids in the aqueous phase, and may increase the transport distance of colloids over the long term (years), as demonstrated in simulations using field study-derived bacterial deposition and re-entrainment rate coefficients (112). In terms of transport; however, re-entrainment demonstrates that the mechanism of deposition in the presence of an energy barrier likely differs from that in the absence of an energy barrier. In experiments examining deposition of polystyrene latex microspheres, deposition in the absence of an energy barrier resulted in negligible re-entrainment (consistent with existing theory); whereas deposition in the presence of an energy barrier resulted in significant re-entrainment (122, 139). In some contexts, deposition is highly reversible, e.g. recent laboratory experiments demonstrated re-entrainment-driven translation of the center of mass of retained bacteria in glass beads over distances of several cm in a few hours (122).

The generality of increasing colloid re-entrainment rate coefficient with increasing fluid velocity is demonstrated in Figure 5, which combines results from experiments examining the transport of biological and non-biological colloids (21, 31, 121, 122, 139, 140). All of the series save one show increasing k_r with increasing fluid velocity. The one series that breaks from the trend (DA001 in quartz at 0.02 M) is the sole series that was not supported by replicate experiments (21). The group of studies demonstrates that even under non-perturbed conditions in the presence of an energy barrier to deposition, fluid drag drives re-entrainment of biological and non-biological colloids.

The most important influence of fluid drag on colloid transport may not be that it drives re-entrainment, but rather, that it mitigates colloid deposition. For example, Figure 6 shows trends in deposition efficiency (α) versus fluid velocity in porous media from various studies (21, 31, 121, 122, 139, 140). Colloid sizes among these studies ranged from 0.025 μm bacteriophage MS2 to 5.7 μm microspheres. The porous media used were either glass beads, quartz, or natural sand, with median grain diameters of 360 μm (140), 510 μm (21, 121, 122, 139), and 350 μm (31), respectively. The differences in the magnitudes of the deposition efficiencies are likely related to the magnitudes of the energy barriers to deposition among the different studies. The overall trend yields about factor of four decreases in deposition efficiency correspondent with factor of ten increases in fluid velocity for the conditions examined.

The overall trend of decreasing deposition efficiency with increasing fluid velocity is not as clear for the bacteria (DA001) in some experiments (i.e. 21). That bacteria follow less closely the overall trend may be due to the structural softness of bacterial cells relative to microspheres and bacteriophage, allowing deformation in response to hydrodynamic drag. The overall trend of decreasing deposition efficiency with increasing flow rate for biological and non-biological demonstrates a mitigating effect of fluid drag on the deposition of colloids in the presence of an energy barrier.

Wedging and Straining

Filtration theory predicts that for a range of colloid sizes, the minimum deposition efficiency will correspond to the 1-2 μm sizes since larger colloids undergo greater interception and gravitational settling, and smaller colloids undergo greater diffusive translation. This expectation is confirmed in experiments involving latex microspheres performed in the absence of an energy barrier (141), as shown in Figure 7.

When an energy barrier is present, the relationship with colloid size expected from filtration theory does not hold, as shown in Figure 8 for the same latex microsphere sizes as shown in Figure 7, but under conditions where an energy barrier to deposition was present (141).

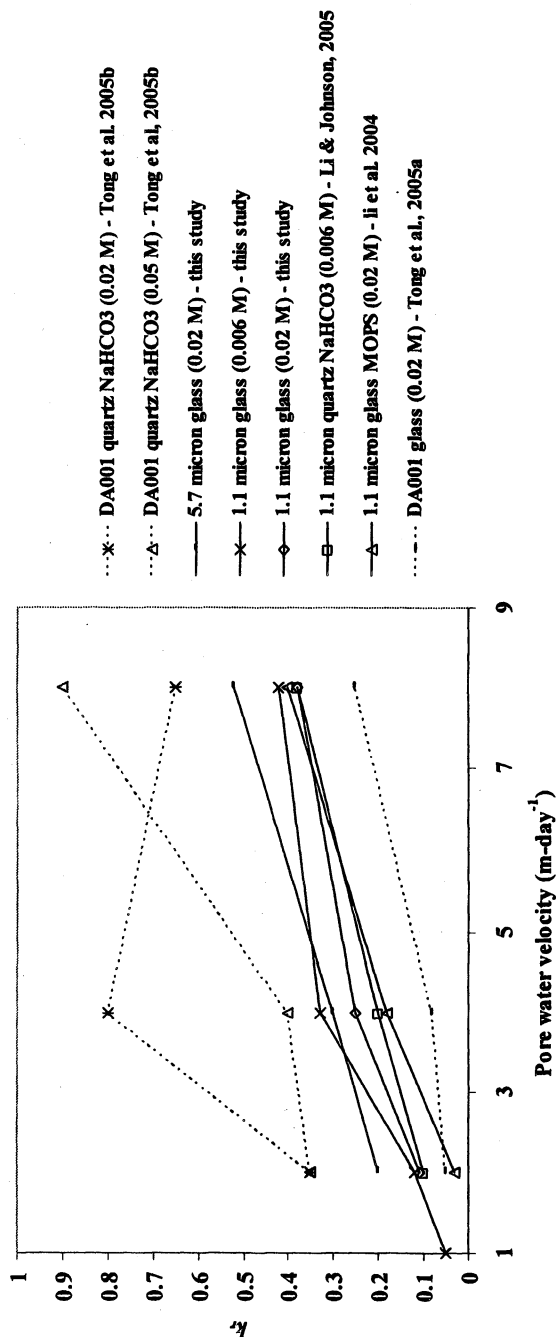


Figure 5. (From 140) Re-entrainment rates (k_p) versus flow rate for biological and non-biological colloids. Data is from the following studies: (21, 121, 122, 139, 140), where "this study" in the legend refers to ref 140. The first number in the series label is the size of the carboxylate modified latex microspheres, or in the case of biological colloids, the first word denotes the microbe. The second word in all cases is the substratum type. Where the buffer is known, it is defined by the third entry; otherwise the third entry denotes ionic strength. The series order in the legend is roughly the same as that from top to bottom in the figure. Dashed lines indicate trends for biological colloids. Solid lines correspond to trends for carboxylate polystyrene latex microspheres. Trends for biological colloids are shown as dashed lines. (Reproduced with permission from reference 140. Copyright 2005 Elsevier.)

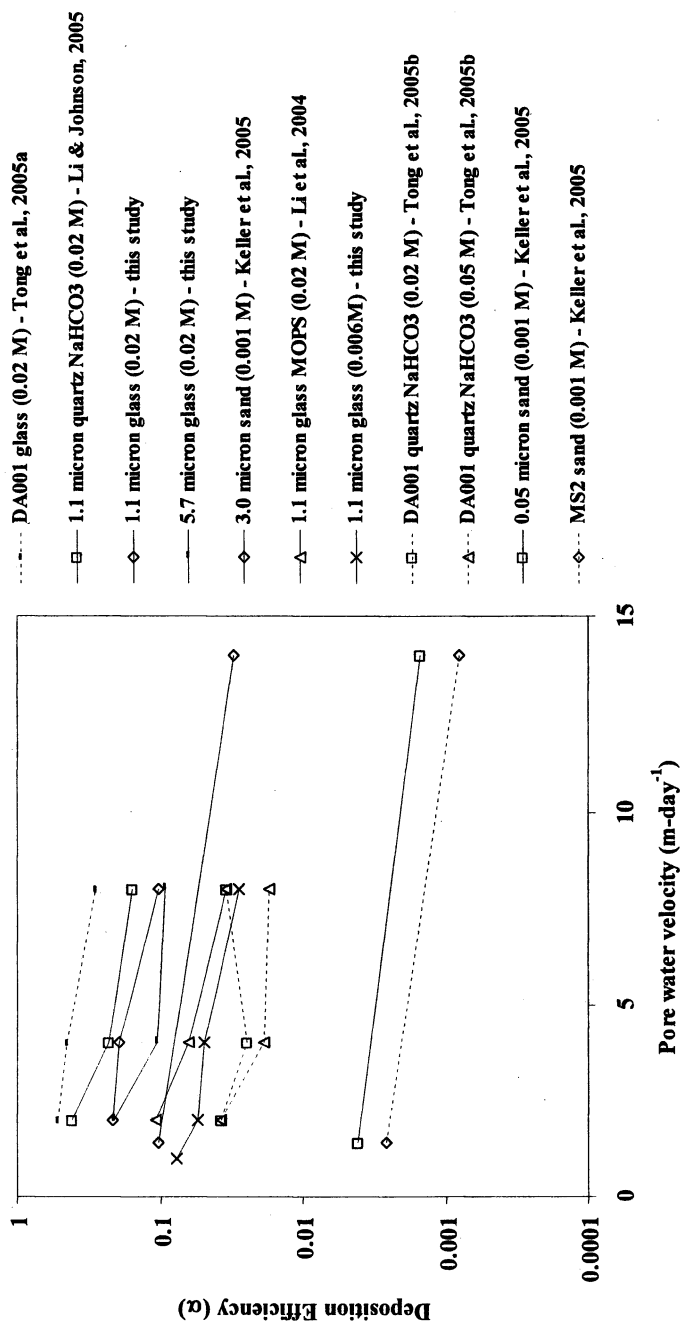


Figure 6. (From 140) Deposition efficiencies (α) versus flow rate ionic strength for biological and non-biological colloids. Data is from the following studies: (21, 31, 121, 122, 139, 140), where "this study" in the legend refers to ref. 140. The series labeling format follows that of Figure 5. (Reproduced with permission from reference 140. Copyright 2005 Elsevier.)

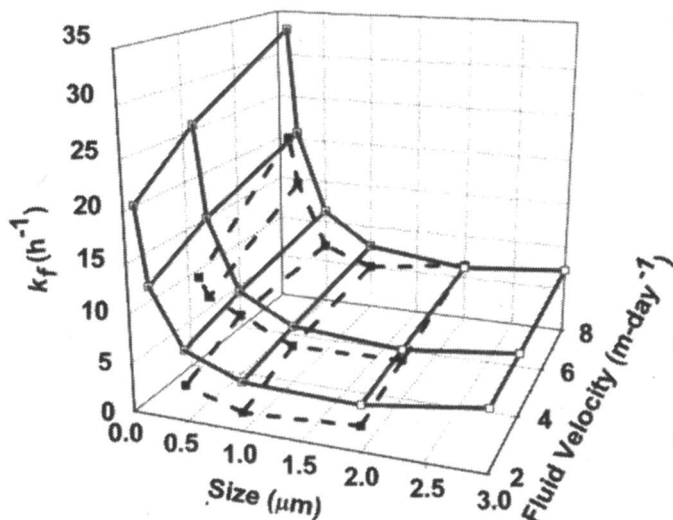


Figure 7. (141) Simulated (open symbols–solid lines) and observed (closed symbols–dashed line) deposition rate coefficients (k_f) in the absence of an energy barrier for five microspheres sizes as a function of fluid velocity in glass beads. Simulated values were calculated using the R-T correlation equation (62).

As shown in Figure 8, in the presence of an energy barrier to deposition, the deposition rate coefficient (k_f) do not yield a clear trend with colloid size, at least one that holds across the range of fluid velocities, likely due to the influence of differences among the surface characteristics of the different microsphere sizes (141) and the influence of changes in the mechanism of deposition in the presence versus the absence of an energy barrier.

Experiments examining colloid deposition in porous media in the presence of an energy barrier demonstrate that for colloid:collector size ratios greater than about 0.005, the deposition rate coefficients increase with increasing colloid:collector size ratio (142–145). This has been interpreted to indicate that physical straining (physical entrapment in pore throats too small to pass) contributes to deposition in the presence of an energy barrier to deposition (142–144). Straining has also been invoked as the mechanism of retention of biological colloids in the presence of an energy barrier (101, 146–148).

The traditional definition of straining is the trapping of colloid particles in pore throats that are too small to allow particle passage (e.g. 101, 144, 149). This mechanism is expected to retain the vast majority of colloids near the entry surface of the porous media (142–144) and this has been invoked as a means of generating the ubiquitously observed hyper-exponential decreases in concen-

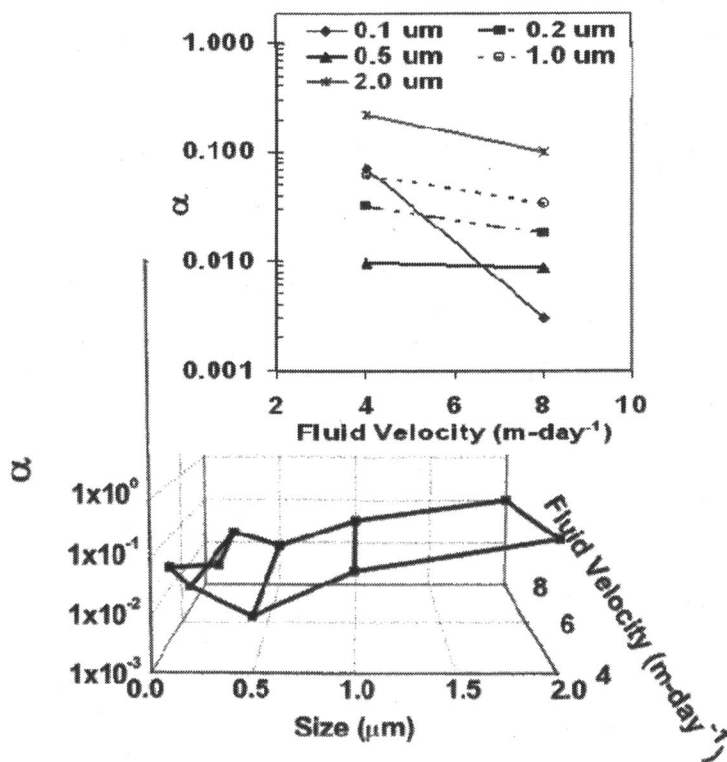


Figure 8. (141) Observed deposition efficiencies for all sizes of microspheres on glass beads as a function of fluid velocity in the presence of an energy barrier to deposition at an ionic strength = 0.02 M and pH = 6.72 (ionic strength = 0.05 M for the 2.0 μm microspheres). The inset highlights the trend of deposition efficiency as a function of fluid velocity for all five microsphere sizes.

trations of retained colloids with distance from the source (142-144). However, the majority of published profiles of retained colloids show significant penetration of colloids into the porous media (e.g. 21, 118, 119, 121, 122), suggesting a mechanism of capture other than straining in pore throats too small to pass. A related mechanism that allows greater colloid penetration into the porous media is wedging, which is defined as capture via confinement between two bounding surfaces (grain-to-grain contacts) (e.g. 150).

The importance of wedging as a mechanism of colloid deposition in the presence of an energy barrier was recently suggested based on mechanistic modeling of particle trajectories within a unit cell that included grain to grain

contacts (151), and was recently demonstrated experimentally (124, 152). To demonstrate the significance of wedging, Li et al. (124, 152) used x-ray microtomography (XMT) to image the deposition locations of near-neutrally buoyant microspheres (Figure 9).

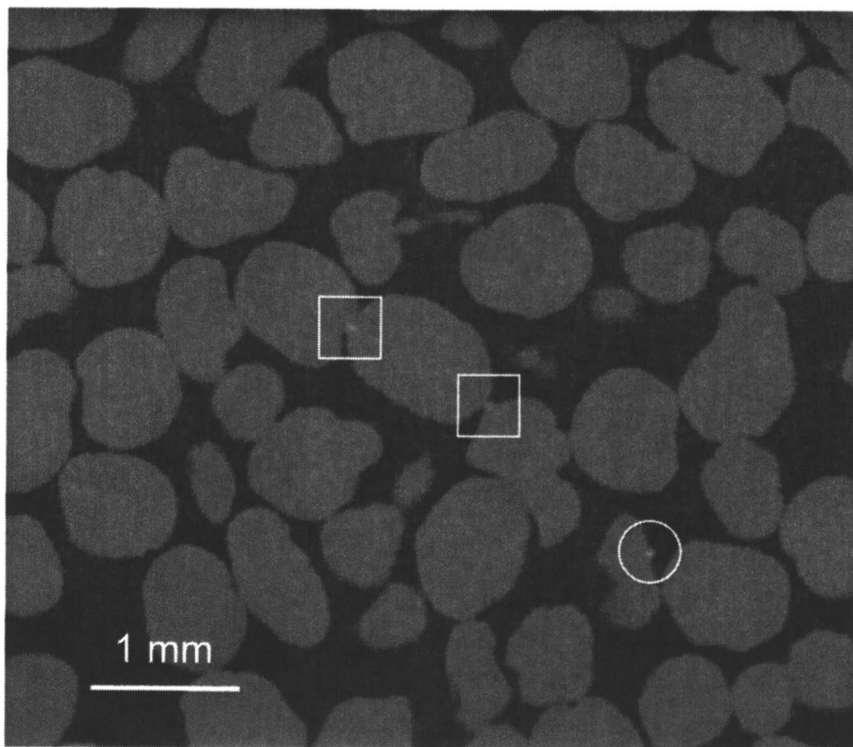


Figure 9. (From 124,152) Representative cross-sectional XMT image of quartz sand (gray areas) and gold-coated hollow microspheres (white spots). Black areas represent pore water. The microsphere in the white circle demonstrates single contact retention. White boxes show retention at grain-grain contacts.

In the absence of an energy barrier, the XMT images showed that deposited colloids were evenly distributed across the collector grain surfaces (in non-contact areas, where 24.6% of all deposition occurred in grain-to-grain contacts), and their concentrations decreased log-linearly with distance from the source, in accordance with expectations from classic filtration theory (Figure 10 top). In contrast, in the presence of an energy barrier, the deposited colloids were

dominantly located in grain-to-grain contacts (84.6% of total deposition), and their concentrations did not decrease with distance from the source according to filtration theory (Figure 10 bottom), but rather varied non-monotonically, with significant penetration into the porous media. These experimental findings demonstrate the importance of colloid wedging in grain-to-grain contacts in the presence of an energy barrier to deposition. Notably, no colloids were observed to reside in pore throats (i.e. captured via straining) despite the fact that the colloid:collector ratios spanned the threshold for which straining has previously been invoked (0.005) (142-145).

Retention in Flow Stagnation Zones

As described above, wedging in grain-to-grain contacts is an important mechanism of deposition of colloids in porous media in the presence of an energy barrier. However, grain-to-grain contacts are one among multiple aspects of pore domain geometry that control colloid deposition in the presence of an energy barrier. This is demonstrated by experiments comparing colloid deposition on flat versus porous media surfaces under conditions where the surfaces in the two systems display equivalent surface characteristics, and where the near-surface tangential fluid velocities are similar in the two systems. The most commonly used system for examining colloid deposition onto flat surfaces is the impinging jet system, in which the solution is directed normal to the flat surface (153-155). Colloid deposition efficiencies (ratio of colloid deposition rate in presence versus absence of an energy barrier) have been demonstrated to be much greater in porous media relative to impinging jet systems (factors of 2 to 50) under equivalent conditions (141, 156-158), suggesting that the vast majority of colloid retention in porous media is not due to surface heterogeneity, which presumably operates in both the impinging jet and the porous media, but rather is related to the pore domain geometry in porous media.

The mechanism of excess colloid retention in porous media (other than wedging) is indicated by the fact that a large fraction of the colloids retained in porous media in the presence of an energy barrier are released as a result of eluting the packed porous media with low ionic strength solution (141, 159-161), whereas elution with low ionic strength solution (and increases in fluid velocity up to a factor of 200) yields negligible colloid release from the impinging jet system (141, 162). These observations indicate that a large fraction of the colloids retained in porous media in the presence of an energy barrier are associated with surfaces via secondary energy minima. O'Melia and co-workers (160, 161) demonstrated reversibility of deposition of the majority of colloids in porous media upon reduction of solution ionic strength, concomitant with elimination of the secondary energy minimum. Release would not occur if the

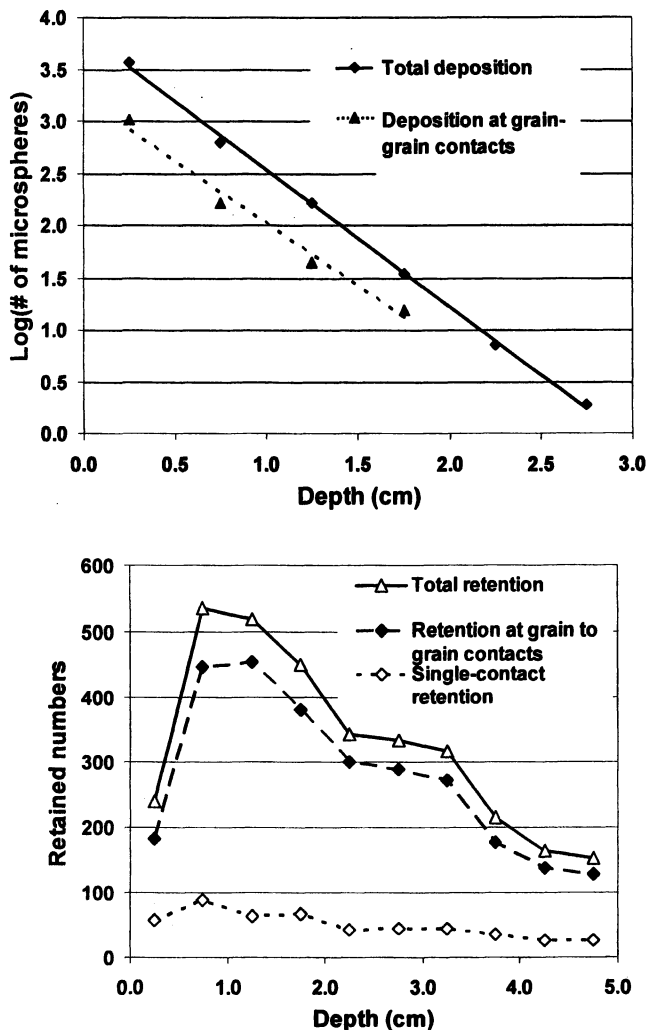


Figure 10. (From 124,152) Profiles of total deposition and deposition at grain to grain contacts in quartz sand at a pore water velocity of $0.25 \text{ cm}\cdot\text{s}^{-1}$, in the absence (top) and presence (bottom) of an energy barrier to deposition.

colloids were deposited in the primary energy minimum, since the barrier to detachment from the primary energy minimum is negligibly changed as ionic strength is decreased (see the interaction energy profiles, Figure 2) (160, 161) associated with secondary energy minima would be expected to translate across the grain surface due to tangential hydrodynamic drag, unless they are retained in zones of flow stagnation (e.g. rear stagnation points or leeward sides of protrusions) (141, 162). Since no zones of flow stagnation exist in impinging jet systems (other than the forward stagnation zone), colloid deposition within an impinging jet system is necessarily restricted to association with the surface via the primary energy minimum, where the colloid is immobilized via direct contact with the surface. The greater deposition efficiency in porous media relative to impinging jets (excess retention) is therefore thought to result from the presence of zones of flow stagnation in the porous media in which the secondary minimum-associated colloids may be retained in loose association with the grain surfaces.

The retention of colloids in zones of flow stagnation in porous media offers a dynamic mechanism of retention in the presence of an energy barrier that explains the observed release of colloids in response to perturbation with low ionic strength solution, and which may also explain re-entrainment in the absence of ionic strength or velocity perturbations (extended tailing), since this mechanism of retention includes a random component (colloid diffusion) that may allow re-entrainment without macroscopic perturbation. Colloid deposition at surface heterogeneities yields direct contact with the surface via the primary energy minimum, and so cannot explain the release of colloids via elution with low ionic strength solution, nor re-entrainment in the absence of perturbations.

Development of New Models

Wedging and Retention in Flow Stagnation Zones

Numerical simulations of colloid trajectories in the Happel sphere-and-cell model form the basis for existing filtration theory by providing the mechanistic results from which the correlation equations for the collector efficiency (η) were developed (59, 60, 62). The simulations were developed by considering fluid drag forces, gravitational forces, colloid-surface interaction forces, and colloid diffusion forces (59, 60, 163). In this model, colloid contact with the collector yields permanent immobilization, since contact yields association with the surface via the primary energy minimum. The Happel sphere in cell model works very well for prediction of collector efficiencies (η) observed in the absence of an energy barrier, and the assumed spatial constancy of the resulting

deposition rate coefficient is reflected in the observed log-linear decreases in colloid concentrations as a function of distance from the source. However, when a significant energy barrier to deposition exists (e.g. $\Delta G_{\min} > 10$ kT), the Happel sphere-in-cell model predicts that no colloid deposition will occur, since the repulsive colloid-surface interaction force cannot be overcome by diffusion, gravitational, or fluid drag forces in environmentally relevant ranges. Since the recent experimental results described above indicate that colloid deposition cannot be explained by surface heterogeneity alone, the Happel sphere-in-cell model lacks the attributes necessary to account for colloid deposition in the presence of an energy barrier.

The observations reviewed in the previous section regarding experimental results indicated the importance of pore domain geometry on colloid deposition in porous media in the presence of an energy barrier. Specifically, the importance of grain-to-grain contacts and zones of flow stagnation as locations of colloid retention were highlighted. Cushing and Lawler (151) developed a 3-D particle trajectory model to investigate the role of grain-to-grain contacts on colloid deposition in the presence of an energy barrier. They incorporated a fluid flow field developed for dense-packed porous media comprised of spherical collectors (164) and numerically examined the deposition of colloids subject to fluid drag, colloid-surface interaction forces, and gravity. Their model yielded significant colloid deposition in grain-to-grain contacts in the presence of an energy barrier, suggesting the importance of these features in colloid deposition. However, their model also displayed insensitivity to energy barrier height, weakening confidence that the model accurately represented colloid deposition in porous media in the presence of an energy barrier. Following the pioneering work of Cushing and Lawler (151), Johnson et al. (165), developed 3-D particle trajectory models incorporating fluid flow fields for dense-packed (164) and loose-packed (166) porous media comprised of spherical collectors, as shown in Figure 11.

The simulations were performed within unit cells representing the two porous media packing structures (Figure 12), with incorporation of the various forces acting on the colloids, i.e. fluid drag, gravity, colloidal interaction, and diffusion (165).

The model of Johnson et al. (165) demonstrates two important mechanisms of colloid retention in the presence of an energy barrier to deposition: 1) wedging; and 2) retention in zones of flow stagnation. It is important to note that these mechanisms of retention were driven by the same forces used in the traditional Happel sphere in cell model. The only significant change was the geometry of the unit collector used (simple and dense packing) to represent the porous media, and the corresponding fluid flow field.

Deposition via wedging and retention in flow stagnation zones is best illustrated by contrast to deposition in the absence of an energy barrier. In the absence of an energy barrier to deposition, the distribution of colloids that do

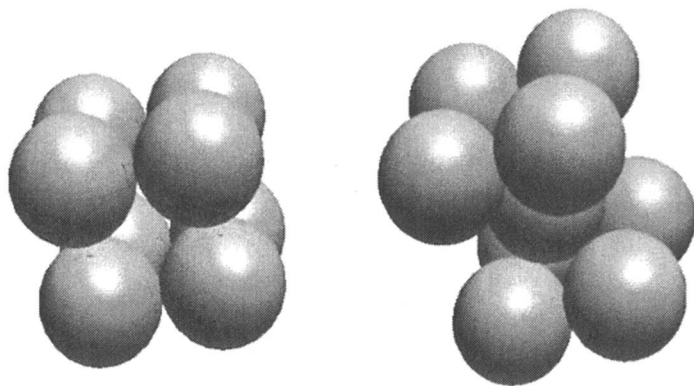


Figure 11. (From 165) Packing arrangement for loose (simple) cubic packing (left) and dense cubic packing (right).

attach is random across the upstream zones of the collector surfaces, as shown by superposition of the simulated locations of attachment onto the unit collectors (Figure 13). The relatively uniform distribution of attached colloids in the absence of an energy barrier to deposition is observed for both unit collectors, and conforms to the distribution of deposition observed in the Happel sphere-in-cell model. As is the case in the Happel model, the fraction of colloids that attach is dependent on colloid size, fluid velocity, and other characteristics that govern the forces acting on the colloids (165).

In contrast to the absence of an energy barrier, colloid deposition in the presence of an energy barrier yields a distribution of retained colloids that is highly dependent on the pore domain geometry. This is shown by mechanistic simulations of colloid trajectories resulting from the forces acting on the colloid after entry into the flow field in the unit collector. The colloid trajectories demonstrate that although the majority of colloids are not retained (e.g. the trajectories in Figure 12), a fraction of the colloids are retained, and the attributes of the pore domain that govern colloid retention are: 1) grain-to-grain contacts; and 2) zones of flow stagnation.

The process of wedging is demonstrated by a 0.4 millisecond portion of a simulated colloid trajectory in the Figure 14. About 275.8 milliseconds after entering the unit collector, the 18- μm (radius) colloid was in secondary energy minimum association with two collector surfaces, as shown by the slight attraction (FCOLL1 and FCOLL2 are negative) and small separation distances (H1 and H2) to two both surfaces (grain to grain contact). The diffusion force (ranging up to $1\text{E}-11$ N), was insufficient to drive the colloid through the energy

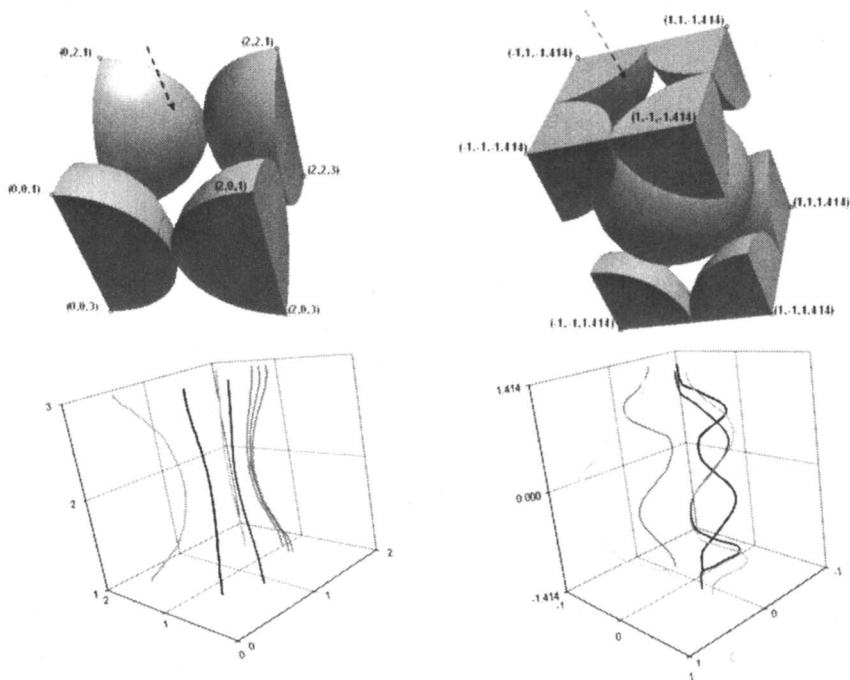


Figure 12. (From 165) Unit collectors for simple cubic packing (top left) and for dense cubic packing (top right). Arrows denote direction of flow in z (upward) dimension. Coordinates (x,y,z) are normalized to the collector radius. Example colloid trajectories in the simple cubic unit collector (bottom left) and the dense cubic unit collector (bottom right).

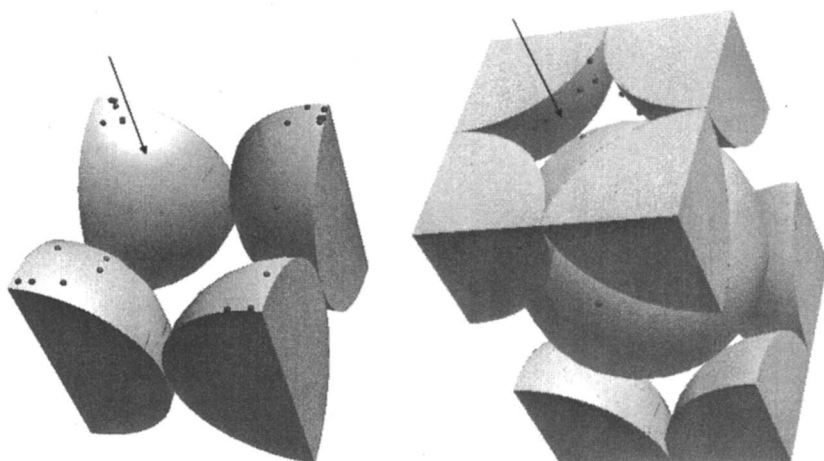


Figure 13. (From 165) Distribution of attached colloids in the absence of an energy barrier to deposition in the simple-packed (loose-packed) unit collector (left), and the dense-packed unit collector (right). The distribution was developed by superimposing locations of attachment determined in the simulations onto the unit collectors. Arrows denote directions of flow in z dimension. Colloid and collectors are not proportionally scaled.

barrier (positive $FCOLL1$ and $FCOLL2$), whereas the fluid drag force overwhelmed the repulsive interaction force, leading to strong primary minimum interactions with one collector, and attachment to that surface.

By superimposing the coordinates of retained colloids it was observed that colloids retained via wedging were retained at grain-to-grain contacts (Figure 15). Note that attached colloids located on the outside of the unit collector were wedged between the center spheres of the unit collector shown, and the adjacent unit-collector.

The simulations demonstrate that wedging (and straining) are physico-chemically equivalent to classic attachment, except that wedging (and straining) constitute attachment that occurs despite the energy barrier to attachment due to the confinement of the colloid between two (wedging) or more (straining) energy barriers (surfaces). Confinement of the colloid between two or more energy barriers causes any movement away from one energy barrier to constitute movement toward another energy barrier, thereby forcing the colloid to overcome one of the energy barriers. A distinction between attachment and straining has been made in recent literature (e.g. 167), whereas the demonstrations shown here indicate that this distinction is false. Wedging and straining are attachment enabled by confinement of the colloid between

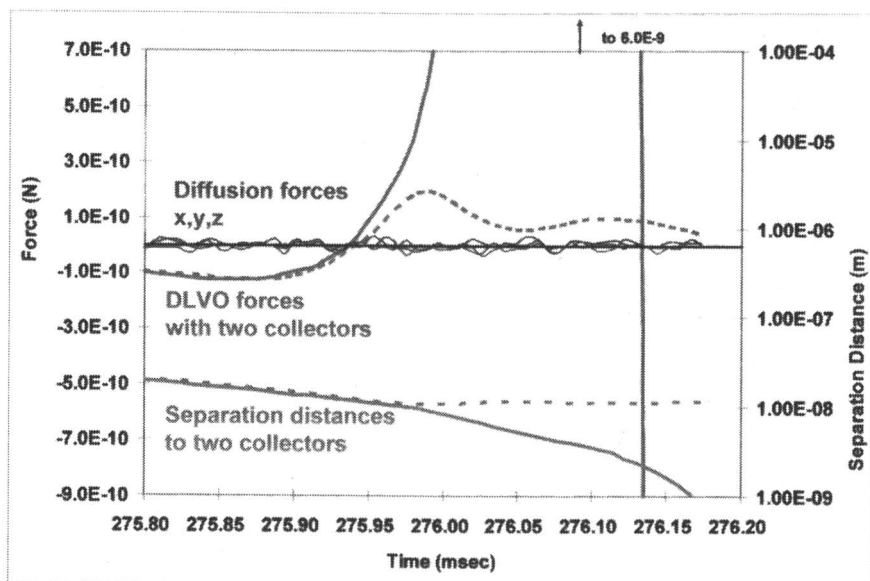


Figure 14. (From 165) Wedging of an 18- μm microsphere in a grain-to-grain contact as demonstrated via a simulated trajectory (superficial velocity = $4.0\text{E-}4$ m-sec $^{-1}$, collector radius = 390 μm , ionic strength = 0.001 M). Diffusion forces are shown by thin lines randomly varying about zero.

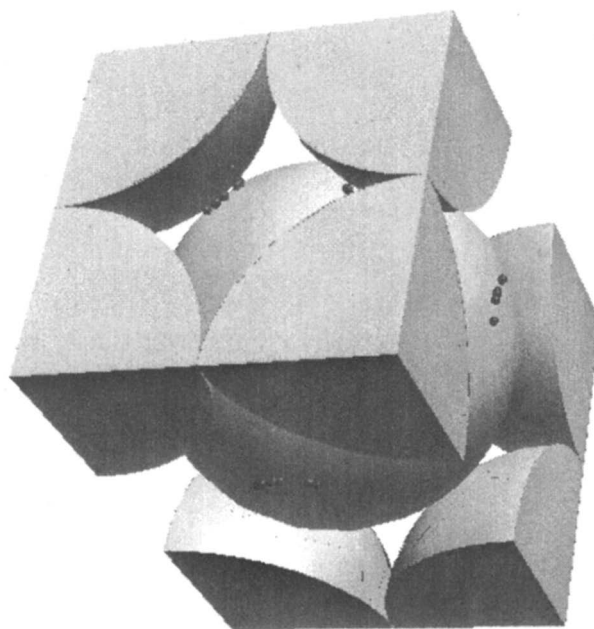


Figure 15. (From 165) Distribution of wedged colloids in the presence of an energy barrier to deposition in the dense cubic unit collector. The distribution was developed by superimposing onto the unit collectors the locations of wedged colloids determined in the simulations. Note that attached colloids located on the outside of the unit collector were wedged between the center spheres of the unit collector shown, and the adjacent unit collector. The direction of flow was from top to bottom.

bounding surfaces; two in the case of wedging, and three or more in the case of straining.

The process of colloid retention in zones of flow stagnation is demonstrated by a 22-second portion of a simulated colloid trajectory in the Figure 16. When the $0.55\ \mu\text{m}$ particle approached the repulsive surface, an equilibrium separation distance was achieved where the attractive van der Waals forces balanced the repulsive electric double layer forces. The attractive force was only on the order of $1\text{E-}12\ \text{N}$, whereas the diffusion forces ranged up to $1\text{E-}9\ \text{N}$ (not shown). The apparent magnitude of the diffusion force is misleading, since it is inversely proportional to time step size; whereas, the randomness of diffusion mitigates the impact of the apparently large force over the series of time steps. The randomness of diffusion allowed continued retention of the colloid in the secondary energy minimum, and the particle translated along the collector surface at the equilibrium separation distance corresponding to the secondary energy minimum.

As the particle translated across the surface, it intercepted a zone of flow stagnation, where it was retained, as shown by superimposing coordinates of colloids that were retained without attachment onto the unit collector (Figure

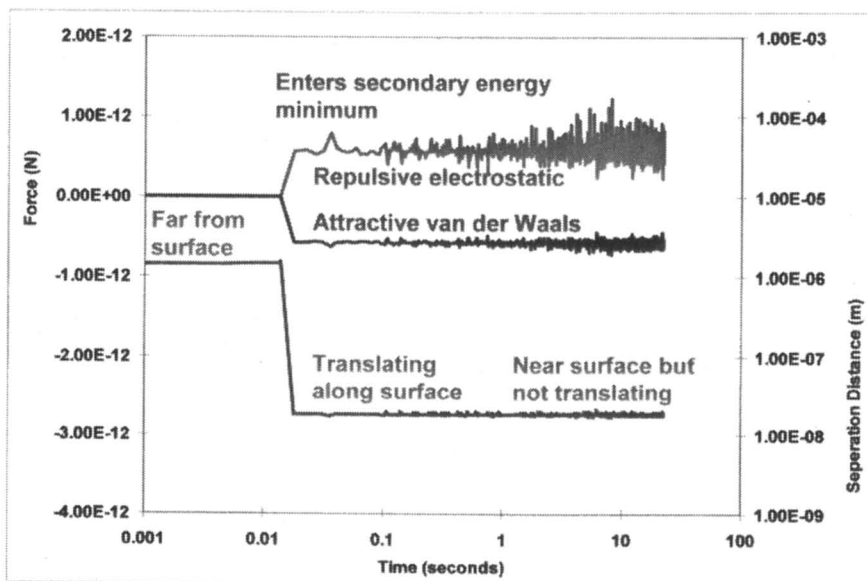


Figure 16. (From 165) Retention of a $0.55\text{-}\mu\text{m}$ microsphere in a flow stagnation zone as demonstrated via a simulated trajectory (superficial velocity = $4.0\text{E-}4\ \text{m-sec}^{-1}$, collector radius = $255\ \mu\text{m}$, ionic strength = $0.001\ \text{M}$).

17). A distinction between attachment and retention in flow stagnation zones is useful, since attachment can be considered for the most part irreversible in the absence of charge reversal (as described above, and e.g. 162), whereas retention in flow stagnation zones is easily reversed, e.g. by decreased ionic strength (elimination of secondary energy minima), or spontaneously by diffusion out of secondary energy minima.

The simulations indicated that wedging was favored by colloid:collector ratios greater than about 0.005 (colloid sizes greater than $1\ \mu\text{m}$, where the collector radius was $255\ \mu\text{m}$), with this threshold ratio increasing with decreasing fluid velocity (165) (Figure 18). Retention in flow stagnation zones

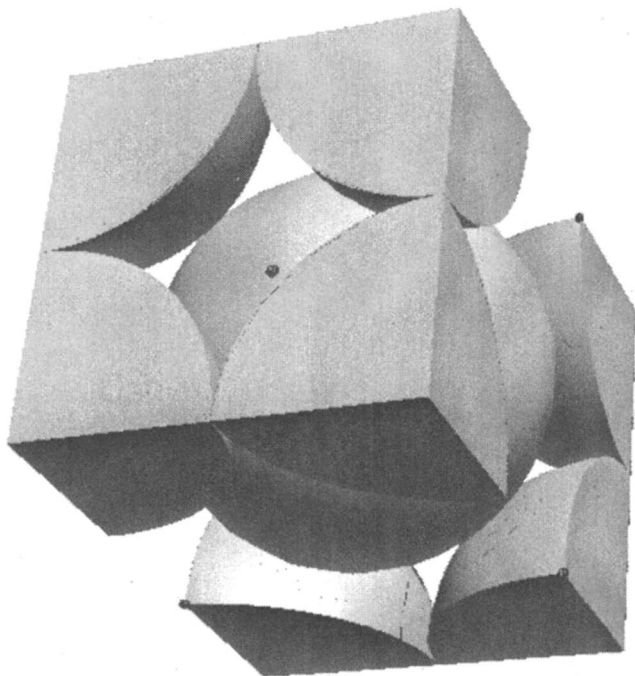


Figure 17. (From 165) Distribution of colloids retained in flow stagnation zones in the presence of an energy barrier to deposition in the dense-packed unit collector. The distribution was developed by superimposing onto the unit collectors the locations of colloids remaining stationary despite remaining unattached in the simulations. Direction of flow was from bottom to top. Colloid and collectors are not proportionally scaled.

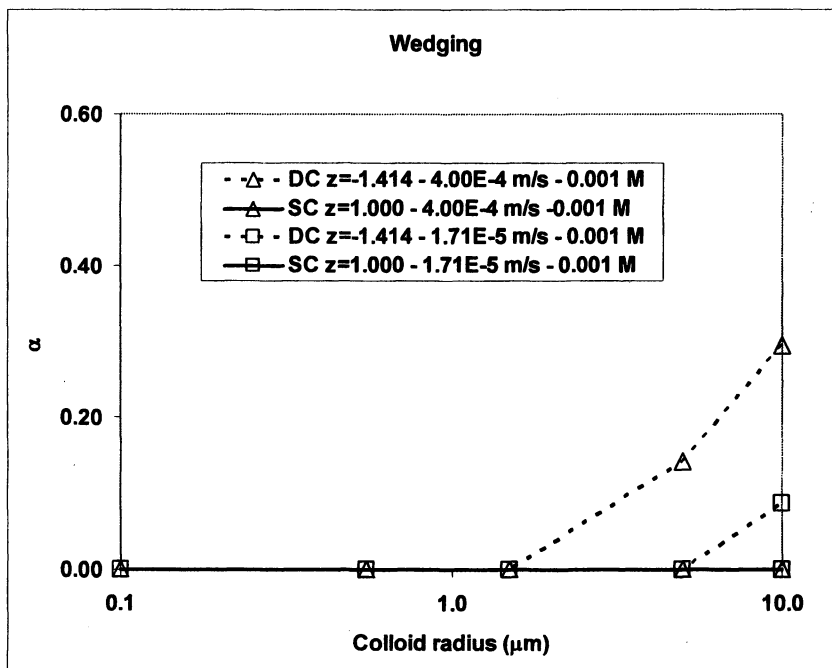


Figure 18 (following page). (From 165) Retention (deposition) efficiency (α) (ratio of collector efficiency in presence relative to absence of energy barrier) in the SC unit collector (entry plane $z=0$ and $z=1$) and the DC unit collector (entry plane $z=-1.414$ and $z=0$) as a function of colloid radius for wedging (top) and retention in flow stagnation zones (bottom). Simulations were conducted for two superficial velocities at an ionic strength of 0.001 M.

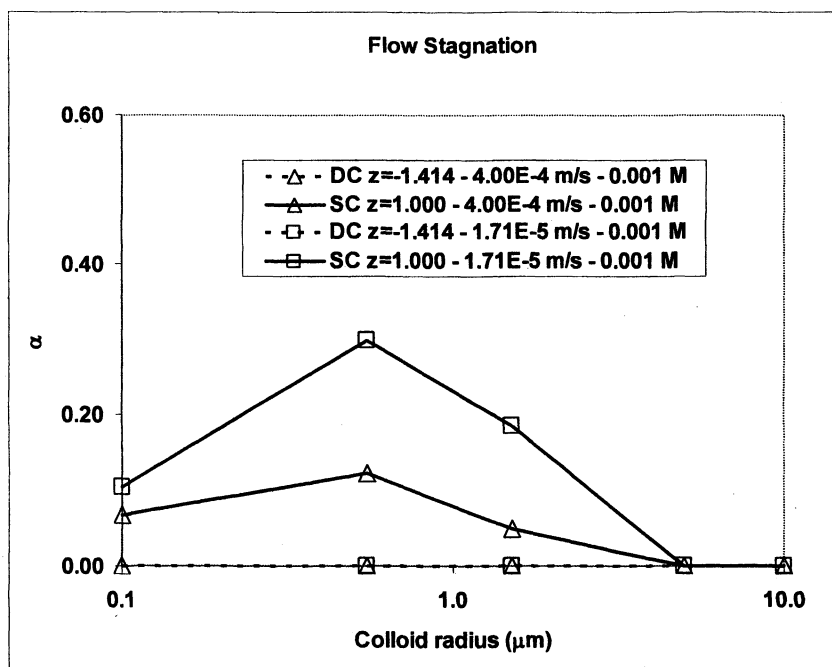


Figure 18. Continued.

was demonstrated to occur for colloid:collector ratios less than about 0.005, with this threshold decreasing with increasing fluid velocity (165) (Figure 18). Both wedging and retention in flow stagnation zones were sensitive to colloid-surface interaction forces (energy barrier height and secondary energy minimum depth) (Figure 19). Notably, the simulations predicted decreased α with increased fluid velocity, as observed in experiments (165).

In the simulations performed in the presence of an energy barrier, increased secondary energy minimum depth increased colloid translation along the collector surfaces and led to increased wedging and retention in flow stagnation zones (Figure 19). This result provides an explanation for the observed (in experiments) sensitivity of colloid deposition to colloid-interaction forces despite the presence of a formidable energy barrier. The colloids that are retained do not pass over the energy barrier, but rather translate along the surfaces in secondary-minimum association with the surface until they become wedged or retained in flow stagnation zones. Note that the term “flow stagnation zone” is provisional as a means of representing retention via secondary energy minima, since colloid retention may also potentially occur via

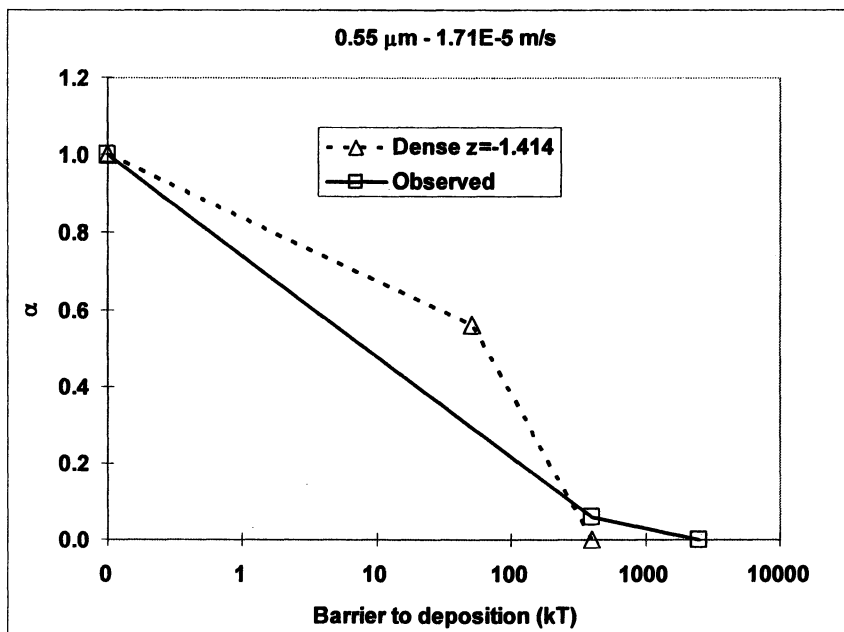


Figure 19 (page after next). (From 165) Top: Total retention (deposition) efficiency (α) (ratio of collector efficiency in presence relative to absence of energy barrier) via combined wedging and retention in flow stagnation zones in the DC unit collector as a function of height of the energy barrier to deposition, which was manipulated via ionic strength. Observed values are from Li et al., (36). Bottom: Retention (deposition efficiency) (α) via wedging versus retention in flow stagnation zones in the DC unit collector as a function of depth of the secondary energy minimum, which was manipulated via ionic strength.

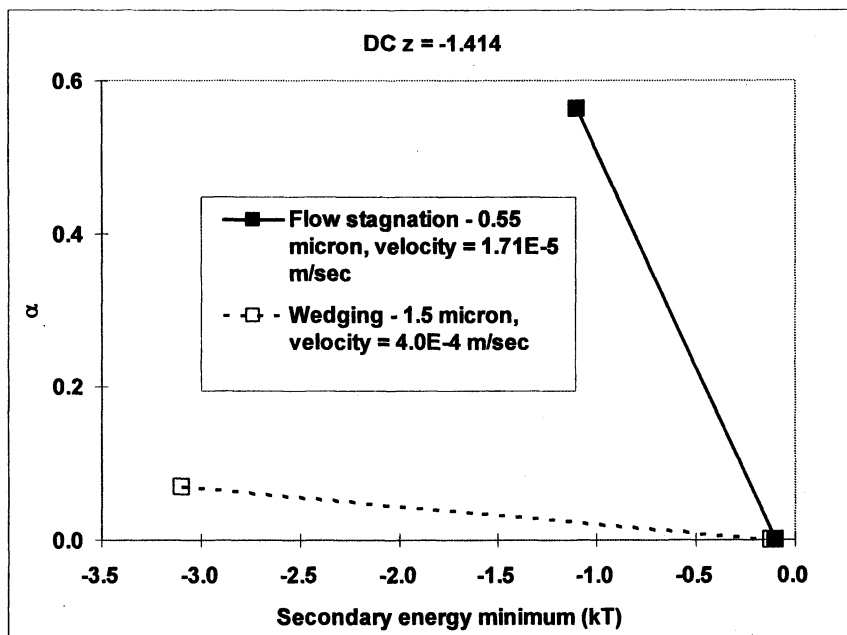


Figure 19. Continued.

secondary minimum interaction with attached or retained colloids in addition to collectors.

Implications for Colloid Retention in Porous Media

The experimental data and simulations presented here demonstrate that colloid deposition in porous media is a much more dynamic process than has been traditionally considered. Colloid deposition is reduced, and re-entrainment is promoted, by decreased solution ionic strength, and increased fluid velocity, both of which can be expected to occur during high runoff events. The dynamic nature of colloid deposition provides a potential explanation for the variety of observed distributions of retained colloids with transport distance, e.g. hyper-exponential or non-monotonic. These distributions challenge our ability to predict transport distances.

The mechanisms of deposition demonstrated here (i.e. retention via secondary energy minima in flow stagnation zones and wedging in grain to grain contacts) display different dependencies on fluid velocity, colloid size (Figure

18), and colloid-surface interaction forces (Figure 19), and provide a potential explanation of the difficulty in generalizing deposition behaviors among different colloids (e.g. 88). These mechanisms, along with surface heterogeneity, lay a foundation for mechanistic prediction of colloid retention in the presence of an energy barrier, one that can be potentially up-scaled via a correlation equation for ready prediction of colloid retention in porous media in the presence of an energy barrier. This goal will involve accounting for colloid-colloid interaction in flow stagnation zones, and the development of dimensionless parameters relating pore domain geometry attributes such as the length and number of grain to grain contacts (124, 152) to readily-measured parameters such as grain size distribution and grain shape. The degree to which these mechanisms can be generalized to microbial surfaces (given their complexity) needs to be tested; however, experimental observations supporting these mechanisms were made for both biological and non-biological colloids (as described above) suggesting their wide relevance. The mechanisms of deposition elucidated here also provide a basis for mechanistic understanding of enhanced colloid deposition at sediment textural interfaces, where pore domain geometry at the interface between textural units differs from within the bounding units. An ability to mechanistically simulate colloid retention at textural interfaces will yield improved models of colloid transport in heterogeneous media.

References

1. Harvey, R. W.; Kinner, N. E.; Bunn, A.; MacDonald, D.; Metge, D. W. *Appl. Environ. Microbiol.* **1995**, *61*(1), 209-217.
2. Grasso, D.; Smets, B. F.; Strevett, K. A.; Machinist, B. D.; van Oss, C. J.; Giese, R. F.; Wu, W. *Environ. Sci. Technol.* **1996**, *30*, 3604-3608.
3. Murphy, E. M.; Ginn, T. R. *Hydrogeology Journal* **2000**, *8*, 142-158.
4. Walker, S. L. *Coll. Surf. B: Biointerfaces* **2005**, *24*, 181-188.
5. Walker, S. L.; Redman, J. A.; Elimelech, M. *Environ. Sci. Technol.* **2005**, *39*(17), 6405-6411.
6. Neu, T. R. *Microb. Rev.* **1996**, *60*, 151.
7. Jucker, B. A.; Zehnder, A. J. B.; Harms, H. *Environ. Sci. Technol.* **1998**, *32*, 2909-2915.
8. Camesano, T. A.; Logan, B. E. *Environ. Sci. Technol.* **1998**, *32*, 1699-1708.
9. Vigeant, M. A. S.; Ford, R. M. *Appl. Environ. Microb.* **1997**, *63*(9), 3474-3479.
10. Vigeant, M. A. S.; Ford, R. M.; Wagner, M.; Tamm, L. K. *Appl. Environ. Microb.* **2002**, *68*(6), 2794-2801.
11. Ohshima, H. *J. Colloid Interface Sci.* **1994**, *163*, 474-483.

12. Ohshima, H. *Colloids Surf. A: Physicochem. Eng. Aspects* **1995**, *103*, 249-255.
13. Jucker, B. A.; Harms, H.; Hug, S. J.; Zehnder, A. J. B. *Coll. Surf. B: Biointerfaces* **1997**, *9*, 331-343.
14. Morisaki, H.; Nagai, S.; Ohshima, H.; Ikemoto, E.; Kogue, K. *Microbiol* **1999**, *145*, 2797-2802.
15. Camesano, T. A.; Logan, B. E. *Environ. Sci. Technol.* **2000**, *34*, 3354-3362.
16. Hayashi, H.; Tsuneda, S.; Hirata, A.; Sasaki, H. *Coll. Surf. B: Biointerfaces* **2001**, *22*, 149-157.
17. Velegol, S. B.; Logan, B. E. *Langmuir* **2002**, *18*, 5256-5262.
18. Burks, G. A.; Velegol, S. B.; Paramonova, E.; Lindenmuth, B. E.; Feick, J. D.; Logan, B. E. *Langmuir* **2003**, *19*, 2366-2371.
19. Abu-Lail, N. I.; Camesano, T. A. *Environ. Sci. Technol.* **2003**, *37* (10), 2173-2183.
20. Abu-Lail, N. I.; Camesano, T. A. *Biomacromolecules* **2003**, *4* (4), 1000-1012.
21. Tong, M.; Camesano, T. A.; Johnson, W. P. *Environ. Sci. Technol.* **2005**, *39* (10), 3679-3687.
22. Buddemier, R. W.; Hunt, J. R. *Appl. Geochem.* **1988**, *3* (5), 535-548.
23. Champ, D. R.; Shroeter, J. *Wat, Sci, Tech.* **1988**, *20* (11-12), 81-87.
24. Bales, R. C.; Gerba, C. P.; Grondin, G. H.; Jensen, S. L. *Appl. Environ. Microb.* **1989**, *55* (8), 2061-2067.
25. Toran, L.; Palumbo, A. V. *J. Contam. Hydrol.* **1992**, *9*, 289-303.
26. Harvey, R. W.; Kinner, N. E.; MacDonald, D.; Metge, D. W.; Bunn, A. *Water Resour. Res.* **1993**, *29*(8), 2713-2722.
27. Vilks, P.; Bachinski, D. B. *J. of Contam. Hyd.* **1996**, *21*, 269-279.
28. Morley, L. M.; Hornberger, G. M.; Miller, A. L.; Herman, J. S. *Water Resour. Res.* **1998**, *34* (8), 1901-1908.
29. Pang, L.; Close, M.; Noonan, M.. *Ground Water* **1998**, *36* (1), 112-122.
30. Zhang, P.; Johnson, W. P.; Piana, M. J.; Fuller, C. C.; Naftz, D. L. *Ground Water* **2001**, *39*, (831-840).
31. Keller, A. A.; Sirivithapakorn, S.; Chrysikopoulos, C. V. *Water Resour. Res.* **2004**, *40*, W08304, doi:10.1029/2003WR002676.
32. Bhattacharjee, S.; Ko, C. H.; Elimelech, M. *Langmuir* **1998**, *14*, 3365-3375.
33. Shellenberger, K.; Logan, B. E. *Environ. Sci. Technol.* **2002**, *36*(2), 184-189.
34. Fontes, D. E.; Mills, A. L.; Hornberger, G. M.; Herman, J. S. *Appl. Environ. Microb.* **1991**, *57*(9), 2473-2481.
35. Scholl, M. A.; Harvey, R. W. *Environ. Sci. Technol.* **1992**, *26*, 1410-1417.
36. Ryan, J. N.; Gschwend, P. M. *Environ. Sci. Technol.* **1994**, *28*, 1717-1726.
37. Ryan, J. N.; Gschwend, P. M. *J. Colloid Interface Sci.* **1994**, *164*, (21-34).
38. Li, Q.; Logan, B. E. *Water Res.* **1999**, *33* (4), 1090-1100.

39. Ryan, J. N.; Elimelech, M.; Ard, R. A.; Harvey, R. W.; Johnson, P. R. *Environ. Sci. Technol.* **1999**, *33*, 63-73.
40. Lenhart, J. J.; Saiers, J. E. *Environ. Sci. Technol.* **2003**, *37* (12), 2780-2787.
41. Schelde, K.; Moldrup, P.; Jacobsen, O. H.; de Jonge, H.; de Jonge, L. W.; Komatsu, T. *Vadose Zone J.* **2002**, *1*, 125-136.
42. Kjaergaard, C.; Poulsen, T. G.; Moldrup, P.; de Jonge, L. W. *Vadose Zone J.* **2004**, *3*, 413-423.
43. Dussart-Baptista, L.; Massei, N.; Dupont, J. P.; Jouenne, T. *J. Hydrol.* **2003**, *284*, 285-295.
44. Kosakowski, G. *J. Contam. Hydrol.* **2004**, *72*, 23-46.
45. Reno, M. D.; James, S. C.; Altman, S. J. *J. Coll. Int. Sci.* **2006**, *300*, (383-390).
46. Gao, B.; Saiers, J. E. *Water Resour. Res.* **2004**, *40*, W08602, doi: 10.1029/2004WR003189.
47. Kjaergaard, C.; Moldrup, P.; de Jonge, L. W.; Jacobsen, O. H. *Vadose Zone J.* **2004**, *3*, 424-433.
48. Darnault, C. J. G.; Steenhuis, T. S.; Garnier, P.; Kim, M. B.; Jenkins, M. B.; Ghiorse, W. C.; Baveye, P. C.; Parlange, J. Y. *Vadose Zone J.* **2004**, *3*, 262-270.
49. Rousseau, M.; Pietro, L. D.; Angulo-Jamarillo, R.; Tessier, D.; Cabibel, B. *Vadose Zone J.* **2004**, *3*, 247-261.
50. Wan, J.; Tokunaga, T. K. *Environ. Sci. Technol.* **1997**, *31* (8), 2413-2420.
51. Sirivithayapakorn, S.; Keller, A. *Environ. Sci. Technol.* **2003**, *32*, 2100-2105.
52. Saiers, J. E.; Lenhart, J. J. *Water Resour. Res.* **2003**, *39*(1), doi:10.1029/2002WR001370.
53. Crist, J. T.; McCarthy, J. F.; Zevi, Y.; Baveye, P.; Throop, J.A.; Steenhuis, T. S. *Vadose Zone J.* **2004**, *3*, 444-450.
54. Zevi, Y.; Dathe, A.; McCarthy, J. F.; Richards, B. K.; Steenhuis, T. S. *Environ. Sci. Technol.* **2005**, *39* (18), 7055-7064.
55. Gao, B.; Saiers, J. E.; Ryan, J. N. *Wat. Resour. Res.* **2006**, *42*, W01410, doi:10.1029/2005WR004233.
56. Wan, J.; Wilson, J. L. *Water Resour. Res.* **1994**, *30* (4), 857-864.
57. Zhuang, J.; Qui, J.; Jin, Y. *Environ. Sci. Technol.* **2005**, *39* (20), 7853-7859.
58. Han, J.; Jin, Y.; Willson, C. S. V. *Environ. Sci. Technol.* **2006**, *40* (5), 1547-1555.
59. Yao, K. M.; Habibian, M. T.; O'Melia, C. R. *Environ. Sci. Technol.* **1971**, *5* (11), 1105-1112.
60. Rajagopalan, R.; Tien, C. *AIChE J* **1976**, *22*(3), 523-533.
61. Logan, B. E.; Jewett, D. G.; Arnold, R. G.; Bouwer, E. J.; O'Melia, C. R. *J. Environ. Eng.* **1995**, *121*, 869-873.
62. Tufenkji, N.; Elimelech, M. *Environ. Sci. Technol.* **2004**, *38* (2), 529-536.

63. Nelson, K. E.; Ginn, T. R. *Langmuir* **2005**, *21* (6), 2173-2184.
64. Happel, J. *AIChE J* **1958**, *4*(2), 197-201.
65. Derjaguin, B. V.; Landau, L. *Acta Physicochim URSS* **1941**, *14*, 633-662.
66. Verwey, E. J. W.; Overbeek, J. T. G. Elsevier: Amsterdam, **1948**.
67. Elimelech, M.; O'Melia, C. R. *Environ. Sci. Technol.* **1990**, *24*(10), 1528-1536.
68. Elimelech, M. *Water Resour. Res.* **1992**, *1*, 1-8.
69. Bai, R.; Tien, C. *J. Coll. Inter. Sci.* **1996**, *179*, 631-634.
70. Vaidyanathan, R.; Tien, C. *Chem. Eng. Comm.* **1989**, *81*, 123-144.
71. Chang, Y.; Whang, J. *Chem. Eng. Sci.* **1998**, *53* (23), 3923-3939.
72. Bai, R.; Tien, C. *J. Coll. Inter. Sci.* **1999**, *218*, 488-499.
73. Davis, J. A. *Geochim. Cosmochim. Acta* **1982**, *46*, 2381-2393.
74. Tipping, E.; Cooke, D. *Geochim. Cosmochim. Acta* **1982**, *46*, 75-80.
75. Song, L.; Elimelech, M. *Coll. Surf. A: Physicochem. Eng. Aspects* **1993**, *73*, 49-63.
76. Song, L.; Elimelech, M. *J. Colloid Interface Sci.* **1994**, *167*, 301-313.
77. Coston, J. A.; Fuller, C. C.; Davis, J. A. *Geochim. Cosmochim. Acta* **1995**, *59*, 3535-3547.
78. Johnson, P. R.; Sun, N.; Elimelech, M. *Environ. Sci. Technol.* **1996**, *30*(11), 3284-3293.
79. Johnson, W. P.; Logan, B. E. *Wat. Res.* **1996**, *30*(4), 923-931.
80. Powelson, D. K.; Simpson, J. R.; Gerbe, C. P. *Appl. Environ. Microb.* **1991**, *57*, 2192-2196.
81. Pieper, A. P.; Ryan, J. N.; Harvey, R. W.; Amy, G. L.; Illangasekare, T. H.; Metge, D. W. *Environ. Sci. Technol.* **1997**, *31* (4), 1163-1170.
82. Foppen, J. W. A.; Oklety, S.; Schijven, J. F. *J. Contam. Hydrol.* **2006**, *85*, 287-301.
83. Thurman, E. M. *Organic Geochemistry of Natural Waters*, Martinus Nijhoff/Junk, Dordrecht, The Netherlands. **1985**
84. Dai, X.; Hozalski, R. M. *Wat. Res.* **2002**, *36*, 3523-3532.
85. Brown, D. G.; Jaffe, P. R. *Environ. Sci. Technol.* **2006**, *40* (1), 195-201.
86. Elimelech, M.; Nagai, M.; Ko, C.-H.; Ryan, J. N. *Environ. Sci. Technol.* **2000**, *34*, 2143-2148.
87. Abudalo, R. A.; Bogatsu, Y. G.; Ryan, J. N.; Harvey, R. W.; Metge, D. W.; Elimelech, M. *Environ. Sci. Technol.* **2005**, *39* (17), 6412-6419.
88. Hijnen, W. A. M.; Brouwer-Hanzens, A. J.; Charles, K. J.; Medema, G. J. *Environ. Sci. Technol.* **2005**, *39* (20), 7860-7868.
89. van Loosdrecht, M. C. M.; Lyklema, J.; Norde, W.; Zehnder, A. J. B. *Microb. Ecol.* **1989**, *17*, 1-15.
90. van Loosdrecht, M. C. M.; Lyklema J.; Norde W.; Zehnder, A. J. B. *Aquat. Sci.* **1990**, *52*, 103-114.
91. Morrow, J. B.; Stratton, R.; Yang, H. H.; Smets, B. F.; Grasso, D. *Environ. Sci. Technol.* **2005**, *39* (17), 6395-6404.

92. van Oss, C. J. *Interfacial Forces in Aqueous Media*. Marcel Dekker: New York, 1994.
93. Chen, G.; Zhu, H. *Coll. Surf. B: Biointerfaces* **2005**, *44*, 41-48.
94. Rijnaarts, H. H. M.; Norde, W.; Bouwer, E. J.; Lyklema, J.; Zehnder, A. J. B. *Appl. Environ. Microb.* **1993**, *59* (10), 3255-3265.
95. Rijnaarts, H. H. M.; Norde, W.; Bouwer, E. J.; Lyklema, J.; Zehnder, A. J. B. *Coll. Surf. B: Biointerfaces* **1995**, *4*, 5-22.
96. Considine, R. F.; Dixon, D. R.; Drummond, C. J. *Wat. Res.* **2002**, *36*, 3421-3428.
97. Kuznar, Z. A.; Elimelech, M. *Environ. Sci. Technol.* **2004**, *38*, 6839-6846.
98. Kuznar, Z. A.; Elimelech, M. *Langmuir* **2005**, *21*, 710-716.
99. Byrd, T. L.; Walz, J. Y. *Environ. Sci. Technol.* **2005**, *39* (24), 9574-9582.
100. Kuznar, Z. A.; Elimelech, M. *Environ. Sci. Technol.* **2006**, *40* (6), 1837-1842.
101. Tufenkji, N.; Dixon, D. R.; Considine, R.; Drummond, C. J. *Water Resour. Res.* **2006**, *40*, 3315-3331.
102. Rehmann, L. L. C.; Welty, C.; Harvey, R. W. *Water Resour. Res.* **1999**, *35* (7), 1987-2006.
103. Ren, J.; Packman, A. I.; Welty, C. *Water Resour. Res.* **2000**, *36* (9), 2493-2500.
104. Barber, L. S. Ph.D Dissertation, University of Colorado at Boulder, CO, 1990.
105. Harvey, R. W.; Garabedian, S. P. *Environ. Sci. Technol.* **1991**, *25* (1), 178-185.
106. Albinger, O.; Biesemeyer, B. K.; Arnold, R. G.; Logan, B. E. *FEMS Microbiol. Lett.* **1994**, *124*, 321-326.
107. DeFlaun, M. F. M.; C. J.; Holben, M.; Scheibe, T.; Mills, A.; Ginn, T.; Griffin, T.; Majer, E.; Wilson, J. L. *FEMS Microbiol. Rev.* **1997**, *20*, 473-487.
108. Baygents, J. C.; Glynn Jr. J. R.; Albinger, O.; Biesemeyer, B. K.; Ogden, K. L.; Arnold, R. G. *Environ. Sci. Technol.* **1998**, *32* (11), 1596-1603.
109. Simoni, S. F.; Harms, H.; Bosma, T. N. P.; Zehnder, A. J. B. *Environ. Sci. Technol.* **1998**, *32* (14), 2100-2105.
110. Bolster, C. H.; Mills, A. L.; Hornberger, G.; Herman, J. *Water Resour. Res.* **1999**, *35*, 1797-1807.
111. Bolster, C. H.; Mills, A. L.; Hornberger, G.; Herman, J. *Ground Water* **2000**, *38* (3), 370-375.
112. Zhang, P.; Johnson, W. P.; Scheibe, T. D.; Choi, K.; Dobbs, F. C.; Mailloux, B. J. *Water Resour. Res.* **2001**, *37* (11), 2687-2698.
113. Bales, R. C.; Li, S. M.; Yeh, T. C. J.; Lenczewski, M. E.; Gerba, C. P. *Water Resour. Res.* **1997**, *33*, 639-648.
114. Schijven, J. F.; Hoogenboezem, W.; Hassanizadeh, S. M.; Peters, J. H. *Water Resour. Res.* **1999**, *35*(4), 1101-1111.

115. Redman, J. A.; Estes, M. K.; Grant, S. B. *Coll. Surf. A: Physicochem. Eng. Asp.* **2001**, *191* (1-2), 57-70.
116. Pang, L.; Close, M.; Goltz, M.; Noonan, M. *J. Contam. Hydrol.* **2005**, *77*, 165-194.
117. Johnson, W. P. *J. Contam. Hydrol.* **2006**, *86*, 160-161.
118. Li, X.; Scheibe, T. D.; Johnson, W. P. *Environ. Sci. Technol.* **2004**, *38* (21), 5616-5625.
119. Tufenkji, N.; Elimelech M. *Langmuir* **2004**, *20*, 10818-10828.
120. Johnson, W. P.; Li, X.; Tong, M. *EOS* **2005**, *86* (18), 179-180.
121. Li, X.; Johnson, W. P. *Environ. Sci. Technol.* **2005**, *39* (6), 1658-1665.
122. Tong, M.; Li, X.; Brow, C.; Johnson, W. P. *Environ. Sci. Technol.* **2005**, *39* (8), 2500-2508.
123. Li-Chong, X.; Logan, B. E. *Coll. Surf. B: Biointerfaces* **2006**, *48*, 84-94.
124. Li, X.; Lin, C. L.; Miller, J.; Johnson, W. P. *Environ. Sci. Technol.* **2006**, *40* (12), 3762-3768.
125. Tong, M.; Johnson, W. P. *Environ. Sci. Technol.* **2007**, *41*(2), 493-499, DOI: 10.1021/es061202j.
126. Yan, Y. D. *Langmuir* **1996**, *12*, 3383-3388.
127. Niehren, S.; Kinzelbach, W. *J. Contam. Hydrol.* **1998**, *36*, 249-259.
128. Cumbie, D. H.; McKay, L.D. *J. Contam. Hydrol.* **1999**, *37*, 139-157.
129. Grolimund, D.; Borkovec, M. *Environ. Sci. Technol.* **1999**, *33* (2), 4054-4060.
130. Grolimund, D.; Barmettler, K.; Borkovec, M. *Water Resour. Res.* **2001**, *37* (3), 571-582.
131. Hornberger, G. M.; Mills, A. L.; Herman, J. S. *Water Resour. Res.* **1992**, *28*, 915-938.
132. Tan, Y.; Gannon, J. T.; Baveye, P.; Alexander, M. *Water Resour. Res.* **1994**, *30* (12), 3243-3252.
133. Lindqvist, R.; Cho, J. S.; Enfield, C. G. *Water Resour. Res.* **1994**, *30*, 3291-3299.
134. McCaulou, D. R.; Bales, R. C.; Arnold, R. G. *Water Resour. Res.* **1995**, *31* (2), 271-280.
135. Johnson, W. P.; Blue, K. A.; Logan, B. E.; Arnold, R. G. *Water Resour. Res.* **1995**, *31*, (11), 2649-2658.
136. Harter, T.; Wagner, S.; Atwill, E. R. *Environ. Sci. Technol.* **2000**, *34*(1), 62-70.
137. McCarthy, J. F. Preprints of Extended Abstracts, 217th ACS National Meeting, Anaheim, CA, **1999**, 270-271.
138. DeBorde, D. C.; Woessner, W. W.; Kiley, Q. T.; Ball, P. N. *Wat. Res.* **1999**, *33* (10), 2229-2238.
139. Li, X.; Zhang, P.; Lin, C. L.; Johnson, W. P. *Environ. Sci. Technol.* **2005**, *39* (11), 4012-4020.

140. Johnson, W. P.; Li, X.; Assemi, S. *Adv. Wat. Resour.* **2006**, doi:10.1016/j.advwatres.2006.05.020.
141. Tong, M.; Johnson, W. P. *Environ. Sci. Technol.* **2006**, *40*(24), 7725-7731, DOI: 10.1021/es061201r.
142. Bradford, S. A.; Yates, S. R.; Bettahar, M.; Simunek, J. *Water Resour. Res.* **2002**, *38*(12), 1327-1338.
143. Bradford, S. A.; Simunek, J.; Bettahar, M.; Genuchten, M. T. Van.; Yates, S. R. *Environ. Sci. Technol.* **2003**, *37*, 2242-2250.
144. Bradford, S. A.; Bettahar, M.; Simunek, J.; van Genuchten, M. Th. *Vadose Zone J.* **2004**, *3*, 384-394.
145. Bradford, S. A.; Simunek, J.; Bettahar, M.; Tadassa, Y. F.; van Genuchten, M. Th.; Yates, S. R. *Water. Resour. Res.* **2005**, *41*, doi:10.1029/2004WR003675.
146. Tufenkji, N.; Ryan, J. N.; Harvey, R. W.; Elimelech, M. *Environ. Sci. Technol.* **2004**, *38*, 5932-5938.
147. Bradford, S. A.; Bettahar, M. *J. Environ. Qual.* **2005**, *34*, 469-478.
148. Foppen, J. W. A.; Mporokoso, A.; Schijven, J. F. *J. Contam. Hydrol.* **2005**, *76*, 191-210.
149. McDowell-Boyer, L. M.; Hunt J. R.; Sitar, N. *Wat. Resour. Res.* **1986**, *22*, 1901-1921.
150. Herzig, J. P.; Leclerc, D. M.; LeGoff, P. *Ind. Eng. Chem* **1970**, *62*, 129-157.
151. Cushing, R. S.; Lawler, D. F. *Environ. Sci. Technol.* **1998**, *32*, 3793-3801.
152. Li, X.; Lin, C. L.; Miller, J.; Johnson, W. P. *Environ. Sci. Technol.* **2006**, *40* (12), 3769-3774.
153. Adamczyk, Z.; Siwek, B.; Szyk, L. *J. Colloid. Interface. Sci.* **1995**, *174*, 130-141.
154. Weiss, M.; Luthi, Y.; Ricka J. *J. Colloid Interface Sci.* **1998**, *206*, 322-331.
155. Yang, C.; Dabros, T.; Li, D.; Czarnecki, J.; Masliyah, J. H. *J. Colloid Interface Sci.* **1998**, *208*, 226-240.
156. Redman, J. A.; Walker, S. L.; Elimelech, M. *Environ. Sci. Technol.* **2004**, *38*, 1777-1785.
157. Walker, S. L.; Redman, J. A.; Elimelech, M. *Langmuir* **2004**, *20*, 7736-7746.
158. Brow, C.; Li, X.; Ricka, J.; Johnson, W. P. *Coll. Surf. A: Physicochem. Eng. Aspects* **2005**, *253*, 125-136.
159. Franchi, A.; O'Melia, C. R. *Environ. Sci. Technol.* **2003**, *37*, 1122-1129.
160. Hahn, M. W.; O'Melia, C. R. *Environ. Sci. Technol.* **2004**, *38* (1), 210-220.
161. Hahn, M. W.; Abadzic, D.; O'Melia, C. R. *Environ. Sci. Technol.* **2004**, *38* (22), 5915-5924.

162. Johnson, W. P.; Tong, M. *Environ. Sci. Technol.* **2006**, *40* (16), 5015-5021.
163. Elimelech, M. *Sep. Technol.* **1994**, *4* (10), 186-212.
164. Snyder, L. J.; Stewart, W. E. *AIChE J* **1966**, *12* (1), 161-173.
165. Johnson, W. P.; Li, X.; Yal, G. *Environ. Sci. Technol.* **2007**, *41*, 1279-1287, DOI: 10.1021/es061301x..
166. Sorensen, J. P.; Stewart, W. E. *Chem. Eng. Sci.* **1974**, *29*, 811-817.
167. Bradford, S. A.; Simunek, J.; Bettahar, M.; van Genuchten, M. Th.; Yates, S. R. *Wat. Resour. Res.* **2006**, *42*, doi:10.1029/2005WR004791.

Author Index

- Abu-Lail, Nehal I., 133
Basel, Matthew T., 199
Bossmann, Stefan H., 199
Brehm-Stecher, Byron F., 29
Camesano, Terri A., 1, 79, 115, 163
Chen, Gang, 245
Curry, Joan E., 217
Daunert, Sylvia, 13
Delehanty, James B., 101
Deo, Sapna K., 13
Feng, Yanshu, 65
Flomenhoft, Deborah, 13
Fowler, Jr., Vance G., 189
Genberg, Carl, 65
Heo, Cheol Ho, 217
Hilton, Amy Chan, 245
Janik, Katharine, 199
Johnson, Brandy J., 101
Johnson, William P., 297
Kumari, Anjali, 13
Lai, Xin-Zhong, 65
Li, Guanglai, 231
Li, Yang, 65
Ligler, Frances S., 101
Lin, Baochuan, 101
Linford, Matthew R., 65
Liu, Yatao, 79, 163
Lofgren, Joel B., 115
Lower, Steven K., 189
Maier, Raina M., 217
McGimpsey, W. Grant, 79
Mello, Charlene M., 1, 51
Milkani, Eftim, 79
Nelson, Gard, 65
Nelson, Kirk E., 261
Niederweis, Michael, 199
Nielsen, Jason, 65
Pasini, Patrizia, 13
Pinzon-Arango, Paola A., 115
Pouliot, Jeffrey R., 115
Savage, Paul B., 65
Shashidhar, Harohalli, 13
Soares, Jason W., 51
Strauss, Joshua, 79
Tang, Jay X., 231
Williams, Mitch, 245
Yongsunthorn, Ruchirej, 189

Subject Index

A

a. See Sticking efficiency

Adhesion, non-specific, *Escherichia coli*, 102–105

Adhesion forces, function of time, bacteria coated samples, 220–228

Adhesion strength, bacterial, micromanipulation measurements, 231–241

See also *Bacterial adhesion entries*

AFM. See *Atomic force microscopy entries*

AHL detection in biological samples with whole-cell sensing systems, 20–23

Amphiphilic structures, alpha-helices, antimicrobial peptides, 66, 68*f*

Antibacterial activities, thin films containing ceragenin, 65–78

Antibacterial testing, foam coated with ceragenin-polymer conjugate, 72–77

Antibody affinity curves, exponential fit and linearization, 55, 58–59*t*

Antibody normalization, peptide binding behavior, methodology, 55, 58–59*t*

Antimicrobial peptide binding, methodology, 60–61*t*

Antimicrobial peptides, membrane selectivity, 52–62

Antimicrobials as detection reagents, external binders, advantages, 44–45

Assembly state and peptide length in bacterial membrane specificity, 53–54

Atomic force microscopy (AFM) contact mode, determination, shear forces, *M. tuberculosis* cells on mica, 206, 208–209

indentation measurements, bacterial cell wall surface elasticity, 153

living bacteria studies, 133–161

Mycobacterium tuberculosis outer membrane, characterization, 199–215

surface characterization (overview), 4–5

Atomic force microscopy (AFM) force profiles

immobilization technique effects on bacterial surface and interfacial properties, 171
role of immobilization method, 184–186*f*

Atomic force microscopy (AFM) imaging, bacteria, 135–137, 138*f*

Atomic force microscopy (AFM) imaging in liquids, bacteria, preparation, 165–166

B

Bacteria coated samples, adhesion forces, function of time, 220–228

Bacteria cultures and harvesting for atomic force microscopy imaging or force measurements, 166–167

Bacteria imaging by atomic force microscopy, 135–137, 138*f*

Bacterial adhesion and transport in the environment, modeling, 245–260

Bacterial adhesion in flow chamber, 118–119

Bacterial adhesion to surfaces, atomic force microscopy imaging investigations, 140–142*t*

- Bacterial adhesion to surfaces, quantification by force measurements, 143, 145*t*
See also Adhesion entries; Force measurements entries
- Bacterial aggregates, sonication for breaking up, 177–178*f*
- Bacterial and colloid transport in the environment, modeling (overview), 6
- Bacterial and surface interactions, specificity, 151–152, 154*f*–155*f*
- Bacterial anti-adhesive coating, cranberry extract, 115–129
- Bacterial attachment, cranberry extract concentration effects, 119–125*f*
- Bacterial attachment effect, time dependence, 121, 123*f*
- Bacterial cell adhesion inhibition by cranberry proanthocyanidins, 101–114
- Bacterial cell morphology and ultrastructure by atomic force microscopy imaging, 136–138*f*
- Bacterial cell softness, atomic force microscopy force curves, 153, 156
- Bacterial cell wall surface elasticity, estimates from atomic force microscopy indentation measurements, 153
- Bacterial chromosome painting (BCP), generation sequence-specific fluorescence signals within whole microbial cells, 34
- Bacterial communication in gastrointestinal disorders, biosensors for quorum chemical signaling molecules, 13–27
- Bacterial contact angles, measurement, 247
- Bacterial contact with self-assembled monolayers slides, 88
- Bacterial culture, self-assembled monolayers on gold-coated surfaces, 84–85
- Bacterial deposition in porous media, modeling, 252–257*f*
- Bacterial deposition rate coefficient in packed-bed systems, 250
- Bacterial endotoxin. *See* Lipopolysaccharide
- Bacterial interactions with porous media, quantification, 247–249
- Bacterial live-dead viability counting, verification, 88–89
- Bacterial membrane specificity, principles, 53–56
- Bacterial pili, 151
- Bacterial properties via atomic force microscopy imaging, 137, 139–141*f*, 142*t*
- Bacterial-protein-coated self-assembled monolayers, interactions, 95
- Bacterial retention and viability, influence of protein-coated self-assembled monolayers, 95
- Bacterial retention experiments, self-assembled monolayers on gold-coated surfaces, 85–86, 89, 92*f*–93*f*
- Bacterial surface biopolymers, heterogeneity, 145*t*, 148–149*f*
- Bacterial surface biopolymers properties, effect on adhesion to surfaces, 147–148
- Bacterial surface lipopolysaccharides and extracellular polysaccharides, 149–150
- Bacterial surface treatment, atomic force microscopy force measurements, 152
- Bacterial transport, mechanistic models for saturated porous media, 261–295
- Bacterial transport models, 249–252
- Bacterial viability and retention in batch assays, 94
- Bacterial virulence, role of quorum sensing, 15, 17–18

- BCP. *See* Bacterial chromosome painting
- Binding forces associated with *Staphylococcus aureus* biofilms on medical implants, 189–197
- Binding selectivity elucidation, peptide binding behavior, methodology, 56–57f
- Biofilm formation, prevention (overview), 2–4
- Biofilm formation, undesirable consequences, 218
- Biofilms, binding forces associated with *Staphylococcus aureus* on medical implants, 189–197
- Biofouling process, 235, 238f
- Biological process incorporation into pore-scale analysis, colloid filtration theory, 287–291
- Biological samples, AHL detection using whole-cell sensing systems, 21–23
- Biomimetics, 42–44
- Biosensing, stimulus responsive polymer brushes, selective bacteria adsorption, atomic force microscopy imaging, 139–141f
- C**
- Carbohydrates in cell-cell interactions, *M. tuberculosis*, 209–213
- Catheter-related infections, 80, 116–118
- Caulobacter crescentus*
 adhesion force measurement, case application, 234f, 235, 237–239f
 bacterial adhesion strength, micromanipulation measurements, 231–241
 cell attachment, stages, 235, 238f
- Cell-based sensors, detection reagents, 45–46
- Cell location for atomic force microscopy using optical microscopy, 192–193
- Cell morphology and ultrastructure by atomic force microscopy imaging, 136–138f
- Cell surface, *Mycobacterium tuberculosis*, biophysical characterization, 199–216
- Cell viability verification through plate counting, 86
- Cell washing, effect on immobilization, 177, 179–180f
- Cellular film preparation, 219
- Central hinge or helix flexibility in bacterial membrane specificity, antimicrobial peptides, 55–56
- Ceragenin containing thin film antibacterial activities, 65–78
 development, 67–68, 69f
 polymer conjugate coating on foam disks, antibacterial testing, 72–77
- Ceragenins, polymeric forms, preparation, 67, 70–72
- Charge and hydrophobicity, bacterial membrane specificity, antimicrobial peptides, 54–55
- Chlorhexidine-releasing foam, antibacterial activity, 72–77
- Chromobacterium violaceum*, pigment production/inhibition for sensing, 19
- Collection efficiency (η), colloid filtration theory
 consistent and inconsistent collector choice, 276, 278–287f
 definition, 263
 equations in colloid filtration theory, 265–270
 Lagrangian method for calculation, 287–291
- Collector choices, consistent and inconsistent, in colloid filtration theory, 276, 278–287f
- Collision efficiency factor in packed-bed systems, 250–251

Colloid deposition in porous media, deposition mechanisms, 328*f*–332

Colloid filtration theory, 301–303
 biological process incorporation, 287–291
 pore-scale analysis, 262–287

Colloid retention in flow stagnation zones, 326–327*f*

Colloid transport in porous media, model development, experimental result effects, 307–332

Colloids, biological and non-biological, retention mechanisms in porous media, 297–339

Colonization, bacteria, imaging by atomic force microscopy, 137, 139

Consistent and inconsistent collectors in colloid filtration theory, 276, 278–287*f*

Contact angle measurements in characterization, self-assembled monolayers on gold-coated surfaces, 82, 87

Contact zone imaging, surface bound bacterial films, 222, 224*f*

Covalent bonding bacterial immobilization for atomic force microscopy imaging or force measurements in liquids, 167–170, 172–175*f*

Cranberry extract, bacterial anti-adhesive coating, 115–129

Cranberry extract concentration effects, bacterial attachment, 119–125*f*

Cranberry juice cocktail, bacteria growth studies, 123, 126*f*

Cranberry proanthocyanidins, bacterial cell adhesion inhibition, 101–114

Cubic packing arrangements in pore domain geometry, effect on colloid deposition, 320–323*f*

D

Deposition rate coefficients, 265

Derjaguin-Landau-Verwey-Overbeek (DLVO) theory, 232, 246–249, 252–257, 303–304

Dose-response curves for standard AHLs, whole-cell sensing systems, 20–21

E

E. coli. See *Escherichia coli*

Electrostatic forces, bacterial immobilization for atomic force microscopy imaging or force measurements in liquids, 170, 173, 175*f*–177

Ellipsometry in characterization, self-assembled monolayers on gold-coated surfaces, 82, 86–87

Energy barriers in numerical models of colloid deposition,

Environment, modeling bacterial adhesion and transport, 245–260

Environmental factors, effects on bacterial adhesion to surfaces, 143, 146–147

Escherichia coli (*E. coli*)
 adhesion in presence of cranberry product, 116–117
 attachment to polymers under flow conditions, study methods, 117–119
 non-specific adhesion, 102–105

Evaporative deposition, bacterial films for use in surface force apparatus, 218–219

Experimental results driving new models, colloid transport in porous media, 307–332

External binders, advantages, antimicrobials as detection reagents, 44–45

Extracellular polysaccharides and lipopolysaccharides, bacterial surface, 149–150

Extracellular roughness, bacteria, variations, by atomic force microscopy, 139

F

Fate and transport in subsurface, models for bacteria, 245–260

Film formation, incomplete, 219–220f

Filtration equation for Happel model in colloid filtration theory, 270–277f

Filtration theory predictions, deviation from experimental data, effect on new model development, 307–310f

Fimbriae. *See* Bacterial pili

FISH. *See* Fluorescence *in situ* hybridization

Flexible micropipette force constant determination, two-micropipette method, adhesion force measurements, 234–236f

Flow cytometry combined with fluorescence *in situ* hybridization, 40–42

Flow stagnation zones, wedging and retention, in new model development, colloid transport theory, 319–331f

Fluid drag influence on new model development, colloid transport theory, 308, 310–313f

Fluorescence *in situ* hybridization (FISH), 35, 36–39 with flow cytometry, 40–42

Foam disks coated with ceragenin-polymer conjugate, antibacterial testing, 72–77

Force binding profiles between *Staphylococcus aureus* and fibronectin-coated probe, 193–196f

Force measurements between bacteria and surfaces, 140, 142–156f

Force measurements over time using surface force apparatus, *Pseudomonas aeruginosa*, 220–228

See also Bacterial adhesion entries

G

Gastrointestinal disorders, bacterial communication, biosensors for quorum chemical signaling molecules, 13–27

Geochemical heterogeneity in porous media, 305–307

H

η . *See* Collection efficiency

Happel collector. *See* Collector choices, consistent and inconsistent, in colloid filtration theory

Happel's sphere-in-cell porous media model, 266, 268f, 269, 270–275, 301–303

Hertz model, application to atomic force microscopy indentation-force data measured on bacterial cells, 153

Heterogeneity, bacterial surface biopolymers, 145t, 148–149f

High-throughput methods for reagent discovery, 44

Honeycomb film preparation, 219

Hospital-induced infections, 116

Hydrophobicity and charge in bacterial membrane specificity, antimicrobial peptides, 54–55

on protein deposited substrates, 87

I

- Imaging parameters for atomic force microscopy imaging, bacterial morphology, 136
- Immobilization
 effect of bacterial cell washing, 177, 179–180f
 mechanical, 182–185f
 optimal conditions, 179, 181–183f
- Immobilization methods
 atomic force microscopy imaging or force measurements in liquids, 167–171
 role on atomic force microscopy force profiles, 184–186f
- Immobilization strength and duration, 179, 181f
- Immobilizing bacteria, atomic force microscopy imaging or force measurements in liquids, 163–188
- In situ* loop-mediated isothermal amplification (LAMP), 36
- In situ* PCR (ISPCR), generation sequence-specific fluorescence signals within whole microbial cells, 33
- In situ* reverse transcription (ISRT), isothermal method of rRNA or mRNA amplification targets, 33–34
- In situ* reverse transcription-PCR (ISRT-PCR), generation sequence-specific fluorescence signals within whole microbial cells, 33
- In situ* rolling circle amplification (RCA), isothermal method of nucleic acid amplification, 35–36
- Inconsistent collectors in colloid filtration theory. *See* Consistent and inconsistent collectors in colloid filtration theory
- Interaction forces in colloid filtration theory, 303–304
- Irreversible bacterial adhesion development, 232

- Isolated collector. *See* Consistent and inconsistent collectors in colloid filtration theory
- ISPCR. *See In situ* PCR
- ISRT. *See In situ* Reverse transcription
- ISRT-PCR. *See In situ* reverse transcription-PCR

L

- Lagrangian method for calculation, collection efficiency (η) in colloid filtration theory, 287–291
- LAMP. *See In situ* loop-mediated isothermal amplification
- Lewis acid/base interaction free energy, surface tension, 247, 248, 252–253
- Lifshitz-van der Waals interactions, 247, 248, 252–254f, 255f–256f
See also Van der Waals interactions
- Lipopolysaccharide and mammalian cells, 108–109
- Lipopolysaccharide and polymyxin B, 106–107f
- Lipopolysaccharides and extracellular polysaccharides, bacterial surface, 149–150
- Live-dead staining kit, use optimization, 88
- Live-dead viability counting, verification, 88–89
- Locked nucleic acids, 43–44

M

- Mechanical bacterial immobilization, 182–185f
 for atomic force microscopy imaging or force measurements in liquids, 171

Mechanistic models, bacterial transport in saturated porous media, 261–295

Medical implants, binding forces associated with *Staphylococcus aureus* biofilms, 189–197

Membrane selectivity, antimicrobial peptides, 52–62

Microbial habitats, 31–32

Microorganisms, whole cell detection methods, 29–51

Micropipette aspiration (overview), 5

Microscopy techniques in microbiology (overview), 164–165

Mobile-immobile region concept, 251–252

Model development, experimental result effects, colloid transport in porous media, 307–332

Modeling bacterial adhesion and transport in the environment, 245–260

Mycobacteria, outer membrane characteristics, 200–201*f*

Mycobacterial surfaces, atomic force microscopy study method, 204–205*f*

Mycobacterium tuberculosis, outer membrane characterization with atomic force microscopy, 199–215

N

N-acylated homoserine lactones. *See* AHL detection

New model development, colloid transport in porous media, 319–332

Nosocomial-acquired. *See* Hospital-induced infections

Nucleic acid-based methods, generating sequence-specific fluorescence signals within whole microbial cells, 32–42

O

Optimizing immobilization conditions, 179, 181–183*f*

Organisms, quorum sensing signaling molecules, 16*t*

Outer membrane characterization with atomic force microscopy, *Mycobacterium tuberculosis*, 199–215

P

P-fimbriae proteins on bacterial cell surface, *E. coli* interaction with human epithelial cells, inhibition by cranberry juice, 104

Pathogenesis, quorum sensing role, 15, 17–18

Peptide length and assembly state in bacterial membrane specificity, antimicrobial peptides, 53–54

Peptide nucleic acids (PNAs), biomimetic reagents, 42–43

Phase imaging, atomic force microscopy for imaging bacteria, 136

Phylogenetic staining. *See* Fluorescence *in situ* hybridization

Plant proanthocyanidins, biological activities, 101–114

“Plate and see” framework, 30

PNAs. *See* Peptide nucleic acids

Polymer bridging model, colloid filtration theory, 289–290*f*

Polymeric forms, ceragenins, preparation, 67, 70–72

Polymyxin B pull-down assay, 106–107*f*

Poly(*N*-isopropylacrylamide), stimulus responsive polymer brushes, 140–141*f*

Pore domain geometry, cubic packing arrangements, effect on colloid deposition, 320–323*f*

Porous media, retention mechanisms of biological and non-biological colloids, 297–339

Preparing bacteria for atomic force microscopy imaging and force measurements in liquids (overview), 165–166

Proanthocyanidin structure, 102, 103*f*

Proanthocyanidins as capture molecules for lipopolysaccharide, 109–111

Proanthocyanidins from cranberries bacterial cell adhesion inhibition, 101–114

purification, 105–106*f*

Protein-coated self-assembled monolayers, *Staphylococcus epidermidis*, retention and viability, 79–99

Pseudomonas aeruginosa, 15
adhesive and elastic properties by surface force apparatus, 217–229
force measurements over time using surface force apparatus, 220–228
tobramycin-resistant, antibacterial activity testing, thin films with ceragenins, 72–77

Q

Quantification by force measurements, bacterial adhesion to surfaces, 143, 145*t*

Quantifying bacterial retention and viability, 85–86

Quorum chemical signaling molecules, biosensors for, 13–27

Quorum sensing, 14–15, 16*t*

Quorum sensing inhibitor selector, 19

R

RCA. *See In situ* rolling circle amplification

Re-entrainment significance, 310

Reagent discovery, high-throughput methods, 44

Residues from *M. tuberculosis* on mica, 204, 206–207*f*

Retention mechanisms, biological and non-biological colloids in porous media, 297–339

Reversible bacterial adhesion development, 232

RT equation for collection efficiency coefficient in colloid filtration theory, 266–268

S

Salmonella-specific fluorescence, 36, 38*f*

Salmonella spp. in raw, cubed pork, direct cytometric detection, 40–41*f*

Saturated bacterial transport models, 249–251

Saturated porous media, mechanistic modeling, bacterial transport, 261–295

Self-assembled monolayers, protein-coated, retention and viability, *Staphylococcus epidermidis*, 79–99

preparation and characterization on gold-coated surfaces, 81–82, 83*f*
protein deposition, bacterial retention assays optimization, 89, 93*f*–94

Sequence-specific fluorescence signals, generation within intact bacterial cells, method comparison, 32–33

SFA. *See* Surface force apparatus

- Shear forces, *M. tuberculosis* cells on mica, atomic force microscopy determination, 206, 208–209
- Signaling and sensing (overview), 2
- Single collector efficiency in packed-bed systems, 251
- Smoluchowski equation, 264
- Sonication for breaking up bacterial aggregates, 177–178f
- Specific binding events, *Staphylococcus aureus* isolates with fibronectin-coated probe, 193–196f
- Specificity, surface and bacterial interactions, 151–152, 154f–155f
- Staining techniques, segregation between live/dead cells, 95–96
- Staphylococcus aureus* biofilms on medical implants, binding forces, 189–197
isolates with fibronectin-coated probe, specific binding events, 193–196f
methicillin-resistant, antibacterial activity testing, thin films with ceragenins, 72–77
- Staphylococcus epidermidis*, retention and viability on protein-coated self-assembled monolayers, 79–99
- Sticking efficiency (α)
calculation in Lagrangian method in colloid filtration theory, 288–289
definition in colloid filtration theory, 263
- Stimulus responsive polymer brushes, selective bacteria adsorption for sensing, atomic force microscopy imaging, 139–141f
- Straining, influence on new model development, colloid transport theory. *See* Wedging and straining
- Strength and duration, bacterial immobilization, 179, 181f
- Streptococcus pneumoniae*, 14
- Substrate properties, effects on bacterial adhesion to surfaces, 147–148f
- Surface and bacterial interactions, specificity, 151–152, 154f–155f
- Surface characterization and microscopy experiments (overview), 4–5
- Surface force apparatus (SFA) and surface characterization (overview), 5
bacteria adhesive and elastic properties measurement, 217–229
- Surface potential, bacterial cell membranes by atomic force microscopy, 139
- Surface tension, Liftshitz-van der Waals component, 247, 248
- T**
- TE equation for collection efficiency coefficient, 269–270
- Thermodynamic theory application to bacterial surfaces, 246–257f
- Thin films containing ceragenin, antibacterial activities, 65–78
- Time dependence, bacterial attachment effect, 121, 123f
- Transport behavior in environmentally porous media, 297–339
- Tuberculosis mortality, 200
- Two-micropipette method, adhesion force measurements, 233–236f
- Two-site saturated bacterial transport models, 249–251
- U**
- Ultrastructure and cell morphology by atomic force microscopy imaging, 136–138f

Unsaturated bacterial transport models, 241–252
Urinary tract infections (UTIs), cranberry juice as preventive, 116

V

Vaccinium macrocarpon. See Cranberry
Van der Waals interactions, 303–304
See also Lifshitz-van der Waals interactions
Van Oss-Chaudhury-Good equation, 247
Verification, cell viability through plate counting, 86
Vibrio fischeri, 14

W

Wedging and retention in flow stagnation zones, new model

development, colloid transport in porous media, 319–331f
Wedging and straining, influence on new model development, colloid transport theory, 311, 314–318f
Whole cell detection methods for microorganisms, 29–51
Whole-cell sensing systems for AHL detection in biological samples, 20–23
Whole-cell sensing systems for quorum sensing, 18–20

Y

YHO equation for collection efficiency coefficient in colloid filtration theory, 265–266